

DEPARTMENT OF PHYSICS  
UNIVERSITY OF JYVÄSKYLÄ  
RESEARCH REPORT No. 5/2018

**Gas-phase chemistry, recoil source  
characterization and in-gas-cell resonance laser  
ionization of actinides at IGISOL**

by

**Ilkka Pohjalainen**

Academic Dissertation  
for the Degree of  
Doctor of Philosophy

*To be presented, by permission of the  
Faculty of Mathematics and Science  
of the University of Jyväskylä,  
for public examination in Auditorium FYS1 of the  
University of Jyväskylä on June 15, 2018  
at 12 o'clock noon*



Jyväskylä, Finland  
June 2018



# Abstract

**Pohjalainen, Ilkka**

**Gas-phase chemistry, recoil source characterization and in-gas-cell resonance laser ionization of actinides at IGISOL**

**Jyväskylä: University of Jyväskylä, 2018, 183 p.**

**Department of Physics Research Report No. 5/2018**

**ISSN: 0075-465X; 5/2018**

**ISBN: 978-951-39-7476-3 (paper version)**

**ISBN: 978-951-39-7477-0 (electronic version)**

**Diss.**

The underlying theme of this thesis focuses on buffer gas purification and relevant gas-phase ion chemistry which critically affects ion beam purity at gas cell-based radioactive ion beam facilities. The achievement of attaining a sub-parts-per-billion level of impurity at the IGISOL facility has enabled subsequent gas cell developments for production of the actinide elements, plutonium and thorium, required for a program of high-resolution optical spectroscopy. Firstly, the construction and characterization of the new IGISOL buffer gas purification system is presented. Off-line ion beam production of plutonium and thorium using in-gas-cell laser resonance ionization combined with filament dispensers has resulted in successful collinear laser spectroscopy of several long-lived plutonium isotopes and has revealed unique collisional phenomena significantly affecting resonance laser ionization in gaseous environments.

Thorium is of particular interest due to  $^{229}\text{Th}$  and its low-energy nuclear isomeric state. By stopping  $^{229}\text{Th}$  recoils from the alpha decay of  $^{233}\text{U}$  in a helium-filled gas cell, a  $^{229}\text{Th}$  ground and isomeric state ion beam can be produced. The recoil efficiency determination of two  $^{233}\text{U}$  sources using direct and implantation foil gamma- and alpha-ray spectroscopy as well as surface characterization by Rutherford back scattering (RBS) measurements have shown the importance of good source quality. The development of a new gas cell to house several such recoil sources is also presented, emphasizing the interplay between gas pressure, size of the gas cell, and diffusion losses during extraction. Finally, this thesis presents the first on-line experiments for the production of  $^{229}\text{Th}$  via proton-induced fusion-evaporation reactions using a  $^{232}\text{Th}$  target.

**Keywords:** nuclear physics, gas cell, gas phase chemistry, resonance laser ionization

**Author's address** Ilkka Pohjalainen  
Department of Physics  
University of Jyväskylä  
Finland

**Supervisors** Prof. Iain Moore  
Department of Physics  
University of Jyväskylä  
Finland

**Reviewers** Prof. Peter Thirolf  
Faculty of Physics  
Ludwig Maximilian University of Munich  
Germany

Dos. Kari Peräjärvi  
Radiation and Nuclear Safety Authority (STUK)  
Finland

**Opponent** Prof. Dave Morrissey  
National Superconducting Cyclotron Laboratory,  
Michigan State University,  
United States



# Preface

The work presented in this thesis has been carried out in the IGISOL group at the Accelerator Laboratory of the University of Jyväskylä during the years 2011-2018.

I would firstly and foremost thank my supervisor Prof. Iain Moore for his invaluable encouragement, support and guidance throughout my thesis work. I want to thank other IGISOL senior persons for their support as well, especially Prof. Ari Jokinen and Prof. Juha Äystö. I also want to thank my pre-examiners Prof. Peter Thirolf and Dos. Kari Peräjärvi for their incredibly thorough review, comments and questions helping me to finalize this work.

I want to thank Sarina Geldhof, Dr. Mikeal Reponen, Dr. Volker Sonnenschein, and Dr. Annika Voss for setting up and helping with the lasers for many of the experiments presented in this thesis as well as Sara El Youbi helping in the construction characterization of the off-line ion guide mass spectrometer system. Big thanks to all present and past members of the IGISOL group with whom I have also had the pleasure spending time outside of the lab. I also owe a great deal of gratitude to all the co-authors of the articles of this thesis and collaborators that have been participating to the experiments presented in this work. I would like to thank all the people of the nuClock consortium especially Prof. Thorsten Schumm and his group who provided all the thorium filaments. I want particularly thank Dr. Hideki Tomita, Noriyoshi Hayashi, Ryohei Terabayashi and Dr. Tobias Kron for all the work related resonance laser ionization of plutonium. I want to thank Prof. Timo Sajavaara and his group for making it possible to use the Pelletron accelerator for Rutherford backscattering measurements and providing support in the interpretation of the results.

I would also like to thank all the people at the mechanical and electrical workshops who have been so helpful and able to carry out all of my rather extraordinary designs with a great precision. A special thanks to Dr. Jaana Kumpulainen who has allowed us to work with all the different actinides.

I also want to thank my parents who have always let me pursue my interests, and finally, I would like to express my deepest gratitude to my husband, Joel,

who has always been extremely supportive of me throughout this journey and endured all my long days at university without a complaint.

Ilkka Pohjalainen  
Jyväskylä, June, 2018

This work presented in this thesis has been supported by the Academy of Finland programme under the Finnish Centre of Excellence Programme 2011–2017 (Project No. 251353, Nuclear and Accelerator-Based Physics Research at JYFL), the European Commission (E.C.) 7th Framework Programme project ENSAR, and the doctoral program in nuclear and particle physics (University of Jyväskylä).



# Contents

<b>Abstract</b>	<b>iii</b>
<b>Preface</b>	<b>viii</b>
<b>List of Included Articles</b>	<b>xi</b>
<b>List of Tables</b>	<b>xiv</b>
<b>List of Figures</b>	<b>xv</b>
<b>1 Introduction</b>	<b>1</b>
<b>2 Theory</b>	<b>7</b>
2.1 Atomic structure and light-atom interaction . . . . .	7
2.1.1 Atomic level structure, angular momentum coupling and notation . . . . .	8
2.1.2 Radiative transitions . . . . .	10
2.1.3 Broadening mechanisms . . . . .	12
2.1.4 Laser resonance ionization . . . . .	13
2.2 Population of atomic states and collisional phenomena . . . . .	15
2.2.1 Thermal population of states . . . . .	15
2.2.2 Collisional quenching and intramultiplet mixing . . . . .	15
2.2.3 Comparison of atomic level density of elements . . . . .	17
2.3 Gas flow kinetics . . . . .	19
2.3.1 Choked gas flow . . . . .	19
2.3.2 Diffusion . . . . .	20
2.3.3 Flow laminarity and Reynolds number . . . . .	22
2.4 Buffer gas chemistry . . . . .	22
2.4.1 Dimerization and charge exchange reactions . . . . .	22
2.4.2 Ion-neutral chemistry . . . . .	24
2.4.3 Estimation of impurity level from ratio of mass-separated atomic-to-molecular fraction . . . . .	26
<b>3 Techniques of buffer gas purification</b>	<b>27</b>
3.1 Article I . . . . .	28

3.2	IGISOL buffer gas purification system . . . . .	41
3.2.1	Purification by condensation . . . . .	42
3.2.2	Purification by adsorbents . . . . .	43
3.2.3	Purification by getter-based purifiers . . . . .	46
3.3	Contaminants beams from target chamber leak . . . . .	46
3.3.1	Contaminant beams as a function of leak rate . . . . .	47
3.3.2	Ionization mechanism outside the gas cell . . . . .	49
3.4	Towards a cryogenic gas cell . . . . .	50
3.4.1	The design of the new cryogenic gas cell . . . . .	52
<b>4</b>	<b>Development of the actinide gas cell and laser ionization of plutonium</b>	<b>55</b>
4.1	Article II . . . . .	56
4.2	Introduction and motivation . . . . .	64
4.2.1	Collinear laser spectroscopy at IGISOL and yield requirement . . . . .	64
4.2.2	Development of the plutonium laser ion source . . . . .	65
4.3	Plutonium ionization scheme . . . . .	65
4.3.1	Three-step blue-IR-IR scheme . . . . .	65
4.3.2	Development of a two-step blue-blue ionization scheme . . . . .	67
4.3.3	Saturation of the two-step blue-blue scheme . . . . .	69
4.4	Ionization scheme investigation with a tunable grating-based Ti:Sapphire laser system . . . . .	71
4.4.1	Experimental setup . . . . .	71
4.4.2	The tunable grating-based Ti:Sapphire laser system with second harmonic generation . . . . .	73
4.5	Results of Pu ionization scheme investigation . . . . .	76
4.5.1	Wavelength spectrum while scanning the grating-based laser $\lambda_2$ . . . . .	76
4.5.2	Second 420.77 nm transition as a possible explanation for $\lambda_1$ -only ionization . . . . .	78
4.5.3	A wider scan range using the grating-based laser . . . . .	81
4.5.4	Observation of collisional de-excitation . . . . .	83
4.5.5	Temporal overlap of $\lambda_1$ and $\lambda_2$ lasers . . . . .	84
4.5.6	Atomic level density in plutonium and comparison to other elements . . . . .	85
4.6	Mass spectra and helium purity . . . . .	86
4.7	Summary and outlook . . . . .	87
<b>5</b>	<b>Developments towards a <math>^{229}\text{Th}</math> ion source</b>	<b>89</b>
5.1	Introduction . . . . .	89
5.2	Article III . . . . .	93
5.3	Laser ion source and resonant ionization of thorium . . . . .	106
5.3.1	Thorium ionization scheme . . . . .	106

---

5.3.2	First excitation step wavelength spectra . . . . .	107
5.4	Suppression of molecular contaminants by size-exclusion . . . . .	111
5.4.1	Mass spectra and identification of impurities . . . . .	111
5.4.2	Consideration of collision induced dissociation . . . . .	112
5.4.3	Technique of size-exclusive extraction . . . . .	113
5.5	$^{233}\text{U}$ alpha recoil source . . . . .	115
5.5.1	Description of the sources . . . . .	117
5.5.2	Source characterization by direct gamma-ray and alpha radiation measurement . . . . .	120
5.5.3	Source characterization by foil implantation . . . . .	122
5.5.4	Source characterization by Rutherford backscattering spectrometry . . . . .	128
5.6	Source characterization by mass spectra . . . . .	134
5.6.1	LMU source in actinide gas cell . . . . .	134
5.6.2	Charge state manipulation . . . . .	136
5.6.3	A new dedicated gas cell for $^{233}\text{U}$ alpha-recoil sources . . . . .	137
5.7	On-line production for $^{229}\text{Th}$ . . . . .	143
5.7.1	Detection of alpha-active radioisotopes . . . . .	144
5.7.2	Production cross sections . . . . .	146
5.7.3	Estimation of $^{229}\text{Th}$ yield . . . . .	148
5.7.4	Target damage and optimal target thickness . . . . .	150
5.8	Summary and outlook . . . . .	151
<b>6</b>	<b>Summary and outlook</b>	<b>155</b>
<b>A</b>	<b>On-line alpha spectra</b>	<b>159</b>
	<b>References</b>	<b>163</b>



# List of Included Articles

This thesis is based on the work described in the three articles listed below as well as a series of experimental studies which have been performed, analysed and interpreted. The author has designed and constructed the IGISOL gas purification system, and performed the majority of the experiments and data analysis in article I. In article II, the author has contributed to the planning of the experiment and has designed, built and characterized the gas cell which was also used in article III. In both article II and III, the author has performed the majority of the experiments, analyzed and interpreted the data both in connection to resonance laser ionization as well as the gamma-ray spectroscopy of the filament-based dispensers. The author has contributed significantly to the writing of all three articles. The experiments discussed in the thesis which are not contained in the articles have been primarily performed by the author, in addition to the data analysis and interpretation of the results. Finally, the author has been involved in IGISOL-related experiments resulting as a co-author in over 30 peer-reviewed publications.

**Article I** I. Pohjalainen, I.D. Moore, T. Eronen, A. Jokinen, H. Penttilä, S. Rinta-Antila, *Gas purification studies at IGISOL-4*, *Hyperfine Interaction* (2014) 227:169–180

**Article II** I. Pohjalainen, I.D. Moore, T. Kron, S. Raeder, V. Sonnenschein, H. Tomita, N. Trautmann, A. Voss, K. Wendt, *In-gas-cell laser ionization studies of plutonium isotopes at IGISOL*, *Nuclear Instruments and Methods in Physics Research B* 376 (2016) 233–239

**Article III** I. Pohjalainen, I.D. Moore, A. Voss, S. Geldhof, T. Schumm, *Laser ionization studies of thorium at IGISOL using filament-based dispensers*, to be submitted to *Nuclear Instruments and Methods in Physics Research B* (2018)

# List of Tables

2.1	The letter equivalences for angular momentum in atomic configurations and term symbols. . . . .	8
4.1	List of the wavelengths of the detected peaks from the grating-based laser scan close to the second step transition at $\lambda_2$ of 422.53 nm . . . . .	79
4.2	List of the detected resonances from the grating-based laser scan with the JYFL laser fixed to the wavelength corresponding to the 422.5 nm transition . . . . .	82
5.1	The currently known hyperfine $A$ and $B$ parameters for the electronic ground state and few excited states of $^{229}\text{Th}$ in several charge states . . . . .	90
5.2	Physical properties of the studied $^{233}\text{U}$ sources. . . . .	118
5.3	Measured activities of $^{233}\text{U}$ and $^{229}\text{Th}$ isotopes in the LMU source and one large area JYFL $^{233}\text{U}$ strip according to a few gamma-ray lines. . . . .	121

# List of Figures

1.1	The IGISOL facility with MCC30/15 light ion cyclotron. . . . .	4
2.1	Laser resonance ionization schemes . . . . .	14
2.2	The potential curves in the Ba-Ar collision . . . . .	17
2.3	The mean level density of elements between energies from 50% to 75% of the ionization potential . . . . .	18
3.1	The vapor pressure curves of several noble gases and molecules of interest . . . . .	43
3.2	Nitrogen gas adsorption isotherms to 13X zeolite at 77 K and 298 K. . . . .	45
3.3	The mass separated ion beam currents as function of the partial pressure of air in the target chamber . . . . .	48
3.4	The concept design for the new cryogenic gas cell. . . . .	51
3.5	The CAD design of cryocooler coupled to the gas cell while being mounted to the off-line ion guide quadrupole mass spectrometer station . . . . .	53
4.1	The initial laser ionization scheme for plutonium using a blue and two IR steps . . . . .	66
4.2	The blue-blue ionization scheme of plutonium . . . . .	67
4.3	The population of the ground- and first five excited states in plutonium as a function of temperature . . . . .	69
4.4	The saturation of the $\lambda_1$ transition as a function of laser intensity	70
4.5	The saturation measurement of the $\lambda_2$ step. Only a linear depen- dence on the laser power was observed. . . . .	70
4.6	Simplified schematic figure of the experimental setup to study the plutonium ionization scheme with a standard and a grating-based Ti:sapphire laser. . . . .	72
4.7	One of the tantalum foils cut to form a filament and a filament mounted between the two vacuum feedthroughs. . . . .	74
4.8	Schematic diagram of the grating-based Ti:sapphire laser pro- vided by the Applied Quantum Beam Engineering group of Nagoya University . . . . .	75

4.9	Wavelength scan of plutonium taken with the grating-based laser in the region around the second step . . . . .	77
4.10	The level scheme constructed from the interpretation of the results obtained from the plutonium studies with the grating-based laser. . . . .	80
4.11	Wavelength scan of plutonium using the grating-based laser while the JYFL laser is fixed on the second-step transition at 422.53 nm . . . . .	81
4.12	The atomic level density of plutonium per 1000 cm <sup>-1</sup> as a stacked bar plot for even and odd parity states. . . . .	85
4.13	Comparison of mass spectra taken under different impurity conditions while doing laser ionization of plutonium. . . . .	86
5.1	The UV-IR-IR laser ionization scheme for thorium . . . . .	107
5.2	Wavelength scans of the UV transition in the ionization scheme of thorium at three different laser powers. . . . .	109
5.3	Wavelength scan of the 420.77 nm transition in the ionization scheme of plutonium. . . . .	109
5.4	Mass spectra recorded at the focal plane of the IGISOL separator during the laser ionization of <sup>232</sup> Th evaporated from a filament dispenser. . . . .	111
5.5	Simulation of ion transmission through the SPIG as a function of collision cross section . . . . .	114
5.6	The ion trajectories in Simion simulations with the SPIG front electrode at -85 V and two different collision cross sections . . . . .	115
5.7	The <sup>233</sup> U decay chain . . . . .	117
5.8	The projected ranges of <sup>229</sup> Th ions and their longitudinal straggling in uranium and uranium tetrafluoride UF <sub>4</sub> . . . . .	119
5.9	The simulated energy distribution and reverse cumulative percentage of the <sup>229</sup> Th recoils coming out of a pure <sup>233</sup> U source . . . . .	120
5.10	Direct gamma spectra of the LMU and JYFL <sup>233</sup> U sources. . . . .	121
5.11	Direct alpha spectra of the <sup>233</sup> U sources. . . . .	122
5.12	The alpha spectrum of the Al foil following a 4-day implantation using the LMU <sup>233</sup> U source. . . . .	123
5.13	Gamma spectrum of the Al foil irradiated for a period of 46.3 days by the LMU <sup>233</sup> U source. . . . .	124
5.14	Gamma spectrum of the Al foil irradiated for a period of 12.6 days by a smaller area JYFL <sup>233</sup> U source strip. . . . .	125
5.15	The decay curves of the <sup>225</sup> Ra in the irradiated foils . . . . .	126
5.16	The decay curves of <sup>225</sup> Ac in the irradiated foils . . . . .	127
5.17	The geometry of the RBS measurement of the <sup>233</sup> U sources. . . . .	129
5.18	The RBS spectra and Simnra simulation of the LMU and JYFL <sup>233</sup> U sources . . . . .	130
5.19	The elemental mass composition as a function of layer depth of the <sup>233</sup> U LMU (a) and JYFL (b) sources according to the Simnra simulation. . . . .	131



5.20	RBS spectrum of JYFL source strip and peak positions at different sample tilt angles . . . . .	132
5.21	The LMU and JYFL source alpha peak at different tilt angles . . . . .	133
5.22	Cross-sectional view of the actinide gas cell CAD model with the LMU $^{233}\text{U}$ recoil source mounted facing the nozzle. . . . .	134
5.23	Initial mass spectrum using the LMU $^{233}\text{U}$ source mounted in the actinide gas cell facing the exit nozzle. . . . .	135
5.24	The mass spectra in regions of $\text{Th}^{3+}$ , $\text{Th}^{2+}$ and $\text{Th}^{1+}$ , with and without the addition of xenon gas. . . . .	136
5.25	A cross-sectional view of the CAD model of the new gas cell design for the $^{233}\text{U}$ sources. . . . .	138
5.26	Photograph of the new gas $^{233}\text{U}$ cell. . . . .	138
5.27	The projected ranges of $^{229}\text{Th}$ ions from 1 keV to 80 keV in helium gas. The range is given for four different pressures. . . . .	139
5.28	The estimated recoil stopping range distribution of $^{229}\text{Th}$ ions in 20 mbar helium gas assuming a recoil energy distribution according to Fig. 5.9. . . . .	140
5.29	Streamlines of the gas flow in the simulated $^{233}\text{U}$ alpha-recoil gas cell. . . . .	140
5.30	The cross sectional helium gas evacuation time isocurves of $^{233}\text{U}$ gas cell . . . . .	141
5.31	The evacuation time as a function of distance from the gas cell nozzle for four radial positions . . . . .	142
5.32	The on-line alpha spectrum recorded at $A/q=227$ . . . . .	145
5.33	The short-lived isotopes in the decay chain of $^{227}\text{Pa}$ . . . . .	146
5.34	The on-line alpha spectrum recorded at $A/q=223$ . . . . .	147
5.35	Estimated production cross sections using Talys for the isotopes evaporated in the $^{232}\text{Th}(p, x)\text{Y}$ reaction with 50 MeV proton beam energy. . . . .	147
5.36	Cross sections of selected isotopes calculated with the Talys simulation software and plotted as a function of proton beam energy. . . . .	148
5.37	The accumulation profile of the isotopes measured during the implantation of the $A/q=227$ . . . . .	149
5.38	Photographs of the $^{232}\text{Th}$ target during the experiment . . . . .	150
5.39	The differential production cross sections and ranges in metallic thorium for $^{229}\text{Th}$ and $^{227}\text{Pa}$ . . . . .	152
A.1	The on-line alpha spectrum recorded at $A/q=222$ . . . . .	160
A.2	The on-line alpha spectrum recorded at $A/q=225$ . . . . .	161

# Chapter 1

## Introduction

The production of atomic nuclei at radioactive ion beam (RIB) facilities around the world has traditionally relied on two main approaches, the Isotope Separator On-Line (ISOL) and the in-flight technique [1]. In the former, a high-energy primary beam impacts on a thick target and the nuclear reaction products are stopped in the target. Thermal diffusion and effusion into an ion source is followed by ionization, from which a low-energy beam is then extracted and transported to experimental stations. In-flight separators rely on a combination of electric and magnetic fields to separate projectiles which are formed via the fragmentation/fission of a high energy (typically 100 to 1000 MeV/u) stable beam passing through a thin target. A hybrid method relies on the thermalization and stopping of radioisotopes in noble gas-filled gas stoppers. These so-called gas cells have seen a rapid evolution in size and complexity since the original development of the ion guide method [2] at the Ion Guide Isotope Separator On-Line IGISOL facility [3, 4] at the Accelerator Laboratory of the University of Jyväskylä. The benefit of stopping reaction products in a noble buffer gas (helium or argon), is in the chemical non-selectivity of the gas. This enables a universal extraction of ions including elements that, due to their refractory nature, are considered to be challenging for the more traditional ISOL technique.

The gas cell technique has also been adapted to in-flight facilities to convert the high energy ions from projectile fragmentation reactions into a beam suitable for low-energy experiments. Due to the high energy of the fragments, these stopping cells are larger in size, need DC- and RF fields for extraction, and sometimes use cryogenic temperatures to achieve a higher buffer gas density. Such gas catchers include, for example, the stopping cell at the low energy beam and ion trap (LEBIT) facility at the National Superconducting Cyclotron Laboratory (NSCL) [5], and the Fragment Recoil Separator (FRS) cryogenic stopping cell at GSI ultimately to be used at the Low-Energy Branch of the

Super-FRS at the Facility for Antiproton and Ion Research (FAIR) [6]. Using buffer gas stopping cells to stop high energy RIBs has also led to specialized devices such as the gas-filled reverse cyclotron at NSCL to create low-energy beams of light and medium-mass fragments [7].

The technique of resonance laser ionization is widely used in combination with the production of radioactive beams and is applied around the world at ISOL facilities [8–11], with the ISOLDE radioactive beam facility hosting the longest running laser ion source, the Resonance Ionization Laser Ion Source (RILIS) [12]. Resonance laser ionization is based on multi-step resonant excitation and ionization of an element, using tunable high repetition rate Titanium Sapphire or dye laser systems. This technique has a high efficiency, is element selective and can be used to produce isobarically pure ion beams when used in combination with a mass separator. The extension of the method to gas cells has led to the development of gas cell-based laser ion sources. On-line resonance laser ionization in a gas cell was pioneered at the Leuven Isotope Separator On-Line (LISOL) facility in Louvain-La-Neuve [13, 14]. Since then, several other facilities have adopted this method including IGISOL [15], the KEK Isotope Separation System [16] and the PARasitic Laser Ion-Source (PALIS) [17] of the fragment separator facility at RIKEN.

New gas cell-based laser ion sources are also currently being developed. A gas cell for REGLIS (Rare Element in Gas Laser Ion source and Spectroscopy) is under development and is to be coupled on-line to the Super Separator Spectrometer ( $S^3$ ) at Système de Production d'Ions Radioactifs Accélérés en Ligne (SPIRAL1) and the future (SPIRAL2) facility at Grand Accélérateur National d'Ions Lourds (GANIL) [18]. Based on a similar design, a new gas cell coupled to a Titanium Sapphire laser facility is planned to be installed for the low-energy branch of the Mass Analysing Recoil Apparatus (MARA) spectrometer [19, 20] at the Accelerator Laboratory of the University of Jyväskylä.

The use of lasers in nuclear physics research is not only limited to the selective production of radioactive ion beams. Lasers are also used to perform high-resolution optical spectroscopy of rare isotopes to gain access to nuclear structure information by probing the small perturbations of the electronic level structure caused by the interaction with the nucleus [21]. Measurements of the isotopic shifts in transition frequencies and hyperfine structure in the atomic spectra of radioactive nuclei provide a model-independent way to quantitatively measure fundamental nuclear properties including ground and isomeric state spins, electromagnetic moments and changes in mean-squared charge radii. Although optical measurements have been extensively performed throughout the nuclear chart, there is a significant lack of information in the heavy element region including the actinides and transactinides. Recently a concerted effort has been initiated at different RIB facilities to focus on the production and study of actinide isotopes using laser spectroscopy.

---

Traditionally, high-resolution optical spectroscopy of rare isotopes has been performed using collinear laser spectroscopy (CLS) and variants thereof, however laser resonance ionization spectroscopy (RIS) [12] has received particularly attention in the last decade. The high sensitivity of the laser resonance ionization technique enables spectroscopy to be performed at low production rates (of the order of 1 ion/s or less) when performed at the ion source. So-called in-source spectroscopy has been demonstrated both in gas cells and hot cavities and has recently been applied to the study of heavy elements. For example, the RIS technique has been used in single-atom-at-a-time spectroscopy of nobelium, by implanting  $^{254}\text{No}$  ions into a catcher filament mounted within an argon buffer-gas stopping cell [22]. RIS has also been combined with the collinear laser spectroscopy technique at CERN-ISOLDE, seeking a compromise between the attractive qualities of both techniques in the collinear resonance ionization spectroscopy (CRIS) setup [23].

Unfortunately, the lack of stable isotopes in the actinide region and beyond limits the knowledge on suitable optical transitions most sensitive to the nuclear structure parameters of interest, and the low production cross sections present a clear challenge to which highly sensitive techniques are required. Nevertheless, some of the most exciting and challenging future experiments lie within the heaviest region of the nuclear landscape and this is reflected in the current efforts. Progress in both experimental techniques and powerful atomic level calculations are a very important foundation towards the future laser spectroscopy and ion chemistry of the superheavy elements [24].

This thesis work concentrates on the production of low-energy actinide beams of plutonium and thorium for the purpose of performing high-resolution collinear laser spectroscopy at the IGISOL facility which is illustrated in Fig. 1.1. In-gas-cell laser ionization has been applied to atoms of these elements evaporated from filament dispensers and has thus far resulted in optical spectroscopy of several isotopes of plutonium, which represents the heaviest element yet measured with the collinear laser spectroscopy technique [25]. Here the focus on the production of thorium beams is not only concentrating on the laser ion source studies, but also towards on-line production and  $^{233}\text{U}$  alpha recoil source developments, which aim to provide access to the  $^{229}\text{Th}$  ground and isomeric states. This work is performed within the nuClock project [26], part of the Horizon2020 EU framework program, which aims to develop a novel type of optical clock based on an extremely low-lying nuclear transition in  $^{229}\text{Th}$  [27, 28]. The nuclear approach to a frequency standard can potentially reach about an order of magnitude higher precision than the current atomic clocks.

Performing resonance laser ionization of actinides in a gaseous environment seems to indicate a significantly lower efficiency when compared to resonance ionization performed in vacuum, for example within a hot cavity. This reduction of efficiency likely originates from the collisional interaction between the buffer

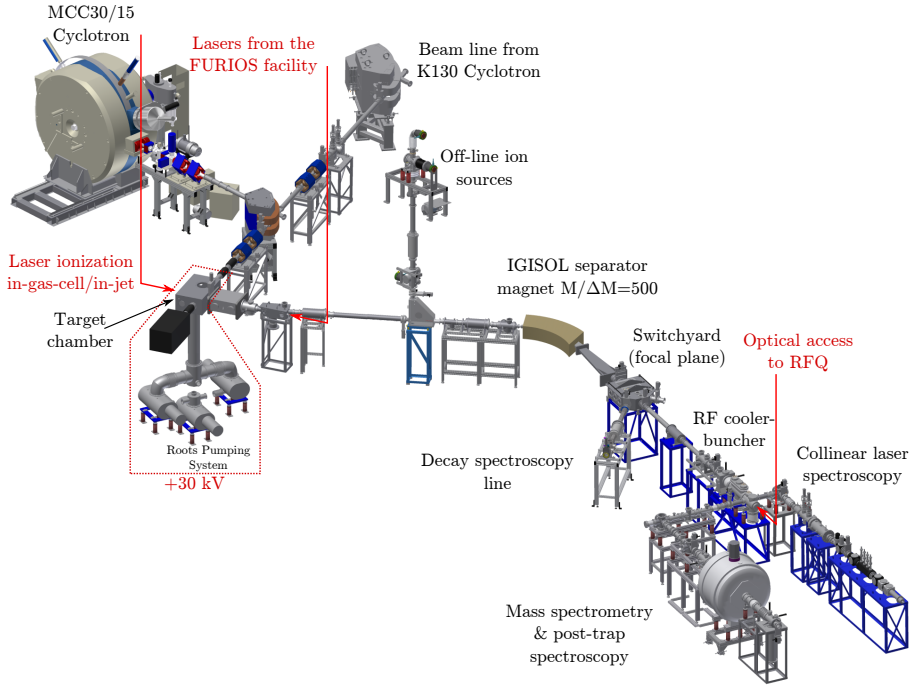


**Figure 1.1.** The IGISOL facility with with MCC30/15 light ion cyclotron.

gas atoms and the complex atomic structure of actinides (and is suggested to extend to elements with a high atomic level density in general, for example the lanthanides). The collisional interaction has been noted in the ionization spectroscopy of nobelium [29] and also recently mentioned in connection to actinium [30]. Now, in this thesis, also plutonium and thorium are shown to be similarly influenced by the gas cell environment.

This thesis is divided into six chapters. Before the research is discussed, selected topics from the theory of atomic physics, fluid dynamics and gas-phase chemistry are presented. The atomic structure and light-atom interaction are highlighted in connection with laser resonance ionization and collisional phenomena. The gas-phase chemistry includes the most important aspects for this work, namely chemical and charge exchange reactions.

Chapter three proceeds with Article I of this thesis, followed by a general description of the methods used in the IGISOL buffer gas purification system and an explanation of the working principle of the purifiers. The origin of contaminant ion beams resulting from a poor extraction vacuum and related gas-phase chemistry in the extraction region is discussed. An initial design concept and plans for a cryogenic gas cell project are summarized.

Extensive studies of the actinides elements of plutonium and thorium in a gaseous environment are presented in chapters four and five. After Article II in chapter four, the laser ionization of plutonium is introduced along with a detailed discussion concerning the impact of collisional phenomena on the ionization scheme. Chapter five summarizes the developments towards a  $^{229}\text{Th}$  ion source with Article III concentrating on the filament-based dispensers for evaporation of atomic thorium and resonance laser ionization. The anomalous resonance structures seen at high laser intensities are discussed in a similar manner to that of plutonium. In order to suppress molecular contaminants, the topic of collision-induced dissociation is introduced as well as the extraction of ion beams based on a novel size-exclusion method.

The latter part of chapter five presents an extensive characterization of  $^{233}\text{U}$  alpha recoil sources whereby a series of gamma- and alpha spectroscopy has been performed using the direct sources as well as via implantation into foils. The Pelletron accelerator within the Accelerator Laboratory of the University of Jyväskylä has been used to further characterize the  $^{233}\text{U}$  source material using Rutherford backscattering spectrometry. The implementation of the source into a gas cell and production of a  $^{229}\text{Th}$  ion beam is discussed. Lastly, the first investigations involving the on-line production of  $^{229}\text{Th}$  are presented with an outlook to future work.



# Chapter 2

## Theory

This chapter presents the different theoretical aspects of atomic physics and gas-cell processes relevant to this thesis. The first section provides an overview of atomic level structure and angular momentum coupling as a basis for the later discussion in the thesis related to electronic transitions by photons, thermal excitation and other collisional phenomena affecting the population of atomic states. The density of atomic levels throughout the periodic table is discussed, highlighting the particularly high level density found within the actinide elements. Following this, a treatment of gas flow kinetics associated with buffer gas cells is presented, namely topics of choked flow through an orifice, diffusion of atoms and laminarity of flow. The latter part of this chapter then introduces the relevant gas-phase chemistry of pertinence to this work, including different charge exchange, bi- and termolecular reactions.

### 2.1 Atomic structure and light-atom interaction

In the following section the theoretical background of the relevant phenomena that affect the population of electronic levels in atoms and ions is presented. A short introduction to atomic structure is given followed by a brief overview of the selective process of resonant excitation and ionization with lasers. Population changes induced by collisional processes are discussed, starting with how low-lying levels are populated in thermal collisions and continuing to more complex processes of collisional intramultiplet mixing and quenching. For many of these subjects only a brief introduction is given and more details can be found in the textbooks and other cited references.



Angular momentum [ $\hbar$ ]	0	1	2	3	4	5	6	7	...
$l$ in orbital configurations:	s	p	d	f	g	h	i	k	...
$L$ in atomic term symbols:	S	P	D	F	G	H	I	K	...
$\Lambda$ in molecular term symbols:	$\Sigma$	$\Pi$	$\Delta$	$\Phi$	$\Gamma$	H	I	K	...
Maximum number of electrons:	2	6	10	14	18	22	26	30	...

**Table 2.1.** The letter equivalences for angular momentum in atomic configurations and term symbols. The last row shows the maximum number of electrons per subshell.

### 2.1.1 Atomic level structure, angular momentum coupling and notation

By applying the basic principles and tools of quantum mechanics to an ensemble of electrons around a positively charged nucleus, a model of atomic orbitals can be derived [31]. In this model the electrons orbiting the atomic nuclei can be described with wavefunctions which are the eigenstates of the Hamiltonian describing the atom. These wavefunctions are the basis of the atomic orbitals each of which can be characterized by a set of quantum numbers  $n$ ,  $l$ , and  $m_l$ . The principal quantum number  $n$  is a positive number and describes the shell of the orbital. The angular momentum of an orbital is defined by the angular momentum quantum number  $l$  which can take the values  $l = 0, 1, \dots, n - 1$  forming a set of subshells. Each subshell contains states according to the quantum number  $m_l$ , the so-called magnetic quantum number that takes the values  $m_l = -l, -l + 1, \dots, l - 1, l$ . As electrons are fermions with spin  $s = 1/2$ , each orbital can, according to Pauli's exclusion principle, include a maximum of two electrons defined with the electron spin quantum number  $m_s = -1/2, +1/2$ . Therefore each subshell, as defined by an integer number  $l$ , can have a maximum of  $2(2l + 1)$  electrons.

In multi-electron atoms each of the orbitals is filled up starting from the lowest energy orbital until the lowest unoccupied state is filled with the last valence electron. This forms the ground state configuration of an atom. When an atom is in an excited state, one or more electrons can be seen to occupy higher energy orbitals above unoccupied lower energy orbitals. The ground state and excited states of an atom are labeled with the atomic configuration, whereby each shell containing electrons is written as  $nl^N$ , so that the subshell  $l$  that contains  $N$  electrons is noted with a letter according to the first row of Table 2.1. The configuration is usually given only with the outer shells explicitly written or the closed core part of the configuration abbreviated with noble gas symbol. For example, the sodium ground state configuration can be written as  $2p^63s$  or  $[\text{Ne}]3s$ .

As each electron in an atomic orbital has its own orbital angular momentum

vector  $\vec{l}_i$  and intrinsic spin angular momentum vector  $\vec{s}_i$ , the atom forms a total angular momentum vector  $\vec{J}$ . Although an atom can have electrons in multiple shells, only unpaired electrons from shells that are not fully occupied contribute to the total angular momentum. The order in which the individual angular momenta are added, according to the angular momentum addition theorem, defines the coupling scheme. The most common coupling schemes are the LS- or Russell-Saunders coupling, which is mostly applicable when describing atomic levels in light elements, and jj-coupling scheme [32], which can be found to be used in heavy elements. Additionally there are several intermediate coupling schemes.

In the LS-coupling scheme all the orbital angular momenta and spins are added together separately to form the total orbital angular momentum  $\vec{L} = \sum_i \vec{l}_i$  and total spin angular momentum  $\vec{S} = \sum_i \vec{s}_i$ . Then the total orbital and spin angular momenta are added together to get the total angular momentum  $\vec{J} = \vec{L} + \vec{S}$ . In the jj-coupling scheme the orbital angular momentum and spin of individual electrons are first added together in order to form the individual total angular momentum for the electron  $\vec{j}_i = \vec{l}_i + \vec{s}_i$ . Then the individual total angular momenta are added together to form the total angular momentum  $\vec{J} = \sum_i \vec{j}_i$ .

In this work, all the atomic states are coupled with LS-coupling and noted using the atomic term symbol:

$${}^{2S+1}L_J^{o/-}, \quad (2.1)$$

in which the total orbital angular momentum quantum number  $L$  is replaced by a capital letter according to Table 2.1. When describing states in a diatomic molecule, instead of having the total angular momentum quantum numbers  $L$  and  $S$ , their projection onto the internuclear axis is performed, noted with  $\Lambda$  and  $\Omega$ , respectively. The orbital angular momentum projection quantum number is marked similarly with capital Greek letters as defined also in Table 2.1.

The parity of an atomic state is also noted. If the term symbol is marked with a superscript letter o, it denotes an odd-parity state and its absence denotes an even-parity state. The parity  $P_s$  of the atomic state  $s$  can be calculated from the configuration:

$$P_s = (-1)^{\sum_i N_i l_i}, \quad (2.2)$$

where  $N_i$  represents the number of atoms in the subshell  $l_i$ . If  $P_s = -1$  the state has an odd parity and conversely if  $P_s = 1$  the state has an even parity.

It should be noted that sometimes in the heavy elements the levels are given

according to the LS-coupling scheme even if  $L$  and  $S$  are no longer good quantum numbers, and jj- or some intermediate coupling would be more appropriate. The LS term symbol simply serves as a convenient way to label the levels in heavy elements. In this work, even though LS-coupling may not be the appropriate way to couple the angular momenta in plutonium or thorium, it is used to identify the levels in order to be in accordance with the labeling in the cited databases and publications.

For many levels in thorium and plutonium the term or configuration has not been determined. In this case the levels are referred here with the following notation:

$$\tilde{\nu}_J^{o/-}, \quad (2.3)$$

where, instead of giving the  $L$  and  $S$  quantum numbers, the level wavenumber  $\tilde{\nu}$  is given with an accuracy of  $1 \text{ cm}^{-1}$  without unit. The subscript number is the total angular momentum quantum number  $J$  and the superscript represents the parity as in the term symbol.

### 2.1.2 Radiative transitions

When an atom emits or absorbs a photon resonantly, in other words when the energy of the photon matches the energy between occupied and unoccupied levels of the atom, a radiative transition happens. The most dominant radiative transitions are electric dipole in nature, sometimes marked as E1-transitions. Due to conservation of angular momentum and symmetry, such transitions can only happen if certain selection rules are met. In general, the following change in the quantum numbers of an electron must hold:  $\Delta l = \pm 1$ ,  $\Delta m_l = 0, \pm 1$ , and  $\Delta J = 0, \pm 1$  with the exception of  $J_i = 0 \rightarrow J_f = 0$ . These rules also imply a parity change. If LS-coupling is applicable, then additionally  $\Delta L = 0, \pm 1$  and  $\Delta S = 0$ .

These selection rules are strictly followed only in the dipole approximation and are broken in other radiative transitions, such as electric quadrupole (E2) or magnetic dipole transitions (M1), which can happen when  $\Delta J = 0, \pm 1, \pm 2$  or no parity change is observed, respectively. However, these so-called forbidden transitions generally happen with much lower transition probability.

The transition probability can be described with so-called Einstein coefficients [33]. If a simple two-level atom with ground state  $|1\rangle$  and excited state  $|2\rangle$  is considered, the spontaneous decay of the excited state can be described as

$$\frac{dN_2}{dt} = -A_{21}N_2, \quad (2.4)$$

where  $N_2$  is the number of atoms (population) in state  $|2\rangle$  and  $A_{21}$  is the spontaneous decay rate in [1/s] or the Einstein-  $A$  coefficient. If level  $|2\rangle$  only decays by spontaneous decay the lifetime  $\tau$  of the state is  $\tau = 1/A_{21}$ .

Similarly, in the interaction of the atom with photons, the Einstein coefficients for stimulated emission  $B_{21}$  and absorption  $B_{12}$  can be assigned between the states. With these coefficients the rate of change in population of the states is dependent on the spectral energy density  $\rho(\nu)$  defined in units of  $[\text{J}/(\text{Hz} \cdot \text{m}^3)]$  at the frequency  $\nu = \nu_{12}$  of the transition energy  $E_2 - E_1 = h\nu_{12}$ . For instance the change in population of state  $|2\rangle$  due to photon absorption from the ground state  $|1\rangle$  is,

$$\frac{dN_2}{dt} = B_{12}N_2\rho(\nu). \quad (2.5)$$

The following relationships between the Einstein coefficients  $A$  and  $B$  can be obtained,

$$B_{12} = \frac{g_2}{g_1}B_{21} \quad (2.6a)$$

$$B_{12} = \frac{g_2}{g_1} \frac{c^3}{8\pi h\nu^3} A_{21} \quad (2.6b)$$

in which  $g_1$  and  $g_2$  are the respective degeneracy of the states  $|1\rangle$  and  $|2\rangle$ . These relationships hold regardless of whether the atoms are in a thermal equilibrium and therefore only one coefficient is needed in order to determine the others. Often, instead of stating  $B$ -values, other equivalent coefficients such as oscillator strengths or transition dipole moments are used [34]. These coefficients can be used when comparing the strength of transitions, which is useful when building efficient excitation schemes.

The study of the two-level atom can be taken further by optical Bloch equations that describe the time evolution of the density matrix  $\rho$  of the two-level system when it is driven coherently. For simplicity, the relevant results that can be derived from the equations are only given here. The equations and their derivation can be found in textbooks [35, 36].

In the excitation of an atom by a coherent source such as a laser, the important density matrix element is the diagonal  $\rho_{22}$ , which describes the population of

the excited state  $|2\rangle$ . It can be shown that the steady state solution for the population of the excited state is related to the saturation  $S$  of the transition

$$\rho_{22} = \frac{1}{2} \frac{S}{1+S}, \text{ where } S = \frac{S_0}{1 + (2\delta/\gamma)^2}. \quad (2.7)$$

The factor  $\delta$  is the detuning of the laser frequency  $\omega_l$  so that  $\delta = \omega_{12} - \omega_l$ , and  $\gamma$  is the decay constant of the excited state, in other words the inverse of the lifetime of the state. In the isolated two-level atom in which the lifetime of the excited state is not affected by the environment,  $\gamma$  would be the Einstein coefficient  $A_{21}$ . When at resonance ( $\delta = 0$ ), the saturation  $S$  is at resonance saturation  $S_0$ , which gives the ratio between the saturation intensity  $I_{\text{sat}}$  and the intensity of the laser light  $I = S_0 I_{\text{sat}}$ . The saturation intensity  $I_{\text{sat}}$  can be related to the decay constant of the state and the laser wavelength  $\lambda$ :

$$I_{\text{sat}} = \frac{\pi h c \gamma}{3 \lambda^3}. \quad (2.8)$$

Equation (2.7) suggests that with a very strong driving of the transition ( $S \gg 1$ ), in other words a strong saturation with very intense laser light, 50% of the population of atoms will be in the excited state at any given time.

Also noteworthy is the Lorentzian shape of the population density with regards to the detuning of the frequency. When saturation of the transition is increased at higher laser intensity, the width of the Lorentzian resonance profile broadens. This is because Eq. (2.7) also expresses the power-broadening mechanism. The width  $\gamma_S$  of the power-broadened Lorentzian profile can be expressed as

$$\gamma_S = \gamma \sqrt{1 + S_0}. \quad (2.9)$$

### 2.1.3 Broadening mechanisms

In addition to power broadening, there are several relevant broadening mechanisms which affect the transition linewidth. The fundamental linewidth of a resonance is the Lorentzian-shaped natural broadening, which stems from the uncertainty principle and the finite lifetime of the electronic states. In gas cells, the natural linewidth is not discernible in simple absorption spectroscopy as it is masked by the larger Doppler broadening effect. Due to the finite temperature of the buffer gas, all atoms undergo constant collisions and therefore produce a velocity distribution according to the Boltzmann-Maxwell distribution. If an atom is moving with a velocity  $v$  with respect to the laser radiation exciting the

transition, the non-relativistic frequency change  $\Delta\nu$  in the resonance frequency  $\nu$  is

$$\Delta\nu = \frac{v}{c}\nu, \quad (2.10)$$

where  $c$  is the speed of light. By combining the velocity distribution with the Doppler effect, one obtains a Gaussian resonance profile with a standard deviation  $\sigma_D$ :

$$\sigma_D = \nu_0 \sqrt{\frac{k_B T}{mc^2}}, \quad (2.11)$$

where  $\nu_0$ ,  $m$  and  $T$  are the resonance transition frequency in the atom of mass  $m$ , and the temperature of the gas, respectively.

In addition to the power and Doppler broadening effects, broadening due to collisions with buffer gas atoms is also observed. This effect arises due to the reduction of the lifetime of the state involved in the transition and therefore broadening of the natural linewidth is observed [37].

### 2.1.4 Laser resonance ionization

The resonant excitation and ionization of atoms using laser radiation proceeds by tuning the frequencies of optical light from multiple lasers to match the level separation of sequential atomic states. When the optical frequencies are in resonance with the levels, as mentioned in the previous sub-sections, the atom is excited and an electron is promoted to a higher atomic level. Then ionization can occur, if these transitions take the electron over the ionization potential of the atom.

Figure 2.1 depicts the three commonly used ionization mechanisms. The scheme on the left of the figure shows a transition to a level above the ionization potential, commonly referred to as an autoionizing (AI) state, which can be understood as a multi-electron excitation which relaxes via ionization. The AI states can have high cross sections for excitation and if discovered by scanning the frequency of the final step, can lead to ionization which happens so fast that the broadening of the natural linewidth (typically several tens of MHz) may increase up to several GHz due to the reduced lifetime of the state.

The second scheme leading to ionization occurs via a transition to a state just below the ionization potential. If a high-lying Rydberg state is populated, ionization can be induced by collisions with other atoms, by an external electric

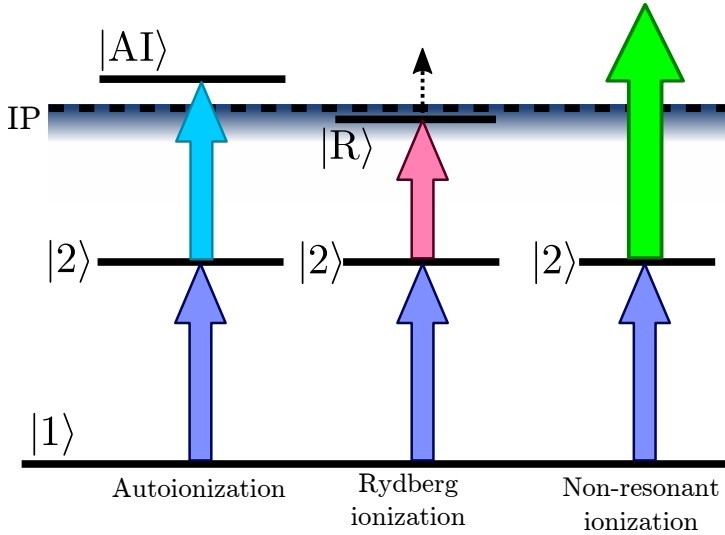


**Figure 2.1.** Different laser resonance ionization schemes. The first step laser excites an electron from the ground state  $|1\rangle$  to an excited state  $|2\rangle$  from which the ionization happens either via an autoionization state  $|AI\rangle$ , a Rydberg state  $|R\rangle$  with collisional or field ionization, or non-resonantly with a high power laser. IP is the ionization potential.

field or by a black body photo-ionization. The third type of ionization happens after excitation by the first (or often second) resonant transition, by non-resonant laser radiation. If a sufficiently high power laser is used, the low cross section for ionization can be compensated. For a more detailed description of each of the aforementioned ionization mechanisms, see for example Ref. [38].

As the atomic levels are specific for each element, resonant laser ionization is a highly selective method of ionization. If the environment does not lead to a large broadening of the atomic transitions and if the laser linewidth is sufficiently narrow, even isotopic selectivity can be achieved. In addition to high selectivity, high efficiencies can also be realized due to the resonant nature of the method. Total ionization efficiencies up to 40% have been reported in hot cavity laser ion sources [11]. Due to the benefits of selectivity and efficiency, laser ion sources for the production of radioactive ion beams have been a tremendous success for the majority of the on-line isotope separator facilities, in particular those utilizing high-temperature cavities [12, 39].

## 2.2 Population of atomic states and collisional phenomena

The laser light absorption and spontaneous decay are not the only mechanisms that cause population change in an external environment. In a gaseous environment, for example the buffer gas cells used in this thesis, atoms of interest undergo constant collisions with gas atoms, causing de-excitation and population mixing. In this section the treatment of thermal collisions and collisional quenching of atomic states is presented.

### 2.2.1 Thermal population of states

Thermal collisions can solely be responsible for the excitation of low-lying levels above the ground state. The important parameters of such collisions are the temperature of the gas and the level energy. By using Boltzmann distribution statistics, the probability of finding a number of atoms  $N_i$  in a state  $i$ ,  $p_i$ , when the atoms have the temperature  $T$ , can be calculated as follows:

$$p_i = \frac{N_i}{\sum_{n=0}^k N_n} = \frac{g_i \exp(-E_i/k_B T)}{\sum_{n=0}^k g_n \exp(-E_n/k_B T)}, \quad (2.12)$$

where  $E_i$  and  $g_i$  are the energy and the degeneracy of the state  $i$  and  $k_B$  is the Boltzmann constant. A state with total angular momentum  $J$  has possible projection quantum numbers of  $m_J = -J, -J + 1, \dots, J - 1, J$  and therefore has the degeneracy of  $2J + 1$ . Normalization is done by summing over all other relevant levels up to the  $k$ th level.

Using the above equation it can be estimated that at room temperature thermal excitations of the low-lying levels become significant if the levels are up to  $800 \text{ cm}^{-1}$  above the ground state. About 25% of all elements have the first excited state below  $800 \text{ cm}^{-1}$ . In hot environments of 1000 K to 2000 K, such as hot cavities or filaments, there is a significant population of the levels if they lie above the ground state up to roughly  $3000 \text{ cm}^{-1}$  and  $5000 \text{ cm}^{-1}$ , which is the case for about half of all elements.

### 2.2.2 Collisional quenching and intramultiplet mixing

In addition to the low-lying levels, collisions can also play a role in the higher excited states of atoms. This becomes important if the atoms that are irradiated with resonant laser light to excited states are de-excited by the collisions



(quenching) with buffer gas atoms in a significant rate. If the reaction rate  $k_{\text{coll}}$  or cross section  $\sigma_{\text{coll}}$  of such collisions are known, simple collision theory can be used to estimate the rate of quenching [40]:

$$R_{\text{coll}} = k_{\text{coll}}N_{\text{G}} = \sigma_{\text{coll}}\langle v \rangle N_{\text{G}} = \sigma_{\text{coll}}\sqrt{\frac{8kT}{\pi\mu}}N_{\text{G}}, \quad (2.13)$$

in which  $N_{\text{G}}$  is the gas atom number density, and  $\langle v \rangle$  describes the mean velocity given according to the Maxwell-Boltzmann distribution. The parameter  $\mu$  is the reduced mass between the gas atom and excited atom.

Previously, collisional de-excitation of atoms by noble gases has been mostly studied in the alkali-earth metals strontium [41] and barium [42–44] and alkali metals or alkali-like ions due to their possible use as frequency standards and the simplicity of their atomic structure [45–47]. Other elements such as cadmium [48], zinc [49], oxygen [50] and sulfur [51] have also been explored. There are also several studies of intramultiplet mixing by noble gases in which population is transferred between the close-lying states belonging to the same term with different  $J$ -values rather than between different terms (for instance [52, 45, 53]). In general, population transfer in intramultiplet mixing is inversely proportional to the energy difference between the levels [54] and seems to be stronger the lighter the colliding noble gas atom.

As is evident from the reaction rate tables of the above references, the quenching seems to have a larger reaction rate with heavier noble gases and to be especially reactive if it occurs via collision with a molecule. This could be attributed to the high number of molecular states at similar excitation energies to the energy levels of the atom of interest thus enhancing the quenching by introducing more level crossings in the collision system than a noble gas atom. In connection with radioactive beams, this property of molecules has been used by adding methane to argon buffer gas in order to quench long-lived metastable states in a resonance cell for on-line optical spectroscopy [55].

A good example of the quenching process by noble gas atoms is given by J.-P. Visticot et al. [44] in which the  $^1\text{P}_1^{\circ} \rightarrow ^3\text{P}_2^{\circ}$  collisional transition in barium induced by argon gas is studied experimentally. Barium atoms are excited resonantly by laser light from the ground state  $6s^2\ ^1\text{S}_0$  to the excited state  $6s6p\ ^1\text{P}_1^{\circ}$ . As argon and barium atoms then collide inelastically, the barium atoms are de-excited to the  $6s6p\ ^3\text{P}_2^{\circ}$  level. This process is depicted in Fig. 2.2, in which the potential energy curves of the Ba-Ar collision system are shown as a function of inter-nuclear distance. If the Ba atom, which is prepared to the  $^1\Pi_1$  state by the laser, and Ar atoms get close enough, the transfer can occur at the crossing between the  $^1\Pi_1$  potential curve and  $^3\Sigma_1$  potential curve which adiabatically correlates with the  $^3\text{P}_2$  level in barium. If the crossing

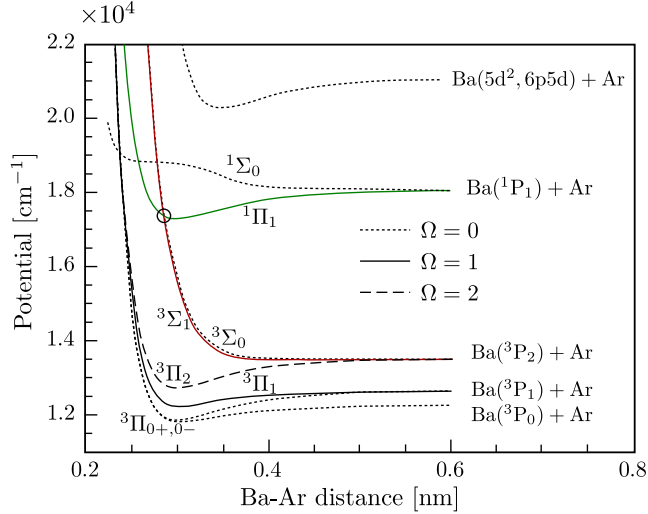


**Figure 2.2.** The potential curves in the Ba-Ar collision system that are involved in the collisional population transfer of  ${}^1P_1^o \rightarrow {}^3P_2^o$ . Most of the transfer happens through the level crossing (indicated by a circle) between the levels  ${}^1\Pi_1$  and  ${}^3\Sigma_1$ . The atomic barium levels are noted at the end of the curves on right. Figure reproduced from reference [44] with permission from the American Physical Society.

happens, the barium atom relaxes to the lower excited state so that the energy difference is transformed into translational energy of the system.

Although collisional population transfer is evidently observed in plutonium and thorium by helium atoms, as shown in the subsequent chapters of this thesis, the exact nature of the collision phenomena, whether it is similar to collisional-induced quenching or intramultiplet mixing, is not known. The picture is complicated in the actinide elements due to their high number of levels. In such a heavy system, a level could have multiple close-by levels not only from the same multiplet but also from different terms and configurations.

### 2.2.3 Comparison of atomic level density of elements

Regardless of whether the population transfer happens via quenching between the levels of different configuration or via intramultiplet mixing between the same term, it seems the high number of levels and the small level separation enhances the probability of collisional population transfer. A good way to investigate differences between the elements is to plot the level density in the region of interest between the ground state and ionization potential. Such a

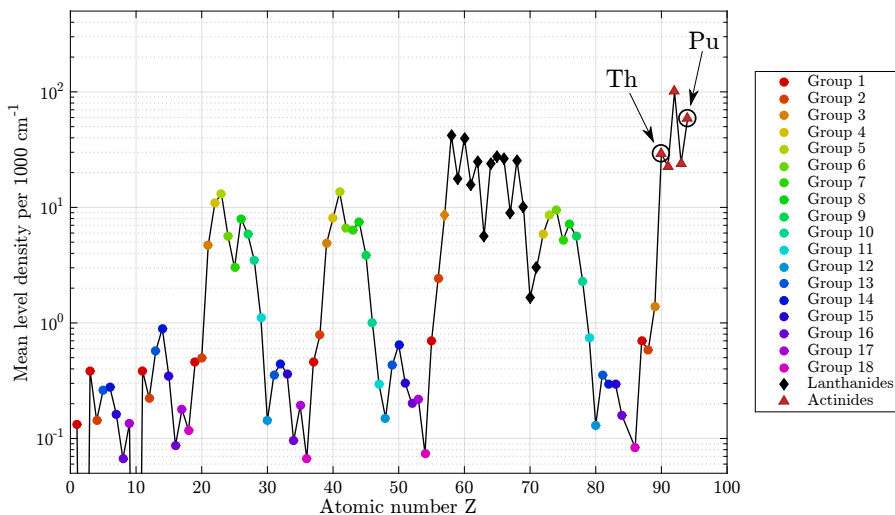


**Figure 2.3.** The mean level density per 1000  $\text{cm}^{-1}$  at energies from 50% to 75% of the ionization potential of all elements up to plutonium. The markers are plotted according to which group the element belongs or if the element is the lanthanides or actinides.

plot can be seen in Fig. 2.3 in which the mean level density per 1000  $\text{cm}^{-1}$  is plotted as a function of atomic number for all elements up to plutonium. The markers are color coded according to the group of the periodic table or whether the element belongs to lanthanide or actinides.

The mean level density for each element is calculated using the atomic levels that lie between 50% to 75% of the ionization potential energy. The levels are taken from the NIST database [56] up to actinium, while actinium levels and above are obtained from the database by J. Blaise and J.-F. Wyart [57]. The upper limit of 75% is set so that the Rydberg states are excluded because for some elements they are known in much higher number than in others. Additionally the 75% limit selects the region where the levels of plutonium are thought to be known and in this way the results are more comparable. The lower 50% limit narrows the range to the intermediate levels where most of the levels lie. It should be noted, however, that the density for some elements, such as promethium compared to other nearby lanthanides, is lower than the actual level density due to the lack of level data.

A clear pattern is visible in the level density plot. All alkali-, alkali earth, and p-block elements show a low-level density, whereas the transition metals especially of group 5 and 6, and in particular the lanthanides show high level density. The high level density of uranium and plutonium compared to other

elements is evident from the figure. If an element has a high level density and a laser excitation is performed on it in a gaseous environment, it may be that possible collisional effects need to be considered.

## 2.3 Gas flow kinetics

### 2.3.1 Choked gas flow

When the ratio between the gas cell pressure  $P_{\text{gc}}$  and the ambient pressure of the expansion chamber  $P_{\text{am}}$  is at or above the critical ratio,  $P_{\text{am}}/P_{\text{gc}} \lesssim 0.5$ , the flow through a nozzle is independent of the downstream pressure and can be considered to be *choked*. The mass flow of a gas with density  $\rho_0$  through a nozzle in a choked condition can be calculated as follows [58]:

$$q_m = C_d A \sqrt{\gamma P_{\text{gc}} \rho_0} \left( \frac{2}{\gamma + 1} \right)^{\frac{\gamma+1}{2(\gamma-1)}}, \quad (2.14)$$

in which  $\gamma$  is the ratio of specific heats,  $C_d$  is the *coefficient of discharge*, and  $A$  is the cross-sectional area of the narrowest part of the nozzle. Because real gases have viscosity, the flow through a nozzle cannot utilize the cross-sectional area entirely and thus the effective area is smaller. To account for this, the area is modified by the coefficient of discharge which describes the ratio between the effective flow rate and theoretical flow rate. Usually, with high Reynolds numbers (laminar flow),  $C_d$  is around 90% [59].

Equation (2.14) can be easily written in volumetric (unit volume per unit time) form assuming an ideal gas and using the ideal gas law:

$$q_v = \frac{\pi}{4} C_d d_t^2 \sqrt{\frac{\gamma k_B T_0}{m}} \left( \frac{2}{\gamma + 1} \right)^{\frac{\gamma+1}{2(\gamma-1)}}, \quad (2.15)$$

where  $m$  is the mass of the gas atom,  $k_B$  the Boltzmann constant and  $T_0$  is the stagnation (upstream) temperature of the gas. The area of the nozzle is also written as the diameter  $d_t$  at the narrowest part. Notably the above equation includes the expression for the speed of sound in an ideal gas,

$$a_{\text{ideal}} = \sqrt{\frac{\gamma k_B T_0}{m}} \quad (2.16)$$

reflecting the fact that the flow at the nozzle reaches the Mach number  $M = 1$  when the flow is choked and forms a supersonic jet in the expansion chamber.

In room temperature helium and argon, when the diameter  $d_t$  is given in mm, the volumetric flow (1/s) of Eq. (2.15) can be simplified to  $q_V(\text{He}) = 0.45d_t^2$  and  $q_V(\text{Ar}) = 0.14d_t^2$  by excluding the coefficient of discharge.

From Eqs. (2.14) and (2.15) it can be seen that the conductance is proportional to the square root of the temperature or its inverse depending on whether volumetric or mass conductance is concerned,

$$q_V \propto \sqrt{T_0} \quad (2.17) \qquad q_m \propto \frac{1}{\sqrt{T_0}} \quad (2.18)$$

Experimentally, this relationship has been seen in this thesis work as a change in buffer gas pressure of a gas cell when an internal filament is heated to high temperatures. For example, in connection with the filament-based dispensers of thorium described in chapter 5, a pressure increase of  $\sim 4$  mbar is seen at an inlet gas pressure of 80 mbar when the filament is heated from room temperature 300 K to 2500 K.

Using the volumetric flow  $q_V$ , an estimation for the evacuation time  $t_e$  of a gas cell that has volume  $V_{gc}$  can be calculated:

$$t_e = V_{gc}/q_V. \quad (2.19)$$

For more accurate and position specific determination of the evacuation time a gas flow simulation is needed because the cross-sectional velocities of the flow of gas do not have the same value. This is the case irrespective of the optimization of the gas cell for laminar gas flow.

### 2.3.2 Diffusion

Diffusion of atoms and ions in the buffer gas medium is an important parameter as it is the cause of one of the significant ion loss mechanisms in a gas cell. In the following a short overview is given to be able to understand how atoms or ions diffuse in a gaseous environment starting from Fick's law and the continuity equation. By solving the diffusion equation, the time evolution of a cloud of atoms in a medium is derived. The derivation can be found in many textbooks, one example being ref. [60].

The diffusion of atoms distributed with a number density  $N(\vec{r}, t)$  can be described by Fick's law:

$$\vec{J}(\vec{r}, t) = -D(\vec{r})\vec{\nabla}N(\vec{r}, t), \quad (2.20)$$

where  $D(\vec{r})$  is the diffusion coefficient and  $\vec{J}(\vec{r}, t)$  is the flux of atoms at time  $t$  and position  $\vec{r}$ . By inserting the above equation into the continuity equation, the diffusion equation is obtained:

$$\frac{\partial N(\vec{r}, t)}{\partial t} = \vec{\nabla} \cdot \left( D(\vec{r})\vec{\nabla}N(\vec{r}, t) \right), \quad (2.21)$$

which, by assuming a constant diffusion coefficient  $D_0$ , can be simplified to

$$\frac{\partial N(\vec{r}, t)}{\partial t} = D_0\nabla^2N(\vec{r}, t). \quad (2.22)$$

This equation can be solved by defining the density of a cloud of atoms at time  $t = 0$  and position  $\vec{r}_0 = (x_0, y_0, z_0)$ ,  $N_0$ , with the aid of a Dirac  $\delta$ -function [61]:

$$N(\vec{r}, \vec{r}_0, 0) = N_0\delta(x - x_0)\delta(y - y_0)\delta(z - z_0). \quad (2.23)$$

The solution is a 3-dimensional normal distribution,

$$N(\vec{r}, \vec{r}_0, t) = \frac{N_0}{(2\pi\sigma^2(t))^{3/2}} \exp\left\{-\frac{(x - x_0)^2 + (y - y_0)^2 + (z - z_0)^2}{2\sigma^2(t)}\right\}, \quad (2.24)$$

with a standard deviation,

$$\sigma(t) = \sqrt{2D_0t}. \quad (2.25)$$

To estimate the magnitude of the diffusion constant  $D_{AG}$  for atoms (or ions) labelled ‘‘A’’ in a gas composed of atoms labelled ‘‘G’’, the Chapman-Enskog equation can be used [62]:

$$D_{AG} = \frac{3}{8} \sqrt{\frac{\pi}{2\mu_{AG}}} \frac{(k_B T)^{3/2}}{P\sigma_{\text{coll}}}, \quad (2.26)$$

where  $T$  and  $P$  are the gas temperature and pressure,  $\mu_{AG}$  is the reduced mass of the system and  $\sigma_{\text{coll}}$  is the collision cross section between species A and G, which can be estimated with respective Van der Waals diameters  $d_A$  and  $d_G$  as  $\sigma_{\text{coll}} = \pi(r_A + r_G)^2$ .

### 2.3.3 Flow laminarity and Reynolds number

Another important phenomenon of gas flow relevant to gas cells is that of turbulence. If the gas cell has sharp turns or otherwise an unsmooth inner shape, the gas flow may become turbulent or produce vortices. If an ion is stopped inside of a vortex, it may not be able to exit the gas cell or, if strong turbulence is otherwise present, ions may be lost by collision with the gas cell walls. Such phenomena may become a problem especially in larger gas cells using high buffer gas pressures.

A simple way to estimate the level of turbulence is to calculate the Reynolds number  $\text{Re}$  [63], which can be used to parameterize the expected flow regime of the gas flow. The Reynolds number can be calculated as [64]

$$\text{Re} = \frac{\rho_m v L}{\eta}, \quad (2.27)$$

where  $\rho_m$  is the mass density of the gas,  $v$  is the gas velocity,  $L$  is a characteristic length such as the diameter of the gas cell, and  $\eta$  is the gas specific dynamic viscosity. For helium the dynamic viscosity  $\eta = 19.9 \mu\text{Pa} \cdot \text{s}$  [65].

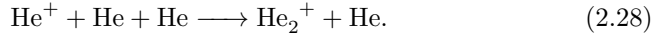
A laminar creeping flow can be assumed if  $\text{Re} \sim 1$  and if  $\text{Re} \sim 12$  the flow is laminar but attached vortices may occur behind objects. At larger Reynolds numbers,  $\text{Re} \sim 120$ , vortex shedding occurs and if the Reynolds number increases to several thousands the flow starts to be fully turbulent [64].

## 2.4 Buffer gas chemistry

### 2.4.1 Dimerization and charge exchange reactions

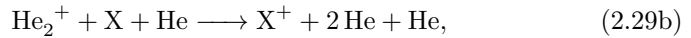
When the buffer gas inside a gas cell is subjected to ionization, for example by the passage of a primary beam through the cell at an on-line radioactive ion beam facility, via stopping of energetic nuclei produced in nuclear reactions or via alpha particles originating from radioactive decay, the buffer gas atoms

become ionized. After ionization the buffer gas ions quickly dimerize in a termolecular reaction. For helium this happens as follows:



This reaction occurs at a rate  $R = k_3\rho^2$ , in which  $\rho$  is the number density of neutral gas atoms and the rate constant  $k_3 = 10.8 \cdot 10^{-32} \text{ cm}^6/\text{s}$  [66].

The impurities in the gas such as  $\text{H}_2\text{O}$  or  $\text{N}_2$  collect the charges from the helium dimers and are preferentially ionized [67]. If impurities are present in sufficiently high densities, they become the dominant charge carriers in the gas [68, 69]. The ionization of impurities happens either in a bimolecular reaction with a helium dimer ion or with the aid of a third helium atom:



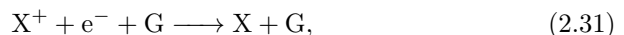
in which X is an atom or molecule. These charge exchange reactions may also be dissociative in nature, for example in the following process involving  $\text{O}_2$  as measured by D. K. Bohme et al. [70]:



Here the percentages note the measured relative beam intensities and only give a rough estimate of the branching.

Because the lifetimes of  $\text{He}^+$  ions and metastable neutral helium  $\text{He}^*$  atoms are small compared to the lifetime of the  $\text{He}_2^+$  dimer even under on-line conditions [15], only a small proportion of the ionization of the impurity is assumed to happen via charge exchange with  $\text{He}^+$  or by Penning ionization. On the other hand, due to the non-selective nature of the ionization by a primary beam, an additional contribution to ionization of impurities in on-line conditions probably happens via direct primary beam ionization.

Due to the creation of buffer gas ion-electron pairs following the passage of a primary beam, a source of electrons is created, which leads to one of the most important reactions on-line, that of three-body recombination:



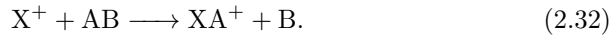


where G is a buffer gas atom. It has been observed in several facilities that with increasing primary beam intensities the efficiency of ion extraction from gas cells is reduced. Detailed discussion of the reactions involving the weak plasma, free electrons and other related on-line phenomena can be found in the article by I. D. Moore [15] and are not discussed in detail here.

### 2.4.2 Ion-neutral chemistry

In addition to charge exchange reactions, gas-phase chemical ion-molecule reactions are commonly observed as the result of bimolecular reactions between an ion and impurity molecule. If the buffer gas purity is not under control, molecular formation may become a significant loss mechanism reducing the efficiency of extracting the atomic ions of interest.

The bimolecular reactions between an ion and a molecule AB consisting of species A and B are dissociative and can be described as follows:



Usually the charge stays with the reaction product containing the original ion especially if the molecule AB is a simple gas molecule, such as O<sub>2</sub>, because of the high ionization potential of B.

The dynamics of the bimolecular reaction, in other words the time evolution of the molecular formation process, can be described by a reaction rate constant  $k_2$  and the differential equation

$$\frac{dN}{dt} = -k_2 N [AB], \quad (2.33)$$

where  $N$  is the number of ions (or atoms) of species X and  $[AB]$  defines the concentration of molecules AB. An impurity concentration of 1 ppm (parts-per-million) at typical gas cell pressures of 100 mbar at room temperature results in a value of  $2 \cdot 10^{12}$  at./cm<sup>3</sup>. Typical bimolecular reaction rates are  $k_2 \leq 10^{-12}$  cm<sup>3</sup>/s for a slow reaction and  $k_2 \geq 10^{-9}$  cm<sup>3</sup>/s for a fast reaction. A time constant  $\tau$  can be associated with the reaction:

$$\tau = \frac{1}{k_2 [AB]}. \quad (2.34)$$

This can be compared with the evacuation time of the ion from the gas cell in order to understand the balance between ion survival and ion loss due to

molecular formation. A useful compilation of the experimental data on gas-phase bimolecular reaction rates of monoatomic ions of most of the stable elements in reactions with various molecules that are of interest to the study of planetary atmospheres and interstellar clouds is presented in Ref. [71].

To examine whether the bimolecular reaction of Eq. (2.32) is energetically possible using Hess's law [72], a simple inequation requirement for bond dissociation energies (BDE) can be evaluated:

$$D_0(X^+ - A) > D_0(A - B), \quad (2.35)$$

where  $D_0$  is the homolytic bond dissociation energy.

If  $D_0(X^+ - A)$  is not known, however  $D_0(X - A)$  as well the ionization potentials for X and XA are, the bond dissociation energy can be calculated from the relation presented in Eq. (2.36) deduced again using Hess's law.

$$D_0(X^+ - A) = D_0(X - A) + IP(X) - IP(XA), \quad (2.36)$$

where  $IP(M)$  is the ionization potential of M. The bond dissociation energies are also of interest for collision-induced dissociation, which is used in connection with gas cells to recover ions that are lost to a molecule by breaking them up in collisions with buffer gas atoms. The collision-induced dissociation mechanism is discussed more in detail in section 5.4.

The second type of reaction often observed in connection with gas cells is the termolecular association reaction, which can be described by the following equation:



in which the atom or molecule A is attached to the ion  $X^+$  by a stabilizing gas atom G. This reaction is notably seen in the dimerization of helium in Eq. (2.28). Similar to the bimolecular reaction, the termolecular reaction can be described by a reaction rate constant  $k_3$  and the following differential equation with a characteristic time constant  $\tau$ ,

$$\frac{dN}{dt} = -k_3 N[A][G], \quad (2.38) \quad \tau = \frac{1}{k_3[A][G]}, \quad (2.39)$$

in which [A] and [G] are the concentrations of the molecule A and gas atoms G.

With helium pressures of 100 mbar, often used in this work, the rate constant  $k_3 \leq 10^{-30}$  cm<sup>6</sup>/s starts to create noticeable molecular formation if an impurity level of 1 ppm is assumed. This reaction is responsible for the water adduct formation that is often observed with ions extracted from gas cells especially in poor purity conditions.

### 2.4.3 Estimation of impurity level from ratio of mass-separated atomic-to-molecular fraction

The presence of molecules in the extracted ion beam can be used to directly estimate the impurity content of the gas if the reaction forming a particular molecule and its corresponding reaction rate are known, and if ions of the element forming the molecule are produced in the gas cell through a selective process. Considering that the atomic ions of an element E are exposed to the impurity M with the concentration [M] in the buffer gas for the duration of the ion evacuation time  $t_i$ , an estimation for the intensity ratio between the relevant molecular ions and the atomic ion can be deduced. A convenient way to define the ratio is to write it between the atomic (elemental) ion intensity  $I_E$  and molecular ion intensity in which not only the intensity of the products  $I_{M,0}$  from the first reaction (described by the known reaction rate) is taken into account but also the intensities of all the subsequent molecules  $I_{M,i>0}$  which are produced from the reaction products and contain the original element E:

$$\frac{\sum_{i=0} I_{M,i}}{I_E} = e^{\frac{t_i}{\tau}} - 1 = e^{\frac{V k_2 [M]}{qV}} - 1, \quad (2.40)$$

in which  $\tau$  represents the characteristic reaction time. The equation can be expanded further by replacing the ion evacuation time  $t_i$  by the gas cell evacuation time  $t_e$  and substituted, according to Eq. (2.19), by the conductance  $q_V$  and the gas cell volume  $V$ , and by replacing the characteristic reaction time with the corresponding bimolecular reaction rate Eq. (2.34).

This simple model is complicated by the fact that ions are rarely created in a single location inside the gas cell and they can be trapped in a vortex if the gas flow is not laminar. Additionally, this model is not applicable if there are any significant loss mechanisms that have a strong preference against a particular ionic species. Therefore, instead of gas cell volume and conductance, a measured ion evacuation time should be used if available and the model only be applied to cases where the buffer gas has only a very weak plasma density as neutralization may also obscure the measurement.

## Chapter 3

# Techniques of buffer gas purification

This chapter proceeds with publication No. I by the author, which describes the new IGISOL buffer gas purification system, designed and constructed by the author during the period in which the IGISOL moved to a new location in the expanded Accelerator Laboratory. This article introduces the first test experiments involving the gas-phase chemistry observed using unpurified and purified helium buffer gas during on-line gas cell operation. Following this, a brief description of the different buffer gas purification techniques used at the new IGISOL facility are presented and estimates of the achieved purification levels are given.

During the commissioning period of the IGISOL facility, some of the contaminant ion beams hindered the success of on-line experiments. This led to a study involving the addition of a controlled leak into the IGISOL target chamber. This chapter presents these studies and illustrates how impurities may be ionized in the environment outside the gas cell. The final part of this chapter introduces an on-going project which aims to couple a cryocooler with a gas cell, in order to investigate the temperature dependence of the gas-phase chemistry as well as the gas cell extraction efficiency.

### 3.1 Article I

The following pages contain the peer-reviewed paper titled *Gas purification studies at IGISOL-4*, published in the journal of *Hyperfine Interactions*, vol 227 (2014), pages 169-180.

## Gas purification studies at IGISOL-4

I. Pohjalainen · I. D. Moore · T. Eronen · A. Jokinen ·  
H. Penttilä · S. Rinta-Antila

Published online: 15 January 2014  
© Springer Science+Business Media Dordrecht 2014

**Abstract** A new gas purification system has been constructed at the upgraded IGISOL facility, Jyväskylä, to meet the need for ultra-high purity helium and argon buffer gas used in the ion guide technique. The purification of helium using liquid nitrogen-cooled cold traps is investigated and compared with unpurified gas using mass spectra obtained at the focal plane of the separator. Neon, an impurity intrinsic to the in-house recycled helium, was seen to have high sensitivity to the impurity level of the gas which is expected to reach sub-parts-per-billion level.

**Keywords** Gas cell · Buffer gas · Gas purification · Gas impurities

### 1 Introduction

Perhaps the most critical factor affecting the efficient use of noble gas-filled ion guides and gas catchers for the production of low-energy radioactive ion beams is the purity of the gas. At the Ion Guide Isotope Separator On-Line (IGISOL) facility at the Accelerator Laboratory of the University of Jyväskylä (JYFL) the ion guide method has been successfully used for over three decades [1]. In brief, a primary beam from a cyclotron impinges on a thin target inside a gas cell filled usually with helium but occasionally argon. The nuclear reaction products recoil out of the target, stop and thermalize in the buffer gas while their charge

---

Proceedings of the 9th International Workshop on Application of Lasers and Storage Devices in Atomic Nuclei Research “Recent Achievements and Future Prospects” (LASER 2013) held in Poznan, Poland, 13–16 May, 2013

---

I. Pohjalainen (✉) · I. D. Moore · A. Jokinen · H. Penttilä · S. Rinta-Antila  
Department of Physics, University of Jyväskylä, Surfontie 9, PL 35 (YFL), 40014 Jyväskylä, Finland  
e-mail: ilkka.pohjalainen@jyu.fi

I. D. Moore  
e-mail: iain.d.moore@jyu.fi

T. Eronen  
Max-Planck-Institut für Kernphysik, Saupfercheckweg 1, 69117 Heidelberg, Germany

state decreases. The ions, primarily singly-charged, are swept out through an exit hole in the ion guide by the gas flow and are guided towards a mass separator via a radiofrequency sextupole ion guide [2].

Trace impurities in the buffer gas play a crucial role in the ion survival during evacuation from the gas cell and understanding the impurity-related processes is necessary for ion guide development. Although the evacuation time of ions is often too fast for molecular formation, the presence of impurities affects the final charge state of the ions during thermalization. The importance of gas phase chemistry comes into play with larger gas cells and with slower evacuation times. In particular, the development of the laser ion source at IGISOL has shown the importance of the gas purity, especially for chemically active elements [3, 4]. Impurities at the level of parts-per-million (ppm) have a significant effect on the ion guide operation by reducing the efficiency of extracting atomic ions of interest due to molecular formation. In order to prevent such losses, gas impurity levels of sub-parts-per-billion (ppb) are required.

The IGISOL facility was recently upgraded and moved to a new experimental laboratory [5]. During the upgrade the gas purification and transport system were fully reconstructed with consideration towards a more rigorous requirement of buffer gas purity. In this work, a detailed description of the new IGISOL gas handling system is given and the performance is investigated by measuring mass spectra under different purification conditions both on-line and off-line. The temporal behaviour of the system as well as the final charge state distribution of recoil ions produced in on-line fission are also briefly discussed.

## 2 The new IGISOL-4 gas purification system

The new IGISOL gas handling system, schematically shown in Fig. 1, consists of the gas supply and purification stage, transport lines and gas feeding control for the ion guide. From the gas bottles, helium or argon is fed through the purification system to the transport line and, via a ceramic insulator, to the 30 kV high voltage area of the IGISOL front end. The neutral gas that flows out of an ion guide is pumped away by a Roots booster pump array while the ions are guided with electric fields through further differential pumping stages towards the mass separator. Currently, lines are being constructed to deliver the pumped helium back to the JYFL helium recycling station.

All piping of the new gas handling system is made using electro-polished stainless steel tubes to reduce the sticking of impurities to the walls. In order to maintain a helium-tight system, Swagelok's all-metal-sealed high purity bellows valves and VCR connectors are used. The gas transport line is wrapped with heating elements allowing baking of the lines at a temperature of over 120 °C. Baking is usually done for about 12 hours before the start of an experiment with a small bleed of purified helium.

Helium and argon are regulated from gas bottles to an absolute pressure of 3–4 bars for the purification and subsequent transport to the ion guide. The helium gas regulation is performed with an automatic switch-over valve between bottles to ensure an uninterrupted flow. Purification of helium is done with liquid nitrogen-cooled cold traps filled with small pellets of zeolite 13-X which collect the impurities due to the porosity of the material. During experiments, while one cold trap is under use, a second is being regenerated by baking it at 250 °C while being pumped to purge the evaporated impurities. The gas purification system also includes a getter (Saes MonoTor PS4-MT15) operated with a heated zirconium alloy for purification of argon and for additional purification of helium. The gas pressure is monitored with several pressure meters throughout the system. At the target chamber, the flow of gas is remotely controlled by on/off valves and motorized needle valves. As shown

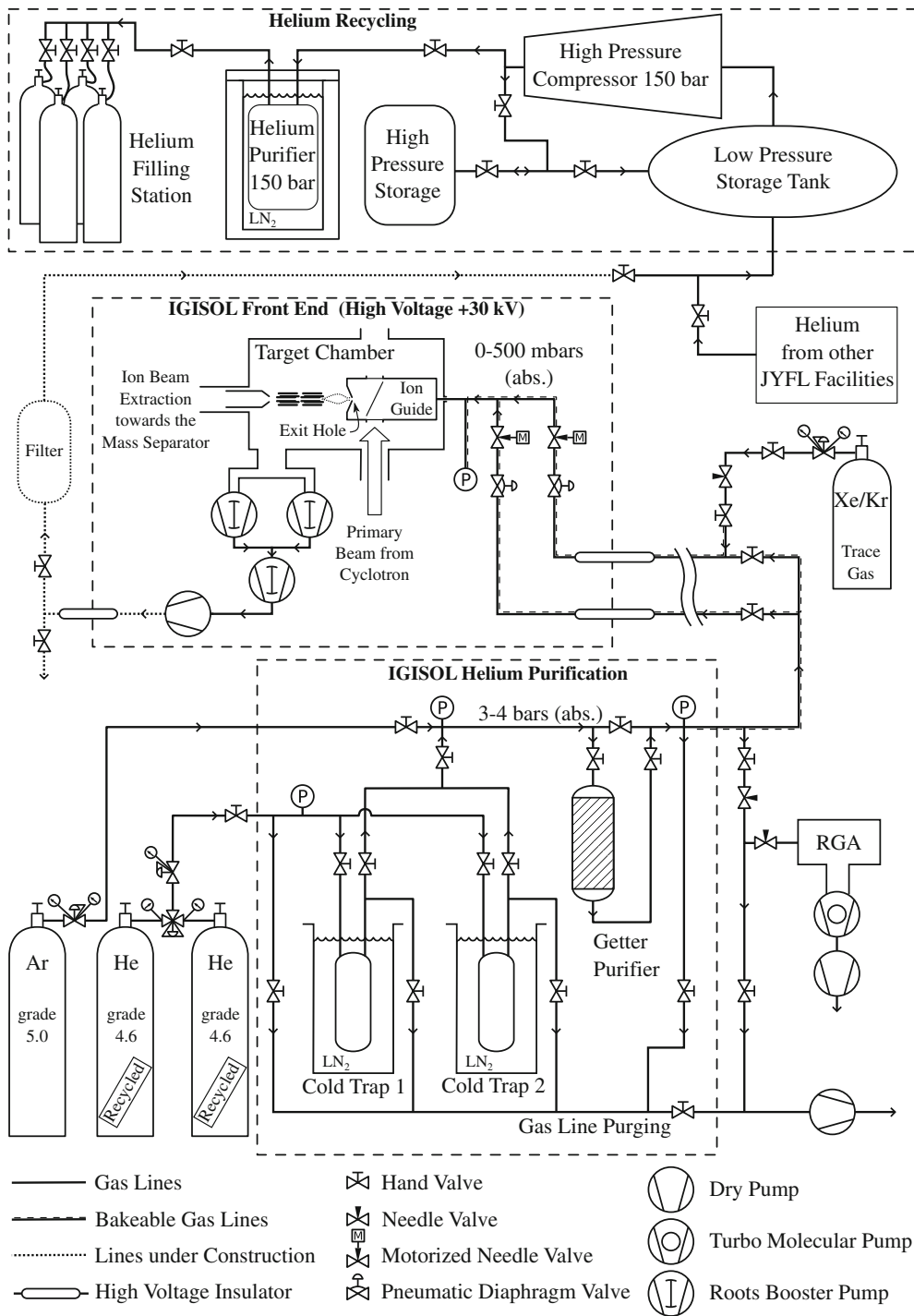


**Fig. 1** Schematic layout of the new IGISOL-4 helium purification and transport system. The helium recycling facility at JYFL is also shown. Approximately 12 m of gas line separate the purification facility from the HV insulators. RGA=residual gas analyser



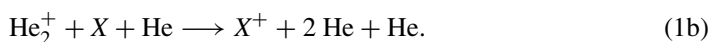
in Fig. 1, it is also possible to add a trace amount of inert gas into the gas line, for example xenon which is often used for mass calibration purposes.

In-house recycled helium is the most frequently used gas at IGISOL, the majority of which comes from evaporated liquid helium. The gas is collected in a low pressure storage tank from where it is compressed to 150 bars either for delivery to a storage battery or directly into the purification unit. The helium is purified by activated charcoal cold traps operating at liquid nitrogen temperatures before being rebottled into 40 litre bottles or a 450 litre mine. At a pressure and temperature of 150 bars and 77 K, gases other than hydrogen, helium and neon are condensed. The recycled helium is estimated to be equivalent to commercial grade 4.6 helium however during the rebottling process a small volume of air ( $\sim 10 \text{ cm}^3$ ) is introduced as the final part of the refilling line is connected to the bottle. This is estimated to result in an impurity level of approximately 2 ppm.

### 3 Gas phase chemistry

In on-line conditions the gas atoms are instantly ionized due to the passage of the primary beam or energetic recoil ions and quickly dimerize in a termolecular association reaction with neutral buffer gas atoms [6].

The dimers subsequently charge exchange with any trace impurity  $X$  either via bimolecular reactions or, at sufficiently high pressures, via termolecular reactions:



With a sufficient density of impurities, these reactions quickly make the impurity molecules the dominant carrier of charge in the buffer gas [6, 7]. The ionized impurity  $X^+$  may react further with another trace impurity  $Y$  via a bimolecular reaction such as charge exchange or proton/hydrogen transfer, or by a termolecular reaction such as three-body association:



Whether or not a reaction involving an ion of interest becomes a significant process during evacuation from a gas cell is determined by the reaction rate coefficient  $k$  and the density of the involved bodies. If these are known then the survival time of an ion of interest can be calculated. This simple picture is complicated by the presence of excited ions, molecules and atoms, and as the densities are difficult to estimate, in this work only reactions between ground states are considered.

The type of trace impurity in the gas cell depends not only on the original impurities in the buffer gas and gas purification process but also on the operation and history of the gas cell and gas lines. For example, it has been regularly seen that the efficiency of an ion guide improves towards the end of an experiment which can be understood as arising from the general cleaning during heating by the primary beam [8]. The main impurities in the recycled helium are known to be  $\text{H}_2\text{O}$ ,  $\text{N}_2$  and  $\text{O}_2$  with concentrations of a few ppm. When compared to commercial grade 4.6 helium there is a considerable amount of neon in the recycled gas. The origin is most probably due to the fact that the helium purifier does not condense neon and thus it is not removed in the recycling process.

The cold traps of the IGISOL gas purification system should remove all impurities which have considerably higher melting points than the temperature of liquid nitrogen (77 K). Therefore, impurities such as water and hydrocarbons are frozen out. It is also possible that nitrogen and oxygen are captured in the traps as their boiling points are  $\sim 90$  K and  $\sim 105$  K, respectively, at the pressure of 3–4 bars. However, the exact temperature inside the cold trap is unknown because the gas flow itself warms the zeolite material. The commercial getter is stated to purify  $\text{H}_2\text{O}$ ,  $\text{N}_2$ ,  $\text{O}_2$ ,  $\text{CO}$ ,  $\text{CO}_2$  and  $\text{CH}_4$  to below the ppb level at the typical gas flow rates used at IGISOL.

A typical low mass range spectrum (mass-to-charge ratio  $< 50$ ) recorded with a Faraday cup at the focal plane of the IGISOL-4 separator during a light-ion fusion-evaporation experiment can be seen in Fig. 2. The ion guide was operated at 200 mbar pressure of purified helium. The mass peaks in the spectrum can be clearly identified with a typical mass resolving power  $M/\Delta M \sim 350$ . Helium ion and helium dimer peaks are visible at  $A/q = 4$  and 8, respectively, and helium hydride  $\text{HeH}^+$  at  $A/q = 5$ . The most prominent peak at  $A/q = 20$  is due to the aforementioned neon impurity that can be easily identified by the characteristic isotopic abundances at the adjacent  $A/q$  values of 21 and 22. Oxygen is seen at  $A/q = 16$  and 32, and water-based impurities at  $A/q = 17$ , 18 and 19 are visible. Nitrogen shows up at  $A/q = 14$  and 28, and possibly carbon dioxide at  $A/q = 44$  which might explain the origin of carbon at  $A/q = 12$ .

It should be noted that the transmission efficiency through the radiofrequency sextupole (SPIG) can vary over large mass-to-charge ranges. In general IGISOL operating conditions, two transformer coils may be used depending on whether lighter masses ( $A/q < 50$ ) or heavier masses are required for experiments. The low mass range spectrum in Fig. 2. was obtained using an appropriate coil ensuring good transmission of the SPIG for low masses. This is reflected in the visibility of the helium mass peak which, with the second coil, would not be visible in the spectrum.

## 4 Impurity level investigations with the fission ion guide

The operation of the new IGISOL gas purification system was investigated through a series of measurements of mass spectra under different helium gas purity conditions using the fission ion guide. A first study was performed using the residual fission fragment radioactivity as a source of ionization following an on-line experiment. The mass-separated beam was recorded with a microchannel plate detector. A second study was made on-line and mass spectra were recorded using a Faraday cup. During both experiments the cold trap purified helium had been flowing through the system uninterrupted until the first mass spectra were taken to ensure a true representation of experimental conditions and to reduce the possibility of memory effects. The mass spectra for the unpurified helium were taken following a bypass of the cold trap. Before the start of both experiments the gas lines were baked.

### 4.1 Temporal behaviour

The temporal behaviour of a number of mass-separated impurity beams was measured during the change of gas flow from purified to unpurified helium. An example of the time profile of  $\text{H}_3\text{O}^+$  at  $A/q = 19$ , measured under off-line conditions at an ion guide pressure of 45 mbar, is illustrated in Fig. 3. Once the cold trap has been bypassed, a duration of  $\sim 100$  s passes before the count rate drops and stays at a relatively low level for over five minutes until a steady increase to a higher saturated rate 20 minutes into the measurement.

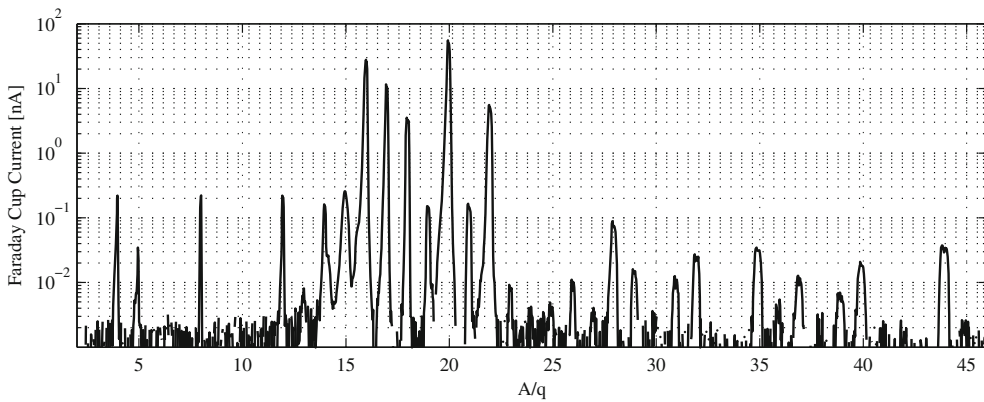


**Fig. 2** Typical on-line mass spectrum taken after the dipole magnet with the light ion guide using helium that is purified with a cold trap. Ion guide pressure: 200 mbars

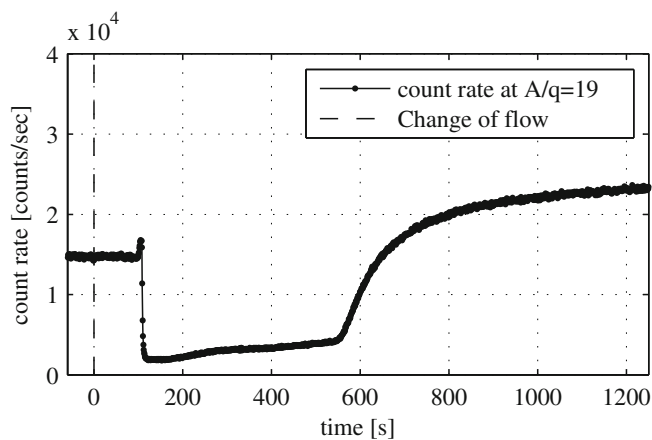


**Fig. 3** Time profile of ion count rate at  $A/q = 19$  corresponding to  $\text{H}_3\text{O}^+$  when changing from purified to unpurified helium

The change in count rate after 100 s reflects the transport time of the gas to the ion guide. With a conductance of 0.65 l/s for a 1.2 mm exit hole using room temperature helium, 100 s corresponds to an evacuated gas line volume of  $\sim 1$  l at the operating pressure of 4 bars. The cause of the longer time scale behaviour is unknown however it is suspected that this reflects the settling of the gas transport line and the ion guide to the new impurity levels. This is supported by a number of very similar time profile measurements of mass peaks corresponding to  $\text{H}_2\text{O}^+$  and  $\text{OH}^+$  impurities. We note therefore that a mass scan (for example that of Fig. 2) portrays a single moment during the operation of a gas cell and the mass spectra themselves may be subject to pronounced changes over long timescales.

#### 4.2 Purified vs. unpurified mass spectra

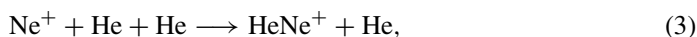
The absolute number density of impurities in the gas can be reliably measured only by introducing a calibrated amount of impurity in a controlled manner [9]. This is not possible with the current IGISOL gas handling system and thus in this work only relative changes

between the mass spectra are investigated. In addition, the changes seen in the mass peaks are not only due to variations in gas purity but also to the rich chemistry (for example the processes discussed in Section 3) and therefore only indirect conclusions on the impurity level can be made.

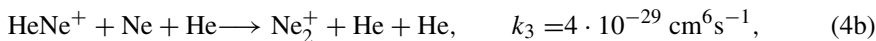
The peak currents of the mass spectra obtained for purified and unpurified helium gas during on-line conditions are presented in Fig. 4. The mass spectrum for unpurified helium was taken almost 90 minutes after the cold trap had been bypassed in order to ensure that system had stabilized. The ion guide pressure was maintained at 245 mbar throughout the measurement. Mass peak assignments have been suggested based on known impurities in the helium gas and wherever possible isotopic abundance ratios have been confirmed.

One notable difference between the mass spectrum in Fig. 4 with that taken using the light-ion ion guide (Fig. 2) is the appearance of strong peaks at  $A/q > 20$ . This can be understood as the evacuation times associated with the volumes of the two ion guides are very different. With an exit hole diameter of 1 mm and a conductance of 0.45 l/s (using helium), the pressure-independent evacuation times are  $\sim 1$  ms and  $\sim 200$  ms for the light ion and fission guide, respectively. Typical bimolecular reactions with a ppb level of impurities have timescales over 1 ms and are thus too slow to be seen with the small volume ion guide.

Similar to Fig. 2, the most prominent mass peak in the spectrum measured with purified helium is at  $A/q = 20$ , suggested to be neon due to the neighbouring peaks with the expected isotopic abundance ratio. Evidence for  $\text{HeNe}^+$  peaks at  $A/q = 24, 25$  and  $26$  can be seen, again with the expected isotopic abundance of neon, formed via the termolecular reaction:



which has a reaction rate coefficient  $k_3 = 2.1 \cdot 10^{-32} \text{ cm}^6\text{s}^{-1}$  [10]. This translates to a reaction time constant  $\tau \approx 1 \mu\text{s}$  at the operating pressure of 245 mbar, orders of magnitude smaller than the typical evacuation time of the fission ion guide. The  $\text{HeNe}^+$  ions react further with neutral neon atoms in the buffer gas through bimolecular and termolecular reactions to form the neon dimer  $\text{Ne}_2^+$ :



where the bimolecular reaction coefficient has been measured by Veatch et al. [11] and the termolecular process is discussed by Bohme et al. [12]. Assuming a typical neon impurity level of 1 ppm, lifetimes of  $\tau \approx 6$  ms and  $\tau \approx 0.7$  ms for the bimolecular and termolecular reaction can be calculated, respectively. These timescales, along with the matching isotopic distribution at  $A/q$  values of 41, 42 and 43, supports the assignment of the neon dimer to the mass peak at  $A/q = 40$ . Other reaction channels leading to the formation of the  $\text{Ne}_2^+$  dimer involve excited neutral neon atoms  $\text{Ne}^*$ , discussed further in [13]. In general, caution should be taken when interpreting the peak current ratios of  $\text{Ne}^+$  ions,  $\text{HeNe}^+$  and  $\text{Ne}_2^+$  molecules as the bond dissociation energies of  $\text{HeNe}^+$  and  $\text{Ne}_2^+$  are somewhat small, 0.69 eV and 1.36 eV, respectively [14]. Molecules may be dissociated upon exit from the ion guide in the guiding field of the rf sextupole thus adding an additional complexity to the interpretation of the mass spectra.

Other peaks in the mass spectrum of purified helium can be associated with the known impurities of nitrogen, oxygen and water-based molecules, summarized further in Table 1. The mass spectrum of unpurified helium shows clear differences to purified helium, the most notable being the strong reduction of neon-based molecules. As highlighted in Table 1,  $\text{Ne}^+$  is reduced by a factor of  $3 \cdot 10^{-4}$ , whereas  $\text{HeNe}^+$  and most likely the neon dimer

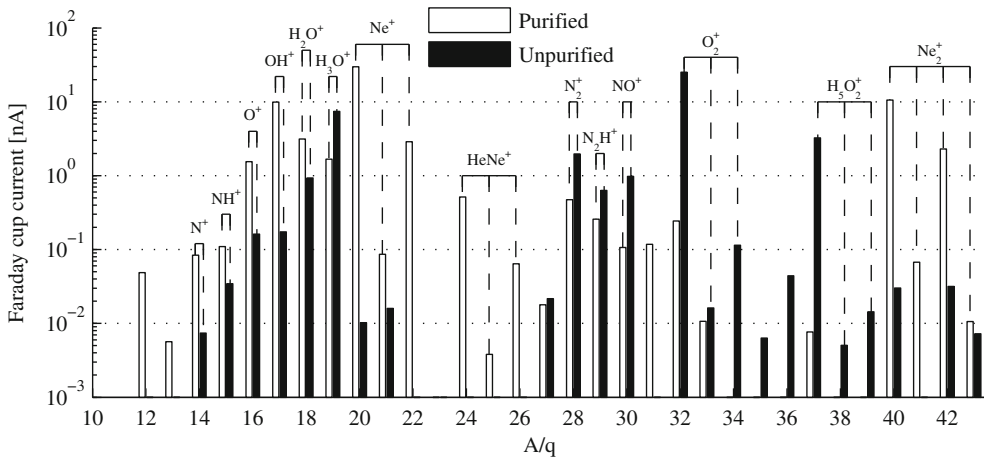


**Fig. 4** Mass peak currents obtained on-line using the fission ion guide for purified and unpurified helium with suggested molecular assignments. A vertical bar is only given for an  $A/q$  value if there is clear peak above a background level of  $10^{-3}$  nA

$\text{Ne}_2^+$  disappear completely. This is an indication that the neon-based ions neutralise via charge exchange reactions with the increased density of impurities. Interestingly, the peak intensities of neon and related compounds were seen to increase as a function of time as the cleanliness of the system improved and show very strong sensitivity to small changes in the operating conditions which affect the gas purity. It could be suggested therefore that neon may be a useful indicator of gas purity conditions in future experiments. Further evidence to support the charge exchange hypothesis as a possible loss mechanism for neon and neon-based impurities arises from the work of Rakshit et al. [15] and Mayhew et al. [16]. For example, the reaction



has a reaction rate coefficient  $k_2 = 8.8 \cdot 10^{-10} \text{cm}^3 \text{s}^{-1}$ . Assuming that the  $\text{H}_2\text{O}$  impurity level increases from ppb to ppm as the cold trap is bypassed, the lifetime of  $\text{Ne}^+$  decreases via reaction (5) from 190 ms to 190  $\mu\text{s}$ . Again, compared to the evacuation time of the ion guide, the lifetimes support the existence of a neon signal with purified helium, and the absence of mass peaks with unpurified helium. Other reaction rate coefficients pertinent to this work are summarized in Table 2.

The strongest peak in the unpurified helium mass spectrum is seen at  $A/q = 32$ , corresponding to  $\text{O}_2^+$ . Oxygen in the gas most likely originates from the introduction of air during the rebottling process and therefore unpurified gas should also contain significant amounts of nitrogen. However, only a small increase in the peak current of  $\text{N}_2^+$  is seen, most likely due to the charge exchange chemistry between impurity molecules. The  $\text{N}_2^+$  molecules quickly lose their charge to neutral  $\text{H}_2\text{O}$  molecules, however  $\text{O}_2^+$  ions do not have any fast reaction channel available and as a result the  $\text{O}_2^+$  impurities maintain their charge.

A significant difference can be seen in the water-based impurities. The  $\text{H}_2\text{O}^+$  signal at  $A/q = 18$  goes down by factor of 0.3 even though the unpurified helium gas is expected to contain considerably more water than the purified gas. Also, the mass speck signal corresponding to  $\text{OH}^+$  is 2 % of that in purified helium. Increases in the water-based impurities

**Table 1** Assignments for mass peaks given separately for the purified and unpurified spectra. If the isotopic distribution can be identified then these are noted. The unpurified/purified peak current ratio ( $I_u/I_p$ ) is given for the base peaks

$A/q$	Assignments		$I_u/I_p$
	Purified	Unpurified	
12	C <sup>+</sup>		< 0.02
14	N <sup>+</sup>	N <sup>+</sup>	< 0.1
16	O <sup>+</sup>	O <sup>+</sup>	0.1
17	OH <sup>+</sup>	OH <sup>+</sup>	0.02
18	H <sub>2</sub> O <sup>+</sup>	H <sub>2</sub> O <sup>+</sup>	0.3
19	H <sub>3</sub> O <sup>+</sup>	H <sub>3</sub> O <sup>+</sup>	4
20	Ne <sup>+</sup>		$3 \cdot 10^{-4}$
21	Ne <sup>+</sup> (M + 1)		
22	Ne <sup>+</sup> (M + 2)		
24	HeNe <sup>+</sup>		< $2 \cdot 10^{-3}$
25	HeNe <sup>+</sup> (M + 1)		
26	HeNe <sup>+</sup> (M + 2)		
28	N <sub>2</sub> <sup>+</sup> , CO <sup>+</sup>	N <sub>2</sub> <sup>+</sup> , CO <sup>+</sup>	4
29	N <sub>2</sub> H <sup>+</sup> , HCO <sup>+</sup>	N <sub>2</sub> H <sup>+</sup> , HCO <sup>+</sup>	2
30	NO <sup>+</sup>	NO <sup>+</sup>	9
32	O <sub>2</sub> <sup>+</sup>	O <sub>2</sub> <sup>+</sup>	100
33		O <sub>2</sub> <sup>+</sup> (M + 1)	
34		O <sub>2</sub> <sup>+</sup> (M + 2)	
37		H <sub>5</sub> O <sub>2</sub> <sup>+</sup>	400
38		H <sub>5</sub> O <sub>2</sub> <sup>+</sup> (M + 1)	
39		H <sub>5</sub> O <sub>2</sub> <sup>+</sup> (M + 2)	
40	Ne <sub>2</sub> <sup>+</sup>		$3 \cdot 10^{-3}$
41	Ne <sub>2</sub> <sup>+</sup> (M + 1)		
42	Ne <sub>2</sub> <sup>+</sup> (M + 2)		
43	Ne <sub>2</sub> <sup>+</sup> (M + 3)		

**Table 2** Reaction rate coefficients (cm<sup>3</sup>s<sup>-1</sup>) for charge exchange between the neon-based ions and the typical helium gas impurities. Reactions can be dissociative in nature

	Ne <sup>+</sup>	HeNe <sup>+</sup>	Ne <sub>2</sub> <sup>+</sup>	Ref.
N <sub>2</sub>	< $3.3 \cdot 10^{-13}$	$9.5 \cdot 10^{-10}$	$8.2 \cdot 10^{-10}$	[16]
O <sub>2</sub>	$6.0 \cdot 10^{-11}$	$3.5 \cdot 10^{-10}$	$7.6 \cdot 10^{-10}$	[16]
H <sub>2</sub> O	$8.8 \cdot 10^{-10}$	–	–	[15]

H<sub>3</sub>O<sup>+</sup> and H<sub>5</sub>O<sub>2</sub><sup>+</sup> by factors of 4 and 400, respectively, are however seen. This can be understood in the following. First, hydronium ions H<sub>3</sub>O<sup>+</sup> form via the reactions:

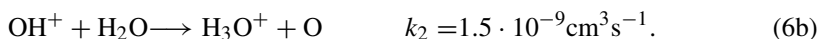
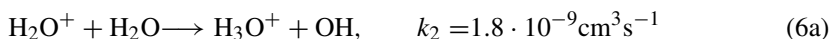
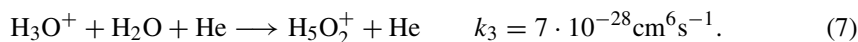


**Table 3** The  $2^+/1^+$  yield ratios for isotopes produced in proton-induced fission of uranium. The molecular formation of yttrium oxide is also shown

Isotope	$2^+/1^+$ ratio	$AO^+/A^+$ ratio
$^{96}\text{Sr}$	0.55	–
$^{96}\text{Y}$	0.09	0.25
$^{100}\text{Y}$	0.07	0.24
$^{143}\text{Ba}$	0.33	–

Then, water molecules start to attach to the hydronium ions via the termolecular reaction [17]:



For a water impurity level of 1 ppm the timescale for the reactions in (6) is  $\sim 100 \mu\text{s}$  and for reaction (7)  $\sim 20 \mu\text{s}$ . Such reaction rates strongly support the clustering of water-based molecules inside the ion guide and explain the reduction in  $\text{H}_2\text{O}^+$  and  $\text{OH}^+$  in unpurified conditions.

In summary, it appears that the general behavior of the changes in the mass spectra are consistent with the expectation that the impurity level in helium is at the ppb level when using the cold traps, and increases to perhaps above the ppm level in many cases when purification is bypassed. The effect of the getter for additional purification of helium was also investigated in a similar manner. The measured spectra did not however show any further reduction in the impurity levels of helium although the getter was able to purify on its own to at least some extent. Further investigations as to the additional benefit of using the getter in parallel with the cold traps are ongoing.

#### 4.3 The charge state and molecular formation of fission fragments

It is well known that impurities within the buffer gas play a strong role in the final thermalized charge state distribution of the recoil ions. Recoils stopping in the helium gas quickly charge exchange with helium atoms until they reach the  $2^+$  charge state which is limited by the ionization potential of helium. A final charge exchange to the  $1^+$  state occurs with the impurities, in particular with molecules due to the high density of states [18]. With good gas purity conditions a considerable fraction of the recoil ions are seen in the  $2^+$  charge state. Indeed, in earlier work at IGISOL-2 a positive effect was often seen on the yield of  $1^+$  ions by bypassing the cold trap and thus adding impurities into the gas cell [19].

Recently, the yields of singly-charged versus doubly-charged fission fragment recoils from proton-induced fission were measured with the aid of gamma-ray spectroscopy for a few isotopes of strontium, yttrium and barium. Because yttrium is a chemically active element it quickly forms an oxide in reactions with  $\text{O}_2$  and  $\text{H}_2\text{O}$  [3], thus the yield of  $\text{YO}^+$  was also measured. On the other hand, the formation of oxides by  $\text{Y}^{2+}$  was not however studied. The measured ratios are summarized in Table 3. As can be seen, there is a notable amount of doubly-charged species. The elemental dependency between the ratios for strontium and barium differ considerably from that of yttrium and may well be due to the noble gas-like closed electronic configuration of doubly-charged barium and strontium isotopes. Separately, doubly-charged species of thorium and uranium have been previously studied at IGISOL-3 in connection with the developments of gas cells for the study of the low-lying isomeric state in  $^{229}\text{Th}$  [20].

## 5 Outlook

Currently, a number of improvements to the gas handling system are being implemented. In order to reduce the desorption of impurities from the walls of the ion guides, mounting of heating elements will allow baking before experiments. Monitoring of the gas purity will be a useful tool and thus a residual gas analyzer (RGA) is being installed (see Fig. 1). The RGA unit has the advantage of being independent to the operation and conditions of the ion guide thus allowing a more direct study of the impurities within the gas. Additionally, the RGA can be run independently enabling monitoring of the gas impurities continuously throughout an experiment.

Although the gas purity has likely reached the ppb level with the new purification and transport system at IGISOL-4, developments to reduce the impurity level even further using cryogenic techniques are planned for the near future. At IGISOL-3, the successful development and demonstration of a cryogenic ion guide was realized [21]. In that work it was shown that liquid nitrogen cooling to  $\sim 90$  K suppressed water-based impurities however lower temperatures would be required to freeze out oxygen and nitrogen. Funding has recently been sought for the purchase of a cryocooler in order to achieve even lower temperatures, with a similar solution having been chosen for the cryogenic gas catcher project for FAIR [22]. Such a system could be used to investigate the molecular formation of chemically active elements as a function of the ion guide temperature, as well as the elemental dependence of the charge state distribution.

**Acknowledgments** This work has been supported by the Academy of Finland programme under the Finnish Centre of Excellence Programme 2012-2017 (Project No. 251353, Nuclear and Accelerator-Based Physics Research at JYFL).

## References

1. Moore, I.D., Dendooven, P., Ärje, J.: *Hyperfine Interact* **223**(1–3), 17 (2014)
2. Karvonen, P., Moore, I.D., Sonoda, T., Kessler, T., Penttilä, H., Peräjärvi, K., Ronkanen, P., Aystö, J.: *Nucl. Instrum. Methods Phys. Res. B* **266**(21), 4794 (2008)
3. Kessler, T., Moore, I.D., Kudryavtsev, Y., Peräjärvi, K., Popov, A., Ronkanen, P., Sonoda, T., Tordoff, B., Wendt, K.D.A., Äystö, J.: *Nucl. Instrum. Methods Phys. Res. B* **266**(4), 681 (2008)
4. Moore, I.D.: *Nucl. Instrum. Methods Phys. Res. B* **266**(19–20), 4434 (2008)
5. Moore, I.D., Eronen, T., Gorelov, D., Hakala, J., Jokinen, A., Kankainen, A., Kolhinen, V.S., Koponen, J., Penttilä, H., Pohjalainen, I., Reponen, M., Rissanen, J., Saastamoinen, A., Rinta-Antila, S., Sonnenschein, V., Äystö, J.: Towards commissioning the new IGISOL-4 facility. *Nucl. Instrum. Methods Phys. Res. B* **317B**, 208 (2013)
6. Moore, I.D., Kessler, T., Sonoda, T., Kudryavstev, Y., Peräjärvi, K., Popov, A., Wendt, K.D.A., Äystö, J.: *Nucl. Instrum. Methods Phys. Res. B* **268**(6), 657 (2010)
7. Morrissey, D.J., Bollen, G., Facina, M., Schwarz, S.: *Nucl. Instrum. Methods Phys. Res. B* **266**(21), 4822 (2008)
8. Penttilä, H., Elomaa, V.-V., Eronen, T., Hakala, J., Jokinen, A., Kankainen, A., Moore, I.D., Rahaman, S., Rinta-Antila, S., Rissanen, J., Rubchenya, V., Saastamoinen, A., Weber, C., Äystö, J.: *Eur. Phys. J. A* **48**(4), 1 (2012)
9. Kudryavtsev, Y., Bruyneel, B., Huyse, M., Gentens, J., den Bergh, P.V., Duppen, P.V., Vermeeren, L.: *Nucl. Instrum. Methods Phys. Res. B* **179**(3), 412 (2001)
10. Jones, J.D.C., Lister, D.G., Wareing, D.P., Twiddy, N.D.: *J. Phys. B* **13**(16), 3247 (1980)
11. Veatch, G.E., Oskam, H.J.: *Phys. Rev. A* **2**, 1422 (1970)
12. Bohme, D.K., Adams, N.G., Mosesman, M., Dunkin, D.B., Ferguson, E.E.: *J. Chem. Phys.* **52**(10), 5094 (1970)
13. Dahler, J.S., Franklin, J.L., Munson, M.S.B., Field, F.H.: *J. Chem. Phys.* **36**(12), 3332 (1962)
14. Dehmer, P.M., Pratt, S.T.: *J. Chem. Phys.* **77**(10), 4804 (1982)



15. Rakshit, A.B., Twiddy, N.D.: *Chem. Phys. Lett.* **60**(3), 400 (1979)
16. Mayhew, C.A.: *J. Phys. B* **25**(8), 1865 (1992)
17. Bierbaum, V.M., Golde, M.F., Kaufman, F.: *J. Chem. Phys.* **65**(7), 2715 (1976)
18. Ärje, J., Äystö, J., Taskinen, P., Honkanen, J., Valli, K.: *Nucl. Instrum. Methods Phys. Res B* **26**(1–3), 384 (1987)
19. Huikari, J., Dendooven, P., Jokinen, A., Nieminen, A., Penttilä, H., Peräjärvi, K., Popov, A., Rinta-Antila, S., Äystö, J.: *Nucl. Instrum. Methods Phys. Res. B* **222**(3–4), 632 (2004)
20. Sonnenschein, V., Moore, I.D., Raeder, S., Hakimi, A., Popov, A., Wendt, K.: *Eur. Phys. J. A* **48**(4), 1 (2012)
21. Saastamoinen, A., Moore, I.D., Ranjan, M., Dendooven, P., Penttilä, H., Peräjärvi, K., Popov, A., Äystö, J.: *Nucl. Instrum. Methods Phys. Res. A* **685**, 70 (2012)
22. Ranjan, M., Purushothaman, S., Dickel, T., Geissel, H., Plass, W.R., Schäfer, D., Scheidenberger, C., de Walle, J.V., Weick, H., Dendooven, P.: *Euro. Phys. Lett.* **96**, 52001 (2011)

## 3.2 IGISOL buffer gas purification system

At IGISOL and other radioactive ion beam facilities that use gas cells for the production of low-energy ion beams, helium and argon gases are used to stop and thermalize high-energy nuclear reaction products or, occasionally, are used as a carrier of evaporated atoms. In reference to the stopping, the term *buffer gas* is used here to refer to helium and argon gases. The purity of buffer gases plays a crucial role in the extraction of ions from gas cells. The gas affects the charge state by often acting as an electron donor such that stopped ions, which are thermalized in helium in the doubly-charged state, may then be reduced to singly-charged. Impurities in the buffer gas often create a variety of contaminant ion beams especially in low mass regions, and if chemically-active species of ions are extracted from large gas cells, molecular formation can be a significant loss mechanism [73, 74]. The yields of neutron-rich nuclei produced using charged-particle-induced fission have been shown to be very sensitive to impurities, with poor purity conditions often resulting in considerably lower yields. Experiments performed at the IGISOL-4 facility which, as described in Article I, now operates using a completely new buffer gas purification system based on the earlier design [75], have shown record yields from fission, which can be at least partly attributed to better gas purity compared to the earlier IGISOL era.

Impurity levels below parts-per-billion (ppb) can be taken as a general requirement for purification. At that level the timescale for molecular ion formation approaches the evacuation time of most gas cells and efficiency losses due to gas impurities are largely minimized [76]. At IGISOL, the required purity conditions are not as stringent if a small gas cell such as that used in connection with light-ion induced fusion-evaporation reactions is used, but with the larger gas cells and especially work in connection to laser ion sources and reactive refractory elements, a high gas purity is required.

The IGISOL gas handling system consists of supply, purification and transportation stages until the IGISOL front-end vacuum system is reached which houses the gas cell (see Fig. 1 of Article I). When the buffer gas is fed from bottles to the gas purification system, it contains several different trace impurities with concentrations at a level of a few parts-per-million (ppm). In helium, which is usually in-house recycled helium, as well in commercially purchased argon, the most abundant impurities are  $\text{H}_2\text{O}$ ,  $\text{O}_2$  and  $\text{N}_2$ . In addition,  $\text{CO}$ ,  $\text{CO}_2$  and a variety of hydrocarbons may be present. Neon is an impurity that is consistently present in the recycled in-house helium, originating most likely from the purification stage in the recycling process. To remove the impurities at IGISOL two methods are used: liquid nitrogen ( $\text{LN}_2$ ) operated cold traps filled with an adsorbent molecular sieve are used for helium, whereas a getter-based purifier (Saes MonoTorr PS4-MT15) is used for argon. The operational pressure of the

purification system and transportation lines is kept in the absolute pressure of  $\sim 4$  bar.

Similar purification systems are being used in other radioactive ion beam facilities for buffer gas, gaseous target and recycled helium purification [77–80]. The low-energy branch of the MARA (Mass Analysing Recoil Apparatus) facility [19] at JYFL is currently under design and will house a dedicated gas-cell setup with a gas purification system [20].

### 3.2.1 Purification by condensation

Simple purification of light noble gases can be performed by bringing the gas into contact with a cold surface. If the temperature of the gas can be lowered so that the partial pressure of a particular impurity drops below the vapor pressure of the impurity, a condensed phase with the cold surface is formed until the partial pressure again reaches the vapor pressure. In this manner the lowest achievable concentration of an impurity at a particular temperature can be inferred from the vapor pressure curve of the impurity. Whether the impurity condenses to solid or liquid phase depends on whether the pressure and temperature are below the triple point.

Figure 3.1 highlights calculated vapor pressure curves for noble gases and other relevant molecules along with their triple points. The curves have been plotted using the Wagner equation [81], which models the vapor pressure using four parameters. The parameters have been determined for  $\text{H}_2\text{O}$  by Nichols [82] and for other gases by L. A. Forero and J. A. Velásquez [83]. The triple points have been obtained from the values tabulated by R. E. Bedford et al. [84] and from the NIST Standard Reference Database Number 69 [85]. It is noteworthy that the Wagner equation best describes the vapor pressure curves between the triple and critical points. In this work the equation is used to extrapolate to low temperature sublimation and therefore curves may deviate from actual values, however, for the discussion here, the accuracy of the curves suffice. Only the sublimation pressure curve for  $\text{CO}_2$  is plotted using the sublimation pressure correlation equation by R. Span [86] due to its high triple point. For more specific determination of the sublimation curves for some of the species, see for example references [87, 88].

Due to the high volatility of the helium gas, it can be purified from lower volatility impurities without any active material by performing simple condensation with  $\text{LN}_2$ . As can be seen from Fig. 3.1, the vapor pressures of  $\text{H}_2\text{O}$ ,  $\text{CO}_2$  and hydrocarbons longer than ethane are already below  $P_v = 10^{-6}$  mbar at  $\text{LN}_2$  temperature, which is marked in the figure as a vertical dashed line. By assuming the helium pressure to be equivalent to the transportation line pressure of the IGISOL gas purification system,  $P_1 = 4$  bar, impurity levels below  $P_v/P_1 < \text{ppb}$

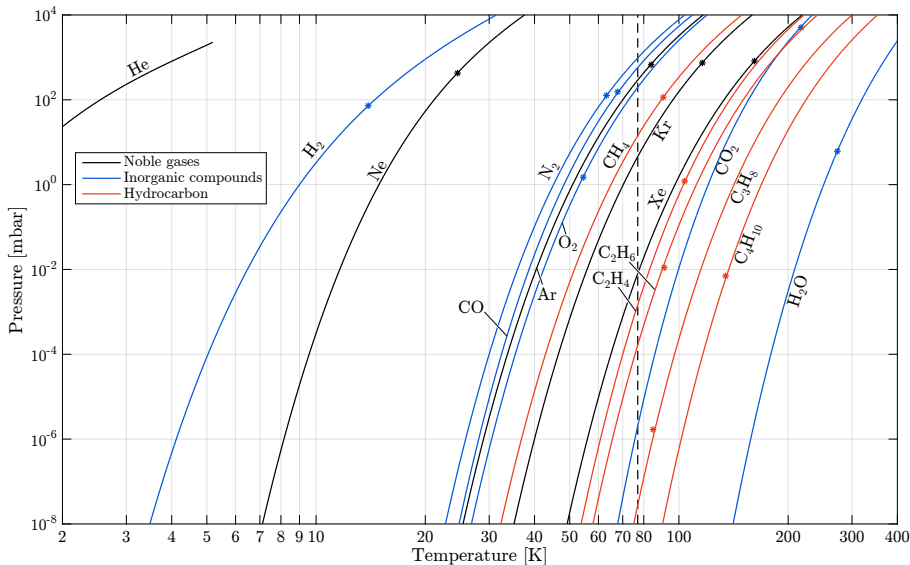


**Figure 3.1.** The vapor pressure curves of several noble gases and molecules of interest. The curves are plotted with equations from references [81, 83, 82, 86]. The asterisks mark the triple points and the vertical dotted line shows the LN<sub>2</sub> temperature at atmospheric pressure. The C<sub>4</sub>H<sub>10</sub> curve is for n-butane.

can be achieved. However, higher volatility impurities such as N<sub>2</sub> cannot be purified to any reasonable concentration as  $P_v(\text{N}_2, 77\text{K})/P_1 = 0.25$ , and either lower temperatures, higher helium pressures or other purification methods are required.

### 3.2.2 Purification by adsorbents

Many molecular sieves such as activated charcoal and zeolites are very good adsorbents due to their porous structure, which results in very high specific surface areas in the range  $A/m = 10^3 \text{ m}^2/\text{g}$  [89]. Zeolites in particular, which are microporous alumina-silicates, are used widely in industry as filters, adsorbents and catalysts, and they are available in a variety of types differing in their crystalline structure and internal cations. Such adsorbent material can be added to a container and cooled to low temperatures with the effect of a considerable adsorption of the surrounding gases through the process called physisorption. This high absorptivity can be exploited for purification of gases and even the higher volatility impurities can be effectively removed because the adsorption of a gas molecule happens already at lower pressures than the vapor pressure.

In practice, an adsorbent material needs to be conditioned before use by evacuating adsorbed gases. This is realized by heating the material to high temperatures while maintaining a good vacuum. Then, by simply cooling the material, a very high adsorption is attained and from a gas mixture, lower volatility compounds are preferentially absorbed before higher volatility compounds. After a certain time period, the adsorbent needs to be regenerated again. The required temperature for conditioning or regeneration depends on the type of adsorbent and the desorbing gas. Generally, it can be stated that the volatile gases are readily desorbed already at room temperature, but to attain a good desorption rate for H<sub>2</sub>O, higher temperatures of about 400 K with activated charcoal and about 550 K with zeolites are required.

As discussed in Article I, LN<sub>2</sub>-cooled “cold traps” filled with an adsorbent are used at IGISOL for helium purification. The purification system includes two cold traps each with a volume of  $\sim 0.8$  l. Only one cold trap is in use during an experiment while the other is under regeneration by pumping it with a dry pump and heating to about 550 K with an electric heating element. The cold traps are rotated every 3 to 4 days to ensure good gas purification. During the construction of the IGISOL gas purification system, zeolite of type 13X (aluminum-sodium-silicate, Linde type X) was chosen to replace the previously used activated charcoal, which contaminated pipes with carbon dust and was generally less safe to use. Each cold trap has approximately 500 g of the 13X zeolite.

The adsorption capability of an adsorbent can be represented by an adsorption isotherm which measures the amount (weight) of adsorbate that is adsorbed per gram of adsorbent material as a function of equilibrium pressure at a constant temperature. The N<sub>2</sub> adsorption isotherms of zeolite 13X at 77 K and 298 K, measured by S. Cavenati et al. [90] and S. A. Stern et al. [91], respectively, are depicted in Fig. 3.2. An isotherm measurement (Cavenati et al.) for zeolite 5A is also given for comparison. These measurements have been performed with a zeolite that has been thoroughly regenerated at temperatures above 600 K. The solid lines are spline fits to the experimental data to show the trend of the isotherms.

By estimating the inlet N<sub>2</sub> impurity content to be  $\epsilon = 1$  ppm and knowing the gas cell throughput  $q_V$  from Eq. (2.15), an estimation for the amount of N<sub>2</sub> gas  $m(\text{N}_2)$  in grams in one cycle of cold trap ( $t_c = 4$  d) usage can be estimated:

$$m(\text{N}_2) = \frac{\epsilon P_{\text{gc}} q_V (T_{\text{gc}}) t_c}{RT_{\text{gc}}} M(\text{N}_2), \quad (3.1)$$

in which  $M(\text{N}_2)$  is the molar mass of N<sub>2</sub>,  $P_{\text{gc}}$  and  $T_{\text{gc}}$  are the gas pressure and temperature in the gas cell. Using the normal operational conditions during fission, i.e. 300 mbar and 300 K, an estimation for the total amount of N<sub>2</sub> that

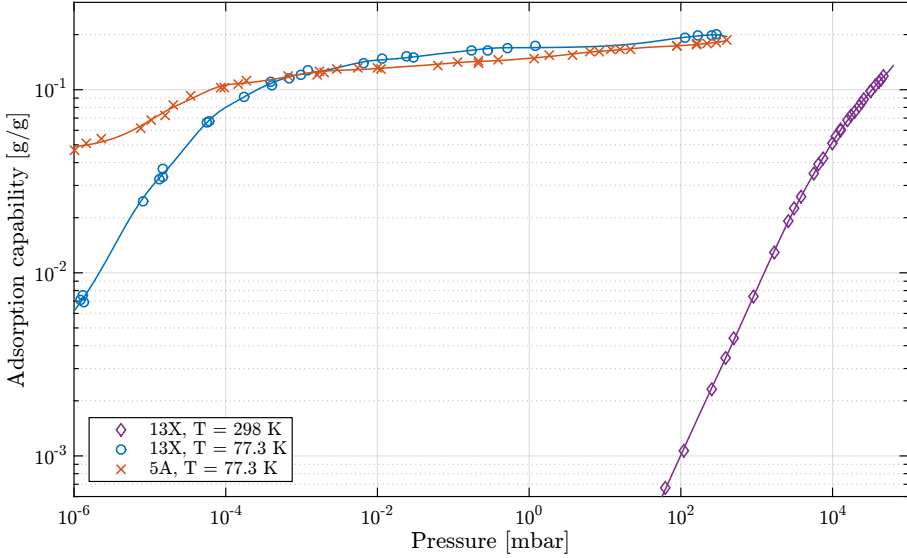


**Figure 3.2.** Nitrogen gas adsorption isotherms for 13X zeolite at room temperature as measured by S. Cavenati et al. [90] and at 77 K along with the adsorption curve of  $N_2$  to A5 zeolite as measured by S. A. Stern and F. S. DiPaolo [91].

has been introduced to the purifier bed can be calculated,  $m(N_2) = 0.08$  g. From this, the mass ratio  $\mu$  between the  $N_2$  impurity and adsorbent can be calculated to be of the order of  $\sim 2 \cdot 10^{-4}$  g/g. Using Fig. 3.2, the adsorption equilibrium pressure for this amount of  $N_2$  can be seen to be very low ( $<10^{-6}$  mbar) at 77 K. Therefore, even after several days of continuous operation, the cold trap can be assumed to be still purifying  $N_2$  well below the ppb level. In reality, it is difficult to provide an accurate estimation of the purification because the isotherms can be affected by other adsorbed impurities, especially with water, and it is not known how close to the equilibrium pressure an impurity reaches in the dwell time of the gas inside the cold trap (20 s to 2 min). Also, for some isotherms there is considerable variation in the reported data between the different authors.

Similar adsorption isotherms can be found in the literature for other gases with 13X zeolite operating at different temperatures [92]. Generally, because physisorption and condensation are the result of the same intermolecular forces, a direct correspondence between boiling points and adsorption volumes of different compounds can be found [93]. For example, from the vapor pressure curves of Fig. 3.1, it is expected that neon would be adsorbed much less than nitrogen. S. A. Stern et al. [91] reports a Freundlich isotherm constant  $k'$  for neon adsorption to zeolite 13X at 77.3 K,  $k' = 3.08 \cdot 10^{-5}$  g/(g · mbar $^{1/n}$ ) with

$n = 1.015$ . Assuming the same impurity content in the gas for neon as for nitrogen, an equilibrium pressure of about 4 mbar can be calculated after four days. Therefore it can be deduced that neon is not expected to be purified. This result is supported by the observation that intense neon ion beams are always present when purified recycled helium gas is used.

### 3.2.3 Purification by getter-based purifiers

With regards to argon as a buffer gas, at the operational pressure of the gas purification system, Fig. 3.1 illustrates that the vapor temperature for argon is above the LN<sub>2</sub> temperature of 77 K. Therefore argon gas cannot be purified in the cold traps as it would liquefy, rather it is passed through a commercial getter purifier (Saes MonoTorr PS4-MT15).

Getter purifiers operate in a fundamentally different way than the aforementioned adsorption purifier. In a getter, instead of physisorption, the adsorption or rather absorption of impurities happens via irreversible chemisorption, in other words the impurities chemically react with a getter material [89]. The chemical reactions usually occur with a Group 4 metal, often in a zirconium alloy that is heated to high temperatures. The commercial getter purifier, according to its specifications, is capable of purifying the typical buffer gas impurities also below the sub-ppb level.

In addition to argon, the purifier at IGISOL can be used to purify helium separately, or in series with the cold trap. However, during test experiments with the buffer gas purification system, no additional benefit to the purity conditions was found following purification of helium with the getter purifier after the cold trap purification. This indicates that the purity conditions are already optimal and any outgassing and other contaminant sources nearer to the gas cell (or indeed from the gas cell walls) are responsible for the residual observed contaminant beams.

## 3.3 Contaminants beams from target chamber leak

Contaminant beams at lighter masses, which are often observed with intensities in the order of nA, can be detrimental to experiments, in particular for mass measurements at the JYFLTRAP Penning trap facility. Because the IGISOL mass separator does not have the resolution to separate molecular and monoatomic ion beams, the experimental apparatus can sometimes be overwhelmed by the stable contaminant, as the radioactive beam intensities of interest are well below

Faraday cup amounts ( $< \text{pA}$ ). For example, the measurement of the superallowed  $\beta$ -decay  $Q_{\text{EC}}$  value for  $^{14}\text{O}$  [94] was not feasible at IGISOL due to a  $\text{N}^+$  contaminant beam, even with the improved gas purification discussed in this thesis. In this section the investigation of the contaminant beams formed due to a poor background pressure of the gas cell pumping system are presented.

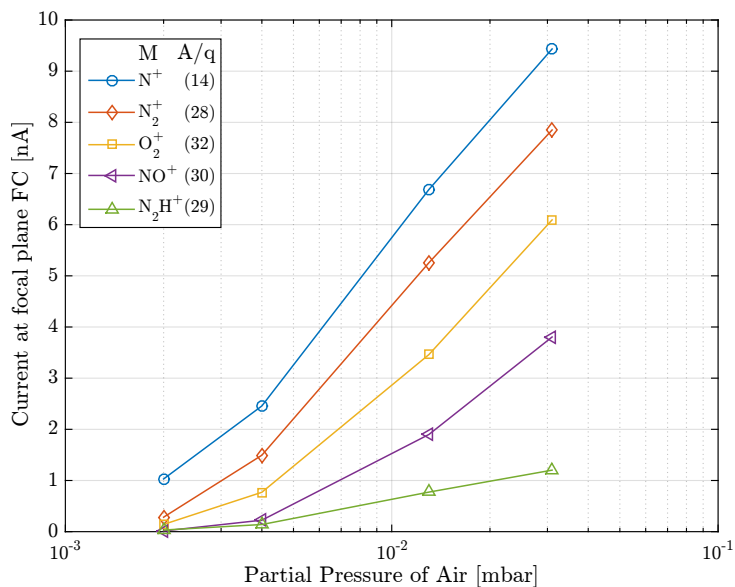
### 3.3.1 Contaminant beams as a function of leak rate

During the  $^{14}\text{O}$  experiment attempted in 2014, it was discovered that a poor target chamber background pressure, i.e. the baseline pressure when no gas is fed to the gas cell, was linked to the creation of contaminant ion beams. At IGISOL, the so-called target chamber is the vacuum chamber which houses the gas cell and which is pumped by a series of roots pumps to evacuate the continuously flowing buffer gas. During that particular period, when no gas was fed, a target chamber pressure of  $2 \cdot 10^{-3}$  mbar was measured indicating a leak as the nominal pressure was expected to be in the range of a few  $10^{-4}$  mbar. More recently, following an upgrade of the roots station, a few  $10^{-5}$  mbar is now the new baseline. To investigate the effect of the leak, a needle valve was added to the target chamber in order to create an additional, but controllable, artificial leak. By recording a mass spectrum as a function of different added partial pressures of air, the mass-separated beam intensities provided a clear indication of the creation of contaminant beams formed by the ionization of the residual air in the target chamber.

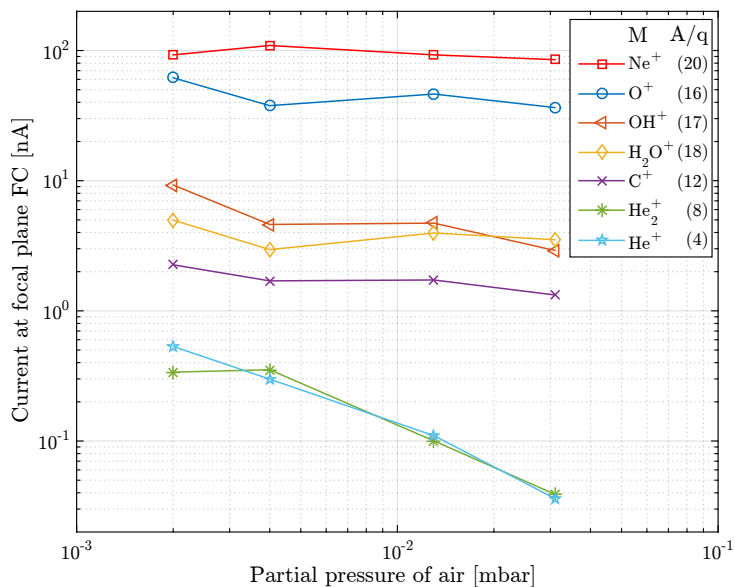
The measured intensities of several identified monoatomic and molecular ion beams are plotted in Figs. 3.3a and 3.3b as a function of the partial air pressure in the target chamber. Figure 3.3a illustrates the species that were observed to increase in intensity when the leak rate was increased, while Fig. 3.3b presents species in which the intensity either decreased or did not change significantly.

All of the ions in Fig. 3.3a contain nitrogen and oxygen and therefore are believed to be related to air which has the volumetric composition of 78.1% of  $\text{N}_2$ , 21.0% of  $\text{O}_2$ , 0.9% of Ar and trace amounts of  $\text{CO}_2$  and other noble gases [95]. On the other hand, the intensity of the ions that were not observed to increase as a function of the leak rate can be considered to belong to the inherent impurities of the buffer gas or outgassing from the walls of the gas cell. Neon,  $\text{Ne}^+$ , as mentioned earlier, is an inherent impurity in the local supply of helium which is not purified in the purification system. The molecules of  $\text{H}_2\text{O}^+$ ,  $\text{OH}^+$  and  $\text{O}^+$  are all thought to be related to water that originates from the walls of the gas cell which was not baked prior to the experiment. Even though  $\text{O}^+$  is also related to the addition of air, its increase was not observed because the intrinsic intensity seen in Fig. 3.3b is much higher than the other air-related ion beams. Therefore,  $\text{O}^+$  is most likely formed due to the primary beam-induced break up of water molecules.





(a)



(b)

**Figure 3.3.** The mass-separated ion beam intensities that are (a) increasing or (b) stable or decreasing as function of the partial pressure of air in the target chamber. The  $A/q$  values for the assignments of atomic and molecular ions are shown in brackets.

Although the buffer gas impurity-related ions in Fig. 3.3b are reasonably stable, there is a notable decrease in the intensities of  $\text{He}^+$  ions and  $\text{He}_2^+$  dimers when the leak rate is increased. This most likely reflects increasing space charge effects within the radiofrequency (RF) sextupole ion guide which guides ions to the high vacuum acceleration region of the mass separator, leading to a reduction in the transmission efficiency of the lightest species. The lower transmission of helium ions and dimers through the SPIG is a common feature of such devices, and explains why the measured focal plane intensities without the additional leak (Fig. 3.3b) are lower than the heavier impurity molecules even though helium is the dominant carrier of charge transported out from the gas cell.

### 3.3.2 Ionization mechanism outside the gas cell

Due to the supersonic flow of the helium gas, the air leaked into the target chamber cannot diffuse back through the exit nozzle into the gas cell. Therefore the increased intensity of the air-related species indicates the existence of an ionization mechanism outside the gas cell. The residual air might be ionized due to some primary beam-related phenomena, such as the scattering of protons ionizing the gas inside the SPIG.

Another explanation for the additional ionization involves charge exchange reactions within the SPIG between the residual air molecules and  $\text{He}^+$  and  $\text{He}_2^+$ . For example,



These charge exchange reactions involve  $\text{N}_2$  and have measured reaction rate coefficients of  $k_2(\text{He}^+) = 1.2 \cdot 10^{-9} \text{ cm}^3/\text{s}$  [96] and  $k_2(\text{He}_2^+) = 1.15 \cdot 10^{-9} \text{ cm}^3/\text{s}$  [97], respectively. Branching of the dissociative reaction has been measured by V. G. Anicich et al. [98]. If a  $\text{N}_2$  number density  $N(\text{N}_2) = 0.781 P_{\text{air}}/(k_{\text{B}}T) = 3.8 \cdot 10^{13} \text{ at./cm}^3$  is assumed from the partial pressure of air  $P_{\text{air}} = 2 \cdot 10^{-3} \text{ mbar}$ , a characteristic time constant of 22  $\mu\text{s}$  can be calculated for both charge exchange reactions using Eq. (2.34). The experimentally measured transport time of ions through the SPIG is  $\sim 100 \mu\text{s}$  [99], therefore it is suggested that the ionization seen outside the gas cell may at least partly be due to the aforementioned reactions. This ionization of residual gas might also contribute to the reduction of  $\text{He}^+$  and  $\text{He}_2^+$  beams seen in Fig. 3.3b.

In previous studies by Kessler et al. [73], similar investigations concerning the

effect of adding a controlled target chamber leak were done in connection to in-gas-cell resonance laser ionization of yttrium. In that work, a clear oxidation and water adduct addition to atomic  $Y^+$  was observed and at a target chamber pressure of  $1 \cdot 10^{-1}$  mbar, the atomic ions extracted from the gas cell were completely redistributed into molecular species.

The work done by Kessler et al. and the measurements in this thesis show that in addition to control over the buffer gas purity, the extraction region vacuum after the gas cell where ions have yet to be accelerated to the typical high voltage potential of IGISOL must also be addressed. To guarantee the beam purity, the pumping chambers in the extraction region should be UHV quality even though the pumping system may not be able to achieve UHV pressures. With the new roots pumping station and more careful operation of the front-end of the IGISOL facility, the purity conditions outside the gas cell have been improved.

### 3.4 Towards a cryogenic gas cell

The currently observed impurities during experiments are expected to result from residual downstream contamination after the gas purification system and transport lines. The most significant mass-separated beams are water-based impurities that are believed to originate from water outgassing from the walls of the gas cell. Moisture in the gas cell always exists due to an unavoidable exposure to air before experiments, and for this reason the gas cells are baked in parallel to the gas lines before every experiment.

To control the purity conditions even further a cryogenic approach is required. A project with the aim of developing a cryogenic-based gas cell was initiated at IGISOL several years ago in which a  $LN_2$ -cooled ion guide for light-ion fusion-evaporation reactions was tested [100]. Prior to these first experiments, S. Purushothaman and colleagues investigated the ion survival and transport efficiency of  $^{219}Rn$  at JYFL, including the effect of ionization of the gas induced by the passage of a proton beam [101]. In other radioactive ion beam facilities, cryogenic gas cells are being used to slow down and stop high-energy beams for delivery to low-energy experimental areas, for example, the cryogenic stopping cell for projectile and fission fragments that has been developed for the Super-Fragment Recoil Separator (Super-FRS) located at GSI, Germany [102, 103], and the cryogenic stopping cell for the Penning-trap spectrometer SHIPTRAP, also located at GSI [104].

Most recently, a dedicated high-power single-stage cryocooler has been purchased for the purpose of coupling it to a gas cell at IGISOL to investigate the possible improvement in the purity conditions achieved by reduction of outgassing and

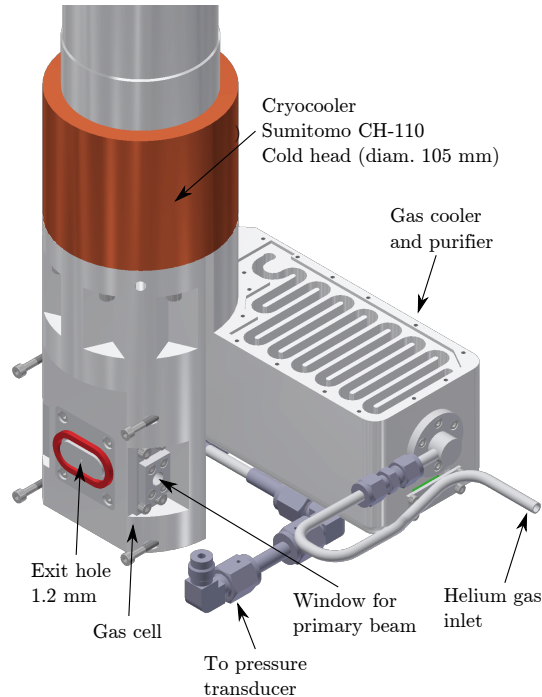


**Figure 3.4.** The design concept for the new cryogenic gas cell. The cold head connects separately to the gas cooler/purifier and to the gas cell.

additional purification of the buffer gas. The cryocooler-based gas cell would also enable the investigation of mass-separated impurities as a function of gas cell temperature, and by combining the gas cell with a  $^{252}\text{Cf}$  fission source it would also allow controlled investigations of the elemental dependence in the extraction efficiency as a function of temperature.

Future cryogenic operation may also lead to an improvement in the fission fragment stopping at IGISOL used for the production of neutron-rich RIBs from charged-particle-induced fission of actinide targets [105]. Currently the stopping efficiency is  $\sim 1\%$  and could be improved with a higher buffer gas density. The challenge, however, may be the increased three-body recombination reaction with free electrons (Eq. (2.31)) which tends to increase with decreasing temperature [100].

### 3.4.1 The design of the new cryogenic gas cell

Figure 3.4 shows the design concept for the new cryogenic gas cell. Initially, this first design has been modeled for connection to a small-volume gas cell ( $\sim 10 \text{ cm}^3$ ) very similar to that used for light-ion induced fusion-evaporation experiments. The helium buffer gas is first fed through a gas cooler and purifier which may be filled with an adsorbent material. This cooler is separately connected to the cryogenic cold head of the cryocooler, which also connects to the gas-cell body. The gas cell has an exit nozzle of diameter 1.2 mm, similar to current designs at IGISOL, and with windows to allow access to the primary beam for future on-line experiments. The temperature is measured from several points throughout the system and heating cartridge elements provide heat input for controlling the temperature.

The estimation of the required cooling power for the cooling of room temperature helium gas to approximately 50 K has been done by assuming a helium flow rate of 9 mmol/s (300 mbar, 0.75 l/s at 300 K), resulting in  $\sim 45 \text{ W}$ . Reduction of this cooling power would require pre-cooling with  $\text{LN}_2$ . A challenge for the design of the system is that the gas cell cannot be located directly inside the pumping chamber because the evacuated helium will cause an increase in background pressure to  $\sim 5 \cdot 10^{-2} \text{ mbar}$ , resulting in several hundred watts of heating of the gas cell due to conduction losses. By enclosing the cryocooler and the gas cell in an isolation chamber which can be pumped separately to a vacuum below  $10^{-3} \text{ mbar}$ , the conduction losses can be reduced to below 10 W. The combined heat losses through the connectors and radiative emission have been estimated to lead to an additional 10-20 W.

Due to the requirement for helium gas cooling a high-power single-stage cryocooler, Sumitomo CH-110, was purchased. According to specifications, the cryocooler can provide a cooling power of 200 W at 90 K, 130 W at 50 K until gradually stalling to 30 W at 25 K. With the estimated heating load and available cooling power, the aim is to reach operational gas cell temperatures below 50 K.

The development and testing of the cryocooler and gas cell is going to be performed in a new off-line ion guide quadrupole mass spectrometer station [106]. The off-line station is an independently-operated mass spectrometer system consisting of a large pumping chamber that can house a variety of gas cells, a differential pumping section with extraction ion optics and a quadrupole mass spectrometer donated by the University of Mainz.

Figure 3.5 presents the CAD design of the gas cell connected to the cryocooler, mounted within the main vacuum chamber of the off-line station. One of the critical design challenges has been to account for up to several mm of thermal contraction during the cooling down phase of the gas cell. The gas

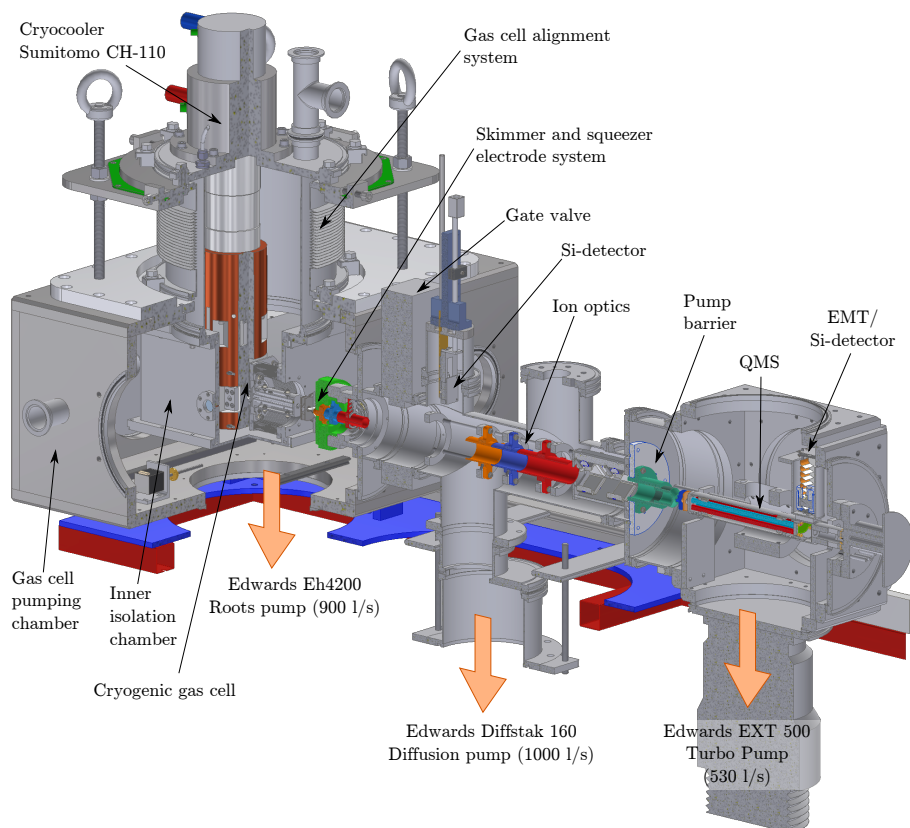


**Figure 3.5.** The CAD design of cryocooler coupled to the gas cell so that the whole system is mounted to the main vacuum chamber of a new off-line ion guide quadrupole mass spectrometer station.

cell, cryocooler and isolation chamber are all connected to one another. An alignment system has therefore been designed, foreseen to suspend these main components above the vacuum chamber via bellows with ISO DN250 flanges. The body of the gas cell is then connected to the isolation chamber with a second set of bellows.

When finalized and constructed, a series of cooling power tests will be performed, followed by pressure tests and ion beam extraction of recoiling daughters from an alpha-recoil source. The quadrupole mass separator connected with electron multiplier tube (EMT) and silicon detectors will allow for ion beam identification, and to probe the intensities of the impurities ionized by the alpha recoils as a function of temperature from 300 K to cryogenic operation. The alpha-recoil source will also allow for the overall efficiency of the off-line station to be measured, which will be of importance when deciding upon the strength of a future  $^{252}\text{Cf}$  spontaneous fission source.

## Chapter 4

# Development of the actinide gas cell and laser ionization of plutonium

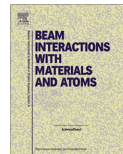
In this chapter the developments for a laser ion source for plutonium using filament-based dispensers mounted in a gas cell are presented. This work initiated the program for studying heavy elements at the IGISOL facility using a combination of laser resonance ionization and collinear laser spectroscopy, resulting in a measurement of the heaviest element to date with the latter technique [25]. This chapter is based on the work done in publication No. II by the author, in which the development of a new gas cell for the filament-based work for actinide elements, laser ionization of plutonium and the gas-phase chemistry and dynamic behavior of plutonium ions in the gas cell is presented. Additionally, the publication includes gamma-ray spectroscopy of the plutonium samples in order to measure their activity and to compare the resulting isotopic distribution with an assay provided by the University of Mainz, Germany.

This chapter concentrates on the detailed investigation and interpretation of the resonant laser ionization scheme of plutonium that was primarily done after the publication of the article. Most of the background information may be found in the publication and is only shortly repeated here in relevant sections.



## 4.1 Article II

The following pages contain the peer-reviewed paper titled *In-gas-cell laser ionization studies of plutonium isotopes at IGISOL*, published in the journal of Nuclear Instruments and Methods in Physics Research Section B, vol 376 (2016), pages 233-239.



## In-gas-cell laser ionization studies of plutonium isotopes at IGISOL



I. Pohjalainen<sup>a,\*</sup>, I.D. Moore<sup>a,\*</sup>, T. Kron<sup>b</sup>, S. Raeder<sup>c,d</sup>, V. Sonnenschein<sup>e</sup>, H. Tomita<sup>e</sup>, N. Trautmann<sup>f</sup>, A. Voss<sup>a</sup>, K. Wendt<sup>b</sup>

<sup>a</sup> University of Jyväskylä, Department of Physics, P.O. Box 35 (YFL), FI-40014 University of Jyväskylä, Finland

<sup>b</sup> Institut für Physik, Johannes Gutenberg Universität, 55128 Mainz, Germany

<sup>c</sup> Helmholtz-Institut Mainz, 55128 Mainz, Germany

<sup>d</sup> KU Leuven, Instituut voor Kern- en Stralingsfysica, B-3001 Leuven, Belgium

<sup>e</sup> Nagoya University, Furo-cho, Chikusa-ku, Nagoya 464-8603, Japan

<sup>f</sup> Institute of Nuclear Chemistry, University of Mainz, Fritz-Straßmann-Weg 2, 55128 Mainz, Germany

### ARTICLE INFO

#### Article history:

Received 1 September 2015

Received in revised form 25 January 2016

Accepted 4 February 2016

Available online 24 March 2016

#### Keywords:

Resonance laser ionization

Gas phase chemistry

Gas cell

Plutonium

### ABSTRACT

In-gas-cell resonance laser ionization has been performed on long-lived isotopes of Pu at the IGISOL facility, Jyväskylä. This initiates a new programme of research towards high-resolution optical spectroscopy of heavy actinide elements which can be produced in sufficient quantities at research reactors and transported to facilities elsewhere. In this work a new gas cell has been constructed for fast extraction of laser-ionized elements. Samples of <sup>238–240,242</sup>Pu and <sup>244</sup>Pu have been evaporated from Ta filaments, laser ionized, mass separated and delivered to the collinear laser spectroscopy station. Here we report on the performance of the gas cell through studies of the mass spectra obtained in helium and argon, before and after the radiofrequency quadrupole cooler-buncher. This provides valuable insight into the gas phase chemistry exhibited by Pu, which has been additionally supported by measurements of ion time profiles. The resulting monoatomic yields are sufficient for collinear laser spectroscopy. A gamma-ray spectroscopic analysis of the Pu samples shows a good agreement with the assay provided by the Mainz Nuclear Chemistry department.

© 2016 Elsevier B.V. All rights reserved.

### 1. Introduction

The actinide elements cover the atomic number range from Ac ( $Z = 89$ ) to Lr ( $Z = 103$ ), beyond which lie the superheavy elements. It is this region which poses some of the most difficult and yet exciting challenges to experimentalists, requiring highly sensitive techniques to make efficient use of the limited quantity of isotopes which can be produced. Nuclear structure information obtained from optical spectroscopy is limited, in particular above Ra ( $Z = 88$ ) which corresponds to the last isotopic chain for which collinear laser spectroscopy has been performed [1]. This reflects a combination of low production cross sections coupled with a lack of stable isotopes, thus only limited knowledge of optical transitions. Traditionally, actinide spectroscopy has been motivated by atomic energy level analysis, with more recent techniques including resonance ionization mass spectrometry applied to determine fundamental atomic properties such as the ionization potential [2]. Probing the evolution of shell structure and the development

of nuclear deformation of the heaviest elements using model-independent laser spectroscopic techniques is a current goal at a number of facilities. It is clear that a step-wise approach will be needed to successfully produce the requisite radioactive beams, including characterization of optical transitions for selective and efficient ionization. Further studies will then be required in order to optimize the optical spectroscopy for high-resolution measurements.

Recently, a new programme to study heavy elements using a combination of laser resonance ionization and collinear laser spectroscopy has been initiated at the IGISOL facility, in the Accelerator Laboratory of the University of Jyväskylä. Several elements above Ra have long-lived isotopes for which sufficiently large sample sizes (ng) of material can be produced at nuclear reactors and safely transported to facilities for nuclear structure studies. In collaboration with the Nuclear Chemistry department of the University of Mainz, samples containing Pu isotopes (<sup>238–240,242</sup>Pu and <sup>244</sup>Pu) were electrolytically deposited onto a tantalum substrate and delivered to Jyväskylä. After electrothermally heating the filament inside a gas cell filled with helium or argon, in-gas-cell resonance laser ionization was applied to selectively ionize the

\* Corresponding authors.

E-mail addresses: [ilkka.pohjalainen@jyu.fi](mailto:ilkka.pohjalainen@jyu.fi) (I. Pohjalainen), [iain.d.moore@jyu.fi](mailto:iain.d.moore@jyu.fi) (I.D. Moore).

plutonium. The yield of the  $\text{Pu}^+$  ionic fraction was sufficient to perform high-resolution collinear laser spectroscopy. The high resolution data is currently under analysis and will be published elsewhere.

In this article preliminary investigations of a new gas cell for off-line heavy element laser ionization will be presented. A careful analysis of resulting mass spectra using the IGISOL separator has been performed in combination with studies of the ion time profiles following laser ionization with pulsed lasers. Such information is of importance to understand the timescales associated with molecular formation during extraction of the  $\text{Pu}^+$  ions from the gas cell. In light of these studies, new modifications are planned to further improve the yield of the element of interest in the form of singly-charged monoatomic ions which directly impacts the sample sizes required for collinear laser spectroscopy. Finally the results of a gamma-ray spectroscopy analysis of one of the plutonium samples is presented, performed in a low-background counting station. This has allowed a direct comparison with the original sample assay provided by Mainz.

## 2. Development of a new gas cell and ionization of Pu

The application of gas cell laser ionization at IGISOL was originally motivated by the goal of improving the rather modest efficiency ( $\sim 1\%$ ) of the heavy-ion fusion-evaporation ion guide (HIGISOL) as well as recognizing the need to move towards a more element-selective approach in the production of radioactive ion beams. A number of considerations were taken into account in the design of the gas cell including efficient evacuation of a large recoil stopping volume (optimized gas flow transport and exit nozzle type), water cooling and baking capabilities, and optional filament feedthroughs as well as dc electrodes. This resulted in a modular construction consisting of a gas feeding part, the main body (with optional filament holder) and a removable exit nozzle/hole [3]. The volume of the main body to the exit hole of  $\sim 250 \text{ cm}^3$  resulted in an evacuation time of 390 ms for a standard 1.2 mm diameter exit hole using helium as buffer gas.

In order for the successful extraction of atomic ions, the requirement for conditions of high gas purity (sub parts-per-billion) has been critical to the success of so-called laser ion guides as well as large gas catchers due to the competition between atomic ion survival against molecular formation and evacuation timescales. For several of the refractory elements that can only be produced with the gas cell method, the reaction rate coefficients which govern the time evolution of molecular formation indicate extremely strong affinity with the main buffer gas contaminants, water and oxygen [4]. In on-line conditions, the critical loss mechanism for an ion of interest is that of neutralization within the high density of (primarily) buffer gas ion–electron pairs created by the passage of a primary projectile beam. The operational principal of laser ionization in a gas cell takes advantage of this fast ion–electron recombination, with re-ionization applied in a volume where the ion–electron density is sufficiently low for a high chance of survival of the photo-ions. One can understand that the operation of the gas cell is strongly dependent on a set of competing time scales. By studying the time distribution profiles of (mass separated) ions one is able to determine the effective volume for laser ionization within the gas cell. At the Leuven laser ion source (LISOL) it was shown that at time scales of approximately 5 ms, recombination losses start to gain importance above an ion–electron density of  $10^7$ – $10^8$  pairs/ $\text{cm}^3$  [5,6]. At IGISOL, similar experiments verified that the accessible neutral fraction in the presence of a primary beam is restricted to the nozzle region, an effective laser ionization volume which is evacuated within milliseconds [7].

The current programme focuses on heavy element studies not requiring the presence of a primary beam. Therefore, much of the gas cell volume necessitated by the stopping distribution of heavy-ion fusion-evaporation recoils is redundant. Long-lived isotopes of actinide elements including plutonium and thorium can be prepared onto substrates for subsequent evaporation into a volume which may be minimized to reduce possible molecular formation or other loss mechanisms such as diffusion to the walls of the gas cell. Ideally, such a volume is limited only by the efficiency of the laser ionization process. Assuming that an atom can be ionized by a single laser pulse and requiring that every atom is irradiated at least once by the lasers, the minimum volume  $V_{\min}$  is set by the repetition rate of the laser system and the conductance  $C$  of the gas cell,

$$V_{\min} = t_{\text{rep}} C = t_{\text{rep}} \cdot 0.45 \cdot \phi^2, \quad (1)$$

where  $t_{\text{rep}}$  is the time between the laser pulses and the conductance  $C$  has been given in terms of the exit hole diameter  $\phi$  in mm for the case of room temperature helium. Considering the 10 kHz repetition rate of the Ti:sapphire laser system used at IGISOL and with a typical exit hole size  $\phi = 1.2 \text{ mm}$ , Eq. (1) results in a volume of  $0.07 \text{ cm}^3$ . However, the assumption that an atom would be ionized by a single laser pulse is unrealistic for a high repetition rate (10 kHz) laser system where the energy per pulse of the fundamental radiation can be a factor of ten lower compared to a medium repetition rate (200 Hz) system. In order for a laser system with a single pulse laser ionization efficiency  $\epsilon_p$  to result in a total laser ionization efficiency  $> 80\%$ , the minimum volume defined by Eq. (1) must be scaled by the factor  $-2/\ln(1 - \epsilon_p)$ .

Currently we have no available data on the single pulse laser ionization efficiency at IGISOL, however a recent experiment at LISOL compared the performance of a similar high repetition rate Ti:sapphire laser system with the medium repetition rate dye laser system in studies of copper and cobalt [8]. In that work, by controlling the synchronization of the Ti:sapphire laser pulses, it was possible to match the repetition rates of both laser systems without affecting the energy per pulse of the Ti:sapphire laser. Whereas the dye laser system could saturate the atomic transitions and was seen to saturate the ion signal at  $\sim 100 \text{ Hz}$  (corresponding to an irradiated volume representing  $\sim 40\%$  of the total volume of the ionization chamber, evacuated in about 10 ms), the Ti:sapphire system was unable to saturate all transitions. Furthermore, when operated at the same repetition rate the ionization efficiency was around 200 times smaller. Ferrer and colleagues use this factor to infer an efficiency per pulse of 0.5% for the Ti:sapphire system in those experiments. This value can be inserted into our scaling factor and when multiplied by the minimum volume results in a required ionization volume of  $\sim 30 \text{ cm}^3$ . We note that by strongly focusing the Ti:sapphire beams in the LISOL experiment the ionization efficiency per pulse was increased to such an extent that the two laser systems performed comparably under on-line conditions.

The gas cell design in the current work was primarily motivated by the wish to reduce the redundant HIGISOL volume while being restricted by the practical consideration to reuse the same filament holder. An additional motivation for a dedicated gas cell took into account the expected surface contamination with long-lived alpha-active isotopes when using actinide sources. Fig. 1 presents a cross-sectional view of the gas cell. Helium or argon buffer gas is fed through an inlet tube into the cell which has a volume of  $\sim 30 \text{ cm}^3$ . This volume of gas, which is kept at a pressure of  $\sim 70 \text{ mbar}$ , is extracted through a 1.2 mm exit hole into a chamber maintained at a pressure of  $\sim 10^{-2} \text{ mbar}$ . With a such a pressure difference the gas flow is choked and thus the conductance is pressure independent. An evacuation time for the whole gas cell volume of  $\sim 50 \text{ ms}$  and  $\sim 150 \text{ ms}$  can be estimated for room

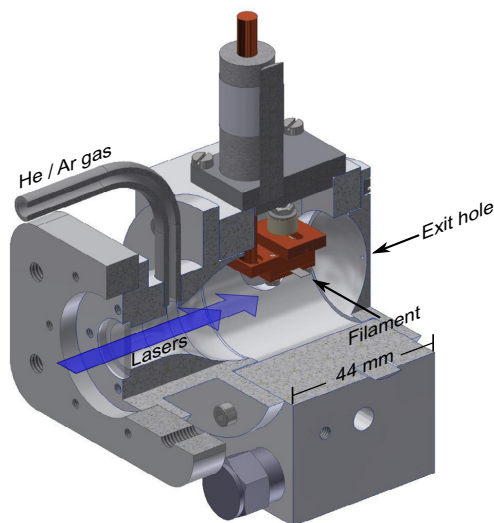


**Fig. 1.** Cross-sectional view of the gas cell used for heavy element studies with the filament in place.

temperature helium and argon, respectively, for any operational pressure. Laser radiation is introduced through a sapphire window mounted on the rear of the gas cell, directed along the extraction axis of the cell very close ( $\sim 1$  mm) to the filament. This geometry was designed to maximize the laser overlap with the highest density of atoms following evaporation from the filament. Additional elements include a heater cartridge added for in situ baking, water cooling, and the possibility to insert windows and targets for future introduction of a primary beam.

In total, six filaments (with dimensions  $11 \times 3.5$  mm, and thickness  $50 \mu\text{m}$ ) were provided from the Nuclear Chemistry department of Mainz. Two of the filaments were blank and were used for testing purposes in order to understand the behavior of the voltage across the feedthroughs on the target chamber as a function of the current applied to the filament, to measure the temperature of the filament with a pyrometer as a function of current (and, at a fixed current, the temperature as a function of gas pressure) and to search for surface ions which could be used to calibrate the magnetic field of the mass separator. The other four samples contained a mixture of Pu isotopes with up to  $\sim 10^{16}$  atoms for the most abundant isotope  $^{244}\text{Pu}$ , to  $\sim 10^{12}$  atoms for  $^{238}\text{Pu}$ . Two of the four samples also contained  $^{239}\text{Pu}$  and were used specifically in connection with the high-resolution laser spectroscopy experiment. In the current work however we focus only on the samples without  $^{239}\text{Pu}$ . To prevent oxidation of the plutonium, the samples were covered with an additional protective Ti layer of about  $1 \mu\text{m}$  on the surface.

During operation the filaments were heated to a temperature of typically  $1000$ – $1200$  °C depending on the desired release rate of the Pu atoms. Variations in gas pressure affected the temperature and thus the evaporation rate. For a measured current of 28A (heating power 99 W), an increase of helium pressure from 50 mbar to 150 mbar resulted in a corresponding temperature decrease from  $1050$  °C to  $950$  °C.

Initially a three-step ionization scheme using laser radiation at wavelengths of 420.76, 847.26, and 750.24 nm was chosen based

on trace analysis studies by Raeder et al. [9]. In that work a full saturation of all optical excitation steps was demonstrated ensuring a high efficiency of the ionization process. At IGISOL the laser light was provided by three broadband Ti:sapphire lasers, the characteristics of which can be found elsewhere [10]. In the gas cell however little or no indication of the effect of the second and third IR steps was seen and it was suspected that the excitation preferentially proceeded via a Rydberg state populated by a photon from the first step transition which was subsequently ionized via buffer gas collisions. Indications for such an effect could be clearly observed in the saturation behavior of the first step. A second laser was therefore introduced operating in the blue wavelength regime, both lasers using intra-cavity second harmonic generation (SHG) [11]. The first step laser, tuned to a wavelength of 420.76 nm, corresponds to a transition from the  $5f^6 7s^2 {}^7F_0$  ground state to an excited state at  $23766.14 \text{ cm}^{-1}$  with configuration  $5f^6 7s 7p {}^7D_1$ . The wavelength of the second step laser was optimized to a resonance observed at a wavelength of 422.53 nm. Further studies showed that the two transitions are able to ionize independently from one another (though with much reduced count rates), which may be explained if the second step is driving population from the lowest-lying metastable state at  $2203.61 \text{ cm}^{-1}$  to a state at  $25870.69 \text{ cm}^{-1}$ . It is of interest for further work to determine whether this state is naturally populated due to the temperature of the hot filament. Nevertheless, ionization will proceed via Rydberg states populated following excitation from the  $23766.14 \text{ cm}^{-1}$  level, and/or non-resonantly or to auto-ionizing states if a second path proceeds via the state at  $25870.69 \text{ cm}^{-1}$ .

Surprisingly, it was seen that the  $\text{Pu}^+$  ion count rate was maximized when both of the Ti:sapphire lasers were operated without the etalons in the resonator cavity. This increases the fundamental linewidth from 4–5 GHz to  $\sim 100$  GHz, or approximately 0.2 nm at a wavelength of 840 nm. The resulting laser linewidth is considerably larger than the atomic linewidth contributions from Doppler and pressure broadening resulting in a lower spectral power density. Nevertheless, the loss in spectral power density may be offset if we are strongly saturating the transition, which is indeed the case for the first step. The modest increase in laser power without the etalon, coupled with the simultaneous population of a number of Rydberg states can explain the higher ion count rate. In order to better understand the ionization process and to scan for Rydberg levels exhibiting a higher ionization cross section, further investigation is required.

### 3. Gas phase chemistry

The cleanliness of the buffer gas and gas cell was characterized by recording mass spectra (Fig. 2) with a microchannel plate (MCP) detector at the focal plane of the IGISOL mass separator using both He and Ar buffer gases at a pressure of  $\sim 75$  mbar. Additionally, a mass spectrum was taken using Ar with a MCP detector situated at the end of the collinear laser line located after the radiofrequency (rf) cooler-buncher. This provided additional insight on the effect of the cooler-buncher on the mass spectra and also confidence in transporting  $\text{Pu}^+$  ions to the laser spectroscopy station. All of the spectra show an isotopic abundance pattern that matches the isotope assay of the samples provided by Mainz, both in the region of singly-charged monoatomic ions and also at higher masses identified with molecular formation of  $\text{Pu}^+$  ions. The transport efficiency through the separator system is believed to be rather constant in this mass range.

The first molecular isotopic pattern is observed 16 mass units heavier than the monoatomic pattern and corresponds to  $\text{PuO}^+$  ions. There are two possible pathways to oxidize plutonium considering  $\text{H}_2\text{O}$  and  $\text{O}_2$  are two of the main impurities in the gas:

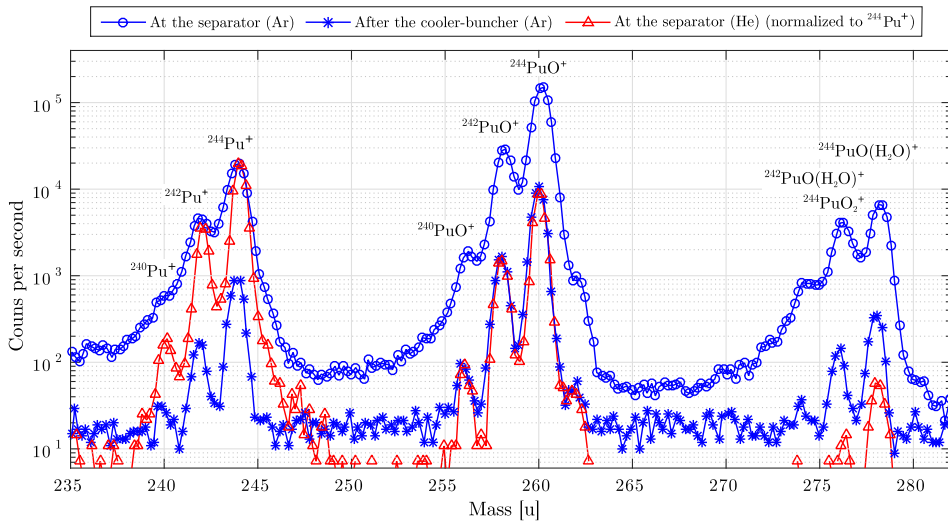
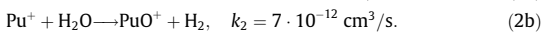
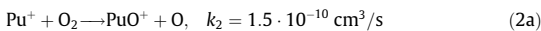


**Fig. 2.** Mass spectra in the region of Pu and related molecules recorded at the focal plane of the IGISOL separator using He and Ar buffer gases and after the cooler-buncher (argon only). See text for details.

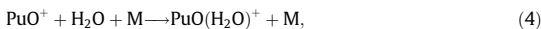


For both reactions, the bimolecular reaction rate  $k_2$  has been calculated from experimental values of reaction efficiencies, or the  $k_2/k_{ADO}$  values, measured by Santos et al. [12]. The accuracy of these values is estimated to be  $\pm 50\%$ . The average dipole orientation collisional rate,  $k_{ADO}$ , was calculated as follows,

$$k_{ADO} = \frac{2\pi q}{\sqrt{\mu}} \left( \sqrt{\alpha} + c\mu_D \sqrt{\frac{2}{\pi kT}} \right), \quad (3)$$

where  $q$  is the charge of the ion and  $\mu$  is the reduced mass [13]. The factor  $c$  is the locking constant,  $\alpha$  and  $\mu_D$  are the polarizability and the permanent dipole of the reagent molecule, respectively, all values of which have been taken from Table 7.1 and Fig. 7.1 in Ref. [14].

After formation, the  $\text{PuO}^+$  ions can react further with water molecules in a termolecular association reaction:



where M is a buffer gas atom. This association reaction accounts for the peaks 34 mass units above the monoatomic  $\text{Pu}^+$  ions. In Ar there also appears to be oxidation of the  $\text{PuO}^+$  through similar reactions as in Eqs. (2a) and (2b) because the count rate at  $(M/q) = 276$  is higher than one would expect from the isotopic ratios.

Even though both helium and argon gases are purified with the IGISOL rare gas purification system [15] and both the gas cell and gas lines are baked before an experiment, the purity conditions appear to be unusually poor. This can be inferred from the large amount of molecular formation as seen in Fig. 2. Assuming molecular formation as discussed, the time constant associated with the process can be defined using  $\tau = 1/k_2[M]$ , where M is the impurity concentration. With an expected impurity level of 1 ppb of purified gas, the  $\text{Pu}^+$  ion survival time is in order of a few seconds, a time-scale much longer than the evacuation time of the gas cell. We therefore suspect that additional impurities result from an unfortunate “dead” volume in the filament holder, which could have

trapped some air, or to outgassing of the gas cell while the filament is being heated.

The most notable difference between the mass spectra obtained using helium and argon is the lower mass resolution in the case of argon. This is a reflection of collisions between buffer gas atoms and ions in the extraction region after the gas cell which leads to an energy spread, more pronounced in the case of argon because of the heavier mass. With argon, the effect of transporting the beam through the RF cooler-buncher is seen in an improvement in the mass resolving power (as well as a reduction in the count rate due to reduced transmission). This can be understood if the cooler-buncher acceptance window of  $\sim 90$  eV is considered. Only the part of the mass-separated beam that has the right energy enters the cooler, reducing the peak widths.

#### 4. Study of the dynamic processes within the gas cell

In order to investigate the dynamic processes inside the gas cell following the creation of a photo-ion, the temporal behavior of mass-separated ions was studied by chopping the laser beams with a fast shutter mechanism. The resulting time structure of the ions was recorded with a multi-channel scaler connected to the MCP located at the focal plane of the mass separator. Fig. 3 shows an example of the time profiles of  $\text{Pu}^+$  and  $\text{PuO}^+$  in He and Ar when the lasers were introduced at time  $t \sim 0$  s and turned off at  $t \sim 1.13$  s. The small peak visible at the start of the time profile of  $\text{Pu}^+$  in helium is caused by the initial ion creation in the nozzle region which is evacuated before molecular formation occurs. This is not seen in argon, probably due to the slower evacuation of the gas cell. Exponential growth and decay curves

$$y(t) = \begin{cases} A_0 \pm A \left( 1 - e^{-\frac{t-t_0}{\tau}} \right) & \text{if } t \geq t_0 \\ A_0 & \text{if } t < t_0 \end{cases} \quad (5)$$

were fitted to the rising and falling edges of the time profile, respectively, to extract a time parameter  $\tau$  for each fit. These parameters represent the time scales during which the ion signal develops at the start of a laser pulse and how it decays once the lasers are

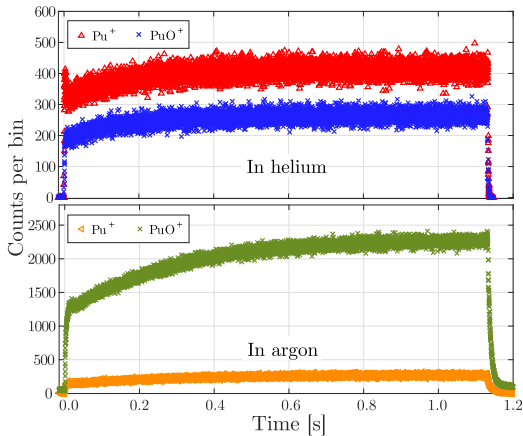


**Fig. 3.** Time distribution profiles of  $\text{Pu}^+$  and  $\text{PuO}^+$  in He (top) and Ar (bottom). In order to quantify the profiles exponential growth and decay curves were fitted to the rising and falling edges of the distribution in order to determine the different time constants  $\tau$ , summarized in Table 1.

blocked. Table 1 summarizes the time scales for the data illustrated in Fig. 3.

One can immediately note from the fit parameters that in both helium and argon the atomic  $\text{Pu}^+$  ions achieve saturation sooner than the corresponding  $\text{PuO}^+$  molecule. This is to be expected as the oxide can only be produced following laser ionization of the atomic species. The slower time scale in Ar reflects the reduced conductance of the exit hole. It is interesting to note that the time parameters for the falling edges of the profiles are somewhat longer than the rising edges and both the atomic and molecular species have the same fit parameter within errors. This likely reflects the fact that both species are extracted from the same effective volume.

In all cases  $\tau$  is notably lower than the total evacuation time of the gas cell indicating a fast loss mechanism of the plutonium (and its corresponding oxide). The alpha particles emanating from the samples in the radioactive decay of Pu are estimated to create an ionization density rate in He,  $Q = 10^5$  ion–electron pairs  $\text{cm}^{-3}\text{s}^{-1}$ , which is negligible if one were to consider recombination losses due to free electrons. In addition, charge exchange between the  $\text{Pu}^+$  ions and buffer gas atoms or typical gas impurities is not possible because of the low ionization potential of Pu. The only conceivable loss mechanisms of the ions are molecular formation and diffusion losses to the walls of the gas cell. The information gained from the mass spectra in Fig. 2 indicates a source of impurities which is independent of whether He or Ar is used and we believe this to be caused by the filament holder as previously mentioned.

Using the known conductance of the exit hole, the time parameter  $\tau$  translates into an effective volume for laser ionization. This

**Table 1**  
Time parameter  $\tau$  for rising and falling edges of the  $\text{Pu}^+$  and  $\text{PuO}^+$  ion signal time profiles illustrated in Fig. 3 for helium and argon.

$\tau$		Helium	Argon
Rising	$\text{Pu}^+$	$0.80 \pm 0.05$ ms	$2.57 \pm 0.16$ ms
	$\text{PuO}^+$	$1.17 \pm 0.09$ ms	$3.25 \pm 0.07$ ms
Falling	$\text{Pu}^+$	$1.13 \pm 0.04$ ms	$6.96 \pm 0.15$ ms
	$\text{PuO}^+$	$1.14 \pm 0.05$ ms	$6.75 \pm 0.07$ ms

effective volume will be different depending on whether one chooses to use the rising or falling edge of the  $\text{Pu}^+$  ion time distribution. We have chosen to use the falling edge as the starting conditions are different to the situation before laser ionization has commenced; all competing processes which create and destroy the ion of interest are in equilibrium. By taking into account the different conductances of the gas cell in He and Ar buffer gases, the effective volume for the ionization of Pu is  $\sim 0.7 \text{ cm}^3$  in He and  $\sim 1.4 \text{ cm}^3$  in Ar, which is only a few percent of the total gas cell volume. This indicates that detected monoatomic laser ions are originating not far from the nozzle region. Gas phase chemistry and related ion time profiles using similarly reactive elements have been previously studied in greater detail at IGISOL and in that work the increase in the effective volume due to a reduction of impurities in the gas was clearly observed [19].

## 5. Gamma ray spectroscopy of the Pu samples

Gamma ray spectroscopy was used to independently analyze the content of a filament, in support of the assay provided by Mainz, and also to have means of monitoring the remaining activity of a partly used filament. The majority of the Pu isotopes in the samples alpha decay directly to the ground state of a long-lived daughter or to a low-lying excited state, which subsequently decays emitting conversion electrons (the branching fraction to decay via gamma radiation is very low,  $<0.05\%$ ). Further difficulties arise in such a measurement because the gamma energies between different isotopes tend to cluster to within  $\sim 1$  keV or less. However, using a long enough measurement time in a low-background station which is coupled to a low-energy high-purity germanium detector, a gamma spectrum of one unused Pu filament was successfully measured in the range from 3 keV to 800 keV.

Fig. 4 shows three regions of interest of the gamma spectrum: the 10–25 keV region containing L X-ray peaks associated with the U daughter; the 40–65 keV region that has the strongest gamma peaks associated with the decay radiation of Pu; a high-energy region around 580 keV showing the gamma rays of  $^{240\text{m}}\text{Np}$  which is in the decay chain of  $^{244}\text{Pu}$ . In addition an  $^{241}\text{Am}$  contaminant was detected along with X-rays of Ta induced by the Pu alpha decay in the sample.

The total activity of the Pu isotopes in the filament was determined separately from the three uranium L X-ray peaks using known isotopic abundances from the assay and branching ratios for each peak of each Pu isotope [16–18]. No information could be found for the branching ratio of these X-rays for  $^{244}\text{Pu}$  in the literature however this does not affect the calculation of the total activity as its activity is under 10 Bq. The peak energies, branching ratios and measurement results are summarized in Table 2. The mean value of  $\sim 1120$  Bq matches well with the stated assay activity of 1154 Bq.

The individual activities of the Pu isotopes in the sample were determined from the peaks in the 43–52 keV region. Although some peaks overlap, by fitting simple Gaussian functions using the peak width extracted from the  $^{241}\text{Am}$  line and the peak energies for each isotope [20], it was possible to obtain the yields for each gamma line. By accounting for the detector efficiency and branching ratio for the gamma rays the activities of the isotopes were calculated (Table 3). The activity of  $^{244}\text{Pu}$  was not directly determined because of its low activity however its decay chain contains short-lived  $^{240}\text{U}$  and  $^{240\text{m}}\text{Np}$  having sufficiently strong branching ratios for gamma rays. Thus the activity of  $^{244}\text{Pu}$  could be indirectly determined. As seen in Table 3 the individual activities agree well with those provided in the assay except in the case of  $^{239}\text{Pu}$  whose measured activity is notably lower. The discrepancy

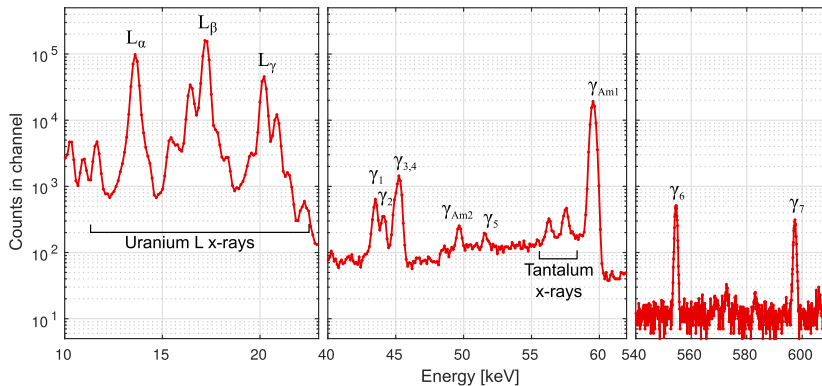


**Fig. 4.** A gamma spectrum from an unused Pu sample. Three energy regions of interest are highlighted. In addition to the gamma radiation associated with the decay of Pu, the spectrum contains low energy X-rays, an  $^{241}\text{Am}$  contaminant and X-rays of Ta, the material from which the filament is made.

**Table 2**

The three uranium X-rays peaks that were used to determine the total activity of a plutonium filament. In addition to peak energies and activities the branching to these peaks are given for each isotope in the filament if found in literature.

Peak	Energy (keV)	Isotope branching (%)				Activity (Bq)
		$^{238}\text{Pu}$ [16]	$^{239}\text{Pu}$ [17]	$^{240}\text{Pu}$ [17]	$^{242}\text{Pu}$ [18]	
$L_\alpha$	13.6	3.81(3)	1.65(4)	3.73(5)	3.2(2)	1130
$L_\beta$	17.22	4.26(3)	1.72(4)	3.95(6)	3.4(3)	1050
$L_\gamma$	20.2	0.992(7)	0.428 (14)	0.95(2)	0.79(9)	1165

**Table 3**

The list of identified gamma rays from the spectrum in Fig. 4 with peak energies and branching ratios [20]. The determined activities of the plutonium isotopes in the filament using these peaks are listed. The activities of  $^{240}\text{U}$  and  $^{240\text{m}}\text{Np}$  can be measured for an indirect determination of the activity of  $^{244}\text{Pu}$ . The assay of the filament is listed for comparison.

Peak	Energy (keV)	Isotope	Branching (%)	Activity (Bq)	Assay (Bq)
$\gamma_1$	43.5	$^{238}\text{Pu}$	0.0392	200	219
$\gamma_2$	44.1	$^{240}\text{U}$	1.05	9	7
$\gamma_3$	44.9	$^{242}\text{Pu}$	0.0373	160	182
$\gamma_4$	45.2	$^{240}\text{Pu}$	0.0447	510	518
$\gamma_5$	51.624	$^{239}\text{Pu}$	0.02722	51	228
$\gamma_6$	554.49	$^{240\text{m}}\text{Np}$	20.9	7	7
$\gamma_7$	597.37	$^{240\text{m}}\text{Np}$	11.7	7	7
$\gamma_{\text{Am1}}$	59.532	$^{241}\text{Am}$	35.9	9	–

was also seen in the isotopic abundance pattern of the plutonium mass spectrum from a filament containing  $^{239}\text{Pu}$  which was made during a later experiment.

## 6. Conclusion

Long-lived isotopes of Pu provided by the Nuclear Chemistry department of the University of Mainz were successfully extracted as low-energy ion beams at IGISOL following resonance laser ionization in a He and Ar buffer gas-filled cell. Although further work is required to fully characterize the ionization scheme, a sufficient yield of monoatomic  $\text{Pu}^+$  ions was produced in preparation for high-resolution collinear laser spectroscopy. Studies of the mass spectra as well as ion time profiles indicate a source of impurities which is likely due to outgassing of “dead” volumes in the filament

holder and perhaps via heating of the filament. A new filament holder is currently being designed to partially address this issue. These successful studies will be continued in the future in order to expand the programme of laser spectroscopy of actinide elements at IGISOL, with immediate interest in  $^{229}\text{Th}$  as part of the new EU Horizon 2020 project, NuClock, which is focused on the study of the low-lying isomeric state.

## Acknowledgements

This work has been supported by the Academy of Finland programme under the Finnish Centre of Excellence Programme 2012–2017 (Project No. 251353, Nuclear and Accelerator-Based Physics Research at JYFL) and the European Commission (E.C.) 7th Framework Programme project ENSAR.

## References

- [1] S.A. Ahmad, W. Klempt, R. Neugart, E.W. Otten, P.G. Reinhard, G. Ulm, K. Wendt, Mean square charge radii of radium isotopes and octupole deformation in the  $^{220}\text{--}^{228}\text{Ra}$  region, *Nucl. Phys. A* 483 (2) (1988) 244–268, [http://dx.doi.org/10.1016/0375-9474\(88\)90534-9](http://dx.doi.org/10.1016/0375-9474(88)90534-9).
- [2] S. Rothe, A.N. Andreyev, S. Antalic, A. Borschevsky, L. Capponi, T.E. Cocolios, H. De Witte, E. Eliav, D.V. Fedorov, V.N. Fedosseev, D.A. Fink, S. Fritzsche, L. Ghyss, M. Huysse, N. Imai, U. Kaldor, Y. Kudryavtsev, U. Köster, J.F.W. Lane, J. Lassen, V. Liberati, K.M. Lynch, B.A. Marsh, K. Nishio, D. Pauwels, V. Pershina, L. Popescu, T.J. Procter, D. Radulov, S. Raeder, M.M. Rajabali, E. Rapisarda, R.E. Rossel, K. Sandhu, M.D. Seliverstov, A.M. Sjödin, P. Van den Bergh, P. Van Duppen, M. Venhart, Y. Wakabayashi, K.D.A. Wendt, Measurement of the first ionization potential of astatine by laser ionization spectroscopy, *Nat. Commun.* 4 (2013) 1835, <http://dx.doi.org/10.1038/ncomms2819>.
- [3] I. Moore, P. Dendooven, J. Årje, The IGISOL technique—three decades of developments, *Hyperfine Interact.* 223 (1–3) (2014) 17–62, <http://dx.doi.org/10.1007/s10751-013-0871-0>.
- [4] G.K. Koyanagi, D. Caraiman, V. Blagojevic, D.K. Bohme, Gas-phase reactions of transition-metal ions with molecular oxygen: room temperature kinetics and periodicities in reactivity, *J. Phys. Chem. A* 106 (2002) 4581.
- [5] M. Huysse, M. Facina, Y. Kudryavtsev, P.V. Duppen, I. collaboration, Intensity limitations of a gas cell for stopping, storing and guiding of radioactive ions, *Nucl. Instrum. Methods Phys. Res. B* 187 (2002) 535.
- [6] M. Facina, B. Bruyneel, S. Dean, J. Gentens, M. Huysse, Y. Kudryavtsev, P.V. den Bergh, P.V. Duppen, A gas cell for thermalizing, storing and transporting radioactive atoms and ions. Part II: on-line studies with a laser ion source, *Nucl. Instrum. Methods Phys. Res. B* 226 (2004) 401.
- [7] I.D. Moore, T. Kessler, T. Sonoda, Y. Kudryavtsev, K. Peräjärvi, A. Popov, K.D.A. Wendt, J. Åystö, A study of on-line gas cell processes at IGISOL, *Nucl. Instrum. Methods Phys. Res. B* 268 (6) (2010) 657–670.
- [8] R. Ferrer, V. Sonnenschein, B. Bastin, S. Franchoo, M. Huysse, Y. Kudryavtsev, T. Kron, N. Levesne, I. Moore, B. Osmond, D. Pauwels, D. Radulov, S. Raeder, L. Rens, M. Reponen, J. Ronagel, H. Savajols, T. Sonoda, J. Thomas, P.V. den Bergh, P.V. Duppen, K. Wendt, S. Zemlyanov, Performance of a high repetition pulse rate laser system for in-gas-jet laser ionization studies with the leuven laser

- ion source @ LISOL, Nucl. Instrum. Methods Phys. Res., Sect. B 291 (2012) 29–37, <http://dx.doi.org/10.1016/j.nimb.2012.08.023>.
- [9] S. Raeder, A. Hakimi, N. Stöbener, N. Trautmann, K. Wendt, Detection of plutonium isotopes at lowest quantities using in-source resonance ionization mass spectrometry, *Anal. Bioanal. Chem.* 404 (8) (2012) 2163–2172.
- [10] M. Reponen, I.D. Moore, T. Kessler, I. Pohjalainen, S. Rothe, V. Sonnenschein, Laser developments and resonance ionization spectroscopy at IGISOL, *Eur. Phys. J. A* 48 (2012) 45.
- [11] V. Sonnenschein, I.D. Moore, I. Pohjalainen, M. Reponen, S. Rothe, K. Wendt, Intracavity frequency doubling and difference frequency mixing for pulsed ns Ti: sapphire laser systems at on-line radioactive ion beam facilities, in: *Proceedings of the Conference on Advances in Radioactive Isotope Science (ARIS2014)*, id.030126, 2015, p. 030126. <http://dx.doi.org/10.7566/JPSCP.6.030126>.
- [12] M. Santos, J. Marçalo, A.P. de Matos, J.K. Gibson, R.G. Haire, Gas-phase oxidation reactions of neptunium and plutonium ions investigated via fourier transform ion cyclotron resonance mass spectrometry, *J. Phys. Chem. A* 106 (31) (2002) 7190–7194.
- [13] T. Su, M.T. Bowers, Chapter 3 – classical ion-molecule collision theory, in: M.T. Bowers (Ed.), *Gas Phase Ion Chemistry*, Academic Press, 1979, pp. 83–118.
- [14] K. Hiraoka, Gas-phase ion/molecule reactions, in: K. Hiraoka (Ed.), *Fundamentals of Mass Spectrometry*, Springer, New York, 2013, pp. 109–144.
- [15] I. Pohjalainen, I.D. Moore, T. Eronen, A. Jokinen, H. Penttilä, S. Rinta-Antila, Gas purification studies at IGISOL-4, *Hyperfine Interact.* 227 (1–3) (2014) 169–180.
- [16] P.N. Johnston, P.A. Burns, Absolute L X-ray intensities in the decays of  $^{230}\text{Th}$ ,  $^{234}\text{U}$ ,  $^{238}\text{Pu}$  and  $^{244}\text{Cm}$ , *Nucl. Instrum. Methods Phys. Res., Sect. A* 361 (1–2) (1995) 229–239.
- [17] M. Lépy, B. Duchemin, J. Morel, Comparison of experimental and theoretical L X-ray emission probabilities of  $^{241}\text{Am}$ ,  $^{239}\text{Pu}$  and  $^{240}\text{Pu}$ , *Nucl. Instrum. Methods Phys. Res., Sect. A* 353 (1–3) (1994) 10–15.
- [18] V.P. Chechev, The Evaluation of  $^{238}\text{Pu}$ ,  $^{240}\text{Pu}$ , and  $^{242}\text{Pu}$  Decay Data, *AIP Conf. Proc.* 769 (1) (2005) 91–94.
- [19] T. Kessler, I. Moore, Y. Kudryavtsev, K. Peräjärvi, A. Popov, P. Ronkanen, T. Sonoda, B. Tordoff, K. Wendt, J. Åystö, Off-line studies of the laser ionization of yttrium at the IGISOL facility, *Nucl. Instrum. Methods Phys. Res., Sect. B* 266 (4) (2008) 681–700.
- [20] National nuclear data center, information extracted from the chart of nuclides database, accessed: 2015-09-01. URL <<http://www.nndc.bnl.gov/chart/>>.



## 4.2 Introduction and motivation

High-resolution optical spectroscopy is a technique used in many radioactive beam facilities to study the nuclear properties of radioactive isotopes [21]. By measuring the hyperfine structure of atoms, fundamental and model-independent data on nuclear spins, electromagnetic moments, and changes in mean-square charge radii can be obtained. Isotopes in the heavy element region, particularly above radium ( $Z=88$ ) [107], have not been extensively studied with optical spectroscopy as often there is a lack of information on optical transitions due to the scarcity of stable isotopes [30]. On-line production of the heaviest elements is challenging, reflecting a combination of low production cross sections and few stable isotopes, however, since several elements have long-lived isotopes an opportunity exists to study samples which may be produced in macroscopic quantities in nuclear reactors, prepared for deposition onto suitable filaments, and then safely brought to the experimental facilities.

The new heavy element program at IGISOL has now commenced. The aim is to apply laser resonance ionization of actinide isotopes evaporated from filament samples mounted in a gas cell and to produce ion beams for the collinear laser spectroscopy station. A brief overview of the collinear laser spectroscopy program at the IGISOL facility is presented in [108]. Plutonium has several long-lived isotopes and as filament samples were available from the Institut für Kernchemie of the University of Mainz, this was the first element chosen to be studied.

### 4.2.1 Collinear laser spectroscopy at IGISOL and yield requirement

The collinear laser spectroscopy station at IGISOL performs optical spectroscopy with a precision of below 100 MHz by overlapping a frequency-locked laser beam with a counter-propagating 30 keV ion beam [108, 109]. By accurately changing the voltage in the laser - ion interaction region, transitions can be driven between electronic states of the ion and detected from the fluorescence emitted following the de-excitation of an excited state. For a collinear laser spectroscopy experiment a yield as low as 100 ions/s has successfully been used in an experiment [110], although higher yields are typically required as the available transition strengths might be weak or the presence of contaminant background from scattered photons limits detectability.

The benefits of using a laser ion source as the ion beam production method in a collinear laser spectroscopy experiment can be seen primarily in the high selectivity of the laser resonance ionization method. Even with a small amount of material (for example nanograms) it is possible to generate an ion beam

without any contaminant beams. This is of particular importance with the isotopes of actinides and other long-lived radioisotopes as some are not easily available and thus expensive to acquire. Furthermore, the quantities of such isotopes are usually limited because handling of radioactive material is difficult especially if the samples exceed the radioisotope exemption limits which in the actinide region are relatively low.

## 4.2.2 Development of the plutonium laser ion source

The following sections describe the development and study of the plutonium laser ion source that successfully provided high ion yield for the collinear laser spectroscopy measurement of the isotopes  $^{239,240,242}\text{Pu}$  and  $^{244}\text{Pu}$  [25]. This experiment marked the heaviest element measured to date with this high-resolution technique. Although the development of the laser ion source was successful, several new findings and unforeseen phenomena were discovered with possible impact on future experiments using resonance ionization on heavy elements in gaseous environments.

During the first experiment, presented in article II, the ionization scheme developed under vacuum conditions [111] was observed to perform very poorly in the gas cell environment. This led to the discovery that an efficient ionization of plutonium can be performed in the gas cell with two Ti:sapphire lasers operating in the frequency-doubled regime close to 420 nm. As the goal of creating sufficiently high ion yield was accomplished, this newly discovered scheme was used in the subsequent collinear laser spectroscopy experiment.

Many questions still remained. Which transitions were being driven by the two lasers, and why was an unusual behavior of having only a minimal requirement for temporal overlap of the laser pulses observed? This resulted in the ionization scheme investigations performed throughout November 2016 with a frequency-doubled, wide-range tunable grating-based Ti:sapphire laser in collaboration with the University of Nagoya, Japan. These investigations are described in the latter part of this chapter.

## 4.3 Plutonium ionization scheme

### 4.3.1 Three-step blue-IR-IR scheme

The first investigation of in-gas-cell laser ionization of plutonium was done with an ionization scheme originally developed for trace analysis studies [111]. The scheme consists of one blue and two infrared steps at wavelengths of 420.77-,

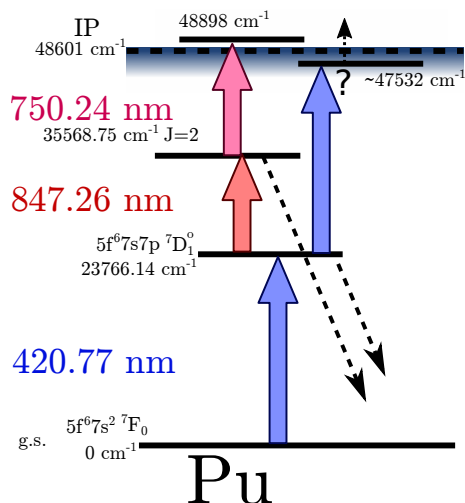


**Figure 4.1.** The initial laser ionization scheme for plutonium using a blue and two IR steps. In the gas cell, the two IR lasers were seen to have little to no effect on the ionization and it was postulated that a transition to a Rydberg state was believed to have been causing the ionization. The dotted lines indicate possible quenching of the excited states - see text for more details.

847.26-, and 750.24 nm of which the last step drives a transition to an auto-ionizing (AI) state (Fig. 4.1). The maximum laser power available for each step at the ionization region was approximately 1 W. It was noticed, however, that only the first step was needed to create resonant laser ions and the two infrared steps did not affect the count rate, observed by preventing the IR laser light from entering the gas cell. Only at a reduced first step laser power was a small response to the count rate detected with the addition of the two infrared steps. Furthermore, the wavelength of the third resonant step was increased to  $\sim 767 \text{ nm}$ , a few  $\text{cm}^{-1}$  below the ionization potential at  $48601 \text{ cm}^{-1}$  [112], to probe for ionization via high-lying Rydberg states. Again, no resonances were seen until the first step laser power was reduced significantly.

As indicated from the atomic level energies in Fig. 4.1, direct ionization from the first excited state is not possible. As the scanning of the first step laser wavelength nevertheless indicated a clear resonant process of ionization, it was assumed to occur through a possible Rydberg state located  $\sim 1070 \text{ cm}^{-1}$  below the ionization threshold. Subsequent ionization would then proceed from the highly-excited plutonium atom via a collision with a helium gas atom (collisional ionization).

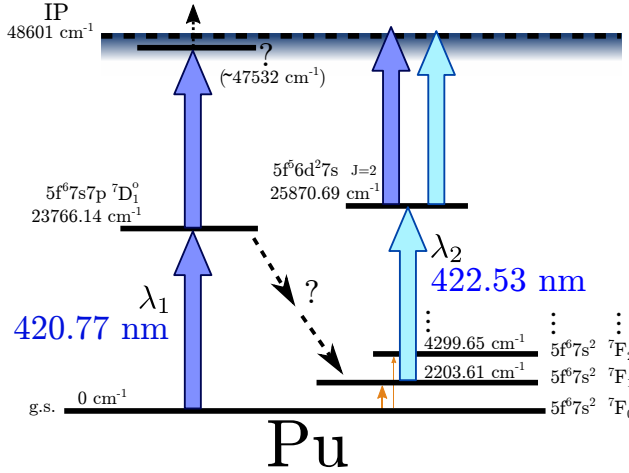


**Figure 4.2.** The blue-blue ionization scheme of plutonium. It involves two lasers operating at 420.77 nm and 422.53 nm, marked as dark and light blue arrows, respectively. The dashed arrow lines depict possible collisional transitions and the orange arrows thermal excitation from the atomic ground state.

### 4.3.2 Development of a two-step blue-blue ionization scheme

The gas cell in this work was operated at a helium pressure of 80 mbar. Such an environment affects the population of the atomic states during the resonant multi-step ionization process. In order to investigate this further, a second Ti:sapphire laser operating with intracavity frequency doubling [113] was set up to provide a wavelength similar to the first step transition of 420.77 nm ( $\lambda_1$ ). By scanning the wavelength of the second laser a transition at 422.53 nm was discovered which enhanced the ionization significantly. This  $\lambda_2$ -transition was tentatively assigned to an excitation from a low-lying level at 2203.61  $\text{cm}^{-1}$  ( $J = 1$ ) to a known  $J = 2$  level at 25870.69  $\text{cm}^{-1}$ . This excited state lies high enough in energy such that both  $\lambda_1$  and  $\lambda_2$  photons cross the ionization threshold. Figure 4.2 illustrates the atomic level structure involved in the ionization scheme.

By blocking  $\lambda_1$  and  $\lambda_2$  in turn, mass-separated ion count rates ( $A/q = 244$ ) of 2000 cps and 1500 cps were detected at the focal plane of the mass separator. These independent rates may be compared to the sum  $\lambda_1 + \lambda_2$ , a rate of 18000 cps. This indicates a connection between the two transitions and we postulate that the low-lying levels above the atomic ground state are populated from higher levels in plutonium. This collisional de-excitation (quenching) would

also explain the negligible effect of the IR transitions in the gas cell. There is a possibility that quenching was also occurring from the  $35569_2$  level, reducing the efficiency of the original ionization scheme even further. Definite conclusions could not, however, be formed and further study of this quenching effect was difficult to accomplish at the time due to the lack of a suitable laser offering a wide tuning range in the second harmonic.

An interesting observation noted in Article II was the ability of the second blue transition,  $\lambda_2$ , to ionize plutonium independent of  $\lambda_1$ . As there is no atomic level known to be directly accessible from the ground state by the  $\lambda_2$  photons, the second laser must be driving population from low-lying levels, which are naturally populated due to thermal excitation from the ground state. The first state at  $2203.61 \text{ cm}^{-1}$  above the ground state is too high in energy to be populated in room temperature conditions, thus natural population must be transferred in the vicinity of the hot filament where the helium gas acts as a thermal bath.

The temperature of the flowing helium gas can be estimated by knowing the initial gas temperature ( $T_i = 295 \text{ K}$ ), pressure  $p$ , gas flow rate  $q_V$  (Eq. (2.15)) and the heating power  $P_h$ , which can be estimated from the filament current  $I_{\text{fil}}$  and the voltage across the filament  $V_{\text{fil}}$ . A lower limit for the gas temperature can be obtained by assuming that the heating happens evenly throughout the gas. The heat input  $H_{\text{in}}$  to the gas in units of joules per mol of gas can be calculated as:

$$H_{\text{in}} = P_h \frac{T_i R}{p q_V} = I_{\text{fil}} V_{\text{fil}} \frac{T_i R}{p q_V}, \quad (4.1)$$

where the  $R$  is the gas constant. Using the heat capacity  $C_p = 20.786 \text{ J}/(\text{K} \cdot \text{mol})$  of helium [114], the final temperature  $T_f$  of the gas can be estimated,

$$T_f = T_i + H_{\text{in}}/C_p. \quad (4.2)$$

Both the filament current and the voltage across the filament can be experimentally measured and thus a gas temperature of slightly over 1000 K is obtained. This approximation does not take into account the heat dissipated through the filament feedthroughs as its magnitude is difficult to estimate. However, the filament temperature is observed to have a very sensitive dependence on the helium gas pressure (noted in Article II) indicating that the helium gas is taking a considerable heat load.

Using the Boltzmann distribution according to Eq. (2.12) and the energies of the first excited levels of plutonium [57], the fraction of atoms in each of the levels have been calculated. In Fig. 4.3 the population of the six lowest levels

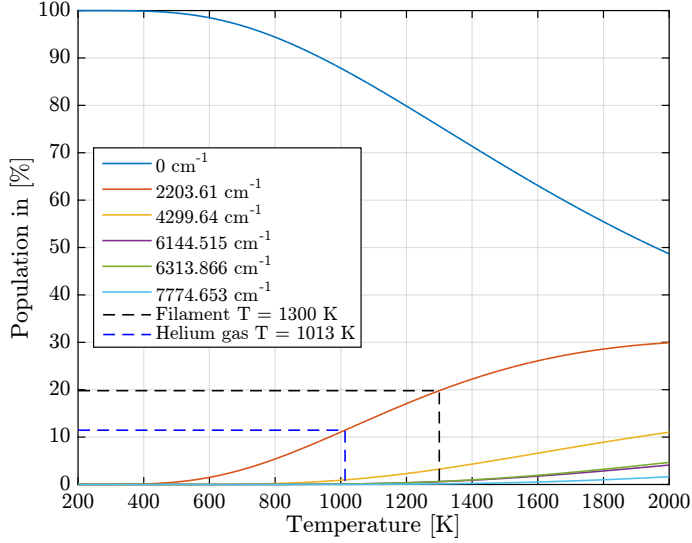


**Figure 4.3.** The population of the ground- and first five excited states in plutonium as a function of temperature. The dashed lines indicate the population at the filament temperature (blue) and the corresponding helium gas temperature (black).

in plutonium are shown as a function of temperature. The black dashed line indicates the approximate filament temperature, 1300 K, whereby plutonium is released in measurable quantities, and the blue dashed line presents the estimation of the evenly heated gas. It is evident from the figure that at room temperature the population of the first excited state is too low ( $p_1 < 0.01\%$ ) to explain the independent ionization by the  $\lambda_2$  laser, but at the gas temperature at which laser ionization occurs, in other words the temperature region bounded by the two dashed lines, the first and second excited state populations  $p_1$  and  $p_2$  are between 11% and 20%, and 1% to 3%, respectively. As the population of the first excited state is relatively large, this is the likely explanation for observation of count rate detected only with the second step ( $\lambda_2$ ) laser light.

### 4.3.3 Saturation of the two-step blue-blue scheme

One important observable which is commonly measured when quantifying the efficiency of a laser ionization scheme is the level of saturation of the various transitions. The two-step blue-blue ionization scheme was investigated for saturation effects by recording the laser ion count rate as a function of laser intensity determined by measurements of laser power and laser beam diameter just before entering the gas cell.

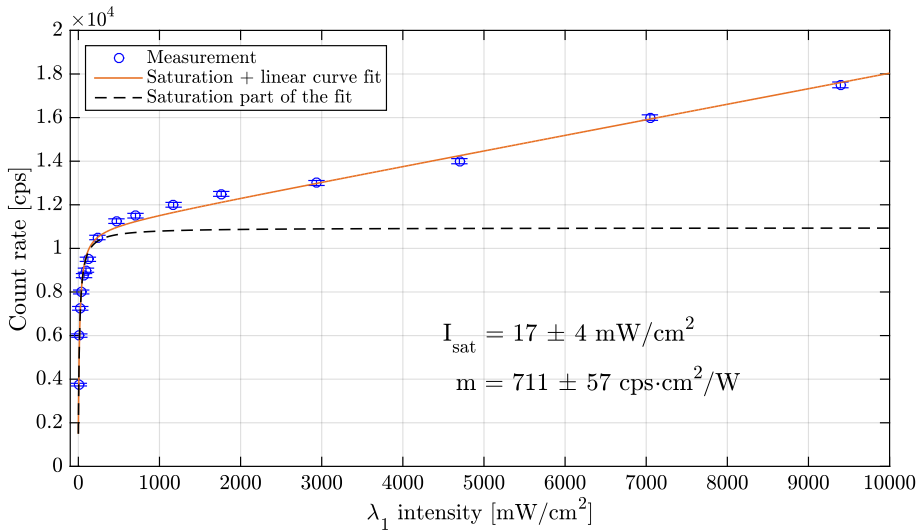


**Figure 4.4.** The saturation of the  $\lambda_1$  transition as a function of laser intensity. The linear increase following saturation suggests a non-resonant transition over the ionization potential. The dashed line assumes a saturation behavior without a non-resonant process.

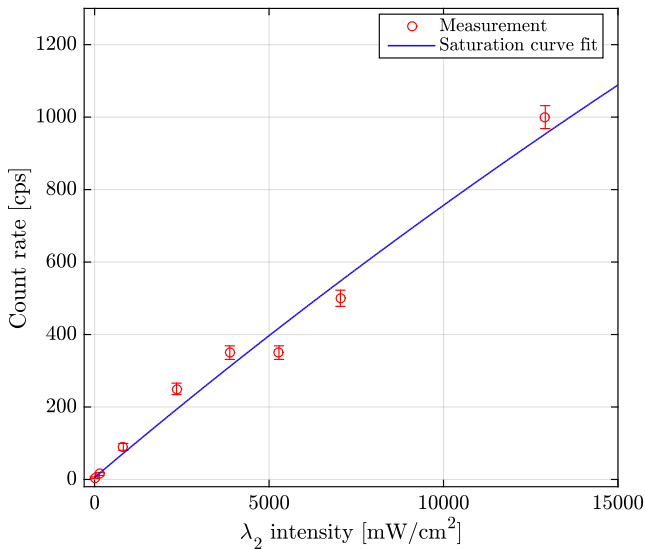


**Figure 4.5.** The saturation measurement of the  $\lambda_2$  step. Only a linear dependence on the laser power was observed.

The  $\lambda_1$  saturation curve is shown in Fig. 4.4, recorded with the maximum available  $\lambda_2$  power. The count rate quickly tends towards saturation at  $\sim 17$  mW/cm<sup>2</sup> and then continues to increase linearly. This type of behavior indicates a saturation of the  ${}^7F_0 \rightarrow {}^7D_1^o$  transition followed by a non-resonant ionization mechanism, most likely from the level  $25871_2^o$  to which the  $\lambda_2$  transition excites. The lineshape of the regular saturation behavior can be deduced by realizing that the population of the excited state, as defined in Eq. (2.7), is directly reflected in the count rate by the factor  $(I/I_{\text{sat}})/(I/I_{\text{sat}} + 1)$ . Adding a constant background as well as a linear term to account for the non-resonant ionization process, a curve as a function of laser power density  $I$  is obtained:

$$A(I) = A_{\text{bg}} + A_0 \frac{I/I_{\text{sat}}}{2(I/I_{\text{sat}} + 1)} + m \cdot I, \quad (4.3)$$

where  $A_{\text{bg}}$  and  $A_0$  are the background and the saturation amplitudes,  $I_{\text{sat}}$  and  $m$  are the saturation power density and the linear coefficient. The data in Fig 4.4 is fitted with this function and is indicated as a solid red line. The saturation part, without the linear term of Eq. (4.3) is shown as a dashed line to highlight the impact of the non-resonant process on the saturation curve.

The  $\lambda_2$  saturation curve (Fig. 4.5) obtained with a maximum first step laser power does not show a sign of saturation behavior. This indicates that the ionization efficiency could be improved if higher laser power was available or by using a different scheme and stronger atomic transitions.

## 4.4 Ionization scheme investigation with a tunable grating-based Ti:Sapphire laser system

As the in-gas-cell plutonium laser ionization scheme was not fully understood at the time of the first experiment, a second experiment was later performed with a new plutonium filament. This work was done in collaboration with the Applied Quantum Beam Engineering group from Nagoya University who had developed a tunable grating-based Ti:sapphire laser, which is operated in the second harmonic and thus was ideal to further expand upon the initial results discussed in the preceding sections.

### 4.4.1 Experimental setup

A more expansive investigation of the two-step blue-blue ionization scheme was performed using a standard JYFL Ti:sapphire laser operating at specific



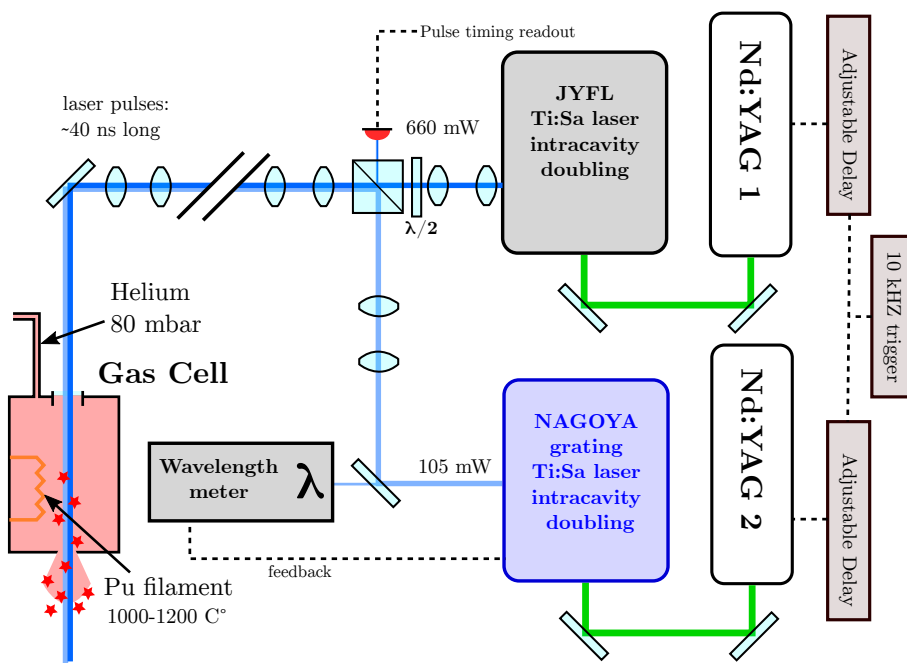


**Figure 4.6.** Simplified schematic figure of the experimental setup to study the plutonium ionization scheme with a standard and a grating-based Ti:sapphire laser.

wavelengths combined with the tunable grating-based Ti:sapphire laser used to scan for additional resonances in the blue wavelength region. Figure 4.6 shows a simplified schematic layout of the measurement setup. The JYFL laser, operating with intracavity second harmonic generation, had a maximum output power of  $\sim 660$  mW, while the Nagoya tunable laser had a maximum power of 105 mW. The diameter of both laser beams was first increased and collimated by telescopes, before being combined in a polarizing beamsplitter cube and transported to the IGISOL front-end into the gas cell. The transport losses were measured to be 75% in total. Both Ti:sapphire lasers had their own Nd:YAG pump lasers making it possible to independently control the timing of the laser pulses to a few ns, monitored by a fast photodiode via the leakage through the beamsplitter cube.

The plutonium sample was again provided by the nuclear chemistry department of the University of Mainz on a tantalum filament and with a thin  $\sim 1$   $\mu\text{m}$  titanium layer to prevent oxidation of the plutonium. In this experiment the isotopic abundance was not of specific interest and therefore the mass separator was tuned to the most abundant isotope,  $^{244}\text{Pu}$ . Figure 4.7a shows the filament before installation and Fig. 4.7b while clamped between the high current vacuum feedthroughs. To get an atomic vapour of plutonium, the filament was heated inside the gas cell operated at a helium pressure of 80 mbar, closely duplicating the front-end conditions of the previous measurement. After evacuation from the gas cell, the ion beam was guided to the high vacuum region of the mass separator using the sextupole ion guide (SPIG) and accelerated to a potential of 30 kV. The ions were mass separated and detected in the focal plane of the separator with a multichannel plate (MCP) detector.

#### 4.4.2 The tunable grating-based Ti:Sapphire laser system with second harmonic generation

The Nagoya Ti:sapphire laser [115] provides access to a wide range of wavelengths without suffering from mode-hopping issues which limit the tunability of traditional broadband Ti:sapphire laser systems in operation at several radioactive ion beam facilities (where the tunability is provided by a combination of birefringent filter and etalon). The unique feature of this particular laser is its intracavity second harmonic generation (SHG) [116] capability, which makes it possible to do a wide-range wavelength scanning from  $\sim 380$  nm to  $\sim 440$  nm. A schematic of the grating-based resonator and relevant aspects for its operation are shown in Fig. 4.8.

The titanium-sapphire crystal is pumped by a 10 kHz repetition rate Nd:YAG laser operating at 532 nm, focused and injected through the rear of one of the anti-reflection coated curved mirrors (CM) of the Z-shaped laser cavity. At one

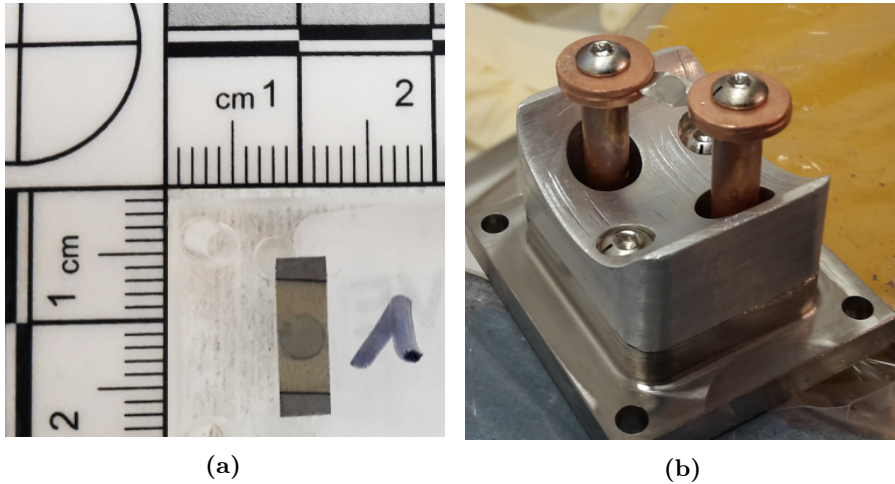


**Figure 4.7.** (a) One of the tantalum foils cut to form a filament and on which plutonium has been electrodeposited. A titanium layer of approximately  $1\mu\text{m}$  thickness is subsequently applied. (b) A filament mounted between the two vacuum feedthroughs. This adapter is then inserted into the gas cell.

end of the resonator a diffraction grating is used in the Littrow configuration so that the first order diffracted light is sent back into the cavity along the same direction as the incoming radiation. As the reflection angle is wavelength dependent and the acceptance of the laser cavity is small, only a narrow range of wavelengths is reflected back. The Ti:sapphire crystal can amplify a wide range of wavelengths from 650 nm to 1100 nm [117] and therefore by simply tuning the angle of the grating, the output wavelength of the laser can be selected. As frequency selection is accomplished using the grating, additional elements such as the birefringent filter and etalon are not required. In order to achieve a desired bandwidth somewhat below  $\sim 10$  GHz (which may be compared with the 4-5 GHz bandwidth of the standard Ti:sapphire laser) a four-prism beam expander magnifies the laser beam diameter in order to illuminate a sufficient number of grooves on the grating. Coarse adjustability of the expanded beam diameter is controlled with the addition of an iris as seen in Fig. 4.8. The iris enables easy control over the linewidth of the output laser light although it was noted that the reduction of the linewidth happens at the expense of output power. Further technical details regarding the characterization of the laser and related resonator calculations used to optimize the cavity design may be found in [118].

The SHG generation happens with a nonlinear beta-barium borate (BBO)

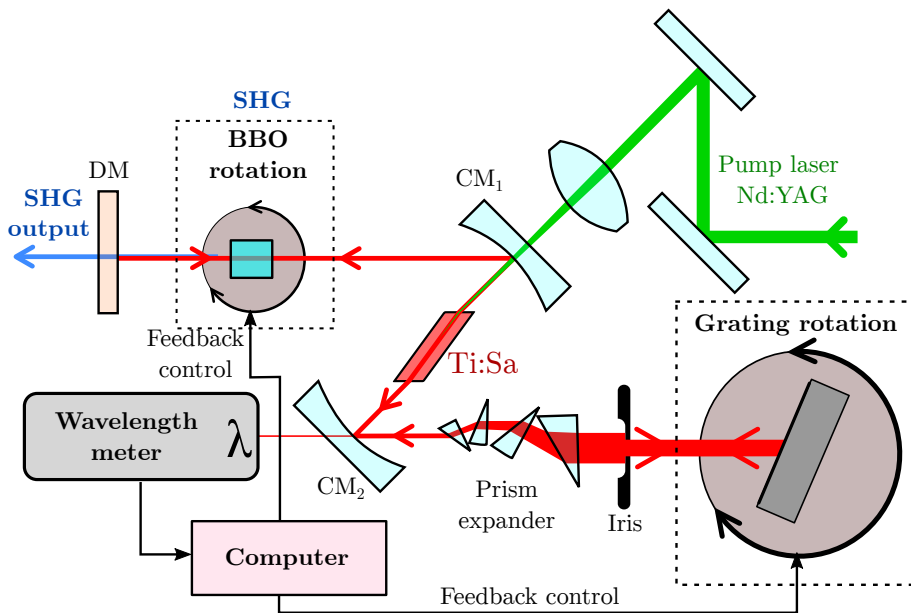


**Figure 4.8.** Schematic diagram of the grating-based Ti:sapphire laser provided by the Applied Quantum Beam Engineering group of Nagoya University for the investigation of the plutonium ionization scheme. Labeling is as follows: DM = dichroic mirror; BBO = beta-barium borate; CM = curved mirror.

doubling crystal [119] placed next to the output coupler, in the so-called intracavity mode. The output coupler is a dichroic mirror (DM), which reflects the near-infrared light back into the laser cavity while transmitting the SHG laser light in the blue wavelength range. As the angle of the BBO crystal at which the phase-matching condition is met for the generation of second harmonic light is wavelength dependent, the BBO is fixed to a motorized mount so that the phase-matching condition can be maintained while scanning the wavelength of the laser. The rotation of both the grating and the BBO crystal mounts is controlled by a computer that reads in the wavelength, which is measured from the leaked infrared light through one of the curved mirrors of the cavity. With the laser operational, a wavelength scanning of the SHG laser can be done with variable speeds and with a reasonable pointing stability so that in this experiment, even though the laser path is about 15 meters long, the spatial direction of laser beam only needs to be adjusted every 5 to 10 nm of wavelength tuning.

## 4.5 Results of Pu ionization scheme investigation

### 4.5.1 Wavelength spectrum while scanning the grating-based laser $\lambda_2$

The investigation of the ionization scheme commenced by tuning the JYFL Ti:sapphire laser to the fixed  $\lambda_1$  wavelength of 420.77 nm and then scanning with the grating-based laser near the second transition that was detected earlier. In Fig. 4.9, the upper blue line shows the resulting spectrum. The lower spectrum (green line), which has a considerably lower count rate, was recorded when the  $\lambda_1$  laser was blocked and only the grating-based laser light enters the gas cell. Both spectra are the result of several wavelength scans that have been summed and averaged with a sliding window of  $\sim 1$  GHz, not only in order to lower the background noise but also to make sure that all the peaks are repeatedly present in all scans.

In both spectra, in addition to the previously detected transition at 422.53 nm, several new resonances are seen. The wavelength of each peak was compared with the available atomic level data [120, 121] which, although comprehensive, is somewhat limited for consistency checking. The search for transitions that can account for the detected peaks was done so that every possible allowed electric dipole (E1) transition between any level close to the detected wavelength was considered. The summary of the assignment of the peak wavelengths  $\lambda_{\text{mea.}}$  to transitions between an initial level  $i$  and final level  $f$  that could be found in the literature is presented in Table 4.1. The level energy  $E$ , parity  $P$ , as well the

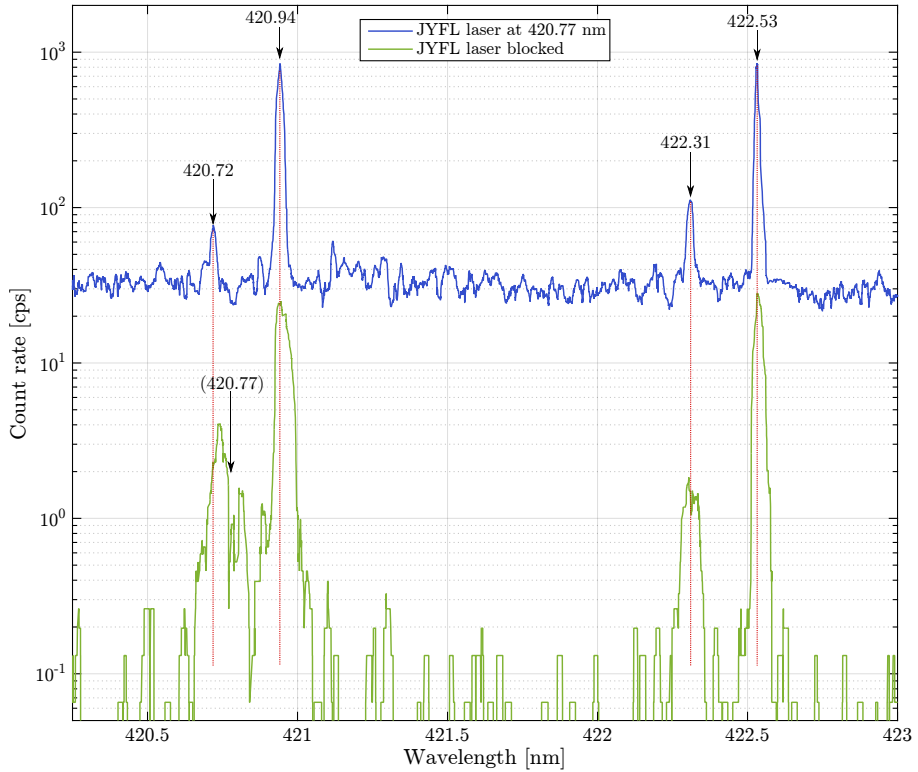


**Figure 4.9.** Wavelength scan of plutonium taken with the grating-based laser in the region around the second step ( $\lambda_2$ ) transition both with (upper spectrum) and without (lower spectrum) the first step ( $\lambda_1$ ) transition. The red dotted lines are drawn from the peak maxima of the upper spectrum to help in a comparison of the peak positions.

total angular momentum change  $\Delta J$  is given for the transitions. Wavelengths are given in vacuum.

All the transitions found appear to be originating from the first four to five excited states of plutonium confirming the initial suggestion for the origin of the 422.53 nm resonance. The two spectra share three transitions, but the transition from the  ${}^7K_4^o$  level is not visibly present in the grating-only spectrum, and, interestingly, the  $\lambda_1$  transition at 420.77 nm from the ground state seems not to be very strong in comparison to those from the first excited states. This was also seen in the previous experiment but now the difference is more pronounced. This may be due to the lower laser power of the grating-based laser, which is insufficient to saturate the transitions. The observed resonance counts are therefore likely to better reflect the actual transition strength of the different transitions. Also, at the exact wavelength of the  ${}^7F_0 \rightarrow {}^7D_1^o$  transition at 420.77 nm in the lower spectrum, the count rate actually has a minimum while peaking on either side of the  $\lambda_1$  wavelength. Very similar behavior was seen with the JYFL Ti:sapphire laser when it was used to scan around the  $\lambda_1$  wavelength but here the asymmetry of the structure is more pronounced. The reason for this behavior is unknown, however, such structural effects have been seen on a number of occasions and is reproducible. A more pronounced behavior has been seen in the laser ionization of thorium and possible interpretation is provided in connection with that work in chapter 5.

Finally, it can be noted that the resolution of the resonances in Fig. 4.9 is slightly worse with the grating-based laser only reflecting differences in the linewidths of the two lasers.

#### 4.5.2 Second 420.77 nm transition as a possible explanation for $\lambda_1$ -only ionization

When both lasers enter the gas cell the first excited states appear to be additionally populated via quenching from higher-lying levels reached via the  $\lambda_1$  transition from the ground state as the most intense three peaks (seen in both scans of Fig. 4.9) are detected with much stronger intensity. The orders of magnitude higher background in the upper spectrum is the result of the first step laser light constantly ionizing on its own. As discussed earlier, this initially was attributed to an excitation to a possible Rydberg state and subsequent collisional ionization. However, during a literature search of all possible transitions a candidate from the  $5f^67s^2 {}^7F_6$  level at  $10238.473 \text{ cm}^{-1}$  to the  $5f^67s7p \text{ J}=5$  level at  $34004.30 \text{ cm}^{-1}$  would result in a resonance at 420.772 nm. This resonance centroid is only  $\sim 8$  GHz away from the first step wavelength at 420.767 nm. Due to the convolution of the few GHz Doppler broadening of atomic lines inside the gas cell with the linewidth of the Ti:sapphire laser ( $> 5$  GHz [122]) in

$\lambda_{\text{mea.}}$ [nm]	$\lambda_{\text{lit.}}$ [nm]	$E_i$ [ $\text{cm}^{-1}$ ]	Configuration	$J_i$	$P_i$	$\Delta J$	$E_f$ [ $\text{cm}^{-1}$ ]	Configuration	$J_f$	$P_f$
420.77	420.767	0	$5f^67s^2\ ^7F_0$	0	even	1	23766.139	$5f^67s7p\ ^7D_1^o$	1	odd
420.72	420.712	6313.866	$5f^56d7s^2\ ^7K_4^o$	4	odd	1	30083.102	-	5	even
420.94	420.942	2203.606	$5f^67s^2\ ^7F_1$	1	even	0	25959.849	$5f^56d^27s$	1	odd
422.32	422.306	4299.659	$5f^67s^2\ ^7F_2$	2	even	0	27979.161	$5f^67s7p$	2	odd
422.53	422.528	2203.606	$5f^67s^2\ ^7F_1$	1	even	1	25870.685	$5f^56d^27s$	2	odd
	422.539	6144.515	$5f^67s^2\ ^7F_3$	3	even	0	29810.974	$5f^67s7p$	3	odd

**Table 4.1.** List of the wavelengths  $\lambda_{\text{mea.}}$  of the detected peaks from the grating-based laser scan close to the second step transition observed in the first experiment at  $\lambda_2$  of 422.53 nm, with assignments to transitions between levels found in literature [120, 121, 57]. The configuration and term of the lower and upper states are given if known. Wavelengths are given in vacuum.



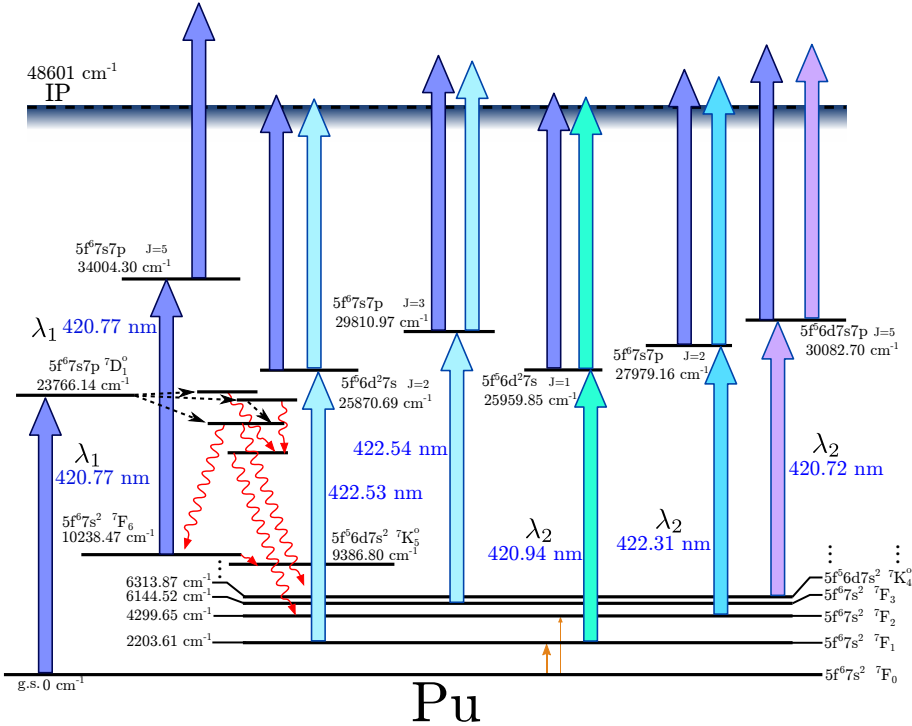


**Figure 4.10.** The level scheme constructed from the interpretation of the results obtained from the plutonium studies with the grating-based laser. Thick arrows correspond to detected laser transitions each with its own color. Dashed arrows show collisional transitions and the wavy lines radiative transitions. The orange arrows from the ground state depict thermal excitation. The level positions are to scale if energy and configuration is given.

the fundamental, which increases by a factor of  $\sqrt{2}$  following second harmonic generation, the atomic resonances are expected to be  $> 8$  GHz wide. Therefore, both transitions are at least partially addressed by the same laser when tuned to the centroid of the  $\lambda_1$  resonance. The final ionization scheme, which has been built upon the above discussions and results, is presented in Fig. 4.10.

The prerequisite for the  ${}^7F_6 \rightarrow 34004_5^0$  transition is that the initial level is populated and that the level lifetime is sufficiently long. The population cannot occur directly from the low-lying levels but may happen if the atomic level at  $23766.14 \text{ cm}^{-1}$  is quenched as described below. Although the  ${}^7F_6$  state might be collisionally depopulated, it can radiatively de-excite only to the  ${}^7K_3^o$  level at  $9386.80 \text{ cm}^{-1}$  as there is no other odd-parity level below to which an  $\Delta J = 0, \pm 1$  transition would be possible. If the  ${}^7F_6$  level is being populated from above and assuming the transition to the level  $34004_5^0$  is sufficiently strong compared

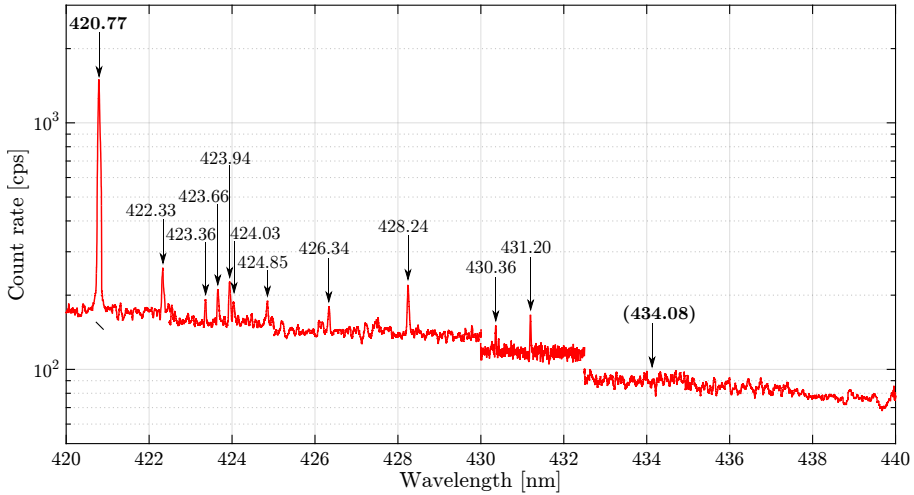


**Figure 4.11.** Wavelength scan of plutonium using the grating-based laser while the JYFL laser is fixed on the second-step transition at 422.53 nm. A wavelength is given for detected peaks. The two bold numbers note possible transitions from the ground state.

to a possible decay to  ${}^7\text{K}_5^0$ , then non-resonant ionization would happen.

### 4.5.3 A wider scan range using the grating-based laser

A second, wider scan was made with the grating-based laser while the JYFL Ti:sapphire laser was fixed at the frequency used to drive the low-lying transition from the thermally populated state at  $2203.61\text{ cm}^{-1}$  (422.53 nm) with the aim of locating further atomic resonances. The resulting spectrum is shown in Fig. 4.11.

As expected according to the scheme depicted in Fig. 4.10, the strongest resonance was found at the ground state excitation of 420.77 nm. Several smaller peaks are then visible at higher wavelength, all of which correspond to transitions from the first excited states probably being continuously fed from higher-lying levels accessed via the transition driven by the fixed wavelength laser. All identified transitions in the spectrum are listed in Table 4.2. The 422.53 nm transition is not observed this in scan as it is already fully saturated by the high power of the JYFL Ti:sapphire laser. The scan was extended also above 434.08 nm where a second possible E1-transition originating from the ground state should appear, however no resonance was observed at that wavelength. This could reflect a weak transition strength to the level at  $23037.43\text{ cm}^{-1}$  or significantly weaker collisional quenching from that level back to the state at

$\lambda_{\text{mea}}$ [nm]	$\lambda_{\text{lit}}$ [nm]	$E_i$ [ $\text{cm}^{-1}$ ]	Configuration	$J_i$	$P_i$	$\Delta J$	$E_f$ [ $\text{cm}^{-1}$ ]	Configuration	$J_f$	$P_f$
420.77	420.767	0.000	$5f^67s^2 \text{ } ^7\text{F}_0$	0	even	1	23766.139	$5f^67s^2 \text{ } ^7\text{D}_1^{\circ}$	1	odd
422.32	422.306	4299.659	$5f^67s^2 \text{ } ^7\text{F}_2$	2	even	0	27979.161	$5f^67s^2 \text{ } ^7\text{P}$	2	odd
423.36	423.351	6144.515	$5f^67s^2 \text{ } ^7\text{F}_3$	3	even	0	29765.568	-	3	odd
423.66	423.659	4299.659	$5f^67s^2 \text{ } ^7\text{F}_2$	2	even	0	27903.565	$5f^56d^2 \text{ } ^7\text{S}^2$	2	odd
423.94	423.939	4299.659	$5f^67s^2 \text{ } ^7\text{F}_2$	2	even	-1	27887.955	-	1	odd
424.03	424.022	7774.653	$5f^67s^2 \text{ } ^7\text{F}_4$	4	even	0	31358.339	-	4	odd
424.85	424.843	7774.653	$5f^67s^2 \text{ } ^7\text{F}_4$	4	even	0	31312.79	-	4	odd
426.34	426.324	4299.659	$5f^67s^2 \text{ } ^7\text{F}_2$	2	even	1	27755.977	$5f^67s^2 \text{ } ^7\text{D}_3^{\circ}$	3	odd
428.25	428.237	4299.659	$5f^67s^2 \text{ } ^7\text{F}_2$	2	even	0	27651.190	$5f^56d^2 \text{ } ^7\text{S}^2$	2	odd
430.36	430.356	4299.659	$5f^67s^2 \text{ } ^7\text{F}_2$	2	even	1	27536.236	-	3	odd
431.20	431.192	4299.659	$5f^67s^2 \text{ } ^7\text{F}_2$	2	even	0	27491.196	-	2	odd

**Table 4.2.** List of the detected resonances from the grating-based laser scan with the JYFL laser fixed to the wavelength corresponding to the 422.5 nm transition. The centroid wavelengths  $\lambda_{\text{mea}}$  are compared to transitions between levels found in literature [120, 121, 57]. The configuration and term of the lower and upper states are given if known. Wavelengths are given in vacuum.

2203.61  $\text{cm}^{-1}$  from which the JYFL laser is driving population eventually to ionization. Finally, the absence of a peak does not mean that the level does not exist as there is also the possibility of imperfect spatial overlap of the two laser beams in the gas cell as this was not possible to monitor rigorously during the scans due to the inaccessibility of the IGISOL front end.

#### 4.5.4 Observation of collisional de-excitation

As the enhancement in the population of the lowest excited states is clearly the result of the  $\lambda_1$  transition to the  ${}^7\text{D}_1^\circ$  state, the lifetime of this state in the gas cell environment appears to be much shorter than the rate for photoabsorption of the IR second step of the original three-step scheme (which dominated in a vacuum environment). It is evident therefore that the  ${}^7\text{D}_1^\circ$  state is being de-excited by inelastic collisions. In other words, the collisional quenching rate  $R_{\text{coll}}$  can be said to be much larger than the absorption rate  $\rho(\nu) B_{12}$  of 847.26 nm photons at the achievable laser power densities:

$$R_{\text{coll}} = \sigma_{\text{coll}} N_{\text{He}} \sqrt{\frac{8kT}{\pi\mu}} \gg \rho(\nu) \frac{g_2}{g_1} \frac{c^3}{8\pi h\nu^3} A_{21}, \quad (4.4)$$

where the indices 1 and 2 refer to the  ${}^7\text{D}_1^\circ$  state and the second excited level  $35569_2$  of the original three-step scheme (Fig. 4.1).  $R_{\text{coll}}$  is written according to equation (2.13) as the relationship between the total collision cross section for quenching  $\sigma_{\text{coll}}$ , the helium gas number density  $N_{\text{He}}$ , and the mean speed  $\langle v \rangle$  between the colliding atoms, which is explicitly given according to the Maxwell-Boltzmann distribution. The right hand side of the equation is the laser-driven transition rate with the power density of  $\rho(\nu)$  according to equations (2.5) and (2.6).

No experimental collision cross section data for quenching of excited levels in plutonium are known to the author or in its chemical homolog samarium. There have been reports of quenching by noble gas collisions in actinide elements in actinium [123, 30, 124] and thorium [125, 126], albeit only of the low-lying excited states, and most recently in nobelium [29]. In this work the quenching effect is expected to happen non-resonantly as the available states in helium are much higher in energy than the excited state driven in plutonium. As discussed in chapter 2, quenching can have a larger cross section if it occurs via collision with a molecule, in which the high number of molecular states at the energies of the excitation enhance the transition. Although there are impurities such as  $\text{O}_2$  present in the buffer gas, the level of impurity is in the ppm range even under poor purity conditions as shown in the next subsection. Impurities are therefore not expected to play a role in the quenching effect observed in this work.

As postulated in chapter 2, the high number of close-lying levels is expected to increase the probability of collisional population transfer. Due to the complex electronic structure of plutonium, there are several states close to the  ${}^7D_1^{\circ}$  level. The  $5f^56d^27s\ {}^9I_4^{\circ}$  level is just  $2.7\text{ cm}^{-1}$  below the  ${}^7D_1^{\circ}$ , and 7 other levels within  $\pm 100\text{ cm}^{-1}$  are present. All of those levels belong, however, to a different configuration than that of the  ${}^7D_1^{\circ}$  level and thus the possible collisional de-excitation might be happening to the levels  $23416_2^{\circ}$ ,  ${}^7F_2^{\circ}$ , and  ${}^9D_4^{\circ}$ , which, although are further away in energy at  $23416.67\text{ cm}^{-1}$ ,  $23315.21\text{ cm}^{-1}$  and  $23274.86\text{ cm}^{-1}$ , as they belong to the same configuration as  ${}^7D_1^{\circ}$ . Still, if the collisional quenching has an inverse dependence on the energy difference, it can be suggested that it is the close-lying levels or those levels with a similar configuration to which the fast collisional quenching of the  ${}^7D_1^{\circ}$  state happens. After the collisional population transfer, subsequent radiative and further collisional mixing and quenching populates possible intermediate levels and finally the low-lying states as well the  $5f^67s^2\ {}^7F_6$  state.

#### 4.5.5 Temporal overlap of $\lambda_1$ and $\lambda_2$ lasers

Additional indication of population of the low-lying levels via quenching was observed when the temporal overlap between the two laser pulses,  $\lambda_1 = 420.77\text{ nm}$  and  $\lambda_2 = 422.53\text{ nm}$ , was modified. Although a maximum count rate of  $12.8 \cdot 10^3\text{ cps}$  reduced when the timing was tuned off “temporal resonance”, a steady count rate of  $9.4 \cdot 10^3\text{ cps}$  was observed even by detuning the second step laser pulse timing by  $8.1\ \mu\text{s}$  after the first step, a time much longer than the  $40\text{ ns}$  pulse width of the individual laser pulses. These count rates are considerably higher than the rates of  $10\text{ cps}$  and  $1.2 \cdot 10^3\text{ cps}$ , which were obtained individually from the first and second step lasers, respectively (note that here the grating-based laser was used and thus the count rates differ from those mentioned in accordance with the first experiment). The background (no lasers) was measured to be  $0\text{ cps}$ . Remarkably, about the same count rate was observed when the second laser step was detuned about  $6\ \mu\text{s}$  before the first step. This indicates that the lifetime of the first excited level in the gas cell is longer than the repetition rate of the lasers at  $100\ \mu\text{s}$ .

The reason for the absence of strong temporal dependence points to the long lifetime of the low-lying states. The long lifetime raises the question of the existence of possible dark states, which may reduce the ionization efficiency as the first-step laser might pump a considerable population to levels from which ionization cannot occur without the addition of further lasers.

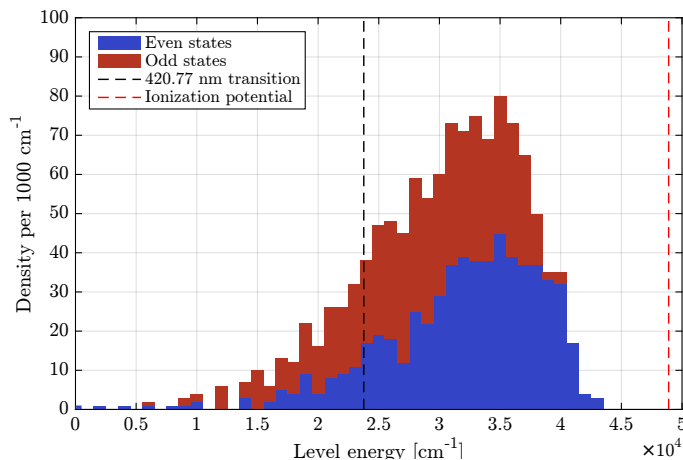


**Figure 4.12.** The atomic level density of plutonium per 1000  $\text{cm}^{-1}$  as a stacked bar plot for even and odd parity states. The position of the  $\lambda_1$  transition and the ionization potential are shown separately as dashed lines.

#### 4.5.6 Atomic level density in plutonium and comparison to other elements

In order to gain a broader picture on the level structure of plutonium and in particular the level density which is relevant to the quenching discussion, the available atomic levels from databases have been further analyzed [57]. The atomic level density is plotted in Fig. 4.12 as a stacked bar plot for odd and even parity levels separately. The figure illustrates the high level density of plutonium especially after  $20000 \text{ cm}^{-1}$ . It should be noted that the drop in the level density after  $35000 \text{ cm}^{-1}$  points to the lack of spectroscopic data of plutonium, a problem shared with most of the actinide elements. The high level density of plutonium compared to other elements is also evident in Fig. 2.3 which highlights the level density of elements throughout the periodic table. In that comparison plutonium has the second highest level density after uranium.

It is evident from the figure that the behavior seen in the ionization of plutonium, which is attributed to the high density of levels in the vicinity of those addressed via the ionization schemes, is in all probability not a feature of these particular states but a feature of all the levels above an energy of about  $20000 \text{ cm}^{-1}$ .

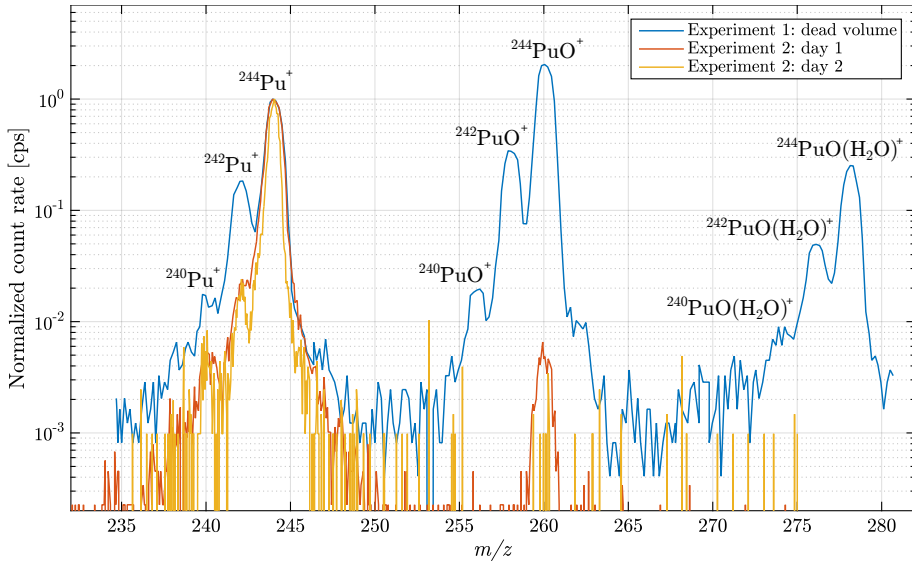


**Figure 4.13.** Comparison of mass spectra taken in different impurity conditions while doing laser ionization of plutonium. All of the spectra are normalized to 1 at the  $^{244}\text{Pu}$  mass peak.

## 4.6 Mass spectra and helium purity

To characterize the gas cell performance and to measure the isotopic abundance of plutonium in the filaments, a series of mass spectra were recorded with the MCP detector at the focal plane of the IGISOL separator. Figure 4.13 shows plutonium mass spectra from three different occasions, all of which are normalized to  $^{244}\text{Pu}$  on which count rates of between 5000 cps and 15000 cps were recorded. All of the spectra show plutonium ions which were entirely created in the laser ionization process as practically zero background was observed without the lasers. The difference in the isotopic abundances between samples is a result of using different batches of filaments, which were created for different purposes. The difference was also evident in the abundances determined using gamma-ray spectroscopy.

The spectrum from experiment 1 (Article II) shows a mass scan taken when the impurity levels were unusually poor due to a dead volume in the filament holder that was suspected to be constantly releasing small amounts of air into the helium gas. The other two spectra are taken during a later experiment with a modified filament holder. A clear difference can be seen in the purity conditions of the two experiments, evident in the amount of molecular ions compared to the atomic species. In experiment 2 there is a further improvement of the purity

conditions visible on the second day compared to the first day. This is most likely due to the steadily improving purity conditions as purified helium is fed through the gas cell and the filament is being baked when it is used.

The impurity content of the oxidizing species in the helium gas can be estimated from the above mass spectra using equation (2.40). The oxidizing impurity in the gas is most probably  $O_2$  and to some extent also  $H_2O$ , which can form  $PuO^+$  in a bimolecular reaction with reaction coefficients of  $k_2 = 1.5 \cdot 10^{-10} \text{ cm}^3/\text{s}$  and  $k_2 = 7 \cdot 10^{-12} \text{ cm}^3/\text{s}$ , respectively. These values are determined from the reactions efficiencies from reference [127] as detailed in Article II. Using the reaction coefficient and known evacuation time of the gas cell, impurity levels of 70 ppb, 0.3 ppb and 0.05 ppb are attained assuming the impurity to be  $O_2$  and 1.6 ppm, 7 ppb and 1 ppb assuming  $H_2O$  for experiment 1, experiment 2 (day 1), and experiment 2 (day 2) respectively. These impurity levels are well in accordance with that expected from an impure and pure operational gas cell system.

## 4.7 Summary and outlook

Despite the substantial advantage of gas cells compared to ISOL facilities with respect to chemical non-selectivity and their ability to be fast and efficient sources even for refractory elements, the gaseous environment can sometimes bring about unexpected phenomena. This has been clearly illustrated by the investigation of the laser resonance ionization of plutonium, which showed a considerable complexity due to its high atomic level density and to the collisional quenching of excited levels by the buffer gas atoms. The quenching had a very strong effect on the ionization scheme successfully developed in a hot cavity environment, reducing its efficiency considerably. Similar to plutonium, in the reported work from laser ionization of actinium, a reduced in-gas-cell laser ionization efficiency was observed when compared to the in-gas-jet ionization and has been attributed to collisional quenching [123]. Laser resonance ion sources using hot cavities [9, 128, 10, 129, 130] have reported high efficiencies of ionization schemes for various elements. In the adaptation of these schemes for in-gas-cell laser resonance ionization, consideration should be given to the fact that the schemes may have very fast collisional channels open that are detrimental to the efficiency, especially for elements with a high atomic level density.

The population of a high number of levels by the quenching effect and the high level density results in a considerable chance that not only one transition but also a second transition, virtually with the same energy, is driven with the same laser so that a path to ionization opens. This type of one-laser two-resonant-step ionization is rarely seen but has been recently reported in radium [131] as well



in silver [132] and samarium [133] although in these instances no quenching is involved but direct transition to a Rydberg and an AI state respectively. Here, in the case of plutonium the same accidental second transition from a collisionally-populated level is most likely the explanation for the very clear, albeit rather low efficiency, resonant ionization with only the first step  $\lambda_1$  laser. Interestingly, this kind of second level has also been found in the case of the laser ionization of thorium as discussed in section 5.3 of chapter 5.

The ionization scheme investigation with the grating-based Ti:sapphire laser developed by Nagoya University, was crucial to show and understand the population of the low-lying levels. Currently, there is a local development underway to build a similar laser that will utilize second harmonic generation in order to have the easy tuning capability in the blue wavelength regime. It is planned to use this laser to continue the investigation of other levels from the plutonium ground state and to search for additional evidence for collisional quenching from other states. Also more quantitative measurements of the lifetimes of levels are planned for the future. As there are many other elements in the heavy element region that lack in spectroscopic level data, a grating-based laser will be a vital tool for building efficient ionization schemes for the heavy elements. Furthermore, in some cases it may well be useful to use an ionization scheme with the final transition to a very broad auto-ionization (AI) state.

# Chapter 5

## Developments towards a $^{229}\text{Th}$ ion source

### 5.1 Introduction

A considerable effort, both theoretical and experimental, is currently being devoted to the  $^{229}\text{Th}$  isotope due to its exceptionally low-lying isomeric state [134, 135]. The currently published estimate of the energy of this state, calculated from doublet differences between higher-lying rotational gamma transitions, is  $7.8 \pm 0.5$  eV [136, 137]. As such a low-lying energy level is expected to have a very long lifetime, it has been proposed to be used to create a nuclear frequency standard that would have orders of magnitude better accuracy than the currently available atomic frequency standards [27, 138, 28]. The  $^{229m}\text{Th}$  isomer has also been proposed for use in other novel applications such as a nuclear-based laser [139] and a probe to measure the variation in the fine structure and strong coupling constants [140, 141]. The current research in Europe focused on the characterization of the isomer and the development of a nuclear clock is well underway since the launching of the nuClock project, which is an EU-supported collaborative effort between several European research groups [26].

At IGISOL, the study of  $^{229}\text{Th}$  and its low-lying isomeric state is of interest due to the possibility of performing high-resolution collinear laser spectroscopy to measure the atomic hyperfine structure and to probe the isomeric shift in the electronic transition frequency. The hyperfine fingerprint provides a model-independent method to measure the nuclear spins, magnetic dipole moments and electric quadrupole moments. The shifts in the transition frequency between isotopes of a given element, or between an isomeric state and a nuclear ground

	Level [cm <sup>-1</sup> ]	Configuration	<i>A</i> [MHz]	<i>B</i> [MHz]	<i>Ref.</i>
$^{229}\text{Th}$	0	$6d^27s^2\ ^3F_2$	39(9)	390(+120,-180)	[143]
$^{229}\text{Th}$	26096	$J = 3, \text{ odd}$	93(+9, -18)	1200(+240,-150)	[143]
$^{229}\text{Th}$	26113	$J = 2, \text{ odd}$	39(9)	-390(+60, -180)	[143]
$^{229}\text{Th}$	38279	$J = 1, \text{ odd}$	630(30)	30(60)	[143]
$^{229}\text{Th}^{1+}$	0	$6d^27s\ ^2D_{3/2}$	-444.2(19)	303(6)	[144]
$^{229}\text{Th}^{2+}$	63.26	$6d^2\ ^3F_2$	151(8)	73(27)	[142]
$^{229}\text{Th}^{2+}$	20711	$5f6d\ ^1P_1^o$	88(4)	897(14)	[142]
$^{229m}\text{Th}^{2+}$	63.26	$6d^2\ ^3F_2$	-263(29)	53(65)	[142]
$^{229m}\text{Th}^{2+}$	20711	$5f6d\ ^1P_1^o$	-151(22)	498(15)	[142]
$^{229}\text{Th}^{3+}$	0	$5f6p^6\ ^2F_{5/2}^o$	82.2(6)	2269(6)	[145]

**Table 5.1.** The currently known hyperfine *A* and *B* parameters for the electronic ground state and low-lying excited states of  $^{229}\text{Th}$  in several charge states. Also the recently reported parameters of a few high lying states are given.

state, gives access to changes in nuclear size via mean-square charge radii [21]. Recently the existence of the isomeric state was confirmed via detection of the electrons emitted from the internal-conversion decay channel in neutral thorium [134]. Following this work, a laser spectroscopic measurement of the hyperfine structure of the doubly-charged  $^{229}\text{Th}^{2+}$  ion in both the nuclear ground and isomeric states allowed the determination of the magnetic dipole and electric quadrupole moments for the isomer,  $\mu^m = -0.37(6)\mu_N$  and  $Q_0^m = 8.7(3)$  eb. From the measured isomeric shift, the difference in the mean-square radii between the two states is  $0.012(2)$  fm<sup>2</sup> [142]. Table 5.1 lists the currently known hyperfine parameters (dependent on both nuclear and atomic structure) for the electronic ground state and low-lying excited states of  $^{229}\text{Th}$  in the neutral atom as well as ionic species from singly- to triply-charged. Parameters of a few high lying states that have been recently reported are also given.

Although the lifetime of the isomer to decay via radiative M1 nuclear decay is expected to be long, minutes to even hours ( $\tau > \sim 10^3$  s) [146, 147], the lifetime in the neutral  $^{229m}\text{Th}$  has been measured to be relatively short, only  $7 \pm 1$   $\mu\text{s}$  [148] due to fast emission of a conversion electron. In neutral  $^{229m}\text{Th}$  the internal conversion decay channel is possible because the energy of the isomer appears to be above the first ionization potential of thorium, which is at 6.31 eV [149]. As the evacuation time of any practical gas cell is at least two orders of magnitude larger and in many cases even longer, working with neutral thorium to study the isomeric state in the gas cell is not possible.

As soon as the thorium is in a charged state, the ionization potential is higher than the energy of the isomer and therefore internal conversion is not allowed.

Nevertheless, the experimentally estimated upper limit to the lifetime of the singly-charged  $^{229m}\text{Th}$  isomeric state is  $\sim 10$  ms [148]. The explanation for the short lifetime may lie in other decay channels such as collisional quenching, bound internal conversion or an electron bridge mechanism whereby the isomeric state relaxes via excitation of an electronic state in thorium [150, 151]. Such a short lifetime for  $^{229m}\text{Th}^{1+}$  is a problem for larger gas cells due to the long evacuation time and therefore small volume cells or electric field guidance of ions are required. In the case of doubly-charged ions and even higher charge states the isomer has a lifetime longer than a minute [134] and therefore no significant loss of the isomer should occur through decay during transport even with long evacuation times.

Currently, the existence and the lifetime of the isomeric state in the  $^{229}\text{Th}^{1+}$  charge state remains an open question. At IGISOL, the on-line production of  $^{229m}\text{Th}$  to study the isomer in the singly-charged state is attractive because the isomer may be strongly fed in fusion-evaporation reactions. Nuclear reaction products in on-line conditions are also predominantly extracted in the  $1+$  charge state. In order to get a hyperfine template measurement of the nuclear ground state in singly-charged  $^{229}\text{Th}$ , a filament dispenser can be used to evaporate thorium inside a gas cell while applying resonance laser ionization, similar to the previous study of plutonium. In this manner a selective and efficient source for  $^{229}\text{Th}^{1+}$  ions may be realized.

In addition to on-line production,  $^{233}\text{U}$  alpha-recoil sources can be used for the production of the isomeric state of  $^{229}\text{Th}$ , albeit the estimated branching ratio is only 2%. The alpha recoil source approach is especially useful in the creation of  $^{229}\text{Th}$  ion beams in higher charge states, typically  $2+$  and  $3+$ , which can subsequently be used to perform a collinear laser spectroscopic measurement on the, as yet unknown, hyperfine structure of the electronic ground states of  $^{229m}\text{Th}^{2+/3+}$ .

The work presented in this chapter concentrates on the developments of the three types of thorium ion sources: filament-based dispensers with laser resonance ionization,  $^{233}\text{U}$  alpha-recoil sources and on-line production of  $^{229}\text{Th}$ . In publication No. III, studies of laser ionization of thorium evaporated from filament dispensers is presented in detail. Additional information regarding the ionization scheme as well as related in-gas-cell processes are discussed following the publication. Also, in connection to the thorium laser ion source, a novel size-exclusion technique for suppression of molecular ion beams from gas cells is introduced. This method takes advantage of the size difference of molecules and monoatomic ions.

The middle part of this chapter focuses on the  $^{233}\text{U}$  source characterization by measurement of direct gamma and alpha radiation from two different sources as well as from implantation foils. Additionally, the sources have been characterized

by Rutherford backscattering spectrometry at a Pelletron accelerator. The latter part of this chapter reports on the the first results from the on-line production of  $^{229}\text{Th}$ , to determine the yield via fusion-evaporation using a  $^{232}\text{Th}$  target bombarded by protons.

## 5.2 Article III

The following pages contain the paper titled *Laser ionization studies of thorium at IGISOL using filament-based dispensers*, to be submitted to the peer-reviewed journal of Nuclear Instruments and Methods in Physics Research Section B.

# Laser ionization studies of thorium at IGISOL using filament-based dispensers

I. Pohjalainen<sup>a,\*</sup>, I.D. Moore<sup>a,\*</sup>, A. Voss<sup>a</sup>, S. Geldhof<sup>a</sup>, T. Schumm<sup>b</sup>

<sup>a</sup>University of Jyväskylä, Department of Physics, P.O. Box 35 (YFL), FI-40014 University of Jyväskylä, Finland

<sup>b</sup>Institute for Atomic and Subatomic Physics, TU Wien, Stadionallee 2, 1020 Vienna, Austria

## 1. Introduction

High-resolution laser spectroscopy of atomic levels is a well-known method to probe fundamental properties of atomic nuclei. Measurements of isotope-dependent shifts in electronic transition frequencies and hyperfine structure of the optical resonance provides model-independent access to nuclear spins, magnetic dipole and electric quadrupole moments, as well as changes in nuclear size via mean-squared charge radii [1]. Additionally, and with pertinence to the current work, laser spectroscopy measures states rather than decays and thus the observation of resonance lines besides those expected from the nuclear ground state is a proof of the existence of isomeric states, which may be too-long lived to be studied by decay spectroscopy or too close in energy to the ground state in order to be cleanly separated. At the IGISOL facility in the Accelerator Laboratory of the University of Jyväskylä [2], collinear laser spectroscopy [3] of actinide elements is a currently ongoing program of research. By combining highly efficient laser resonance ionization [4] in the IGISOL gas cell with thermal desorption of long-lived actinide elements, an efficient ion source may be achieved even with trace amounts of isotopes. There are several isotopes in the actinide region which have sufficiently long lifetimes to be produced for example in nuclear reactors, deposited onto filament dispensers and transported to a separate location with appropriate experimental facilities for detailed study. The deposited isotopes can then be converted to an ion beam without the requirement of a primary beam from an accelerator. Recently, the first successful laser ion source at IGISOL for plutonium was realized in this manner [5] and subsequent high-resolution collinear laser spectroscopy of  $^{239,240,242,244}\text{Pu}$  was performed, the heaviest element studied to date with this technique [6].

In recent years thorium has attracted considerable interest as  $^{229}\text{Th}$  is known to possess an excited isomeric state in the energy range of only a few electronvolts [7, 8], with a variety of possible applications, most notably the suggestion to use the low-energy transition as the frequency reference in a highly precise nuclear-based clock [9, 10]. We do not intend to provide an extensive summary of the numerous theoretical and experimental efforts currently focused on this isomer, however we

note the most recent highlights which include the detection of electrons emitted from the internal-conversion decay channel of the isomer in neutral thorium [11], the measurement of the half-life of the isomer in a closely-linked adaptation of this first experiment [12] and the successful laser spectroscopic investigation of the hyperfine structure of the doubly-charged ion, which led to the first direct determination of the magnetic dipole and electric quadrupole moment, as well as the nuclear charge radius [13].

At IGISOL, complementary efforts are underway to measure the hyperfine structure of the isomer and the ground state of  $^{229}\text{Th}$  using collinear laser spectroscopy. Earlier efforts focused on a measurement of the ground-state hyperfine structure of neutral  $^{229}\text{Th}$  with hyperfine coupling constants measured for the atomic ground state and three excited states [14]. Following the measurement of the lifetime of the isomeric state in neutral form ( $7 \pm 1 \mu\text{s}$ ) [12], our attention turned towards the study of singly-charged  $^{229m}\text{Th}$  where open questions still remain. For example, it was noted that no signal indicating internal conversion of the isomeric state in  $^{229m}\text{Th}^+$  was obtained, which may point to other decay channels such as collisional quenching, bound internal conversion or an electron bridge mechanism [15, 16]. With the availability of on-line production of  $^{229g,m}\text{Th}$  through the fusion-evaporation reaction  $^{232}\text{Th}(p, p3n)^{229g,m}\text{Th}$  at IGISOL, a laser ion source for thorium using filament-based dispensers of  $^{229}\text{Th}$  would afford access to a measurement of the hyperfine parameters for a ground state-only beam of  $^{229}\text{Th}^+$  ions. This would pave the way to a future measurement of both ground state and isomer using the on-line reaction.

Although filaments have been successfully used in gas cells as sources for monoatomic vapors of a variety of elements for the purpose of doing laser resonance ionization in connection with different gas cell-based experiments [17–20], the heavy actinide region generates a new challenge for filament-based sources as the volatility of many actinide elements is relatively poor and the scarcity of some of the isotopes complicates the filament manufacturing. This is especially the case with  $^{229}\text{Th}$  as the availability of high-purity  $^{229}\text{Th}$  is limited and thorium is the most non-volatile of the actinide elements, therefore high filament temperatures are required, which can be detrimental to the purity conditions of a gas cell environment.

This work concentrates on the developments towards a filament-based atomic vapor source for thorium and the phenomena and challenges faced while using such a source in com-

\*Corresponding author.

Email addresses: [ilkka.pohjalainen@jyu.fi](mailto:ilkka.pohjalainen@jyu.fi) (I. Pohjalainen), [iaain.d.moore@jyu.fi](mailto:iaain.d.moore@jyu.fi) (I.D. Moore)

combination with resonance laser ionization for the selective production of a singly-charged thorium ion beam. Three different filament types have been studied in a series of offline experiments, which led to the realization of a high yield  $^{232}\text{Th}^+$  ion source. The manufacturing of the filaments is described and the laser ionization of thorium is presented with an estimate of the total ionization efficiency. Mass spectra obtained using the IGISOL mass separator are analyzed in order to understand the gas phase chemistry obtained from the different filament types following which a novel, collision-probability-based method of ion beam purification of molecular contaminants is presented as an alternative explanation to the normally discussed purification by collision-induced dissociation.

## 2. In-gas-cell filament source for thorium

The measurements presented in this work have been done with a dedicated gas cell developed for use with electrothermally-heated filaments that are fabricated in order to evaporate the element of interest in a neutral monoatomic state. In-gas-cell resonant laser ionization is performed on evaporated atoms to selectively (and efficiently) produce an ion beam which is extracted from the cell, guided through a differential pumping stage towards the high vacuum region of the mass separator and accelerated to a potential of typically 30 kV for mass separation, with a nominal mass resolving power of  $M/\Delta M = 500$ . The ions may be detected at the focal plane of the separator using either a Faraday cup or multichannel plate (MCP) detector. The gas cell has been characterized and described in earlier work [5] and therefore only a brief description is provided in the following.

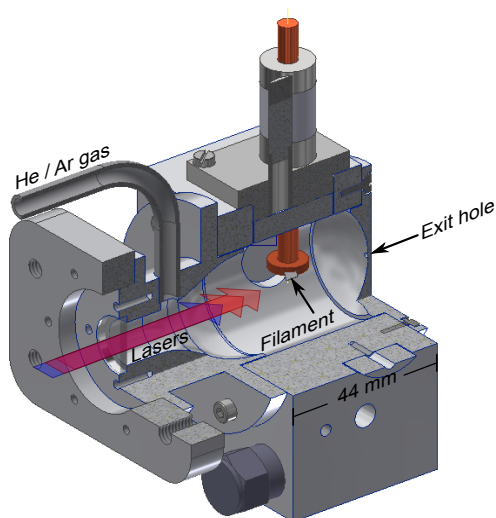


Figure 1: Cross-sectional view of the gas cell. The filament is barely visible, connected to one of the high current feedthroughs.

A cross-sectional view of the gas cell is shown in Fig. 1. The gas cell consists of a volume of about  $30\text{ cm}^3$  into which helium gas is fed by the transverse pipe located next to the sapphire window used for optical access. The buffer gas, along with filament atoms, laser ions and contaminants is extracted through a 1.2-mm diameter exit hole into a vacuum chamber at a pressure of approximately  $10^{-2}$  mbar. The evacuation time of the gas cell volume is estimated to be  $\sim 50$  ms and is independent from the gas pressure, which in this work is maintained at 80 mbar. The filament is mounted between two high current feedthroughs located close to the exit hole of the gas cell and  $\sim 1$  mm above the central extraction axis of the cell. This geometry results in an optimal spatial overlap between the lasers and filament atoms in order to probe the highest density of atomic vapor. In this work the filament holder has been simplified in order to correct for a source of impurities due to outgassing which had been observed during the plutonium studies, thereby improving the gas purity conditions considerably.

The purity of the carrier gas has been shown to be critical for the survival efficiency of ions during the extraction from the gas cell in an atomic form. Therefore the IGISOL gas purification system [21] is used to purify the helium before it is fed to the gas cell. Purification of the gas to a sub parts-per-billion level of impurity is needed to prevent loss of the atoms to molecules before the laser ionization process or correspondingly, the atomic ions to a molecular species following ionization. The ions of actinide elements in particular can be strongly reactive towards oxidizing reactants of which  $\text{O}_2$  and  $\text{H}_2\text{O}$  are the most abundant impurities in the helium gas. Ions of thorium compared to other actinide elements exhibit large reaction rate coefficients, emphasizing the importance of cleanliness of the gas in this work [22].

## 3. Description and operation of the filaments

### 3.1. Structure, manufacturing and preparation of the filaments

The prerequisite for resonant laser ionization of neutral atoms is to have the element of interest in monoatomic form. Evaporation of various actinide elements in atomic form has been successfully demonstrated using so-called *actinide sandwiches*, in which an actinide is electrolytically deposited on a substrate and then covered by a layer of reducing agent, as demonstrated by Eichler *et al.* [23]. In that work they showed that the most promising method for actinide elements was using a tantalum substrate with a titanium layer covering the deposition. This resulted in stable sources of atoms delivering a nearly constant flux for long periods of time. In our approach, tantalum was selected as a substrate material but, instead of electrodeposition, the thorium was applied on the tantalum substrate in a hydrate form, namely thorium nitrate ( $\text{Th}(\text{NO}_2)_4 \cdot x\text{H}_2\text{O}$ ), which was added in a repeated drip-dry method.

In this work two types of filaments were tested. First, as a proof-of-concept for a thorium laser ion source, stable  $^{232}\text{Th}$  filaments were prepared with approximately  $10^{15}$   $^{232}\text{Th}$  atoms covered either with a titanium or zirconium reducing layer





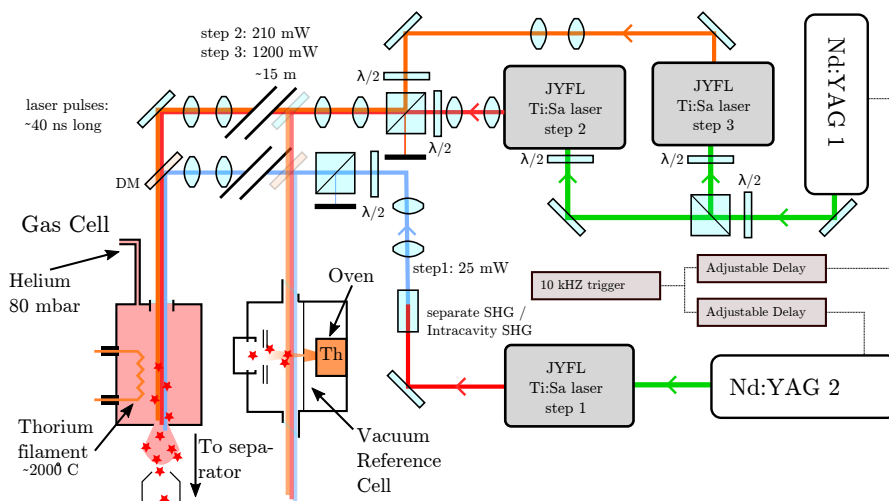
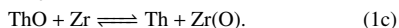
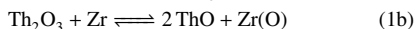
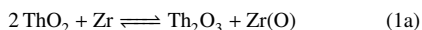


Figure 4: The experimental setup for laser resonance ionization of thorium from a filament dispenser. In addition to laser ionization in the gas cell, a separate reference cell was used to study the ionization under vacuum. This latter setup was only used with stable  $^{232}\text{Th}$ . DM = dichroic mirror, SHG = second harmonic generation. See text for further details. Colour on-line.

at least 12 hours. During this time, the filaments were heated to a low temperature ( $< 900^\circ\text{C}$ ) in order to bake out additional impurities which were seen to be continually released at higher temperatures.

### 3.2. Decomposition and reduction of the thorium nitrate

The dried thorium nitrate hydrate,  $\text{Th}(\text{NO}_3)_4 \cdot x\text{H}_2\text{O}$ , is expected to decompose into  $\text{ThO}_2$  in a series of evaporation processes when the temperature increases from  $330^\circ\text{C}$  to  $630^\circ\text{C}$  [29, 30]. At the operational temperature near  $2000^\circ\text{C}$ , the reduction of thorium oxide to thorium is expected to happen with the aid of zirconium through the following steps [23]:



Thorium starts to evaporate out of the filament at the operational temperature which can be increased further to get a larger release rate of atoms. The upper limit to the temperature is restricted by the evaporation of the tantalum substrate. In order to reach evaporation temperatures for thorium, a heating current between 15 A to 30 A is applied depending on the width of the filament, resulting in  $\sim 1$  V across the filament feedthroughs and about 15 W to 30 W of heating power. Considerable dissipation of this heat happens through the constantly flowing helium gas. This effect is seen as a strong dependence of the filament temperature on the gas pressure.

## 4. Laser resonance ionization of thorium

Resonance photo-ionization has been a very successful method to produce isobarically pure ion beams from neutral atom sources in both hot cavities as well as buffer gas stopping cells [31, 32]. At IGISOL, the FURIOS laser facility provides tunable pulsed laser beams for the purpose of doing laser resonance ionization, spectroscopy as well as optical manipulation [33]. Laser resonance ionization can be performed even in small gas cells with fast extraction times. By carefully selecting an appropriate ionization scheme, high ionization efficiencies can be achieved in short laser exposure times and with modest laser powers. For these reasons, laser ionization was a natural choice for ionization of the thorium atoms evaporated from the filaments.

The ionization scheme chosen for the resonance ionization of thorium was developed by Liu and Stracener [34] based on earlier ionization studies by Raeder *et al.* [35]. A high overall efficiency of 40% was measured in their hot cavity ion source. The scheme consists of an ultraviolet (UV) first excitation step at  $372.049$  nm corresponding to the transition from the ground state  $^3F_2$  to the  $^3G_3^o$  excited state, followed by two infrared (IR) steps at  $827.897$  nm and  $831.67$  nm, which results in the population of an autoionizing (AI) state at  $50980.96$   $\text{cm}^{-1}$ . The laser light for the three steps was produced by three broadband Titanium:sapphire (Ti:sa) lasers operated at a repetition rate of 10 kHz with  $\sim 40$  ns pulse duration. In order to generate the UV light of the first step two approaches were implemented. Intra-cavity second harmonic generation was used for high output power [36] and single-pass external doubling was preferred when wavelength scanning was required. The first step Ti:sa laser was pumped separately with its own Neodymium YAG (Nd:YAG) laser, which gave independent control over the tim-

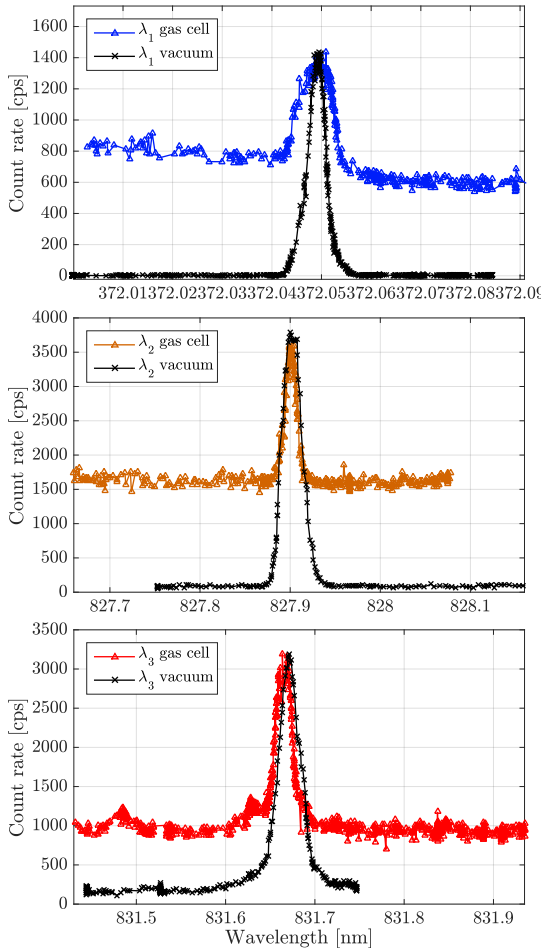


Figure 5: The ion count rate as a function of laser wavelength for mass-separated ions at  $A/q = 232$  from the actinide gas cell for each of the three laser resonance excitation steps (triangle symbols). The solid lines with data as crossed symbols present the same wavelength scans done in a vacuum reference cell without mass separation.

ing of the first step laser pulses. The second and third step lasers were pumped by a second Nd:YAG laser and the temporal overlap was adjusted by fine tuning the pump laser power to each resonator. Figure 4 shows a simplified schematic picture of the laser setup.

#### 4.1. Wavelength spectra

It is essential to study the mass-separated ion beam at the correct mass-to-charge ( $A/q$ ) ratio of thorium by scanning the frequency of the lasers across the expected resonant frequency for each of the three excitation steps. Detection of the cor-

responding signal can be used to confirm whether the mass-separated ions are resonantly-produced thorium ions, the selectivity (in other words the fraction of laser-ionized thorium to non-resonant ions) as well as the contribution of the total thorium signal from each individual laser step. Simply verifying a laser response in the mass-separated ion signal by (un)-blocking the laser light is not necessarily sufficient confirmation for laser ionization of thorium as the beam usually contains ions that have not originated from thorium atoms but from contaminant molecules which nevertheless respond to the lasers. This is because of the tendency of contaminant molecules to be ionized by UV laser light in a non-resonant manner due to the low ionization potential of molecules.

Resonance frequency scans for thorium were performed in two environments, the gas cell and a separate vacuum reference cell. The ion count rate from the gas cell was measured by recording the mass-separated ( $A/q = 232$ ) ion beam with the MCP detector, whereas ions generated in the vacuum reference cell were recorded using an electron multiplier tube (EMT) detector without mass selection. The reference cell contains a resistively heated tantalum tube that acts as an oven to evaporate a small sample of  $^{232}\text{Th}$  wrapped in zirconium foil. Following heating, an atomic thorium vapor is formed, a fraction of which passes through a small aperture above the oven and is intersected in a perpendicular geometry by the cross-propagating laser beams. The resonantly ionized thorium ions are deflected to the detector using electric fields. Due to the laser-atom overlap geometry, a nearly Doppler-free method of spectroscopy can be performed and compared to the environment of the gas cell.

Figure 5 illustrates the measurements of the frequency scans for each of the three excitation and ionization steps in both the gas cell and vacuum reference cell. The spectra of the reference cell are normalized to the maximum count rate of the gas cell for comparison. In all steps, the resonance peak obtained in the reference cell is located at the expected wavelength corresponding to the atomic states in the laser ionization scheme, and there is little or no background detected at either side of the peaks. The resonance peak width is a convolution of the bandwidth of the laser light (in the fundamental this is typically  $\sim 5$  GHz) and a power broadening effect.

The spectra measured in the gas cell also show resonant peaks according to the laser ionization scheme but there is a significant background in all three laser scans. In the case of the second and third step scans the background is mainly due to the first step UV laser light non-resonantly ionizing the thorium by first populating the first excited state and then ionizing directly across the ionization potential. There is also a constant background count rate that most likely was due to impurities on the same nominal mass as  $^{232}\text{Th}$  or possibly to thorium that is already in an ionic form as it leaves the hot filament.

In the case of the first excitation step the background can only be due to impurities or thorium leaving the hot filament as an ion. The worse signal-to-background ratio in the first step wavelength scan is mainly due to the higher temperature being applied to the filament as the measurement was made towards the end of the filament life. The linewidth of the resonance of

the first step is significantly larger in the gas cell, and is attributed to strong power broadening as the reference scan was obtained in a separate experiment (and at a lower laser power). Finally, it is notable that a small frequency shift of the final step frequency scan is seen between the gas cell and the reference cell. This is likely to be due to the well-known pressure shift of transitions to both AI and Rydberg states in helium (or argon) gas. We did not probe this effect further as a variation in the pressure resulted in a strong dependence on the temperature and thus release rate of thorium atoms.

#### 4.2. Saturation of the laser signal

The level of saturation of each resonant excitation step was measured in the gas cell and additionally in the vacuum reference cell for comparison. In Fig. 6 the ion count rates are shown as a function of the laser intensity, which was determined from measured laser powers and transportation losses, as well from the laser beam spot sizes at the ionization regions. The laser powers were adjusted for each individual step by using a combination of the rotation of a half-waveplate combined with a beam splitter cube and a series of neutral density filters. The errors on the measurement data points are statistical only.

All of the excitation steps both in the reference cell and gas cell exhibit the typical saturation behavior in which the signal  $A$  as a function of the intensity  $I$  is described by,

$$A(I) = A_{\max} \frac{I/I_{\text{sat}}}{1 + I/I_{\text{sat}}}, \quad (2)$$

where the parameters  $I_{\text{sat}}$  and  $A_{\max}$  are the saturation intensity and the signal amplitude when the transition efficiency approaches unity. In other words,  $A_{\max}$  is the maximum attainable signal if the laser intensity of a particular transition was increased towards infinity. Fits of such saturation curves to the data are shown with solid lines together with the measured saturation intensity and expected maximum signal values. In all transitions, the measured data is closely reproduced by the saturation equation but there is a much larger scattering in the data points than the statistical error of the ion count rate. This is due to fluctuations in the output power of the Nd:YAG laser pumping the Ti:sapphire laser used for the first excitation step. Even though the Ti:sapphire laser power does not necessarily fluctuate so strongly with small variations of the pump power, the effect is primarily observed in a temporal jitter in the timing of the first step laser pulses with respect to the second and third step and hence is reflected in a variation of the ion count rate.

The saturation of the system is directly proportional to the efficiency of the laser ionization process. When saturation is observed, the number of available atoms for ionization is comparable to the number of already ionized atoms and hence the efficiency can be considered to be high. In order to obtain more quantitative information, the effect of the volume of the gas cell on the saturation parameters needs to be considered. In our previous work on plutonium [5], the interplay between the laser ionization efficiency and the size of the gas cell volume was highlighted, however saturation curves could not be obtained due to a lack of information on the ionization scheme. In the

current studies on thorium the saturation curves illustrated in Fig. 6 can be used therefore to further this discussion.

In gas cell-based studies, which do not require a geometry optimized for the stopping of fusion-evaporation recoils, the gas cell volume can be reduced in order minimize ion loss mechanisms which are dependent on the extraction time, for example molecular formation or diffusion to the walls of the gas cell. However, a reduction of the gas cell volume also reduces the number of laser pulses that the atoms are exposed to thus impacting the total laser ionization efficiency. In general, by using a laser system operating with a high pulse energy but low repetition rate (200 Hz), the requirement that the atoms should be exposed at least once to the ionizing lasers before evacuation from the ionizing volume, should be fulfilled for maximum efficiency [37]. On the other hand, with modern solid state laser systems operating at high repetition rates (10 kHz) the energy per pulse is considerably lower and therefore the estimation of the minimum required volume depends on the probability of ionization in a single laser pulse. As the lifetimes of the excited atomic states in an ionization scheme are often considerably smaller than the time interval between laser pulses (in this work three lasers are used to ionize thorium, with a time interval between the synchronized pulses of  $100\mu\text{s}$ ), we can assume that consecutive laser pulses ionize the atoms independently. A simple relationship can be deduced between the minimum volume  $V_{\min}$  that the gas cell can have and the total laser ionization efficiency  $\epsilon_{\text{tot}}$  at a given laser repetition rate:

$$V_{\min} = \frac{t_{\text{rep}} C \ln(1 - \epsilon_{\text{tot}})}{\ln(1 - \epsilon_p)}, \quad (3)$$

where  $C$  is the conductance of the exit hole of the gas cell and  $t_{\text{rep}}$  is the shot-to-shot time interval between laser pulses. The important parameter in this relationship is the *single-shot efficiency*  $\epsilon_p$ , which defines the probability of ionizing a neutral atom at a specific laser intensity in a single train of synchronized laser light pulses. A similar relationship has been presented in a comparison between two different laser systems at the Leuven Isotope Separator On-Line (LISOL) facility in a study of the laser ionization of copper and cobalt [38]. The single-shot efficiency is a useful parameter to describe such a system as it is independent from the overall exposure time, the geometry and the environment in which the ionization occurs. Such a variable would be essential in simulations of laser resonance ionization within complicated gas cell geometries.

The total ionization efficiency  $\epsilon_{\text{tot}}$  can be determined by realizing that the efficiency of each laser ionization step is directly reflected in the saturation curves. The efficiency can be calculated from the measured count rate and the amplitude  $A_{\max}$  extracted from the fit of Eq. (4.2). By taking into account the background count rate, the total ionization efficiency can be calculated for a  $n$ -step ionization scheme:

$$\epsilon_{\text{tot}} = \prod_{i=1}^n \frac{A_{\text{exp},i} - A_{\text{bg},i}}{A_{\text{max},i} - A_{\text{bg},i}}, \quad (4)$$

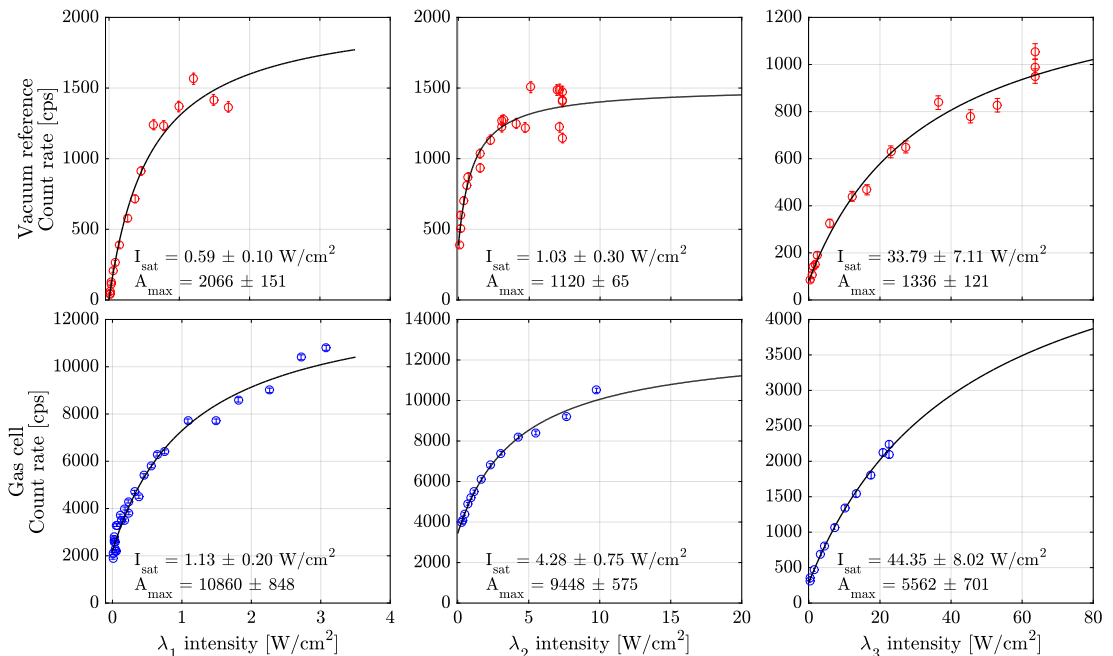


Figure 6: The saturation curves measured in the vacuum reference cell (top row) and in the gas cell (bottom row). All curves show a deviation from a linear behavior towards saturation.

where  $A_{\text{exp},i}$  is the experimentally achieved maximum count rate during the saturation measurement of the  $i^{\text{th}}$  excitation step. When the total ionization efficiency has been determined, the single-shot efficiency can be calculated via Eq. (4.2) if  $V_{\text{min}}$  can also be measured. Indeed, it is possible to extract a value for  $V_{\text{min}}$  by measuring the evacuation time profiles of the photo-ions from the gas cell. This is discussed in more detail in section 5.1.

This simple picture can be complicated by the fact that the flow trajectories the atoms take inside the gas cell may not intersect with the laser ionization volume (which in this work can be considered as a cylinder of laser light along the axis of the cell) until very close to the exit hole. This could lead to an overestimation of exposure of the atoms to the laser light and thus an underestimation of the single-shot efficiency. In particular, when there is a strong photo-ion loss mechanism such as molecular formation or recombination, the *effective volume* of ionization may be considerably smaller than the gas cell volume [39], or in other words, smaller than the minimum volume  $V_{\text{min}}$ . This would result in an artificially low single-shot efficiency when determined from the saturation curves. Thus it is important to try to estimate losses inside the gas cell or measure them by obtaining time profiles of the ions in order to calculate the effective volume.

Using the parameters obtained from the saturation curves

measured in the gas cell (Fig. 6), the total laser ionization efficiency according to Eq. (4.2),  $\epsilon_{\text{tot}}$ , is calculated to be 36%. Folding in the gas cell conductance, the laser repetition rate and the effective volume, determined in section 5.1 to be  $35 \text{ cm}^3$ , a single-shot efficiency  $\epsilon_p$  of about 0.08% can be calculated. This efficiency is obtained at laser pulse energy densities and laser spot diameters of  $0.3 \text{ mJ/cm}^2$  and  $3 \text{ mm}$  for the UV step,  $1.0 \text{ mJ/cm}^2$  and  $2.5 \text{ mm}$  for the second transition, and  $2.3 \text{ mJ/cm}^2$  and  $2 \text{ mm}$  for the final transition. It should be noted that the total and the single-shot ionization efficiencies presented here only apply to the atoms that are exposed to the laser radiation. They do not take into account losses of atoms for example to molecular species prior to ionization.

By slowly increasing the filament temperature, the maximum intensity of photo-ions using the  $^{232}\text{Th}$  dispensers at  $A/q=232$  was  $\sim 10^7$  ions/s, a yield which was dominated by  $^{232}\text{Th}^+$  ions. At such high intensities, observed using a Faraday cup, the longevity of the filament reduced to approximately 30 mins. However, for collinear laser spectroscopy experiments a yield of typically  $10^4$  ions/s is more than sufficient.

## 5. In-gas-cell processes and gas phase chemistry

The required high temperature of the filament for efficient evaporation of thorium atoms has the disadvantage that a considerable amount of contaminants is also evaporated from the

filament. This has been observed to be a more critical problem if the filament is not heated slowly and initially baked at a low temperature. The evaporating contaminants result in intense ion beams due to direct surface ionization (given a sufficiently low ionization potential) or non-resonant ionization by the UV laser light. The contaminant ions may undergo further chemical reactions or form adducts with impurities in termolecular reactions with the helium atoms inside the gas cell or downstream in the adiabatically expanding supersonic gas jet. As will be presented in this work, the mass-separated ion beam is formed of a large variety of molecular species, unfortunately often overlapping with the mass of interest.

To investigate the ionization of thorium and possible losses of ions through molecular formation reactions with the evaporated contaminants during evacuation from the gas cell, the dynamic behavior of the  $^{232}\text{Th}^+$  ions was investigated by mechanically chopping the laser light. To further study the chemistry occurring inside the gas cell, a series of mass spectra were recorded at the focal plane of the IGISOL separator at different stages of the filament heating.

### 5.1. Estimation of ion loss mechanisms from dynamic behavior

By measuring the temporal behavior of the ion time profiles when the laser light is periodically chopped, it is possible to probe for losses of the ions while they are transported inside the gas cell towards the exit hole [17]. Any strong loss mechanism will be imprinted onto the time profile as a shorter rise and fall time of the laser ion signal compared to the evacuation time of the gas cell. Figure 7 illustrates the time profiles of the thorium ions and its corresponding oxide, measured by connecting the MCP signal to a multi-channel analyzer, triggered by a timing signal from a labview control program which also controlled a TTL signal to the mechanical shutter. The overall timing cycle was 2.5 s of which 1.4 s was used to allow the UV laser radiation into the gas cell. Several hundreds of time profiles were recorded consecutively to obtain sufficient statistics for subsequent fitting and to ensure repeatability of the time profile.

We note that the spectra in Fig. 7 are dominated by the atomic  $^{232}\text{Th}^+$  ions and therefore indicate the high purity of the gas cell conditions. This is in clear contrast with time profiles obtained using plutonium-based filament dispensers [5] in which a source of impurities was suspected from a “dead” volume in the filament holder. In order to characterize the time profiles, rising and falling exponential decay curves were fitted to the data. The corresponding time parameter,  $\tau$ , is tabulated in Table 1. The falling edge of the profile describes the system evolving from a steady state of laser ionization and thus is a more natural parameter to use in the determination of an effective volume. The characteristic time  $\tau$  for  $\text{Th}^+$  ions presented in Table 1, 54.8 ms, can be converted to an effective volume of  $V_{\text{eff}} = C\tau = 35 \text{ cm}^3$  using the exit hole conductance  $C = 0.45d_t^2 \text{ [l/s]}$ , in which  $d_t$  is the exit hole throat diameter in mm. The effective volume matches very well with the the volume of the gas cell ( $\approx 30 \text{ cm}^3$ ), and therefore it can be concluded that there are no significant loss mechanisms to the atomic ions during evacuation from the gas cell. It is interesting to note that if a turbulent region of flow would exist inside the

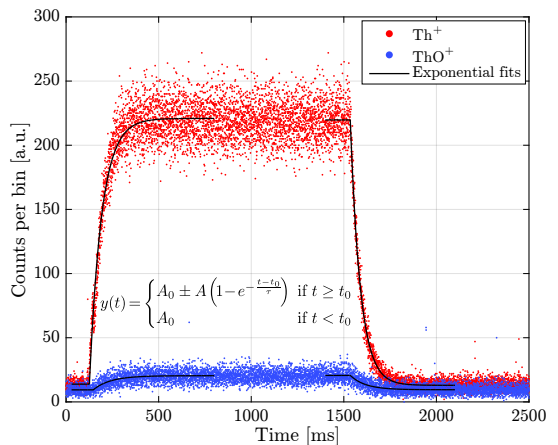


Figure 7: Dynamic behavior of the  $\text{Th}^+$  and  $\text{ThO}^+$  ion signal when the UV laser radiation is mechanically chopped. Growth and decay times are determined by fitting the rising (+) and falling (-) edges with an exponential decay function.

$\tau$ parameter	Rising	Falling
$\text{Th}^+$	$65.8 \pm 1.0 \text{ ms}$	$54.8 \pm 0.6 \text{ ms}$
$\text{ThO}^+$	$93 \pm 8 \text{ ms}$	$81 \pm 8 \text{ ms}$

Table 1: The parameter  $\tau$  of the rising and falling edges of  $\text{Th}^+$  and  $\text{ThO}^+$  time profiles extracted from the exponential fits of the data presented in Fig. 7.

gas cell, trapping the atomic ions for a longer period of time before extraction, then under the assumption of no molecular formation the effective volume could be larger than the gas cell volume.

The reason for the longer  $\tau$  parameters for the  $\text{ThO}^+$  molecule compared with the atomic  $\text{Th}^+$  is due to the formation process of the oxide. This proceeds initially from laser ionization of Th atoms followed by oxidation with a characteristic time constant  $\tau_{\text{mol}} = 1/([M]k_2)$ , defined by the  $\text{O}_2$  and  $\text{H}_2\text{O}$  impurity concentrations  $[M]$  and the bimolecular reaction rates  $k_2 = 1.12 \cdot 10^{-9} \text{ cm}^3/\text{s}$  and  $k_2 = 5.70 \cdot 10^{-10} \text{ cm}^3/\text{s}$ , respectively [40]. The obtained time parameters for  $\text{ThO}^+$  are a convolution of the gas cell evacuation time with the molecular formation time. In this case, if one converted the molecular time constant  $\tau$  into an effective volume, it would result in a larger volume than the physical volume of the gas cell. This simply indicates that, firstly, molecular formation is not a dominant loss mechanism in this experiment and, secondly, that the gas flow in the cell is not fully laminar. This is unsurprising due to the presence of the filament feedthroughs.

### 5.2. Mass spectra from a $^{232}\text{Th}$ filament

Figure 8 shows mass spectra recorded in the mass region  $A/q$  from 230 to 290, with (solid red and blue lines) and without (solid black line) the UV laser radiation entering the gas cell while a  $^{232}\text{Th}$  filament dispenser was being heating at a tem-

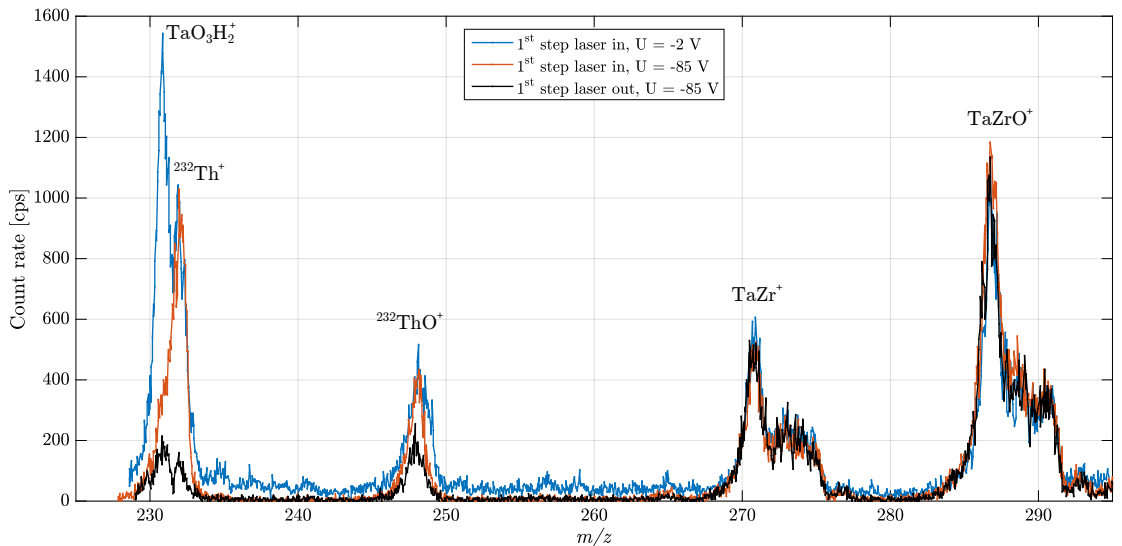


Figure 8: Mass spectra recorded at the focal plane of the IGISOL separator while using a  $^{232}\text{Th}$  filament dispenser. The red solid line shows the effect of the resonant laser ionization enhancing the yield of thorium and its corresponding oxide in comparison to the mass spectrum obtained with the UV laser radiation blocked (black solid line). A mass spectrum with laser ionization and without molecular suppression is shown as a blue solid line. For more details see text.

perature of  $\sim 2000^\circ\text{C}$ . A clear enhancement of the ion signal is seen at  $A/q = 232$  corresponding to a successful laser ionization of  $^{232}\text{Th}$  atoms. At 16 mass units above atomic thorium a mass peak is observed which corresponds to  $\text{ThO}^+$ . Although the molecule is not expected to be ionized directly by the lasers, there is a noticeable response to the laser radiation, which reflects formation of  $\text{ThO}^+$  following laser ionization of neutral thorium atoms. Impurities seen at even higher masses, for example above  $A/q=270$ , usually do not respond to the laser radiation although occasionally an increase was seen indicating non-resonant ionization of molecules by the UV laser radiation.

Even without the UV laser radiation of the first resonant step, mass peaks corresponding to  $A/q=232$  and  $A/q=248$  can be identified, implying that either some impurity is present at those mass values or, more likely, that the thorium and its oxide in the filament are being ionized through a non-resonant process. This has the effect of reducing the selectivity provided by laser resonance ionization. The only conceivable process to account for this would be surface ionization at the hot filament.

The Saha-Langmuir equation may be used to estimate the fraction of atoms evaporating as ions [41]. By combining the work functions of tantalum ( $\phi^- = 4.25 \text{ eV}$  [42]) and zirconium ( $\phi^- = 4.05 \text{ eV}$  [43]) as well as the ionization potentials of Th ( $6.3067 \text{ eV}$  [44]) and ThO ( $6.1 \text{ eV}$  [45]) results, however, in only small fractions produced ( $n_{+1}/n_0 \ll 10^{-4}$ ). As the ratio of photo-ion to non-resonant ions at  $A/q = 232$  is approximately 10, having such a low  $n_{+1}/n_0$  fraction would indicate quite a low total laser ionization efficiency. The exact work function, however, is difficult to estimate. For ion emission  $\phi^+$  is usually

higher than the electronic  $\phi^-$  especially for polycrystalline surfaces, and the work function can be significantly increased due to adsorption of electronegative elements such as oxygen which is known to be present as an impurity [46]. There is therefore a possibility that the work function is over  $1 \text{ eV}$  higher than the values stated above leading to significant surface ionization of Th and ThO ( $n_{+1}/n_0 = 10^{-2}$ ). A more quantitative estimation is difficult to provide because the sample conditions are not known accurately.

When the measured yield of mass-separated impurities became significant around the thorium mass region, an accelerating potential immediately after the gas cell was introduced and was used to suppress the transmission of these beams. This was realized by applying a larger negative voltage on the front electrode of the radiofrequency sextupole ion guide (SPIG) [47], which captures and guides the ion beam from the gas cell towards the  $30 \text{ keV}$  acceleration stage of the IGISOL separator. The typical operating voltage of this first electrode is a few volts below zero (used in the mass scan with laser ionization shown by the solid blue line of Fig. 8). By providing additional kinetic energy to the ions in the supersonic jet region, often complete suppression of the molecular ion signal was observed without a pronounced decrease in the atomic ion signal. In connection to Fig. 8, an applied voltage of  $-85 \text{ V}$  was used for the mass scans represented by the red and black solid lines. The background count rates seen with this voltage are clearly lower and an additional intense mass peak visible at  $A/q=231$ , postulated to arise from  $\text{TaO}_3\text{H}_2^+$ , has been suppressed. We note that intense beams of  $\text{Ta}^+$ ,  $\text{TaO}^+$  and  $\text{TaO}_2^+$  were seen concurrently along

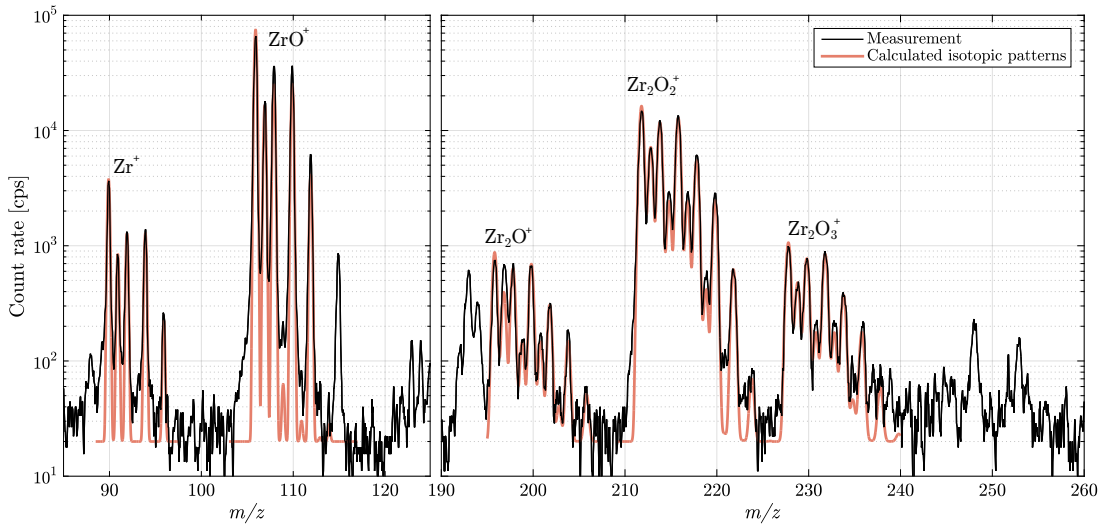


Figure 9: A mass spectrum using a  $^{229}\text{Th}$  filament dispenser. Considerable amounts of zirconium and its oxide are being produced and ionized at the filament, and heavier clusters can also be seen. Each identified molecule is shown with its calculated isotopic pattern highlighting a good concordance.

with frequent water adduct formation and that  $\text{TaO}_3\text{H}_2^+$  and related compounds have been observed experimentally [48]. The impurities seen at  $A/q=271$  and 287, which can be attributed to  $\text{TaZr}^+$  and  $\text{TaZrO}^+$  according to the mass values and isotopic patterns, do not exhibit any evidence of suppression.

Initially the suppression of molecules was attributed to collision induced dissociation (CID) as this mechanism has been reported in connection with gas cells in similar configurations [49–51]. Even though the helium atoms have a light mass, with a sufficiently strong potential some molecules may be broken up if the bond dissociation energy (BDE) is low. It is, however, increasingly difficult to perform CID when the mass of the molecule increases and when the buffer gas consists of light atoms. A more qualitative picture of the mechanisms leading to the observed suppression of larger molecular contaminants is provided in [52]. Detailed simulations indicate that molecules are not dissociated as previously assumed, rather a close relationship between the collision cross section and the acceleration potential applied within the helium gas jet environment leads to a mass-selective (geometrical size) suppression.

### 5.3. Results from $^{229}\text{Th}$ drip-dry filament dispensers

The set of  $^{229}\text{Th}$  dispensers were also investigated in the gas cell in same configuration as described for the  $^{232}\text{Th}$  filaments. As indicated in Fig. 3, the drip-dry method for the application of  $^{229}\text{Th}$  onto the tantalum substrate resulted in a considerable build-up of material over a larger surface area compared with the  $^{232}\text{Th}$  dispensers. As a result, the contaminant concentration was notably higher, and a large yield of zirconium and its oxide compounds was seen evaporating and being surface-ionized at the filament. Figure 9 indicates two mass regions of interest

recorded at a filament temperature close to  $2000^\circ\text{C}$ . In the lower mass region ion beams of  $\text{Zr}^+$  and its oxide  $\text{ZrO}^+$  are observed, while in the higher mass region three other zirconium oxide compounds  $\text{Zr}_2\text{O}^+$ ,  $\text{Zr}_2\text{O}_2^+$  and  $\text{Zr}_2\text{O}_3^+$  are highlighted. These compounds form the majority of the impurity signal detected from these filaments. For each compound the natural isotopic pattern for zirconium was calculated and plotted as normalized curves overlaid with the experimental mass spectra, precisely matching the mass peaks and thus validating the mass identification.

This illustrates the problem that can arise if elements having a high number of stable isotopes are used in filament-based dispensers in combination with a significant number of impurities transferred in the preparation of the source. Although the mass peaks of the zirconium isotopes (used as the required reducing agent) and corresponding oxides are not at the same nominal mass as  $^{229}\text{Th}^+$  and  $^{232}\text{Th}^+$ , the combination of dimerization and additional molecular formation leads to wide isotopic patterns, which in this case overlapped with the expected thorium mass peaks. Even with the additional acceleration voltage used to suppress the transmission of molecules the background was simply too high to see any signal of either  $^{229}\text{Th}^+$  or  $^{232}\text{Th}^+$ . Additionally, the large concentration of nitrate and water transferred due to the repeated drip-dry process appears to have oxidized the reducing zirconium layer, evident from the amount of detected zirconium oxide. This might have reduced or hindered the oxygen absorption by the zirconium layer resulting in the thorium being released only in oxide form, which would not be affected by the laser ionization process.



## 6. References

- [1] P. Campbell, I. Moore, and M. Pearson. *Progress in Particle and Nuclear Physics*, **86**, (2016) 127. doi:https://doi.org/10.1016/j.pnpnp.2015.09.003.
- [2] I. Moore, P. Dendooven, and J. Ärje. *Hyperfine Interactions*, **223**(1-3), (2014) 17. doi:10.1007/s10751-013-0871-0.
- [3] B. Cheal and D. Forest. *Hyperfine Interactions*, **223**(1-3), (2014) 223. doi:10.1007/s10751-012-0621-8. Cited By 1.
- [4] M. Reponen, I. Moore, I. Pohjalainen, V. Sonnenschein, and A. Jokinen. *Nuclear Instruments and Methods in Physics Research Section B: Beam Interactions with Materials and Atoms*, **317**, (2013) 422. doi:https://doi.org/10.1016/j.nimb.2013.05.061. XVth International Conference on ElectroMagnetic Isotope Separators and Techniques Related to their Applications, December 2–7, 2012 at Matsue, Japan.
- [5] I. Pohjalainen, I. Moore, T. Kron, S. Raeder, V. Sonnenschein, H. Tomita, N. Trautmann, A. Voss, and K. Wendt. *Nucl. Instrum. Methods Phys. Res., Sect. B*, **376**, (2016) 233. doi:10.1016/j.nimb.2016.02.019.
- [6] A. Voss, V. Sonnenschein, P. Campbell, B. Cheal, T. Kron, I. D. Moore, I. Pohjalainen, S. Raeder, N. Trautmann, and K. Wendt. *Phys. Rev. A*, **95**, (2017) 032506. doi:10.1103/PhysRevA.95.032506.
- [7] B. R. Beck, J. A. Becker, P. Beiersdorfer, G. V. Brown, K. J. Moody, J. B. Wilhelmy, F. S. Porter, C. A. Kilbourne, and R. L. Kelley. *Phys. Rev. Lett.*, **98**, (2007) 142501. doi:10.1103/PhysRevLett.98.142501.
- [8] B. R. Beck, C. Wu, P. Beiersdorfer, G. V. Brown, J. A. Becker, K. J. Moody, J. B. Wilhelmy, F. S. Porter, C. A. Kilbourne, and R. L. Kelley. *Proceedings - 12th International Conference on Nuclear Reaction Mechanisms, LNBL-PROC*, (2009) 415170.
- [9] E. Peik and C. Tamm. *EPL (Europhysics Letters)*, **61**(2), (2003) 181.
- [10] C. J. Campbell, A. G. Radnaev, A. Kuzmich, V. A. Dzuba, V. V. Flambaum, and A. Derevianko. *Phys. Rev. Lett.*, **108**, (2012) 120802. doi:10.1103/PhysRevLett.108.120802.
- [11] L. von der Wense, B. Seiferle, M. Laatiaoui, J. B. Neumayr, H.-J. Maier, H.-F. Wirth, C. Mokry, J. Runke, K. Eberhardt, C. E. Düllmann, N. G. Trautmann, and P. G. Thirlof. *Nature*, **533**, (2016) 47. doi:10.1038/nature17669.
- [12] B. Seiferle, L. von der Wense, and P. G. Thirlof. *Phys. Rev. Lett.*, **118**, (2017) 042501. doi:10.1103/PhysRevLett.118.042501.
- [13] J. Thielking, M. V. Okhapkin, P. Glowacki, D. M. Meier, L. von der Wense, B. Seiferle, C. E. Düllmann, P. G. Thirlof, and E. Peik. *Nature*, **556**(7701), (2018) 321. doi:10.1038/s41586-018-0011-8.
- [14] V. Sonnenschein, S. Raeder, A. Hakimi, I. D. Moore, and K. Wendt. *J. Phys. B: At., Mol. Opt. Phys.*, **45**(16), (2012) 165005. doi:10.1088/0953-4075/45/16/165005.
- [15] F. F. Karpeshin and M. B. Trzhaskovskaya. *Phys. Rev. C*, **76**, (2007) 054313. doi:10.1103/PhysRevC.76.054313.
- [16] S. G. Porsev, V. V. Flambaum, E. Peik, and C. Tamm. *Phys. Rev. Lett.*, **105**, (2010) 182501. doi:10.1103/PhysRevLett.105.182501.
- [17] T. Kessler, I. Moore, Y. Kudryavtsev, K. Peräjärvi, A. Popov, P. Ronkanen, T. Sonoda, B. Tordoff, K. Wendt, and J. Äystö. *Nucl. Instrum. Methods Phys. Res., Sect. B*, **266**(4), (2008) 681. doi:https://doi.org/10.1016/j.nimb.2007.11.076.
- [18] Y. Kudryavtsev, T. Cocolios, J. Gentens, M. Huyse, O. Ivanov, D. Pauwels, T. Sonoda, P. V. den Bergh, and P. V. Duppen. *Nuclear Instruments and Methods in Physics Research Section B: Beam Interactions with Materials and Atoms*, **267**(17), (2009) 2908. doi:https://doi.org/10.1016/j.nimb.2009.06.013.
- [19] Y. Hirayama, Y. Watanabe, N. Imai, H. Ishiyama, S.-C. Jeong, H. Miyatake, M. Oyaizu, Y. H. Kim, M. Mukai, Y. Matsuo, T. Sonoda, M. Wada, M. Huyse, Y. Kudryavtsev, and P. V. Duppen. *Nuclear Instruments and Methods in Physics Research Section B: Beam Interactions with Materials and Atoms*, **317**, (2013) 480. doi:https://doi.org/10.1016/j.nimb.2013.06.032. XVth International Conference on ElectroMagnetic Isotope Separators and Techniques Related to their Applications, December 2–7, 2012 at Matsue, Japan.
- [20] M. Laatiaoui, W. Lauth, H. Backe, M. Block, D. Ackermann, B. Cheal, P. Chhetri, C. E. Düllmann, P. van Duppen, J. Even, R. Ferrer, F. Giacoppo, S. Götz, F. P. Heßberger, M. Huyse, O. Kaleja, J. Khuyagbaatar, P. Kunz, F. Lautenschläger, A. K. Mistry, S. Raeder, E. M. Ramirez, T. Walther, C. Wraith, and A. Yakushev. *Nature*, **538**, (2016) 495 EP.
- [21] I. Pohjalainen, I. D. Moore, T. Eronen, A. Jokinen, H. Penttilä, and S. Rinta-Antila. *Hyperfine Interact.*, **227**(1-3), (2014) 169. doi:10.1007/s10751-013-1006-3.
- [22] M. Santos, J. Marçalo, A. P. de Matos, J. K. Gibson, and R. G. Haire. *The Journal of Physical Chemistry A*, **106**(31), (2002) 7190.
- [23] B. Eichler, S. Huebener, N. Erdmann, K. Eberhardt, H. Funk, G. Herrmann, S. Koehler, N. Trautmann, G. Passler, and F.-J. Urban. *Radiochim. Acta*, **79**(4), (1997) 221. doi:10.1524/ract.1997.79.4.221.
- [24] E. Tretyakov, N. Tretyakova, V. Konyaev, Y. Khrudev, A. Beda, G. Kartashev, and I. Vishnevskii. *Bull. Acad. Sci. USSR, Phys. Ser.* **34**, (1971) 763.
- [25] G. Ardisson, J. Gasparro, V. Barci, and R. K. Sheline. *Phys. Rev. C*, **62**, (2000) 064306. doi:10.1103/PhysRevC.62.064306.
- [26] R. K. Sheline, C. F. Liang, and P. Paris. *Phys. Rev. C*, **51**, (1995) 1192. doi:10.1103/PhysRevC.51.1192.
- [27] J. Chen and F. Kondev. *Nuclear Data Sheets*, **126**, (2015) 373. doi:https://doi.org/10.1016/j.nds.2015.05.003.
- [28] B. Eichler, C. Frink, N. Trautmann, and G. Herrmann. *Fresenius' Zeitschrift für analytische Chemie*, **335**(7), (1989) 656. doi:10.1007/BF01204066.
- [29] S. Dash, M. Kamruddin, P. Ajikumar, A. Tyagi, B. Raj, S. Bera, and S. Narasimhan. *J. Nucl. Mater.*, **278**(2), (2000) 173. doi:10.1016/S0022-3115(99)00261-5.
- [30] G. A. Hussein and H. M. Ismail. *Colloids Surf., A*, **99**(2), (1995) 129. doi:10.1016/0927-7757(95)03089-V.
- [31] V. N. Fedosseev, Y. Kudryavtsev, and V. I. Mishin. *Physica Scripta*, **85**(5), (2012) 058104.
- [32] B. A. Marsh. *Review of Scientific Instruments*, **85**(2), (2014) 02B923. doi:10.1063/1.4858015.
- [33] M. Reponen, I. D. Moore, T. Kessler, I. Pohjalainen, S. Rothe, and V. Sonnenschein. *Eur. Phys. J. A*, **48**, (2012) 45. doi:10.1140/epja/i2012-12045-2.
- [34] Y. Liu and D. Stracener. *Nucl. Instrum. Methods Phys. Res., Sect. B*, **376**, (2016) 68. doi:10.1016/j.nimb.2015.12.015.
- [35] S. Raeder, V. Sonnenschein, T. Gottwald, I. D. Moore, M. Reponen, S. Rothe, N. Trautmann, and K. Wendt. *J. Phys. B: At., Mol. Opt. Phys.*, **44**(16), (2011) 165005. doi:10.1088/0953-4075/44/16/165005.
- [36] V. Sonnenschein, I. D. Moore, I. Pohjalainen, M. Reponen, S. Rothe, and K. Wendt. *Intracavity Frequency Doubling and Difference Frequency Mixing for Pulsed ns Ti:Sapphire Laser Systems at On-Line Radioactive Ion Beam Facilities*, chapter 209. doi:10.7566/JSPSCP.6.030126.
- [37] Y. Kudryavtsev, J. Andrzejewski, N. Bijnens, S. Franchoo, J. Gentens, M. Huyse, A. Piechaczek, J. Szerypio, I. Reusen, P. V. Duppen, P. V. den Bergh, L. Vermeeren, J. Wauters, and A. Wöhr. *Nucl. Instr. and Meth. in Phys. Res. B*, **114**, (1996) 350.
- [38] R. Ferrer, V. Sonnenschein, B. Bastin, S. Franchoo, M. Huyse, Y. Kudryavtsev, T. Kron, N. Leccese, I. Moore, B. Osmond, D. Pauwels, D. Radulov, S. Raeder, L. Rens, M. Reponen, J. Roßnagel, H. Savajols, T. Sonoda, J. Thomas, P. V. den Bergh, P. V. Duppen, K. Wendt, and S. Zemlyanov. *Nucl. Instrum. Methods Phys. Res., Sect. B*, **291**, (2012) 29. doi:10.1016/j.nimb.2012.08.023.
- [39] I. D. Moore, T. Kessler, T. Sonoda, Y. Kudryavtsev, K. Peräjärvi, A. Popov, K. D. A. Wendt, and J. Äystö. *Nucl. Instrum. Methods Phys. Res., Sect. B*, **268**(6), (2010) 657. doi:10.1016/j.nimb.2009.12.001.
- [40] H. H. Cornehl, R. Wesendrup, M. Diefenbach, and H. Schwarz. *Chem. - Eur. J.*, **3**(7), (1997) 1083. doi:10.1002/chem.19970030716.
- [41] M. J. Dresser. *Journal of Applied Physics*, **39**(1), (1968) 338. doi:10.1063/1.1655755.
- [42] R. G. Wilson. *J. Appl. Phys.*, **37**(8), (1966) 3170. doi:10.1063/1.1703180.
- [43] D. E. Eastman. *Phys. Rev. B*, **2**, (1970) 1. doi:10.1103/PhysRevB.2.1.
- [44] N. Trautmann. *J. Alloys Compd.*, **213**(Supplement C), (1994) 28. doi:10.1016/0925-8388(94)90876-1.
- [45] E. G. Rauh and R. J. Ackermann. *J. Chem. Phys.*, **60**(4), (1974) 1396. doi:10.1063/1.1681210.
- [46] H. Kawano. *Prog. Surf. Sci.*, **83**(1), (2008) 1. doi:10.1016/j.progsurf.2007.11.001.
- [47] P. Karvonen, I. Moore, T. Sonoda, T. Kessler, H. Penttilä, K. Peräjärvi, P. Ronkanen, and J. Äystö. *Nucl. Instrum. Methods Phys. Res., Sect. B*, **266**(21), (2008) 4794. doi:10.1016/j.nimb.2008.07.022.
- [48] S. Zhou, J. Li, M. Schlagen, and H. Schwarz. *Angewandte Chemie International Edition*, **55**(25), (2016) 7257. doi:10.1002/anie.201601965.
- [49] S. Raeder, B. Bastin, M. Block, P. Creemers, P. Delahaye, R. Ferrer,

- X. Fléchar, S. Franchoo, L. Ghys, L. Gaffney, C. Granados, R. Heinke, L. Hijazi, M. Huyse, T. Kron, Y. Kudryavtsev, M. Laatiaoui, N. Leecesne, F. Luton, I. Moore, Y. Martinez, E. Mogilevskiy, P. Naubereit, J. Piot, S. Rothe, H. Savajols, S. Sels, V. Sonnenschein, E. Traykov, C. V. Beveren, P. V. den Bergh, P. V. Duppen, K. Wendt, and A. Zadornaya. Nuclear Instruments and Methods in Physics Research Section B: Beam Interactions with Materials and Atoms, **376**, (2016) 382 . doi:<https://doi.org/10.1016/j.nimb.2015.12.014>. Proceedings of the XVIth International Conference on Electromagnetic Isotope Separators and Related Topics (EMIS2015), Grand Rapids, MI, U.S.A., 11-15 May 2015.
- [50] Y. Kudryavtsev, B. Bruyneel, M. Huyse, J. Gentens, P. V. den Bergh, P. V. Duppen, and L. Vermeeren. Nucl. Instrum. Methods Phys. Res., Sect. B, **179**(3), (2001) 412. doi:10.1016/S0168-583X(01)00575-4.
- [51] P. Van Duppen, B. Bruyneel, M. Huyse, Y. Kudryavtsev, P. Van Den Bergh, and L. Vermeeren. Hyperfine Interact., **127**(1), (2000) 401. doi:10.1023/A:1012657431795.
- [52] I. Pohjalainen. *Gas-phase chemistry, recoil source characterization and in-gas-cell resonance laser ionization of actinides at IGSOL*. Ph.D. thesis, University of Jyväskylä, 2018.

## 5.3 Laser ion source and resonant ionization of thorium

The details of using laser resonance ionization to create a laser ion source for thorium evaporated from filament dispensers is described in detail in article III as well as more general aspects in article II. Here, additional information and studies on the in-gas-cell ionization of thorium and its ionization scheme are presented.

### 5.3.1 Thorium ionization scheme

Laser ionization of thorium from filament-based dispensers was performed in the actinide gas cell in the same manner as with the plutonium filaments, but with hotter filament temperatures. With thorium, approximately 2300 K is required to achieve sufficient evaporation. The ionization scheme was developed by Y. Liu and D. Stracener [152] and consists of three resonant excitation steps as indicated in Fig. 5.1. A UV excitation at 372.049 nm excites thorium from its atomic ground state  $6d^27s^2\ ^3F_2$  to an excited state  $6d^27s7p\ ^3G_3^o$ . Two infrared transitions at wavelengths 827.987 nm and 831.67 nm further excite the thorium to an AI state at  $50980.96\ \text{cm}^{-1}$ , above the thorium IP at  $50867\ \text{cm}^{-1}$ .

The figure also depicts pathways across the IP which can occur with the first step UV laser only. As the first step excitation energy is above half of the IP, non-resonant ionization happens with the UV radiation. We have also identified a transition from the excited  $5f6d7s^2\ ^3G_3^o$  state to the  $37405_3$  level having almost exactly the same energy as the first step with a difference of only 1 GHz, well within the laser linewidth.

Experimentally it was observed that approximately 60% of the resulting ion count rate is due to first-step only ionization. This could be direct non-resonant ionization from the first excited level or, if collisions between thorium and helium atoms are quenching its population to the  $5f6d7s^2\ ^3G_3^o$  level, the ionization can happen through the secondary path. It is worth noting that if there is a significant ionization through the secondary path, this would be strikingly analogous to that of plutonium as described in chapter 4. However, in the case of thorium the two infrared steps do have a notable contribution to the count rate suggesting either stronger infrared transitions or weaker collisional quenching compared that of plutonium.

One supporting observation to indicate that the UV-only ionization happens through the secondary path via collisional quenching comes from vacuum-mode laser resonance ionization. When the thorium ionization scheme was investigated in vacuum by heating a sample to a sufficiently high temperature in a tantalum

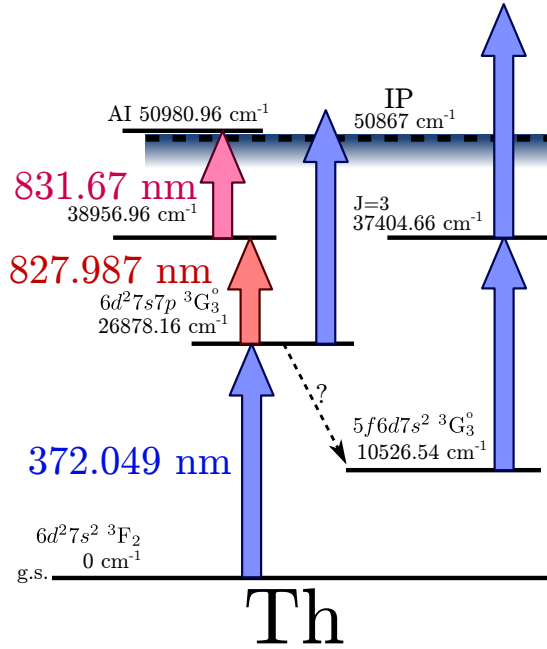


**Figure 5.1.** The UV-IR-IR laser ionization scheme for thorium based on work performed in reference [152]. Additional pathways to ionization using only the first step UV radiation are shown. The dashed line depicts the tentative collisional de-excitation by the buffer gas atoms.

oven (explained in detail in article III), only 2% of the total signal was measured with the UV-only scheme. Similar results were obtained in the study of laser ionization of thorium at Oak Ridge National Laboratory [152]. In that work the same UV-IR-IR scheme was applied in vacuum, in a hot cavity ion source. In comparison to the full ionization scheme, when the UV-only ionization was recorded, the ion rate was less than 1% of the total [153]. As the vacuum-mode ionization as well as the in-gas-cell ionization are both operating at or near saturation in all resonant steps, the considerably higher UV-only ionization in the gas cell suggests that it occurs via the  $5f6d7s^2\ ^3G_3^o \rightarrow 37404_3$  transition.

### 5.3.2 First excitation step wavelength spectra

While the resonant nature of the laser resonance ionization of thorium and plutonium was confirmed by performing frequency scans of the excitation steps, the first step resonance sometimes showed conspicuously anomalous behavior. If the first step laser power is reduced significantly, a normal behavior of the resonance transition is observed as seen in the spectra obtained using UV laser

powers of 0.4 mW and 1.3 mW, illustrated in Fig. 5.2. However, when the laser power is increased to the maximum, the resonance becomes extremely wide, sometimes approaching 100 GHz. Interestingly, such a broad structure was only observed in the first step frequency scans. The second and third IR step did not exhibit a similar behavior. An identical behavior was also observed in plutonium as shown in Fig. 5.3 with approximately the same level of broadening. The striking feature of these broad resonance structures is the “dip” in the middle, which happens exactly at the resonant frequency of the transition. A further notable feature is the slight asymmetry of the structure, which is visible particularly in Fig. 5.2. The structure also seems to be present in the grating-based laser scan of Fig. 4.9, explaining why the first step resonance appears to be absent in the grating spectrum with the pump laser blocked.

Broad resonances are often attributed to either Doppler broadening or power broadening effects. Doppler broadening is an inhomogeneous effect and results from a Maxwell-Boltzmann distribution of velocities dependent on the temperature of the atoms. However, via Eq. (2.11), even if the filament temperature was raised to 3000 K, the broadening would only be  $\sim 2$  GHz for heavy elements. If the laser ionization happens near the nozzle of the gas cell, in the region where the gas flow is already approaching sonic velocity, there might be a significant Doppler shift in the resonance frequency. This shift could become considerable if the filament temperature is hot and the buffer gas is being strongly heated as the speed of sound has a square root dependence on the temperature. By combining Eqs. (2.16) and (2.10), an estimation for the maximum broadening due to this effect is  $\sim 10$  GHz. Power broadening on the other hand is a homogeneous effect thus it addresses all atoms uniformly. It is known that for strong transitions, a high laser intensity can lead to a very broad Lorentzian linewidth and thus in both plutonium and thorium the large spectroscopic linewidths may be primarily attributed to this effect [154]. Unfortunately, in this work, we do not have intermediate scans between the 1.3 mW and 28.3 mW data of Fig. 5.2 and therefore a series of frequency scans at increasing UV laser intensity should be considered in the future to explore this mechanism further. We note that pressure (collision) broadening is also homogeneous and for resonant transitions, at least for lighter elements, occurs at the level of  $\sim 10$  MHz/mbar [37, 155, 156]. Assuming a similar pressure broadening coefficient for this work, only  $\sim 1$  GHz is obtained in a gas pressure environment of 80 mbar contributing only a small fraction of the UV resonance linewidth.

Due to the homogeneous nature of the power broadening effect it cannot explain the visible dips seen in Figs. 5.2 and 5.3. We therefore propose that these peculiar features may be explained by a specific combination of inhomogeneous Doppler broadening coupled with the propagation of laser light within the gas cell. In so-called saturation absorption spectroscopy experiments, a narrow bandwidth laser is used to probe Doppler-broadened atoms in a vapor cell with “pump” and “probe” beams spatially overlapped in counter-propagating

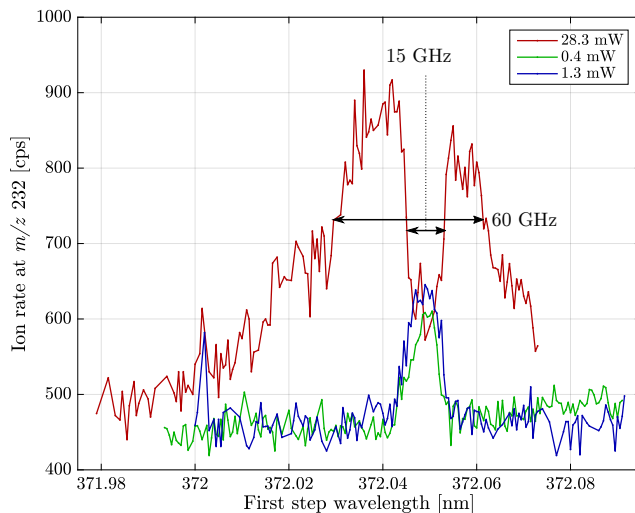


**Figure 5.2.** Wavelength scans of the UV transition in the ionization scheme of thorium at three different laser powers. At high power (28.3 mW), the count rate does not increase at the resonance wavelength but shows an unusual behavior with a dip at the resonance position and high yield on both sides.

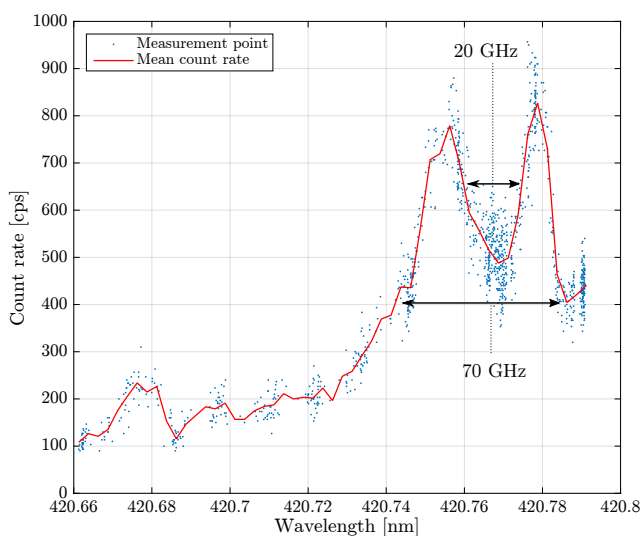


**Figure 5.3.** Wavelength scan of the 420.77 nm transition in the ionization scheme of plutonium. The red line shows the averaged data. The same kind of behavior as in thorium is observed with the dip also exactly at the resonance position.

directions. This method of spectroscopy is Doppler-free as the same atomic velocity class of atoms is addressed when they move perpendicular to the laser beams. The dominant pump beam excites many atoms while the effect of the weaker (counter-propagating) probe beam is very small; the population has already been driven into saturation and therefore the probe is only weakly absorbed. This results in a so-called Lamb dip in the Doppler-broadened profile which, with a sufficiently narrowband laser, has a Doppler-free linewidth, in other words the natural linewidth limit is achieved [31, 157].

To translate such a picture to the gas cell, one must realize that the inner surface of the exit nozzle is rather reflective and thus a considerable fraction of the laser light is reflected back in a counter-propagating direction to the general flow of the atoms. If a sufficiently large combination of inhomogeneous Doppler broadening effects exceed the laser linewidth, a similar cancellation of Doppler-shifted velocities can foreseeably occur. The difference to “standard” saturation absorption spectroscopy in vapor cells is that we observe the cancellation as a drop in the ion count rate. In the atomic system of both thorium and plutonium, as well likely in other elements exhibiting high atomic level densities, a single UV laser at a resonant transition (in thorium the laser is in fact driving two resonant transitions), combined with collisional de-excitation of an excited level, ultimately couples to the continuum. We therefore propose that it is via the final coupling of the laser which both probes a selected class of atomic velocities while in parallel ionizes the atoms, leads to the observable drop in the ion rate at the resonance frequency.

We have performed a literature search to investigate other possible phenomena which could explain these effects. For example, similar drops in absorption have been observed at resonance frequencies in connection to coherent atomic phenomena such as electromagnetically induced transparency [158]. Such effects cannot be ruled out, however no adequate three-level system, which is a requirement, has been found in this work. If indeed the dip structure is correlated to a “pump - probe” effect one method to answer this would be to coat the inner surface of the gas cell to reduce any possible reflection of laser light. Additional studies in the vacuum reference cell could also be performed with  $^{232}\text{Th}$  in order to verify the rather low ionization probability in vacuum, measured in this work to be  $\sim 2\%$  of the three-step scheme. In order to mimic the effect of collisional quenching as depicted in Fig. 5.1, a transition between the initial and final states involved in the quenching could be resonantly driven with an additional laser tuned to 611.560 nm, as long as the transition is not too forbidden.

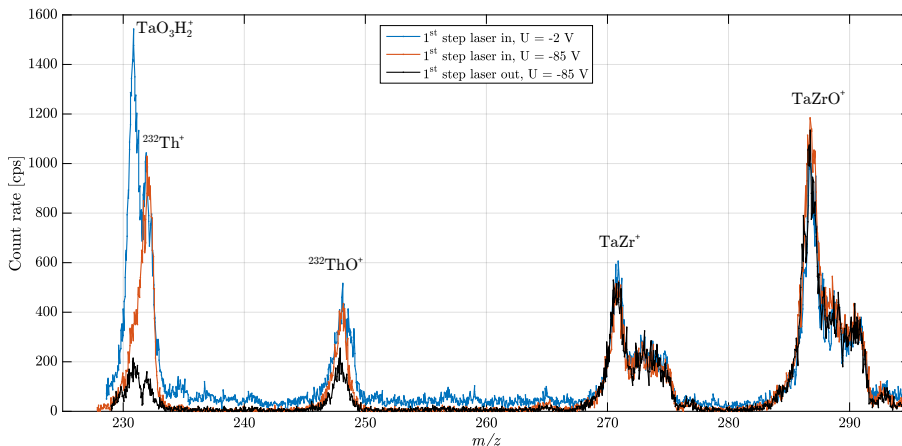


**Figure 5.4.** Mass spectra recorded at the focal plane of the IGISOL separator during the laser ionization of  $^{232}\text{Th}$  evaporated from a filament dispenser. The spectrum plotted in blue shows the signal obtained without the accelerating potential ( $U = -2$  V), whereas the red spectrum is the result of lowering the potential ( $U = -85$  V). The mass spectrum reproduced as a solid black line has been obtained with the UV laser blocked and is given as a reference.

## 5.4 Suppression of molecular contaminants by size-exclusion

During the laser ionization of thorium evaporated from filament-based dispensers, intense molecular contaminant beams were observed in the mass region of interest in particular with the filaments produced by the thorium nitrate drip-dry method. Occasionally such contaminants completely overwhelmed the resonant laser ion signal of thorium and therefore an accelerating potential immediately after the gas cell was introduced by applying an increasingly negative voltage on the front electrode of the radiofrequency sextupole ion guide (SPIG) [99]. The induced acceleration of ions through the high density region of the supersonic helium gas jet often resulted in a complete suppression of the molecular ions without a pronounced decrease in the atomic ion signal.

### 5.4.1 Mass spectra and identification of impurities

In Fig. 5.4 the effect of suppression of a molecular ion is illustrated by plotting the mass spectra recorded with and without the additional potential. The blue solid line shows the signal obtained without suppression in normal operational conditions ( $\sim -2$  V applied to the front electrode) while the red solid line shows



the mass spectrum with the same conditions except for the potential of the front electrode which has been lowered to -85 V. The count rate at  $A/q=231$  is clearly reduced when the potential is lowered. Both spectra are obtained during the laser ionization process. The black solid line has been obtained when the first resonant step laser is blocked.

The peak at  $A/q=231$  is assigned to the complex molecule  $\text{TaO}_3\text{H}_2^+$ , formed via an association reaction between  $\text{TaO}_2^+$  and  $\text{H}_2\text{O}$ . The mass identity has been surmised because beams of  $\text{Ta}^+$ ,  $\text{TaO}^+$  and  $\text{TaO}_2^+$  were seen concurrently along with frequent water adduct formation. In addition,  $\text{TaO}_3\text{H}_2^+$  and related compounds have been observed experimentally [159]. The impurities seen at  $A/q=271$  and 287, which can be attributed to  $\text{TaZr}^+$  and  $\text{TaZrO}^+$  according to the mass values and isotopic patterns, do not exhibit any evidence of suppression.

#### 5.4.2 Consideration of collision induced dissociation

Initially the suppression of molecules was attributed to collision induced dissociation (CID) as this mechanism has been reported to have been used with gas cells in similar configurations [123, 78, 14]. Even though the helium atoms have a light mass, with a sufficiently strong potential some molecules may be broken up if the bond dissociation energy (BDE) is low enough. It is, however, increasingly difficult to perform CID when the mass of the molecule increases and when the buffer gas consists of light atoms as demonstrated in the following.

In order to have a more qualitative picture of the possible breakup process, the energetics of the collisional dissociation need to be investigated. To dissociate a group G within a larger molecular ion A, an inelastic collision between the ion A and a neutral particle X must happen so that a sufficiently large amount of translational energy of the ion is transferred to its internal energy. The internal energy can then break the bond between the individual groups. Not all of the kinetic energy of the accelerated ion in the laboratory frame  $E_{\text{lab}}$  is available for the dissociation. Rather, the maximum energy is limited to the center-of-mass energy between the molecular ion A and the neutral particle X.

To transfer all of the center-of-mass energy in the collision, the ion and the neutral particle would need to adhere together and form a collision complex, which can then dissociate a molecular group, by undergoing a chemical reaction. In this work the neutral particle is a helium atom and therefore adherence followed by a chemical reaction is unlikely. In helium, the collision induced dissociations would more likely occur as a result of an “impulsive-type” of dissociation, in which only a single atom or group of the projectile molecular ion interacts with the colliding helium atom. The maximum energy  $E_{\text{max}}$  transferable to a group G with mass  $m_G$  can be derived from kinematics [160]:

$$E_{\max} = 4 \frac{m_G m_X}{(m_X + m_G)^2} \frac{m_X}{m_A} \frac{m_A - m_G}{m_A} E_{\text{lab}}, \quad (5.1)$$

where  $m_A$  is the mass of the molecular ion A in a collision with the neutral particle X with mass  $m_X$ . Because the supposed dissociation happens with the aid of helium atoms ( $m_X = 4$  u) only a fraction of the projectile energy, approximately 1.0% for  $\text{TaO}_3\text{H}_2^+$ , can be used in the best case for a light group or atom, for example  $\text{H}_2\text{O}$ . In the other commonly used buffer gas argon, the energetics are better. About 14% of the projectile energy can be transferred to a water molecule.

It should be noted that the 85 V of accelerating potential does not translate into 85 eV in collision energy in the laboratory frame because the ions undergo a large number of collisions thereby continuously losing their kinetic energy before reaching the SPIG front electrode. Monte-Carlo simulations with the ion-optical simulation software Simion (version 8.1) [161] show that the mean maximum collision energy between the helium and ions in the gas jet region is 20-30 eV, translating into 0.2 to 0.3 eV for the maximum available energy for collisional dissociation.

As the  $\text{TaO}_3\text{H}_2^+$  is most likely the product of  $\text{H}_2\text{O}$  addition to  $\text{TaO}_2^+$ , we assume that the dissociation would happen between  $\text{TaO}_2$  and  $\text{H}_2\text{O}$  groups. The dissociation energy  $D_0(\text{TaO}_2^+ - \text{H}_2\text{O})$  is 2.6 eV determined by a CCSD(T) quantum chemical calculation [162, 159]. This dissociation energy is an order of magnitude higher than the estimated maximum energy transferable for dissociation from the collision with helium atoms and hence the suppression of the molecular species cannot be a result of CID. Moreover,  $[\text{TaO}_2(\text{H}_2\text{O})]^+$  is most likely going to rearrange to  $[\text{TaO}(\text{HO})_2]^+$  which is even more bound [162].

### 5.4.3 Technique of size-exclusive extraction

Here a different kind of mechanism for the suppression of molecular species is proposed. As the suppression is clearly induced by the application of an accelerating potential between the gas cell and the SPIG, there is a strong indication that the suppression mechanism happens in the gas jet location. The Simion software was used to further investigate the dynamics of the ion and helium atom collisions at different SPIG front electrode voltages using a hard-sphere collision model applied to pressure and temperature model of supersonic jet. A clear relationship between the collision cross section and the transmission through the SPIG can be demonstrated.

Figure 5.5 presents the simulation results of the transmission of ions through the SPIG as a function of collision cross section, for different SPIG front electrode

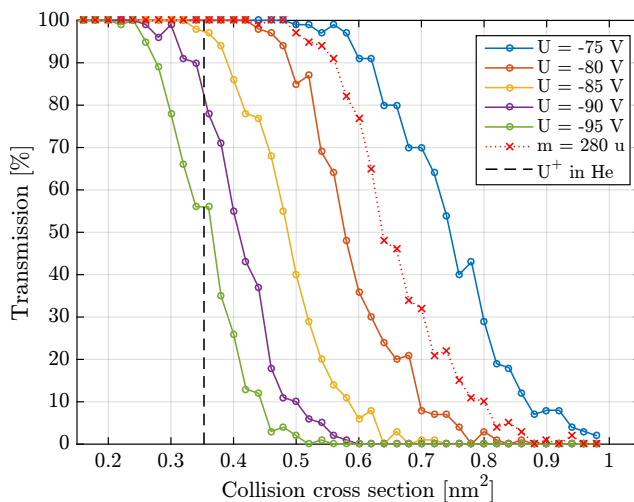


**Figure 5.5.** Simulation of ion transmission through the SPIG as a function of collision cross section using mass 231 u at different SPIG front electrode voltages. The dotted red line illustrates the effect of using a heavier ion and a potential of -85 V. The vertical dashed line shows the collision cross section of a uranium ion in helium [163].

voltages. Each data point corresponds to a simulation of 100 ions with a mass of 231 u. There is a clear drop in the transmission over a few  $0.1 \text{ nm}^2$  in collision cross section when the potential of the electrode is lowered. The position of the edge can be controlled by adjusting the potential so that with a more negative acceleration, ions with a smaller collision cross section can be suppressed. The position of the edge is also mass dependent as demonstrated with the additional simulation of ions with mass 280 u using a suppression voltage of -85 V. This could be an explanation of why the tantalum-zirconium compounds are not suppressed. These heavier compounds (Fig. 5.4) contain fewer atoms than  $\text{TaO}_3\text{H}_2^+$ , most likely resulting also in a smaller geometrical size and collision cross section.

The vertical dashed line in Fig. 5.5 provides a direct comparison of the simulated cross sections to an experimentally measured cross section. This line represents a uranium ion collision cross section deduced from an ion-mobility measurement in helium gas [163] (to our knowledge, no similar ion-mobility measurements have been made with thorium ions in helium gas). A good agreement between the experimental cross section and the choice of suppression voltage used to filter the thorium ion beam is evident.

The reason for the drop in the transmission with increasing collision cross section can be seen from the simulated ion trajectories (Fig. 5.6). When ions undergo

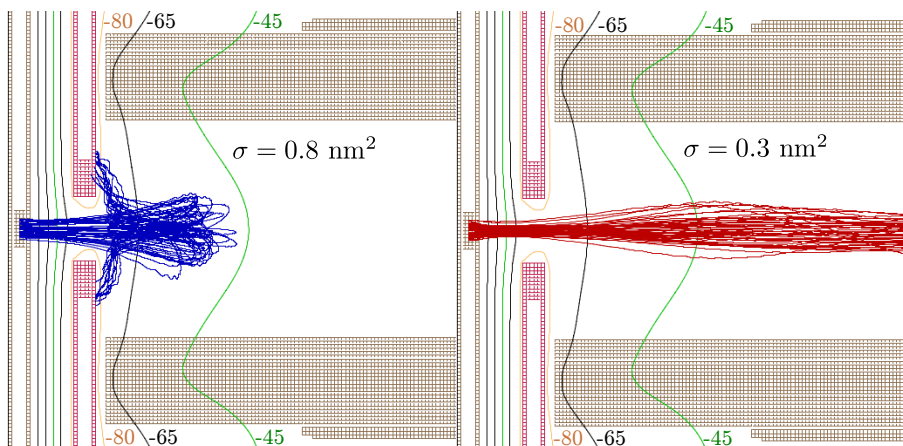


**Figure 5.6.** The ion trajectories in Simion simulations with the SPIG front electrode at  $-85\text{ V}$  and two different collision cross sections. Ions with a larger collision cross section ( $0.8\text{ nm}^2$ ) cannot “climb” the potential of the SPIG rods because they lose energy in collisions with helium atoms. In these figures the gas cell is located on the left and the direction of the mass separator on the right.

a large number of collisions in the acceleration region, they lose so much kinetic energy to the helium atoms that they cannot “climb up” to the potential of the SPIG rods ( $\approx -40\text{ V}$ ) but turn back and collide with the front electrode. Generally, the size of the molecules is larger than that of the monoatomic ions and therefore the collision cross section can be expected to be substantially larger. The suppression of molecular species can therefore be understood as a creation of a filter where the molecular ions extracted from the gas cell are separated from the atomic ions by their size. This technique of size-exclusive extraction is particularly useful in this work because CID was not possible due to the low energy of the ions and the light carrier gas.

## 5.5 $^{233}\text{U}$ alpha recoil source

A convenient method to create  $^{229}\text{Th}$  and its isomeric state is to use  $^{233}\text{U}$ , which alpha decays directly to  $^{229}\text{Th}$ . By placing such a source into a gas cell and stopping the recoils of the alpha decay in a buffer gas, an off-line source for  $^{229}\text{Th}$  ions can be produced with the possibility to extract the ions in several charge states.

The benefit of using an off-line alpha-recoil emitter is the absence of a primary

beam-induced plasma, which can be a significant source of free electrons causing recombination and neutralization of the ions of interest [15]. Although there is a significant amount of alpha radiation emanating from the  $^{233}\text{U}$  sources, ionization of the buffer gas is insignificant. If a  $^{229}\text{Th}$  ion is stopped in helium gas, the high ionization potential of helium (24.6 eV) ensures that a helium atom can only donate electrons to thorium if the charge state is above 3+. If the buffer gas is additionally purified from contaminant molecules which have lower ionization potentials, the  $^{229}\text{Th}$  ions can remain in a 3+ charge state during extraction from a gas cell.

The branching in the alpha decay of  $^{233}\text{U}$  to the isomeric state has been estimated to be 2% [164]. This somewhat low value has the unfortunate consequence that the source strength has to be sufficiently large enough to meet the required ion beam intensity (for a collinear laser spectroscopy experiment). Assuming a requirement of  $\sim 1000$  ions of  $^{229m}\text{Th}$  per second, without taking into account the efficiency of the source this already means a  $^{233}\text{U}$  source strength of 50 kBq. Taking into account losses due to recoil efficiency, stopping and extraction from the gas cell may result in an initial activity requirement of several MBq.

$^{233}\text{U}$  and  $^{229}\text{Th}$  have long half-lives of  $1.6 \cdot 10^5$  years [165] and  $7.9 \cdot 10^3$  years [166], respectively, and thus  $^{233}\text{U}$  as a source can be manufactured and used without any expected depletion of the material. On the other hand, the long half-life complicates the handling of the sources due to any long-lived contamination. Unfortunately the sources cannot be covered by any protective layer as this would hinder the alpha recoil efficiency.

The decay chain of  $^{233}\text{U}$  is shown in Fig. 5.7. Due to the long half-life of  $^{229}\text{Th}$ , it starts to build up in the source material and the source becomes activated with all isotopes in the decay chain. In particular with an aged source, in addition to  $^{229}\text{Th}$ , alpha recoils of all isotopes are produced that are daughters of alpha-active mothers.

Despite the small branching ratio to the isomeric state, using  $^{233}\text{U}$  as a production mechanism for a  $^{229}\text{Th}$  source should be a viable method to produce a high flux if the efficiency can be optimized. This approach has already been studied previously at the IGISOL facility [154]. Several iterations of the gas cell were implemented and tested in order to improve the extraction efficiency of the  $^{229}\text{Th}$  recoils. The best efficiency reported, however, was only 1.6%, attained with ion extraction using an electron emitter that created a strong electric field inside the gas cell effectively “pulling” the positively-charged ions out.

The focus in the current work has shifted to the sources themselves and developments have continued with the study of a new  $^{233}\text{U}$  source in addition to the existing sources. A more careful study of the recoil efficiency of the source has been performed as this critical factor is sensitive to many parameters. In

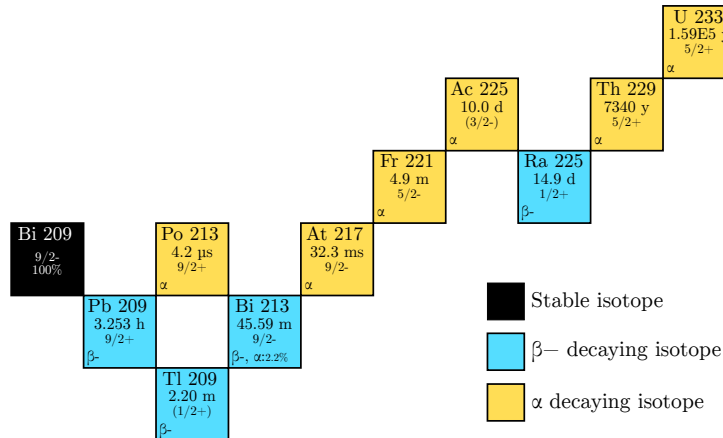


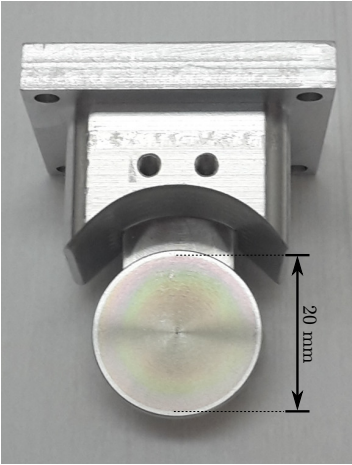
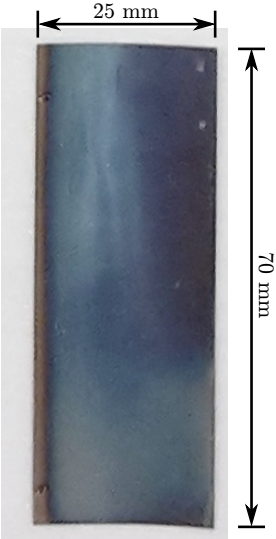
**Figure 5.7.** The  $^{233}\text{U}$  decay chain. The decay mode with possible branching, half-life and ground-state spins are given for each isotope.

in this section the results of spectroscopic analyses of  $^{233}\text{U}$  sources are presented. Characterization measurements have been done using the alpha- and gamma radiation emitted directly from the sources and via the radiation emanating from alpha recoils collected on implantation foils.

### 5.5.1 Description of the sources

The spectroscopic analysis was performed on two different types of  $^{233}\text{U}$  source. One was provided by the Ludwig Maximilian University of Munich [167] and hereafter will be referred to as the LMU source. The source was made by evaporating uranium tetrafluoride on an aluminium backing until an activity of 230 kBq was accumulated within a circular area of 20 mm in diameter. Using the known density of  $^{233}\text{UF}_4$ , 6.7 g/cm<sup>3</sup> [65], a source thickness of  $\sim 420$  nm is inferred.

The existing  $^{233}\text{U}$  source, originally manufactured by McGill University through neutron capture of  $^{232}\text{Th}$ , is a set of stainless steel foils on which  $^{233}\text{U}$  was electrodeposited in a thin layer [168]. Henceforth, these sources will be referred to as the JYFL sources. A total activity of 2.3 MBq of  $^{233}\text{U}$  is available, distributed over six strips with dimensions 25 mm  $\times$  70 mm, and sixteen strips with dimensions 12 mm  $\times$  70 mm; in total about 240 cm<sup>2</sup>. Assuming the uranium is evenly deposited and is pure, a thickness of 12 nm can be deduced. Table 5.2 provides a summary of the source specifications along with photographs.

		
<i>Source</i>	LMU	JYFL
<i>Composition</i>	$\text{UF}_4$	U
<i>Backing</i>	Aluminium	Stainless steel
<i>Deposition</i>	Evaporated	Electroplated
<i>Surface activity</i>	$73.2 \text{ kBq/cm}^2$	$10.2 \text{ kBq/cm}^2$
<i>Surface density</i>	$530 \cdot 10^{15} \text{ at./cm}^2$	$74 \cdot 10^{15} \text{ at./cm}^2$
<i>Geometry</i>	disc dia. 20 mm	$25 \text{ mm} \times 70 \text{ mm}$
<i>Total area</i>	$3.1 \text{ cm}^2$	$240 \text{ cm}^2$
<i>Thickness</i>	$0.27 \text{ mg/cm}^2$ (420 nm)	$0.03 \text{ mg/cm}^2$ (12 nm)
<i>Total activity</i>	230 kBq	2.3 MBq

**Table 5.2.** Physical properties of the studied  $^{233}\text{U}$  sources. Thicknesses are given assuming  $\text{UF}_4$  and pure U metal for the LMU and JYFL sources, respectively.

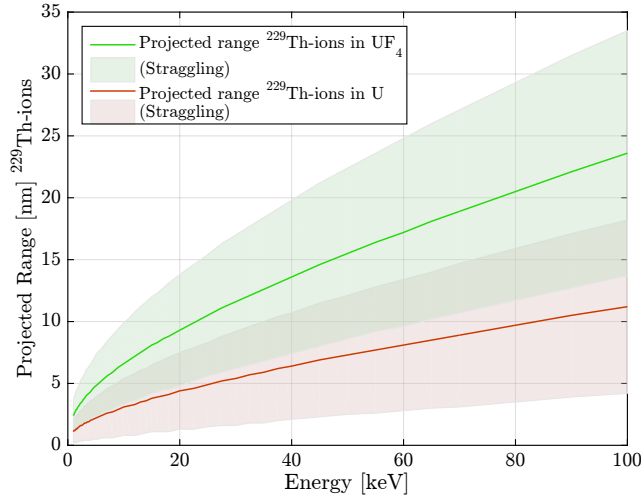


**Figure 5.8.** The projected ranges of  $^{229}\text{Th}$  ions and their longitudinal straggling in uranium (red) and uranium tetrafluoride  $\text{UF}_4$  (green).

As the recoil energy of the daughter nucleus  $T_D = m_\alpha / (m_\alpha + m_D) Q_\alpha$  is low, only  $\sim 84$  keV, the source characteristics need to be very well controlled in order to obtain the maximum number of recoils. If the source is too thick, has poor homogeneity, contains a large number of impurities, has a contaminant surface layers, or the substrate roughness is not controlled, significant recoil losses can already occur in the source material. Therefore it is important to characterize and measure the efficiency of the sources.

The limit for the source thickness can be taken as the distance in which the recoils from the lowest  $^{233}\text{U}$  atomic layer are stopped inside the source material and do not yield any significant number of recoils out of the surface. In order to have a quantitative number for this limit, the software package Stopping and Range of Ions in Matter (SRIM) [169] was used to calculate the stopping ranges of  $^{229}\text{Th}$  ions in pure uranium metal and in  $\text{UF}_4$ . In Fig. 5.8 the projected ranges of the thorium ions in the materials are shown between the energies 1 keV to 100 keV. The densities of uranium and  $\text{UF}_4$  have been included as  $19.0 \text{ g/cm}^3$  and  $6.7 \text{ g/cm}^3$ , respectively. The longitudinal straggling is highlighted with shaded areas. Here the straggling is defined as the square root of the position variance  $\sqrt{\langle(\Delta x)^2\rangle}$ .

The TRIM Monte-Carlo processor of the SRIM software package was used to estimate the recoil energy and the recoil efficiency from a pure  $^{233}\text{U}$  layer with thickness  $75 \cdot 10^{15} \text{ at./cm}^2$ , approximately matching the  $^{233}\text{U}$  layer in a JYFL source strip. The energy distribution of the  $^{229}\text{Th}$  recoils, which exit the source material, is shown with the blue stair plot in Fig. 5.9, illustrating a



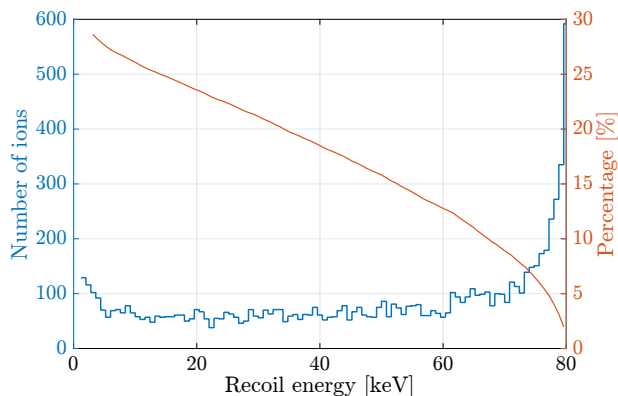


**Figure 5.9.** The simulated energy distribution (blue stair line) and reverse cumulative percentage (orange line) of the  $^{229}\text{Th}$  recoils coming out of a pure  $^{233}\text{U}$  source with thickness  $75 \cdot 10^{15}$  at./cm $^2$ .

somewhat constant distribution between energies of 0 to 60 keV after which the distribution increases exponentially. This increase is the result of the very top layer of atoms of the source decaying in which there is very little material for the recoils to lose energy.

The recoil efficiency is shown also in Fig. 5.9 as a reverse cumulative percentage of the total number of decays. If the recoils with an energy above 10 keV are considered, a recoil efficiency of approximately 25% is expected and can be taken as the best possible recoil efficiency attainable with such a source thickness.

### 5.5.2 Source characterization by direct gamma-ray and alpha radiation measurement

In order to verify the strength of the two sources and to measure the amount of activity of the daughter isotopes, a gamma-ray spectroscopic measurement was performed in a low-background counting station. Figure 5.10 highlights the X-ray and gamma-ray peaks identified in the lower energy region of the spectra, from a few keV to above 400 keV for the two sources. The overall background of the JYFL source is lower reflecting a lower source strength from a single strip as well reduced daughter and contaminant activities.

Following peak identification, activities of  $^{233}\text{U}$  and  $^{229}\text{Th}$  were determined by integration of selected gamma-ray peaks while taking into account the branching ratios and detection efficiency. In this manner, the activity for the LMU source was measured to be 230 kBq of  $^{233}\text{U}$  and  $\sim 1.2$  kBq of  $^{229}\text{Th}$ , while a single

Isotope:	U-233	U-233	U-233	Th-229	Th-229
Peak [keV]:	320.55	317.17	245.35	210.85	193.52
JYFL Activity:	190 kBq	201 kBq	198 kBq	386 Bq	334 Bq
Munich Activity:	228 kBq	240 kBq	234 kBq	1333 Bq	1154 Bq

**Table 5.3.** Measured activities of  $^{233}\text{U}$  and  $^{229}\text{Th}$  isotopes in the LMU source and one large area JYFL  $^{233}\text{U}$  strip according to a few gamma-ray lines.

(large area) JYFL strip resulted in activities of 200 kBq and 350 Bq, respectively. Table 5.3 lists the gamma lines and individual activities extracted from this measurement. The main cause for the variation in the values determined from different gamma lines is thought to be due to the absolute detector efficiency, which was not possible to be determined with high precision.

By using a silicon charged-particle detector (Ortec U-017-300-500) with an intrinsic resolution of 17 keV, 500  $\mu\text{m}$  depletion depth and 300  $\text{mm}^2$  detection area, a direct measurement of the alpha decay from the two sources was compared. By measuring the alpha-particles coming out of the source, the activities of  $^{233}\text{U}$ , its daughter and impurities can be obtained in a similar manner to the gamma-ray measurement. Alpha particles also reveal possible surface characteristics from the straggling as they pass through the material.

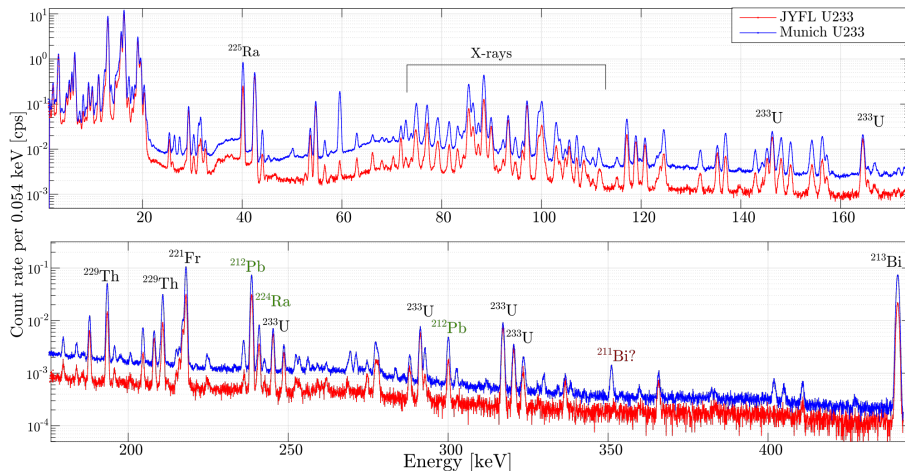


**Figure 5.10.** Direct gamma spectra of the LMU and JYFL  $^{233}\text{U}$  sources between the energy range 5 keV to 500 keV. All the identified  $^{233}\text{U}$  decay chain isotopes are marked with black labels and other identified isotopes with green labels.

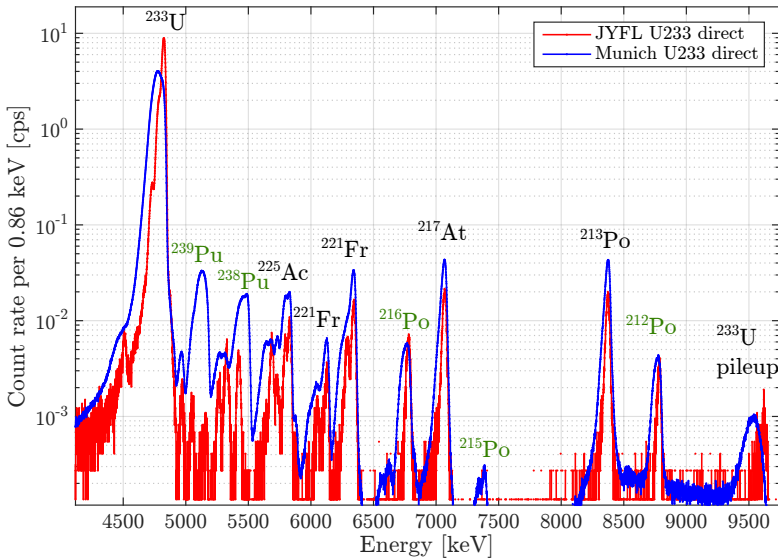


**Figure 5.11.** Direct alpha spectra of the  $^{233}\text{U}$  sources. All the identified  $^{233}\text{U}$  decay chain isotopes are marked with black labels and other identified isotopes with green labels. The larger alpha peak widths of the LMU spectrum are due to a thicker source layer.

Figure 5.11 shows the resulting alpha spectrum, again highlighting a direct comparison of the two sources. In addition to the decay chains of  $^{233}\text{U}$  and  $^{232}\text{U}$ , lines of  $^{238}\text{Pu}$  and  $^{239}\text{Pu}$  are visible, the latter decays particularly noticeable in the LMU source. A direct measure of the alpha decays from  $^{229}\text{Th}$  is not possible due to overwhelming background from the alpha line associated with the decay of  $^{233}\text{U}$ . Finally, the typical alpha-decay peak width of the LMU source was measured to be 100 keV, while that of the JYFL source, 30 keV. The width reflects a possible combination of the source thickness as well as any contaminants on top of the source. The increasing width of the alpha peak when the source is tilted at an angle to the silicon detector is demonstrated in the Rutherford Backscattering measurement discussed in section 5.5.4.

### 5.5.3 Source characterization by foil implantation

In order to measure the rate of alpha recoils, including  $^{229}\text{Th}$ , released from the LMU and JYFL  $^{233}\text{U}$  sources, a foil implantation experiment was performed. To collect the recoils, aluminium foils were mounted at a distance of approximately 2 mm from the  $^{233}\text{U}$  source surface in a chamber connected to a scroll vacuum

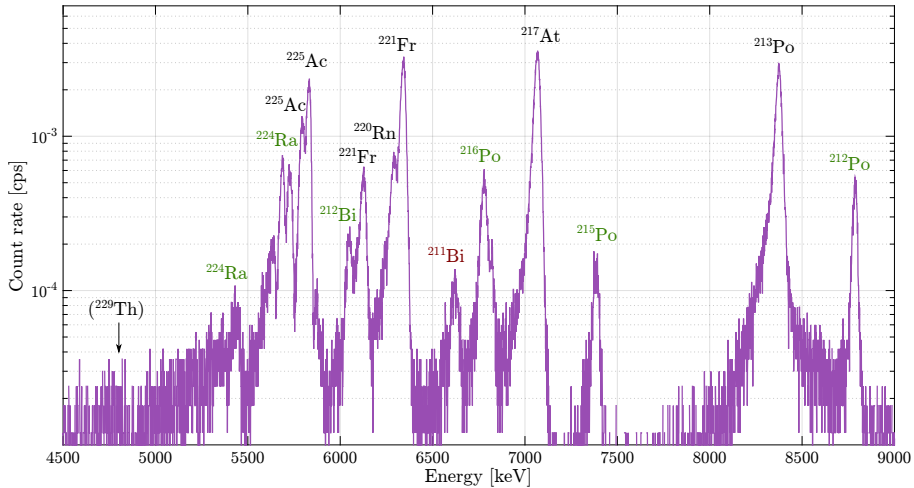


**Figure 5.12.** The alpha spectrum of the Al foil following a 4-day implantation using the LMU  $^{233}\text{U}$  source. Several isotopes belonging to the  $^{233}\text{U}$  decay chain (black labels) and others from  $^{232}\text{U}$  and possibly  $^{227}\text{Ac}$  chains are identified. Unfortunately, due to the long half-life of  $^{229}\text{Th}$ , its alpha decays were not detected above background.

pump. A vacuum of  $\sim 10^{-1}$  mbar was required during the implantation process as the recoil stopping in air would otherwise be significant. The implantation was performed over a duration of approximately 12.6 days for the JYFL source and 46.3 days for the LMU source.

Figure 5.12 shows the alpha spectrum of the foil implanted using the LMU source, measured with the Si detector for 4 days. A clear activity of isotopes from the  $^{233}\text{U}$  decay chain can be seen. As the alpha decays from the  $^{229}\text{Th}$  recoil ions are not visible due to the long half-life of  $^{229}\text{Th}$  and background counts, we can only assign an upper limit of about 30000 recoil ions per second implanted or about 13% of the total activity of the LMU source. Because the  $^{229}\text{Th}$  activity was not directly visible in the alpha spectrum, the implanted foils were measured in the low-background gamma radiation detection station in the hope of detecting the 193.5 keV and 210.9 keV gamma lines as they have a reasonable branching of 4.3% and 2.8%, respectively [170].

Unfortunately, even with the long implantation time using the LMU source and a 30-day measurement in the low-background gamma station, the 193.5 keV gamma line was barely visible above background, as seen in the gamma-ray spectrum shown in Fig. 5.13. Nevertheless, the integration of the area of the 193.5 keV peak was possible suggesting a recoil ion efficiency of  $\sim 3\%$ , a factor of two lower than the estimate provided by L.v.d. Wense et al. [167] for the same

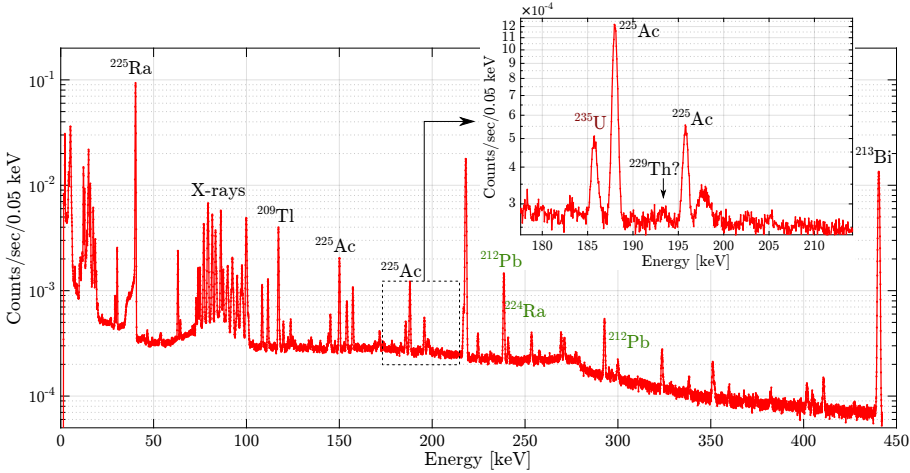


**Figure 5.13.** Gamma spectrum of the Al foil irradiated for a period of 46.3 days by the LMU  $^{233}\text{U}$  source. All identified isotopes belonging to the  $^{233}\text{U}$  decay chain are labeled in black and other assignments are labeled in green. The enlarged region shows the expected position of the  $^{229}\text{Th}$  peaks of which the 193.5 keV is barely visible above background.

source. This direct measurement of the  $^{229}\text{Th}$  recoil efficiency can be taken only as a upper limit because the gamma line is not clearly apparent.

Similar measurements of recoil ion implantation and gamma-ray analysis was performed using the JYFL source with the resulting gamma spectrum shown in Fig. 5.14. Worryingly, the gamma line was not at all visible above the background, which can at least partly be associated with a shorter implantation time.

As the  $^{229}\text{Th}$  activity was not directly discernible in the implantation foils, a determination of the recoil efficiency of the sources must rely on the implantation of  $^{225}\text{Ra}$  daughter isotopes. Similar to  $^{229}\text{Th}$  recoils of  $^{233}\text{U}$ , the  $^{225}\text{Ra}$  are recoiling out of the sources due to the decay of  $^{229}\text{Th}$  which has accumulated to the amounts that were determined from the direct gamma radiation. As the number of daughters in the implantation foil depends not only on their recoil rate but also on the mother isotopes decaying in the foil, a set of differential equations describing the implantation system must be solved. Starting from the implantation of  $^{229}\text{Th}$ , the equation for describing the number of  $^{229}\text{Th}$  atoms  $N_{\text{Th}}$  in the implantation foil is:

$$\frac{dN_{\text{Th}}(t)}{dt} = R_{\text{Th}} - \lambda_{\text{Th}}N_{\text{Th}}(t), \quad (5.2)$$

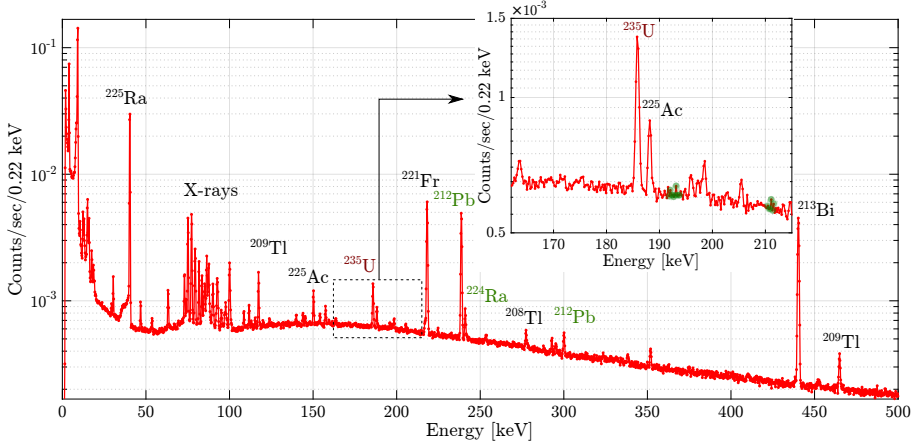


**Figure 5.14.** Gamma spectrum of the Al foil irradiated for a period of 12.6 days by a smaller area JYFL  $^{233}\text{U}$  source strip. All identified isotopes belonging to the  $^{233}\text{U}$  decay chain are labeled in black and other assignments are labeled in green. The enlarged region shows the expected position of the  $^{229}\text{Th}$  peaks (green highlight).

where  $R_{\text{Th}}$  is the recoil rate of  $^{229}\text{Th}$ , and  $\lambda_{\text{Th}}$  its radioactive decay constant. The equation has the simple solution:

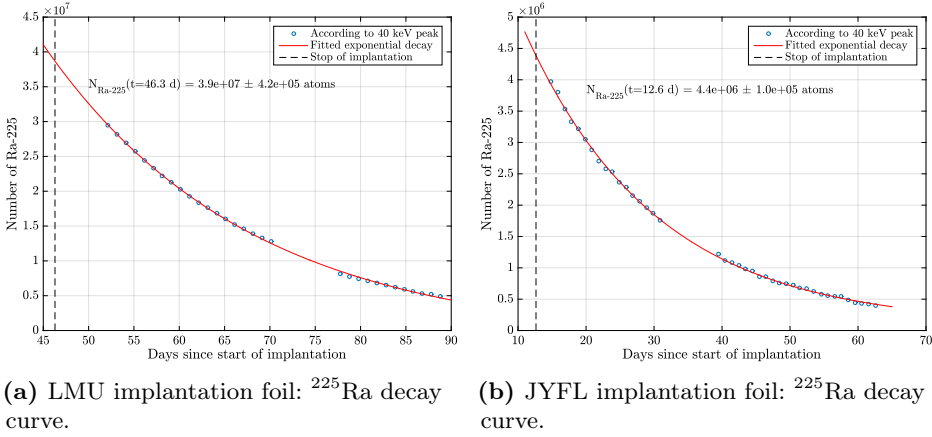
$$N_{\text{Th}}(t) = \frac{R_{\text{Th}}}{\lambda_{\text{Th}}} (1 - e^{-\lambda_{\text{Th}}t}). \quad (5.3)$$

The equation describing the number of  $^{225}\text{Ra}$  atoms, the daughter of  $^{229}\text{Th}$ , is:

$$\frac{dN_{\text{Ra}}(t)}{dt} = R_{\text{Ra}} + \lambda_{\text{Th}}N_{\text{Th}}(t) - \lambda_{\text{Ra}}N_{\text{Ra}}(t), \quad (5.4)$$

where  $R_{\text{Ra}}$  is the recoil rate of  $^{225}\text{Ra}$  from the source and  $\lambda_{\text{Ra}}$  its radioactive decay constant. The derivation of the solution is not shown here but Eq. (5.4) can be solved using methods for first-order linear ordinary differential equations. The exact solution is:

$$N_{\text{Ra}}(t) = \frac{1}{\lambda_{\text{Ra}} - \lambda_{\text{Th}}} \left( \left( R_{\text{Ra}} - \frac{\lambda_{\text{Th}}}{\lambda_{\text{Ra}}} (R_{\text{Th}} + R_{\text{Ra}}) \right) (1 - e^{-\lambda_{\text{Ra}}t}) + R_{\text{Th}} (1 - e^{-\lambda_{\text{Th}}t}) \right). \quad (5.5)$$



(a) LMU implantation foil:  $^{225}\text{Ra}$  decay curve.

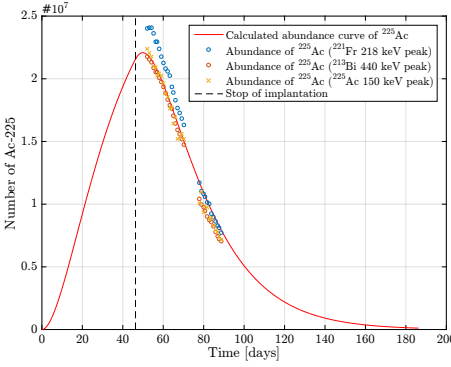
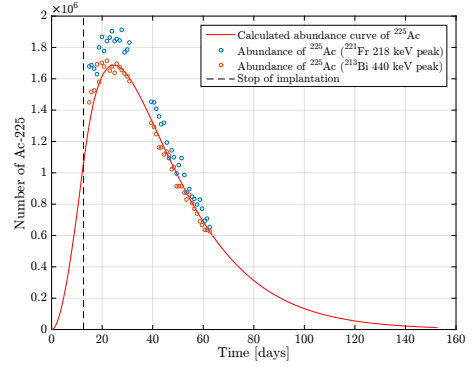
(b) JYFL implantation foil:  $^{225}\text{Ra}$  decay curve.

**Figure 5.15.** The decay curves of the  $^{225}\text{Ra}$  in the irradiated foils by a LMU  $^{233}\text{U}$  source (a) and the JYFL source (b). The dashed line marks the stop time of the implantation.

$^{225}\text{Ra}$  has one detectable gamma line at 40 keV with a 30% branch [170]. The area of the 40 keV peak from the implantation foil gamma spectra has been plotted as a function of measurement time since the end of the implantation in Fig. 5.15 for both sources. By fitting an exponential decay curve to the intensity change and noting that the curve practically reduces to the background, it can be inferred that the  $^{225}\text{Ra}$  activity in the foil is dominated by the direct implantation of the  $^{225}\text{Ra}$  recoils rather than emerging as a decay product of  $^{229}\text{Th}$  in the foil. By extrapolating back to the implantation stop time, the amount of implanted  $^{225}\text{Ra}$  can be deduced as is shown for both foils in Fig. 5.15. Then, by using Eq. (5.5) with the assumption that the decay of  $^{229}\text{Th}$  does not contribute significantly to the number of  $^{225}\text{Ra}$ , the implantation rate of  $^{225}\text{Ra}$ ,  $R_{\text{Ra}}$ , can be calculated as 23.6 1/s for the LMU source and 5.3 1/s for the JYFL source.

As the  $R_{\text{Ra}}$  values were only determined using one gamma line, the recoil rates were cross-checked against the  $^{225}\text{Ac}$  activity in the foil. Because the  $^{225}\text{Ra}$  is beta decaying, the decay does not produce enough recoil for the daughter to leave the  $^{233}\text{U}$  source and hence any  $^{225}\text{Ac}$  activity directly results from the decay of  $^{225}\text{Ra}$  in the implantation foil. Therefore the number of  $^{225}\text{Ac}$  atoms in the foil can be described simply by the following differential equation:

$$\frac{dN_{\text{Ac}}(t)}{dt} = \lambda_{\text{Ra}}N_{\text{Ra}}(t) - \lambda_{\text{Ac}}N_{\text{Ac}}(t), \quad (5.6)$$

(a) LMU implantation foil:  $^{225}\text{Ac}$  decay curve.(b) JYFL implantation foil:  $^{225}\text{Ac}$  decay curve.

**Figure 5.16.** The decay curves of the  $^{225}\text{Ac}$  in the irradiated foil by the LMU source (a) and by the JYFL  $^{233}\text{U}$  source (b). As the gamma line branches of  $^{225}\text{Ac}$  are small, its activity was not possible to be plotted for the JYFL foil. The red curve is not a fit but the expected activity according to equations (5.7) and (5.8).

which, by again assuming that  $N_{\text{Ra}}(t)$  is dominated by the direct implantation, has the solution,

$$N_{\text{Ac,imp}}(t) = \frac{R_{\text{Ra}}}{\lambda_{\text{Ra}} - \lambda_{\text{Ac}}} (e^{-\lambda_{\text{Ra}}t} - e^{-\lambda_{\text{Ac}}t}) + \frac{R_{\text{Ra}}}{\lambda_{\text{Ac}}} (1 - e^{-\lambda_{\text{Ac}}t}) \quad (5.7)$$

during the implantation. After the implantation has stopped at time  $t_{\text{imp}}$ , the following solution can be obtained for the amount of  $^{225}\text{Ac}$ :

$$N_{\text{Ac,dec}}(t) = \frac{N_{\text{Ra}}(t_{\text{imp}})\lambda_{\text{Ra}}}{\lambda_{\text{Ra}} - \lambda_{\text{Ac}}} (e^{-\lambda_{\text{Ac}}t} - e^{-\lambda_{\text{Ra}}t}) + N_{\text{Ac,imp}}(t_{\text{imp}})e^{-\lambda_{\text{Ac}}t}. \quad (5.8)$$

As the number of  $^{225}\text{Ac}$  atoms in the foil can be calculated from the deduced  $R_{\text{Ra}}$  values using the above equation, it can be directly compared to the number of atoms determined from the  $^{225}\text{Ac}$  gamma line at 150 keV, or from the daughter activity of  $^{221}\text{Fr}$  (218 keV) and  $^{213}\text{Bi}$  (440 keV), which quickly reach equilibrium due to their short half-life. Figure 5.16 shows this comparison for the LMU and JYFL irradiated foils. The data points indicate the amount of  $^{225}\text{Ac}$  as a function of time from the gamma spectrum and the solid red curve from the



differential equations. It should be emphasized that the red curve is not a fit but rather an independent determination from the  $R_{\text{Ra}}$  values demonstrating the validity of the deduction.

Using the  $^{233}\text{U}$  and  $^{229}\text{Th}$  activities from the direct gamma radiation measurements, the recoil efficiency of  $^{225}\text{Ra}$  of 3% for the JYFL source and 2% for the LMU source can be calculated. Assuming that the ratio between the recoil implantation rates of  $^{229}\text{Th}$  and  $^{225}\text{Ra}$  is the same as the detected activity ratio of  $^{233}\text{U}$  and  $^{229}\text{Th}$  in the sources, the deduced recoil efficiency for  $^{225}\text{Ra}$  can be taken as an approximate number for the  $^{229}\text{Th}$  recoil efficiency. It should be noted that the efficiency may be underestimated if the decaying  $^{229}\text{Th}$  distribution reaches deeper than the  $^{233}\text{U}$  distribution or overestimated if  $^{229}\text{Th}$  atoms are implanted into a contaminant layer on top of the  $^{233}\text{U}$  layer.

Still, considering the low daughter recoil efficiency and the low detected amount of  $^{229}\text{Th}$ , which should have been easily directly detectable if efficiencies would have been optimum, it is obvious that the recoil efficiency needs to be improved, especially for the JYFL source where the simulated recoil efficiency was about 25% as was shown by the SRIM simulations.

The measured recoil efficiency of 2% for the LMU source is about a factor of two to three lower than that estimated for the same source (and also using the daughter activity) by L.v.d. Wense et al. [167]. The value presented here is close to the recoil efficiency of  $\sim 1.6\%$  which was estimated by L.v.d. Wense [135] for 360 nm of  $^{229}\text{UF}_4$  material using a SRIM calculation and a model for isotropic emission of alpha recoils. The higher recoil efficiency estimate was attributed to possible channeling of the recoils in a crystallized surface layer. With thicker sources it is clear that the recoil efficiency cannot be improved significantly and therefore the approach of L.v.d. Wense et al. [135, 134] to use a thinner 290 kBq source that was deposited on a Ti-sputtered Si wafer of 100 mm in diameter, is the correct approach, resulting in a significantly improved recoil efficiency of  $\sim 35\%$ .

#### 5.5.4 Source characterization by Rutherford backscattering spectrometry

Rutherford backscattering spectrometry (RBS) is a non-destructive ion beam analysis technique in which the elemental composition of thin film samples can be quantitatively determined [171]. Usually RBS is performed by irradiating a sample in vacuum with a 1.0-2.5 MeV helium beam from an accelerator and then detecting the back scattered primary helium ions with a charged particle detector at different angles and different sample orientations. By using known scattering cross sections and stopping powers for helium ions in materials, the layer thicknesses and their composition can be obtained. The

RBS technique is most sensitive detecting heavier elements with quantities above  $10^{12}$  at./ $\text{cm}^2$  on light substrates with a resolution of about 10 nm to depths of a few  $\mu\text{m}$ . For lighter elements, especially below oxygen, the technique has limited sensitivity [172, 173].

Due to the low recoil efficiencies of the  $^{233}\text{U}$  sources as shown by the implantation measurements, the RBS analysis technique was used to investigate the composition of the source layers. A 1505 keV He beam was produced with the 1.7 MV NEC Pelletron accelerator located within the JYFL Accelerator Laboratory. The He beam was directed to the sources which were mounted inside a dedicated RBS measurement chamber. Using IBM geometry with  $\beta - \alpha + \theta = 180^\circ$ , depicted in Fig. 5.17, both of the sources were characterized using two detectors at backscattering angles of  $\theta_1 = 170^\circ$  and  $\theta_2 = 118^\circ$ .

The experimental RBS spectra of the LMU and JYFL sources measured with detector 1 at a tilt angle  $\alpha = 0^\circ$  are shown in Fig. 5.18. The  $^{233}\text{U}$  is visible in both spectra as the backscattering with the highest energy. In the JYFL source, in which the  $^{233}\text{U}$  layer is much thinner ( $\sim 74 \cdot 10^{15}$  at./ $\text{cm}^2$ ) than in the LMU source, the uranium appears as a sharp peak at  $\sim 1400$  keV with the stainless steel substrate as the continuous structure starting from about 1100 keV. The interesting feature of the spectrum is the peak between the uranium and the substrate, which has been identified as a thin layer of zinc. Also, on the substrate there is clear peak in the signal at around 500 keV indicating an oxide layer.

Because the  $^{233}\text{U}$  layer is much thicker ( $\sim 530 \cdot 10^{15}$  at./ $\text{cm}^2$ ) in the LMU source, the corresponding uranium peak is much wider and shows structural variations in the source layer. As the substrate is aluminium its edge is found at lower energy than for stainless steel. As a light element, the fluorine in the source layer is also found in the low energy region. The diffusiveness of the substrate to the uranium layer reflects the surface roughness of the aluminium on top of

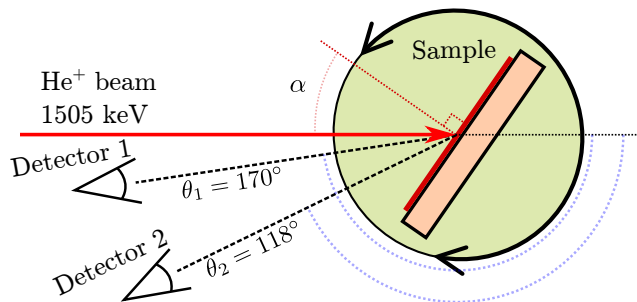


**Figure 5.17.** The measurement geometry for the RBS measurement of the  $^{233}\text{U}$  sources.

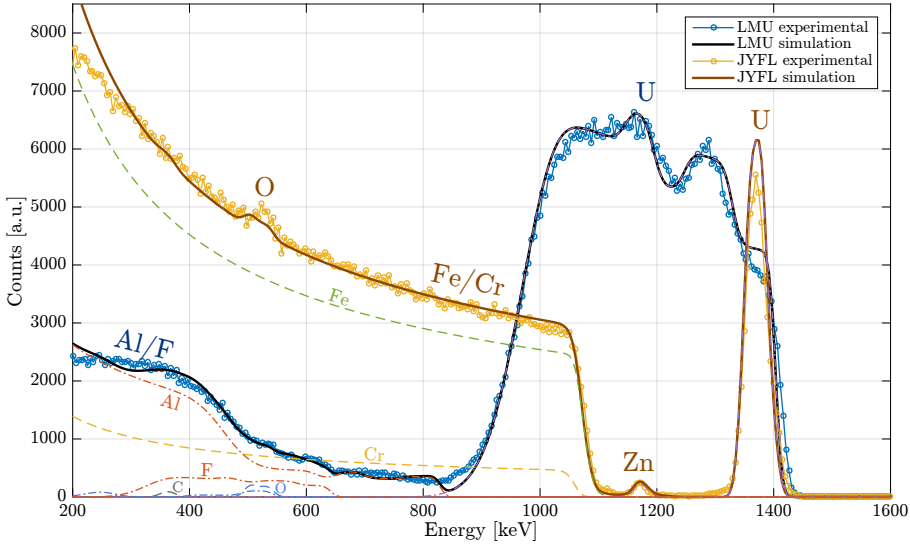


**Figure 5.18.** The RBS and Simnra simulation spectra of the LMU and JYFL  $^{233}\text{U}$  sources. The individual elements in the simulation are plotted with dashed lines for the JYFL source simulation and dash-dotted lines for the LMU source simulation.

which the  $\text{UF}_4$  has been evaporated.

For both spectra the elemental composition was determined by using the RBS simulation software Simnra [174]. Figure 5.18 shows the simulation results as solid lines with individual elements as dashed lines for the JYFL source and dash-dotted lines for the LMU source. In order to get a good fit to the experimental data, the source structures were defined as several separate layers and the layer composition was then optimized to obtain the best fit. As the sources were measured at several tilt angles ( $\alpha = 0^\circ, 5^\circ, 10^\circ$  and  $15^\circ$ ) with two detectors, the layer structure was iteratively optimized until the simulation consistently matched to all applicable data. This method gave confidence to the simulation.

The elemental composition of sources as a mass percentage according to the simulations is shown in Fig. 5.19 as a function of depth. The surface layer is the rightmost layer. In the LMU source the layer composition has been assumed to be  $\text{UF}_4$  into which aluminium was added in order to get the uranium peak width and the high energy tail of the substrate correct. This is believed, at least partly, to be due to the surface roughness of the aluminium substrate. Also, small layers of oxygen are assumed to be present on top of the aluminium substrate and source material. According to the simulations the amount of  $^{233}\text{U}$  was  $460 \cdot 10^{15}$  at./ $\text{cm}^2$  matching reasonably well the estimated thickness as derived

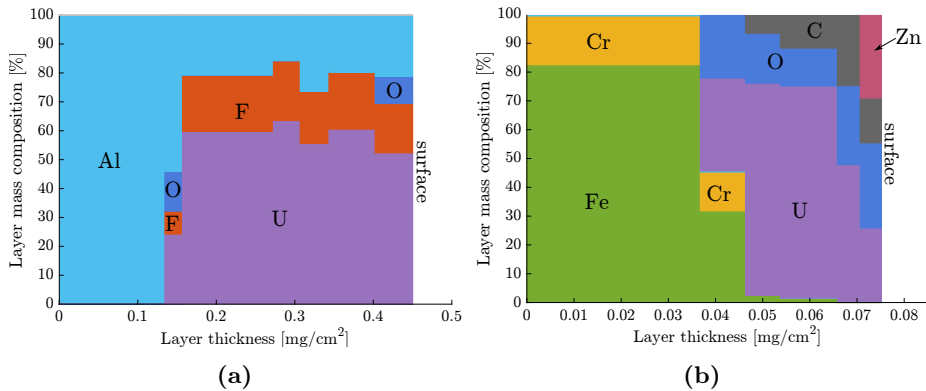


**Figure 5.19.** The elemental mass composition as a function of layer depth of the  $^{233}\text{U}$  LMU (a) and JYFL (b) sources according to the Simnra simulation.

from the activity.

The elemental composition of the JYFL source (Fig. 5.19b) was similarly attained by iteratively simulating multiple layers. The best match for the stainless steel substrate was obtained with a mixture of 81.5% Fe, 18% Cr and 0.5% Mo. The uranium layer needed a considerable amount of oxygen in order to replicate the experimental spectrum as well as the peak in the 500 keV region. Additionally, in order to get the uranium peak width and position correct as well as the substrate, some carbon needed to be added. “Carbon” does not necessarily represent the element carbon but can express any light element below oxygen. Finally the zinc layer is positioned on the surface. The Simnra simulations estimate the  $^{233}\text{U}$  layer thickness to be  $\sim 54 \cdot 10^{15}$  at./ $\text{cm}^2$ , which is about 73% of the calculated thickness. Variation in the thickness can be expected from the uneven coloration of sources, which can be clearly seen in the photograph of the source in Table 5.2. The dark discoloration may also point to considerable oxidation of the uranium as indicated also by the presence of the oxide peak in the RBS spectra according to which the inner uranium layer has 2 to 3 times the number density of oxygen than that of uranium. When exposed to room temperature air, uranium metal oxidizes rapidly so that within 3-4 days the surface of uranium has changed from a metallic coloration to a surface with a black appearance [175]. As this layer is not protective, the  $^{233}\text{U}$  layer in the source has probably oxidized throughout.

The unexpected zinc layer was already seen in a set of earlier RBS measurements with a different source strip confirming its presence in multiple strips. In this

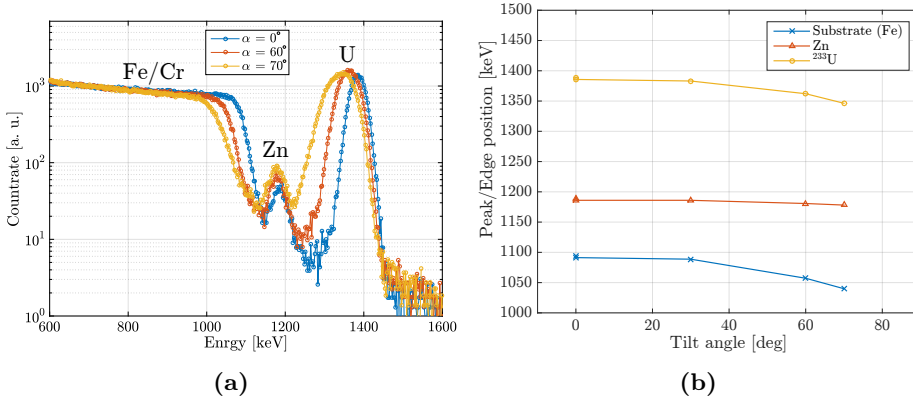


**Figure 5.20.** (a) The experimental RBS spectrum of a JYFL source strip shown at three different sample tilt angles. The  $\alpha = 60^\circ$  and  $70^\circ$  spectra are normalized to the  $\alpha = 0^\circ$  spectrum. (b) The peak position for the  $^{233}\text{U}$ , the Zn layer and the substrate edge as a function of tilt angle.

previous set of measurements a different geometry was used,  $\beta + \alpha + \theta = 180^\circ$ , with the detector  $\theta = 165^\circ$  and with four different tilt angles  $\alpha = 0^\circ, 30^\circ, 60^\circ$  and  $70^\circ$ . This allowed the arrangement of the layers and elements to be determined. In Fig. 5.20a the experimental RBS spectra are shown for three different angles. As the tilt angle is increased, the peak positions move toward lower energy because the backscattered helium ions need to travel through more material in order to get to the detector which is fixed at the  $\theta$  angle. By comparing the movement of the peaks and the substrate edge at different tilt angles the ordering of the layers can be inferred. Because the peak originating from the zinc layer does not move nearly as much as the  $^{233}\text{U}$  or the stainless-steel substrate, as illustrated in Fig. 5.20b, the zinc layer has to be positioned on top of the uranium.

Finally, the composition of the back side of the JYFL source strip was measured. As expected only the stainless steel substrate was detected and no other element, including zinc, was found.

Although the simulations estimated the thickness of the zinc layer to be only  $1 \cdot 10^{16}$ - $2 \cdot 10^{16}$  at./ $\text{cm}^2$ , which is capable of stopping approximately a 10 keV thorium ion, the fact that a contaminant layer was detected on top of the source is worrying. In particular because there seems to be some other “light” element on top, it is suspected that the low measured recoil efficiency is due to the surface contaminants. The zinc suspiciously points to the electron emitter gas cell because the components of the housing of the hot filament, used to

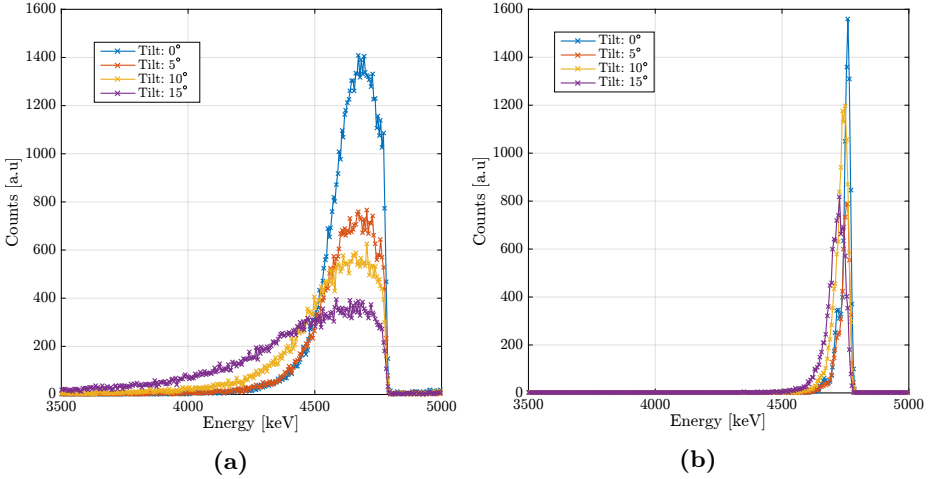


**Figure 5.21.** The LMU and JYFL source alpha peak at different tilt angles using the  $\beta - \alpha + \theta = 180^\circ$  geometry with  $\theta = 118^\circ$ .

create the high flux of electrons, are made of brass, an alloy metal containing approximately 50% zinc.

Interestingly, the source thicknesses are also evident from the intrinsic  $^{233}\text{U}$  alpha peaks that were visible as a constant background at higher energies during the RBS measurement. Figure 5.21 shows the LMU and JYFL source alpha peak at different tilt angles detected with the  $\theta_2$  detector. In comparison to the JYFL source, the LMU source shows significant spreading of the alpha line especially at the largest tilt angle. Although it is difficult to get a quantitative estimation of the source or contaminant layer thicknesses by measuring the  $^{233}\text{U}$  alpha line at different angles, the spectra illustrate that this method can be used to compare sources and to detect possible problems without needing a dedicated accelerator and RBS setup.

It is clear from our work and that of L.v.d Wense and colleagues [167] that a thinner  $^{233}\text{U}$  source layer is advantageous for a higher recoil ion efficiency. The preparation of thin  $^{233}\text{U}$  sources is a critical aspect to this work and is now being supported by TU Wien within the nuClock collaboration. There will also be future measurements in which the RBS is performed on one of the JYFL  $^{233}\text{U}$  source strips that were not used in the electron emitter gas cell in order to confirm the suspected origin of the zinc or other contaminant layers.

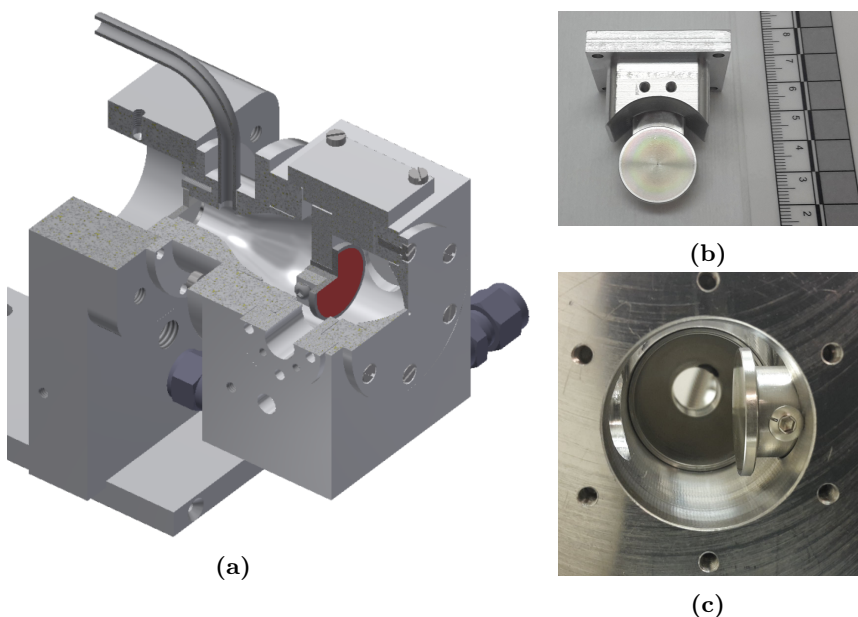


**Figure 5.22.** (a) Cross-sectional view of the actinide gas cell CAD model with the LMU  $^{233}\text{U}$  recoil source mounted facing the nozzle. (b) Photograph of LMU source mounted to the source holder. (c) Photograph of the LMU source positioned sideways into the gas cell.

## 5.6 Source characterization by mass spectra

### 5.6.1 LMU source in actinide gas cell

To study the ion yield and charge state distribution of  $^{229}\text{Th}$  ions from the LMU source, the source was mounted into the actinide gas cell (used in the filament-based dispenser studies) and ions extracted were detected at the focal plane of the IGISOL mass separator with a MCP detector. Figure 5.22a shows a cross-sectional view of the actinide gas cell and the location of the  $^{233}\text{U}$  source facing the exit nozzle, while Fig. 5.22b shows the photograph of the LMU source in its holder. The second geometry that was studied is shown in Fig. 5.22c in which the source is positioned sideways in order to obtain a smoother gas flow near the surface of the source. However, we note that the actinide gas cell has not been designed for optimal gas flow or for the extraction of recoil ions from a “large area” alpha-recoil source and thus the gas flow near the exit nozzle is likely to suffer from turbulence. Diffusion losses to the walls of the cell are also expected to be high.

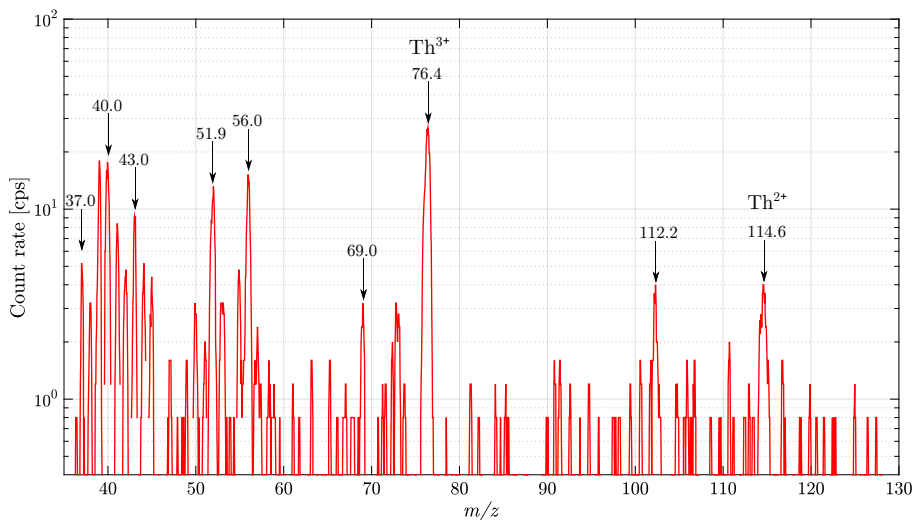


**Figure 5.23.** Initial mass spectrum using the LMU  $^{233}\text{U}$  source mounted in the actinide gas cell facing the exit nozzle.

The mass spectrum recorded with the source directly facing the exit nozzle is shown in Fig. 5.23, with a clear peak at  $A/q = 76.4$  corresponding to  $^{229}\text{Th}^{3+}$ . The count rate at the mass peak was optimized around a rather narrow window of pressure, nominally 30 mbar. The extracted total ion count rate for  $^{229}\text{Th}$  was low; only about 30 cps. The low yield was partly a result of the non-optimal gas flow conditions and also to possible damage of the MCP detector due to extensive use at IGISOL. Unfortunately there was no way to estimate the detector efficiency and so only a lower limit of 50 ions per second, about 1% of the estimated number of recoils exiting the LMU source, were detected. Since then the detector has been replaced. Interestingly, and supporting the observations of previous characterizations by L. v. d. Wense [167], which were made with considerably higher yields, the dominant fraction of  $^{229}\text{Th}$  is extracted in a triply-charged state. A peak was also detected at  $A/q = 114.6$  corresponding to  $^{229}\text{Th}^{2+}$  but with approximately an order of magnitude smaller intensity. The identification of the triply- and doubly-charged  $^{229}\text{Th}$  ions can be confirmed by the fact that the mass peaks appear in fractional mass units which is very rarely seen during IGISOL operation. No other peaks above  $A/q = 115$  were detected, including at the region where singly-charged  $^{229}\text{Th}^{1+}$  would be expected.



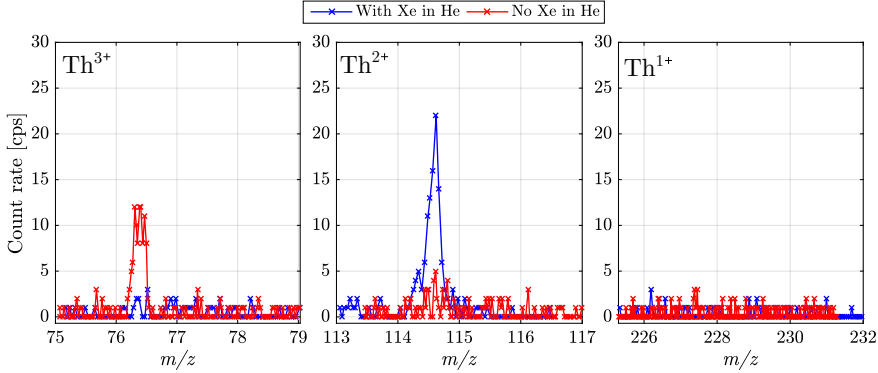


**Figure 5.24.** The mass spectra in regions of  $\text{Th}^{3+}$ ,  $\text{Th}^{2+}$  and  $\text{Th}^{1+}$ , with and without the addition of xenon gas. A clear charge state manipulation from  $\text{Th}^{3+}$  to  $\text{Th}^{2+}$  is observed. The absence of a  $\text{Th}^{1+}$  fraction is notable.

### 5.6.2 Charge state manipulation

An attempt to manipulate the charge state of  $^{229}\text{Th}$  was performed by bleeding in a small amount of Xe gas into the gas lines, normally done for mass-calibration purposes. With an ionization potential (IP) of 12.13 eV [176], Xe atoms may charge exchange with  $^{229}\text{Th}^{3+}$  ions, which release 18.3 eV when recombining to  $^{229}\text{Th}^{2+}$  [177], resulting in  $\text{Xe}^+$  ions and an electron being transferred to thorium. In other words  $^{229}\text{Th}^{2+}$  is being produced via the reaction:

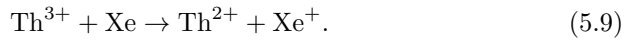


Figure 5.24 shows the mass spectra with and without xenon in the helium gas and the clear impact in the count-rate distribution of  $^{229}\text{Th}^{3+}$  and  $^{229}\text{Th}^{2+}$  mass peaks. We also note the total absence of ion counts other than background in the  $^{229}\text{Th}^{1+}$  region. The most likely reason why the same charge transfer reaction is not observed between  $^{229}\text{Th}^{2+}$  and Xe to form singly-charged thorium ion is due to the lower IP of  $^{229}\text{Th}^{1+}$  compared to xenon. Interestingly, the latest estimate places the second ionization potential of thorium,  $12.1 \text{ eV} \pm 0.2 \text{ eV}$  [178], very close to the ionization potential of Xe.

The capability of manipulating the charge state of thorium ions may be useful in the future when deciding on which charge state to perform laser spectroscopy. Based on energetics, in addition to xenon, also krypton with an IP of 14.00 eV [179] or argon with an IP of 15.76 eV [180] could be used to reduce the thorium ion charge state from 3+ to 2+. Such studies are planned as part of a future measurement campaign in connection to a new gas cell design discussed

in the following section.

### 5.6.3 A new dedicated gas cell for $^{233}\text{U}$ alpha-recoil sources

In order to improve the gas cell extraction efficiency for  $^{229}\text{Th}$  recoils stopped in the buffer gas, a new gas cell has been designed, optimized for gas flow and with a geometry such that all of the available  $^{233}\text{U}$  sources can be mounted. Although it has been shown that the current JYFL sources have a poor recoil efficiency, notably those which have been installed in a previous gas cell which used an electron-emitter, we present the new gas cell design and in parallel note that new electroplated  $^{233}\text{U}$  sources are currently being developed and manufactured by TU Wien.

To avoid the complexity of adding dc and rf electrode structures in a larger-volume gas cell, the first iteration of the design will function with gas flow only. The challenge in constructing a gas cell for  $^{233}\text{U}$  alpha-recoil sources that can provide a sufficiently high flux of  $^{229}\text{Th}$  ions is the large surface area of the sources. Because the optimal thickness of the  $^{233}\text{U}$  layer cannot be much greater than the current JYFL sources ( $\sim 12$  nm), the surface area cannot be reduced without a reduction of the source activity. The necessary large volume of the gas cell may be detrimental to the extraction efficiency because the combination of a low buffer gas pressure (to stop the recoils) and long ion extraction times may lead to significant diffusion losses via the neutralization of ions by collision with the gas cell walls. An increased extraction time can also result in enhanced molecular formation if the gas purity is not well controlled.

In practice, the parameters that have defined the shape and size of the gas cell are the size and surface area of the current JYFL sources, the contoured shape to produce a smooth flow of buffer gas and the physical size of the vacuum chamber in which the gas cell is mounted. A cross-sectional view of the CAD model showing the new design is illustrated in Fig. 5.25, and in Fig. 5.26 the constructed gas cell is shown on the left with the  $^{233}\text{U}$  source holder that connects to the nozzle funnel. A smooth gas flow is produced by the funnel-like structures at both ends of the gas cell. As the resulting gas cell volume was rather large, slightly over  $600\text{ cm}^3$ , the evacuation of recoil ions was made faster by having an exit hole of 2.5 mm in diameter. Compared to normal exit hole diameters at IGISOL, approximately 1 mm, the exit hole is considerably larger resulting about 5 times larger volumetric flow. However, the gas load for the vacuum pumps is not above nominal due to the low operational gas pressure.

The helium pressure required to stop the low-energy  $^{229}\text{Th}$  recoil ions can be simulated using the TRIM processor of the SRIM software package [169]. This was used to calculate the stopping of 1- to 80 keV  $^{229}\text{Th}$  ions in helium at four different pressures. The calculations of the projected ranges are shown

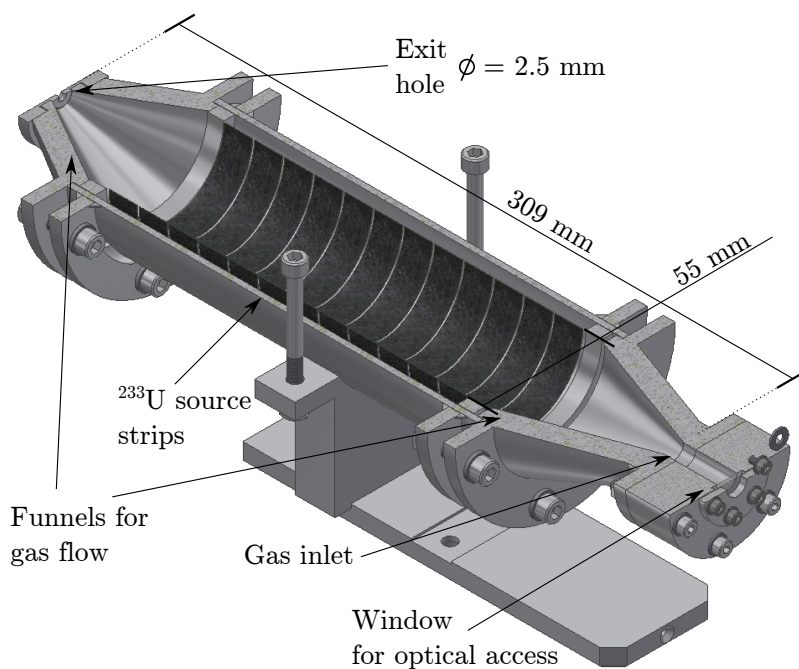


**Figure 5.25.** A cross-sectional view of the CAD model of the new gas cell design for the  $^{233}\text{U}$  sources.

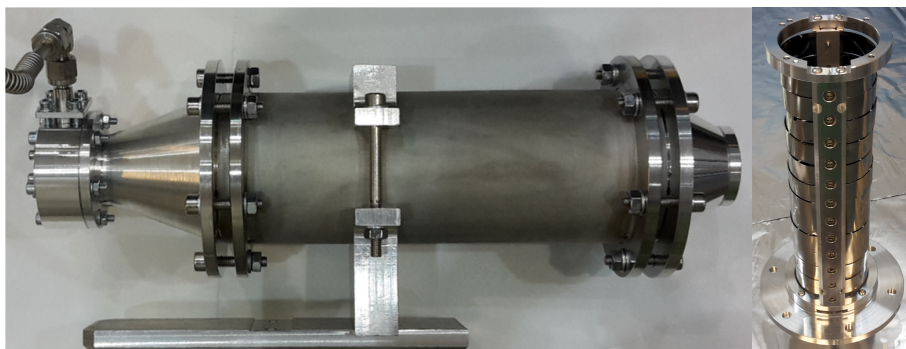


**Figure 5.26.** Photograph of the new gas cell. The  $^{233}\text{U}$  source holder is shown on the right and is attached to the nozzle cone. The bracket holding the gas cell is mounted on the baseplate of the IGISOL vacuum chamber. Helium gas is fed in through the flexible bellow on the left and is evacuated through the nozzle located on the right.

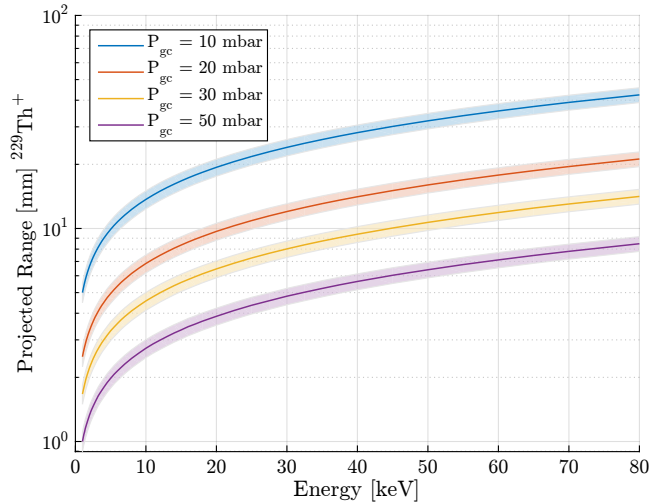


**Figure 5.27.** The projected ranges of  $^{229}\text{Th}$  ions from 1 keV to 80 keV in helium gas. The range is given for four different pressures.

in Fig. 5.27 from which a pressure of only  $\sim 20$  mbar is needed to stop the 80 keV recoil in 20 mm. The stopping of the recoils in 20 mbar helium was also simulated by TRIM using the energy recoil distribution (Fig. 5.9) obtained from the simulation of a pure  $^{233}\text{U}$  source with a thickness of about  $75 \text{ at./cm}^2$ . In Fig. 5.28, the number of stopped  $^{229}\text{Th}$  ions is given per 0.5 mm as a function of distance from the source surface. The total number of simulated ions was 30000. The ions can be seen to be stopping rather evenly between 3 mm and 20 mm with some ions extending to 25 mm, which is approximately the distance (27.5 mm) from the source strip to the center line of the new gas cell.

A series of computational fluid dynamics (cfd) simulations were also performed to study the gas flow in the cell. The cfd module of the COMSOL Multiphysics v5.0 [181] simulation software package was used, into which a simplified 3D CAD model of the gas cell was imported and then simulated using the  $k$ - $\omega$  turbulent flow model [182, 183]. Even though the Reynolds numbers at the source position are below 50 in the typical operational conditions for the helium buffer gas (therefore the flow should be laminar), the turbulent model was used to simulate the flow in the inlet region, where there is a sharp  $90^\circ$  bend in which the Reynolds number can be over 500. The initial conditions included the gas cell inlet flow rate, calculated using Eq. (2.15), and a pressure on the outlet boundary close to the nozzle. The fluid material was defined as room temperature helium gas. In order to keep the flow below a Mach number  $M = 0.3$ , the very tip of the gas cell was not simulated.

Figure 5.29 shows the result of the simulation as streamlines plotted from the

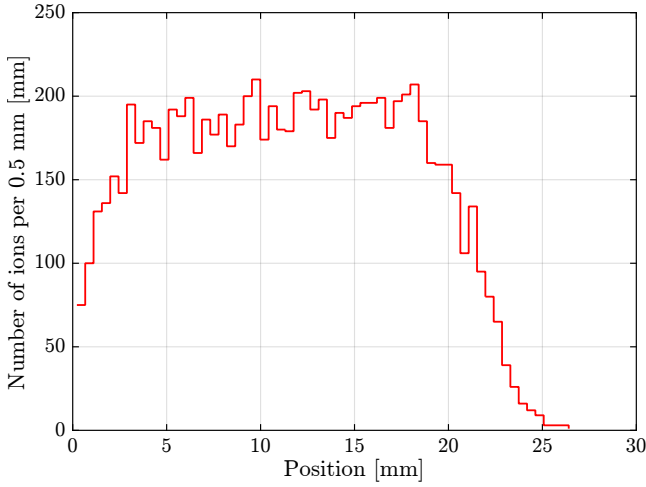


**Figure 5.28.** The estimated recoil stopping range distribution of  $^{229}\text{Th}$  ions in 20 mbar helium gas assuming a recoil energy distribution according to Fig. 5.9.

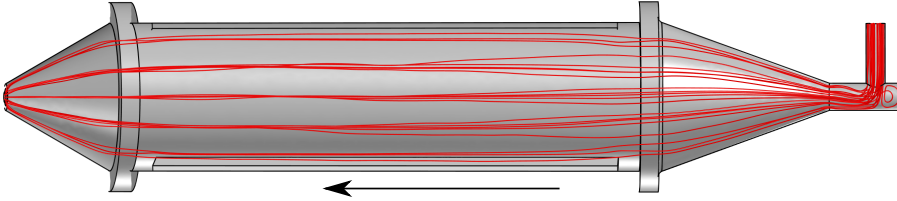


**Figure 5.29.** Streamlines of the gas flow in the simulated  $^{233}\text{U}$  alpha-recoil gas cell. The streamlines are initiated at the nozzle and are calculated backwards until the gas inlet.

gas flow velocity field. The streamlines start from the outlet boundary and are then calculated backwards until they reach the gas inlet that is at a  $90^\circ$  angle to the center axis of the gas cell. As can be seen, the gas flow smoothly covers the whole cell without any dead volumes and without noticeable turbulence until the sharp corner at the gas inlet. The funnels at both ends were critical in order to get the flow even throughout the cell. The largest deviations observed in the streamlines are those closest to the walls.

The simulation results were also used to study the evacuation time from different points within the gas cell, obtained by a line integral in the scalar field of the total gas velocity along the helium flow streamlines. The evacuation time from position  $r_a^{\vec{}}$  to the exit hole position  $r_e^{\vec{}} = (0, 0, 0)$  along the streamline  $L$  is calculated as,

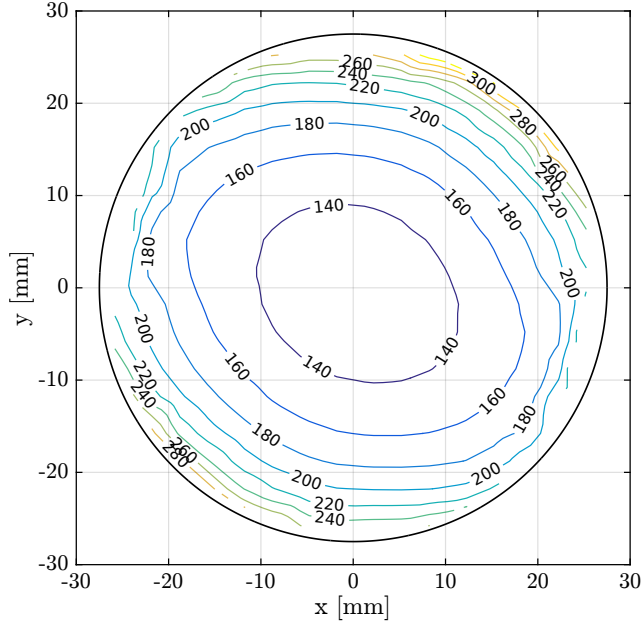


**Figure 5.30.** Gas cell evacuation times [ms] shown as contour lines within a cross-sectional slice at the location of the first  $^{233}\text{U}$  sources.

$$t_e(\vec{r}_a) = \int_L \frac{1}{v(\vec{r})} ds = \int_a^0 \frac{1}{v(\vec{r}(t))} |\vec{r}'(t)| dt. \quad (5.10)$$

Using the data from the Comsol simulation, a numerical integration according to this equation was performed along streamlines starting  $\sim 23$  cm upstream from the nozzle, where the furthest  $^{233}\text{U}$  source strips are positioned. In Fig. 5.30 these calculated evacuation times are indicated as a contour map within a cross-sectional slice of the gas cell at 23 cm, with the circle representing the circumference of the gas cell. The fastest evacuation time of 130 ms (not indicated) is obtained from the central axis. As one starts the simulation at larger diameters, in other words closer to the gas cell walls, the evacuation time increases. The asymmetry of the flow pattern is due to the structure that is holding the  $^{233}\text{U}$  sources in place.

The evacuation time as a function of distance from the exit hole is plotted in Fig. 5.31 for four different radial positions (5 mm, 12 mm, 19 mm and 26 mm) from the source surface to the central axis. The location of the closest  $^{233}\text{U}$  source to the exit nozzle as well as the furthest source is represented by the two vertical dashed black lines. A clear linear relationship between the distance from the exit hole and the evacuation time can be seen until the nozzle funnel.

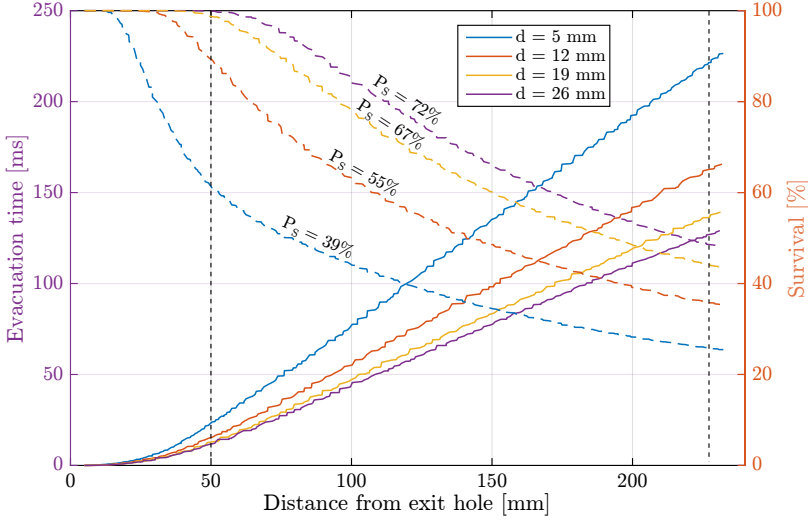


**Figure 5.31.** The evacuation time as a function of distance from the gas cell nozzle for four radial positions (solid lines). The estimated survival probability of ions against diffusion is indicated as the dashed lines for the four radial positions. The source location is shown between the vertical dashed lines.

As expected, the faster evacuation time is evidently nearer the central axis.

Because diffusion is expected to be a cause of significant loss to the stopped ions in the gas cell, the magnitude of this loss mechanism has been estimated. When a  $^{229}\text{Th}$  ion is stopped and thermalized in helium, the ion will be transported by the gas flow until it reaches the exit hole or is lost to neutralization due to collision with the gas cell walls. This assumption is valid if the gas purity is sufficiently high such that no losses to molecular formation happens. The probability of the ion hitting the wall can be estimated from the time-dependent distribution, Eq. (2.24), that was solved from the diffusion equation. This distribution can be used to estimate how far the ions drift transversely due to diffusion as they travel with the gas flow. By asserting that the ion is lost if it drifts further than a cylinder with the same radius as the inner radius of the gas cell from an initial position on the central axis, the following equation for the survival probability  $P_S(t, \vec{r}_0)$  as a function of evacuation time  $t$  and stopping position  $\vec{r}_0$  can be deduced:

$$P_S(t, \vec{r}_0) = \frac{1}{N_0} \int_{-\infty}^{\infty} \int_{-\infty}^{\infty} \int_{-\infty}^{\infty} C(x, y) N(\vec{r}, \vec{r}_0, t) dx dy dz, \quad (5.11)$$

where  $N(\vec{r}, \vec{r}_0, t)$  is the ion distribution according to Eq. (2.24) and  $C(x, y)$  describes the cylinder,

$$C(x, y) = \begin{cases} 1 & \text{if } \sqrt{x^2 + y^2} < r_{\text{gc}} \\ 0 & \text{if } \sqrt{x^2 + y^2} \geq r_{\text{gc}} \end{cases}, \quad (5.12)$$

where  $r_{\text{gc}}$  is the gas cell inner radius.

In order to evaluate the distribution  $N(\vec{r}, \vec{r}_0, t)$ , the diffusion coefficient between the  $^{229}\text{Th}$  ion and helium atom has been estimated using Eq. (2.26), at room temperature and with a pressure of 20 mbar using non-bonded helium and uranium with van der Waals radii of 140 pm and 186 pm, respectively [184]. To our knowledge, the equivalent radii for Th appears not to have been measured and therefore U is taken for this evaluation. With these input parameters, Eq. (5.11) was then numerically integrated. The calculated survival probabilities are plotted as a function of distance from the gas exit hole for same four different radial positions from the source surface, indicated with dashed lines in Fig. 5.31. As expected, the ion survival is largest at the radial distance  $d = 26$  mm, almost on the central axis of the gas cell, and is lowest near the source surface at  $d = 5$  mm. Also, the survival from the back of the gas cell in all of the calculated radial distances is smaller than near the front of the cell as the ions have more time to expand and therefore have a larger probability of hitting the cell wall. By integrating the survival probability between the vertical dashed lines marking the start and end of the source strips, at 50 mm and 231 mm, a mean survival probability for each radial stopping distance can be deduced. The percentages are marked next to the lines.

If a good recoil efficiency (20%) for the  $^{233}\text{U}$  strips is assumed and the maximum amount of source material (2.4 MBq) available is used, after diffusion losses, the isomer intensity can be estimated to be around 5000 isomers/sec. If other loss mechanism such the molecular formation and transportation losses through the IGISOL mass separator can be minimized, a collinear laser spectroscopy measurement should be readily possible even if the  $^{229}\text{Th}$  ion beam is distributed over several charge states. Additionally the charge state can be manipulated as shown in the previous section.

## 5.7 On-line production for $^{229}\text{Th}$

The on-line production of  $^{229}\text{Th}$  via light-ion induced fusion-evaporation reactions is attractive due to the favourable production of low-spin states in the final nuclei. This may result in a greater production of the isomeric state compared with the 2% decay branch in the alpha decay of  $^{233}\text{U}$ . The reaction



mechanism is in regular use at the IGISOL facility for the production and study of neutron-deficient isotopes, using a so-called light-ion ion guide, which was traditionally designed for use with H and He primary beams. In this type of gas cell, a stable (thin) target is mounted directly in the stopping volume since the recoil energy of the reaction products is small. Due to the small stopping volume ( $\sim 3\text{ cm}^3$ ) the delay time can be as short as one millisecond, highlighted by a measurement of the  $64\text{ }\mu\text{s}$   $^{204}\text{Tl}$  isomer, to our knowledge the shortest half-life ever measured in on-line mass separation with this gas cell [3]. The overall efficiency of the IGISOL technique for some heavier elements in which the recoil ranges are well within the stopping distance, i.e. the diameter of the target chamber, was measured over 30 years ago with several cases reaching almost 10% [2]. More recently, proton-induced fusion-evaporation reactions were used to populate isotopes several neutrons from stability using a combination of high primary beam energies and intensities [185]. For the production of  $^{229}\text{Th}^+$  in the singly-charged state, the small evacuation time of the gas cell is important as the upper limit of the lifetime of the isomeric state was recently suggested to be 10 ms [148].

The first on-line experiment at the IGISOL facility to determine the production rate of  $^{229}\text{Th}$  via the fusion-evaporation reaction  $^{232}\text{Th}(p, p3n)^{229}\text{Th}$  was performed at the end of 2017 using 50 MeV protons on a  $^{232}\text{Th}$  target installed in the light-ion ion guide. A pressure of approximately 100 mbar helium buffer gas was used to stop the reaction products, which were subsequently measured by MCP and silicon detectors at the focal plane of the IGISOL separator. The detection and verification of  $^{229}\text{Th}$  was realized to be difficult prior to the experiment as the long half-life prevents the direct detection of the alpha radiation. Measuring the ion count rate of the mass-separated  $A/q=229$  ion beam can only provide an upper limit for the production rate because it includes all other produced isotopes within the same isobar and possible molecular contaminants at that mass. Even for the JYFL Penning trap acting as a high resolving mass purifier [186, 187], isotopes with masses on the  $A = 229$  isobaric chain are too close in frequency in order to cleanly separate them. For example, the frequency difference between  $^{229}\text{Th}$  and  $^{229}\text{Pa}$  is only about 0.6 Hz (311 keV).

### 5.7.1 Detection of alpha-active radioisotopes

As the direct detection of  $^{229}\text{Th}$  is not possible without a laser spectroscopy measurement, the  $^{229}\text{Th}$  production had to be indirectly inferred via the decay radiation of other fusion-evaporation reaction products and scaling by the ratio of cross sections. In order to optimize the mass separator and settings of the gas cell and extraction optics, it is preferable to use activity with a short half-life (in an optimal scenario the lifetime of such activity would be below 1 minute).

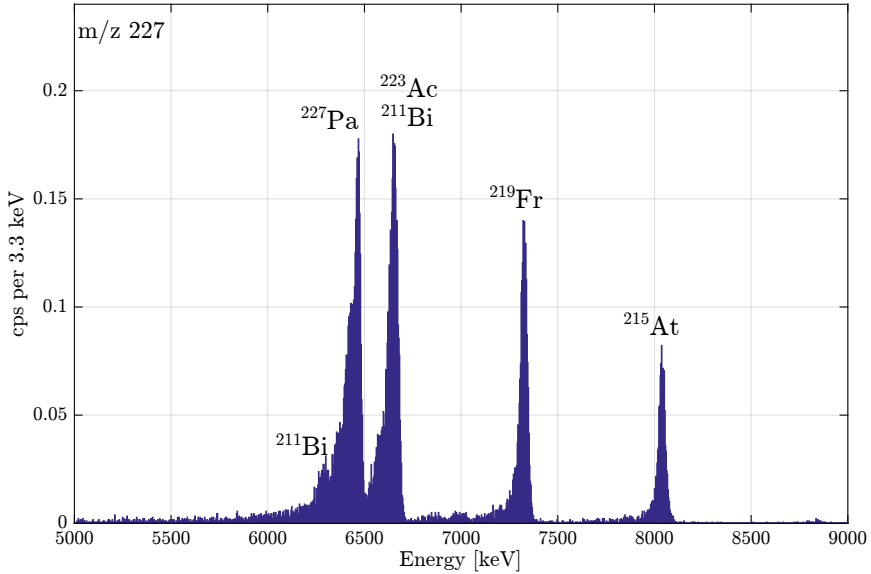


**Figure 5.32.** The alpha spectrum recorded from a Si detector onto which the mass-separated ion beam ( $A/q=227$ ) was implanted. The alpha lines were identified to belong to isotopes in the decay chain of  $^{227}\text{Pa}$  (shown in Fig. 5.33). The peak width (Full Width at Half Maximum) is  $\sim 40$  keV.

Within the mass region, isotopes of  $^{230}\text{Ac}$  and  $^{231}\text{Ac}$  have half-lives of 122 s and 7.5 m [188], respectively, however no beta activity was detected at the separator setting for  $A/q = 230$  and 231 despite reasonable cross section estimates (using the Talys v1.6 simulation software [189]) of 9 mb and 5 mb, respectively. No experimental cross sections for these isotopes are known to the author. Due to the lack of short-lived isotopes, the ion beam tuning had to be done with the sputtered target ions of  $^{232}\text{Th}$ .

Several alpha-active isotopes were detected at a number of isobars with the silicon charge-particle detector onto which the mass-separated ion beam was directly implanted. At  $A/q=227$ , the alpha radiation from isotopes in the decay chain of  $^{227}\text{Pa}$ , including  $^{227}\text{Pa}$  ( $t_{1/2} = 38.3$  min) [190], was clearly observed. The peak energies in the obtained alpha spectrum, shown in Fig. 5.32, were used to confirm the identification conclusively. The short-lived isotopes of the  $^{227}\text{Pa}$  decay chain with the relevant reactions are shown in Fig. 5.33.

At  $A/q=223$ , a similar alpha spectrum was recorded, shown in Fig. 5.34. We note that this spectrum was collected before the  $A/q=227$  implantation and therefore there has been no buildup of  $^{227}\text{Pa}$  on the detector surface which alpha decays into  $^{223}\text{Ac}$ . The main alpha lines of the  $^{223}\text{Ac}$  and  $^{211}\text{Bi}$  are not resolved

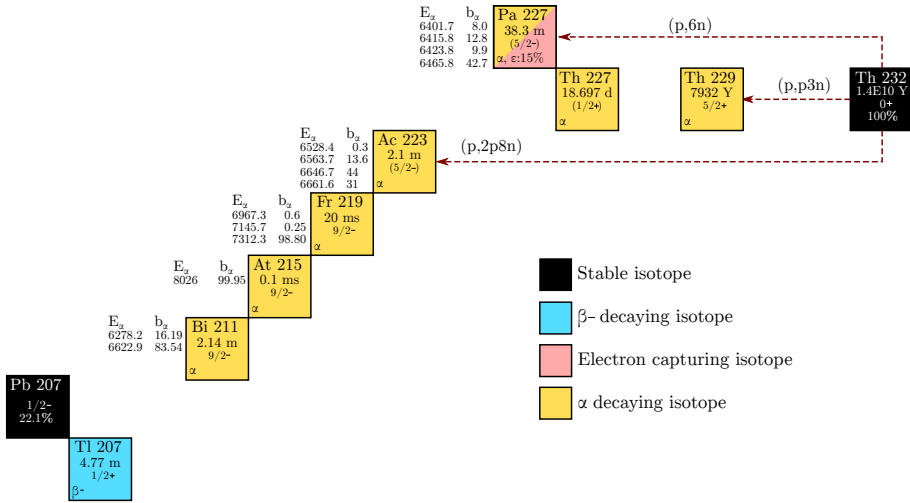


**Figure 5.33.** The short lived isotopes in the decay chain of  $^{227}\text{Pa}$  along with alpha lines for selected isotopes. The reactions producing the possible observed product isotopes are also shown. Data from reference [190] and the National Nuclear Data Center Chart of Nuclides [188].

from each other due to limited detector resolution and have both accumulated on the  $\sim 6640$  keV peak. By integrating the counts in the 6278 keV  $^{211}\text{Bi}$  alpha line, we can estimate that about 23% of the area of the  $\sim 6640$  keV peak belongs to  $^{211}\text{Bi}$ .

The production of  $^{223}\text{Ac}$  can be either due to the direct fusion-evaporation reaction (p,2p8n) and/or as a recoil from the alpha-decay of  $^{227}\text{Pa}$  if this isotope builds up in the  $^{232}\text{Th}$  target. According to a Talys simulation of the cross sections, the production of  $^{223}\text{Ac}$  (22 mb) should be comparable to that of  $^{227}\text{Pa}$  (16 mb). Again, experimental cross section data was not found for  $^{223}\text{Ac}$ . A future experiment would be required whereby the target would be removed from the gas cell and analyzed in the low-background counting station. Finally, at  $A/q=225$  and  $224$ , no  $^{225}\text{Pa}$ ,  $^{225}\text{Th}$  or  $^{224}\text{Th}$  was observed.

Further alpha spectra recorded at other  $A/q$  values are provided in the appendix A.

### 5.7.2 Production cross sections

To our knowledge, no experimental cross section is known for the reaction  $^{232}\text{Th}(p, p3n)^{229}\text{Th}$  and therefore the production cross sections for the isotopes produced in proton-induced fusion-evaporation reactions with  $^{232}\text{Th}$  were esti-

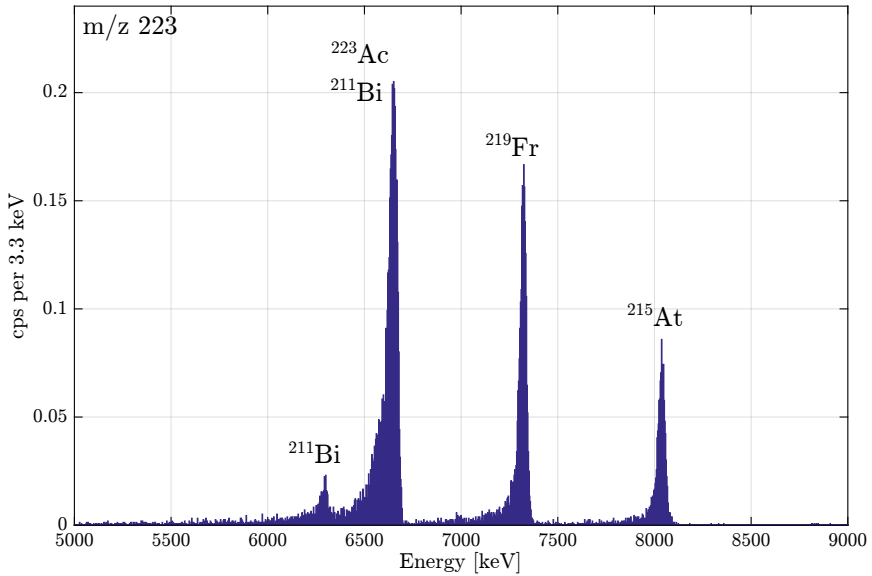


**Figure 5.34.** The alpha spectrum recorded following implantation of  $A/q=223$ . The alpha lines were identified to belong to isotopes in the decay chain of  $^{223}\text{Ac}$ .

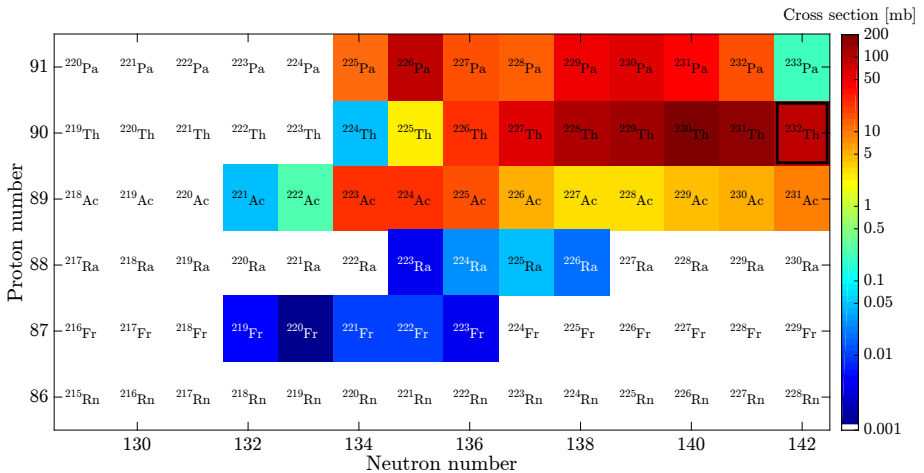


**Figure 5.35.** Estimated production cross sections using Talys for the isotopes evaporated in the  $^{232}\text{Th}(p, x)\text{Y}$  reaction with 50 MeV proton beam energy. The cross section is colored only if it is above 1  $\mu\text{b}$ .

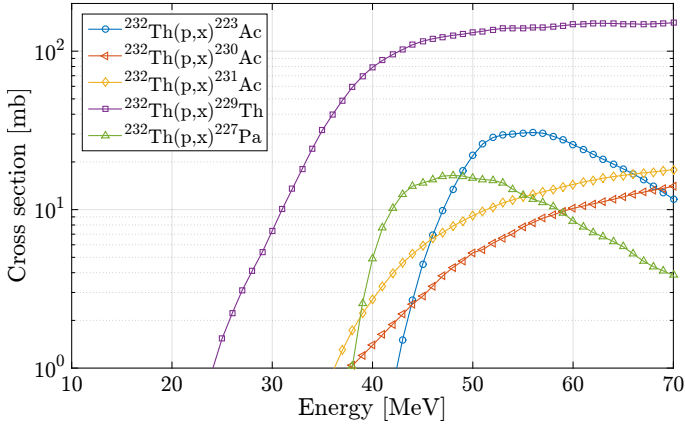


**Figure 5.36.** Cross sections of selected isotopes calculated with the Talys simulation software and plotted as a function of proton beam energy.

mated using the Talys software [189]. The cross sections from the simulation at the experimental proton beam energy of 50 MeV are illustrated in Fig. 5.35, which reproduces the relevant part of the nuclear chart. Figure 5.36 further plots the simulated cross sections of few relevant isotopes as a function of energy.

Absolute experimental cross sections for  $^{232}\text{Th}(p, 6n)^{227}\text{Pa}$  at 50 MeV has been measured by H. C. Suk et al. [191], M. Lefort et al. [192] and W.W. Meinke et al. [193]. There is, however, considerable disagreement in the experimental data: W. W. Meinke has measured a cross section of 2 mb whereas H. C. Suk et al. and M. Lefort report the cross section to be 12 mb and 30 mb, respectively. Also the shape of the cross section curve as a function of energy varied significant from author to author. Talys estimates the  $^{227}\text{Pa}$  cross section to be 15 mb at 50 MeV.

Otherwise, when checking against available cross-section data from the Exfor experimental nuclear reaction database [194], Talys simulations appear to give correct cross sections within factor of  $\sim 2$  for  $^{230-232}\text{Pa}$ ,  $^{228,230,231}\text{Th}$  and  $^{225-228}\text{Ac}$ . For some isotopes such as  $^{226,229}\text{Pa}$  and  $^{226}\text{Th}$ , there appears to be a gross over-estimation, with Talys suggesting over an order of magnitude higher cross section than that reported in the experimental data.

### 5.7.3 Estimation of $^{229}\text{Th}$ yield

As experimental cross sections are available for  $^{227}\text{Pa}$  and because it was clearly detected during the on-line experiment, the yield estimation of  $^{229}\text{Th}$  was determined via the yield of  $^{227}\text{Pa}$ . To obtain the yield of  $^{227}\text{Pa}$  an accumulation

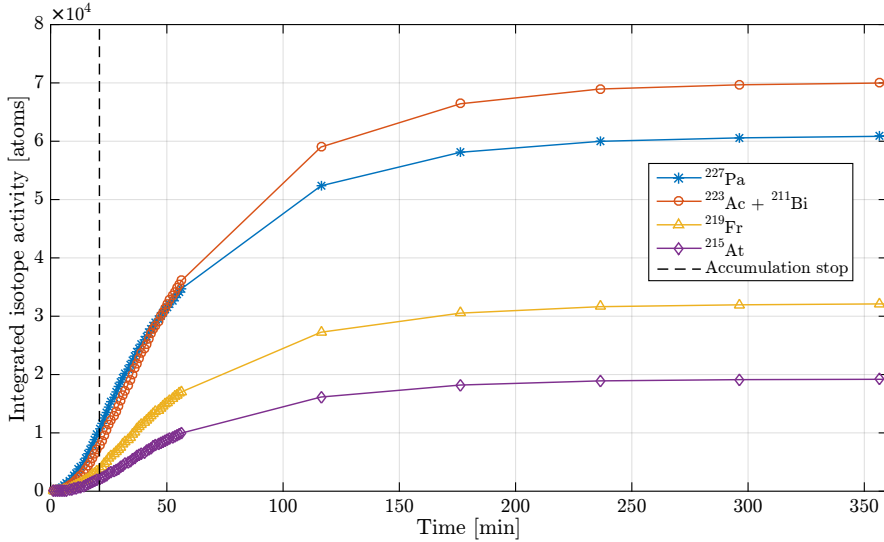


**Figure 5.37.** The accumulation profile of the isotopes measured during the implantation of the  $A/q=227$  ion beam onto the Si detector. The dashed line shows the time when the beam was stopped.

profile was measured by implanting the  $A/q=227$  ion beam directly onto the silicon detector. By integrating the alpha peak areas from spectra taken sequentially during and after the implantation, and then by calculating the number of isotopes in the silicon detector using the alpha branching ratios and assuming a 50% detection efficiency, the accumulation curves in Fig. 5.37 were attained. The implantation was started at time  $t=0$  minutes and stopped at the vertical black dashed line, after which the spectra are measured for several half-lives of  $^{227}\text{Pa}$  until the majority of the  $^{227}\text{Pa}$  has decayed.

According to the accumulation profile, the number of  $^{227}\text{Pa}$  during an implantation time of 1260 s was  $\sim 61 \cdot 10^3$  ions, in other words 49 ions/s at a primary beam intensity of  $1 \mu\text{A}$ . By scaling the  $^{227}\text{Pa}$  yield with the cross section ratio between  $^{229}\text{Th}$  and  $^{227}\text{Pa}$  (using Talys, a cross section for  $^{229}\text{Th}$  of 131 mb at 50 MeV is used), a yield of 200 ions/s/ $\mu\text{A}$  to 3000 ions/s/ $\mu\text{A}$  is obtained for  $^{229}\text{Th}$  depending on which experimental  $^{227}\text{Pa}$  cross section is used.

An upper limit for the yield of  $^{229}\text{Th}$  was also estimated from the MCP count rate at  $A/q=229$ . With the installation of new set of microchannel plates prior to this experiment, the ion detection efficiency should be close to the 60% value estimated from the active area. With this detection efficiency a yield of 500 ions/s/ $\mu\text{A}$  is obtained for the mass-separated ion beam at  $A/q=229$ . This value not only includes the  $^{229}\text{Th}$  ions, but all other fusion-evaporation reaction

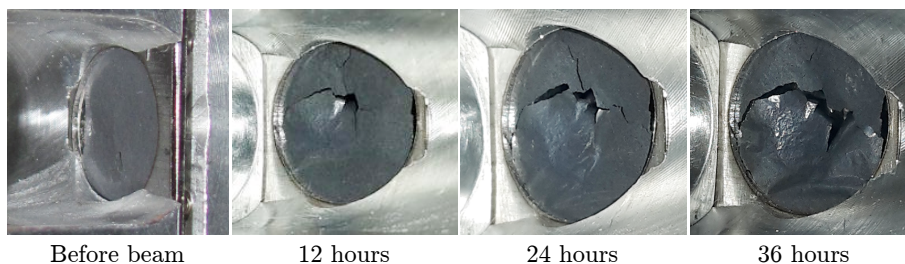


**Figure 5.38.** Photographs of the  $^{232}\text{Th}$  target during the experiment. A clear progressive degradation of the target can be seen.

products at  $A/q=229$  as well as possible contaminant molecules.

#### 5.7.4 Target damage and optimal target thickness

During the on-line experiment, progressively worsening yields were observed. In an earlier on-line test in which no radioactive beams via fusion-evaporation were detected, it was realized that the  $^{232}\text{Th}$  targets are sensitive and may not tolerate the primary beam for extended periods of time. In the earlier test, a target with a thickness of  $1.7\text{ mg/cm}^2$  was completely destroyed. Therefore in this experiment a thicker target of  $2.6\text{ mg/cm}^2$  was used to obtain better durability. However, as the target was visually checked for any damage during the experiment, a clear degradation was observed as shown in Fig. 5.38.

The reason for reducing the thickness of the thorium target is to try to reduce the effect of the competing strong fission channel which at a proton bombarding energy of 50 MeV has a cross section exceeding 1 b [195]. The fission fragments are expected to create significant ionization of the helium gas and therefore unwanted neutralization of the products may occur due to the presence of free electrons. Due to the energy of the fragments, they can exit the target from much deeper than fusion-evaporation recoils and thus an optimal target thickness would be one from which the fusion-evaporation products may still efficiently recoil.

In order to obtain a quantitative number for the effective layer thickness for fusion-evaporation products, the energy differential cross section as a function of the recoil energy for  $^{229}\text{Th}$  and  $^{227}\text{Pa}$  was simulated with the Talys software along with a SRIM calculation of the stopping range of  $^{229}\text{Th}$  and  $^{227}\text{Pa}$  ions in metallic  $^{232}\text{Th}$ . The differential cross sections and the ranges are shown in Fig. 5.39. The range is plotted for  $^{229}\text{Th}$  ions, however, it can also be taken as the range for  $^{227}\text{Pa}$  as there was little difference between the two.

By comparing the two plots in Fig. 5.39, a thickness of about  $0.6 \pm 0.3 \mu\text{m}$  ( $0.7 \pm 0.4 \text{ mg/cm}^2$ ) of pure metallic thorium can be deduced to provide approximately 90% of all  $^{229}\text{Th}$  fusion-evaporation recoils. Therefore a pure thorium target of thickness  $1 \text{ mg/cm}^2$  should be the most optimum both from the viewpoint of requiring minimal fission fragment yield with almost maximum fusion-evaporation recoil rate. A noteworthy feature in the differential cross sections is the higher maximum position for  $^{227}\text{Pa}$  than that of  $^{229}\text{Th}$ . This might indicate a slightly better recoil efficiency for  $^{227}\text{Pa}$ .

The targets that were used in the on-line experiments were manufactured by rolling metallic thorium foils until the preferred thickness was attained. The limit for rolling was about  $1.5 \text{ mg/cm}^2$  after which the thorium foil started to break and became too fragile to handle. The thicker  $2.6 \text{ mg/cm}^2$  target was considerably stronger but it could not still withstand the primary beam and, as shown above, a clear target degradation was observed. In typical proton-induced fusion-evaporation reactions at IGISOL, primary beam intensities of  $10 \mu\text{A}$  are regularly used in order to maximize the yield of secondary reaction products. In order to continue the on-line studies of the production of  $^{229}\text{Th}$ , new target manufacturing concepts are currently being considered. Solutions could include sputtering thorium on a backing material such as a thin nickel foil or applying a novel Drop-on-Demand inkjet printing technique [196] to produce a thin thorium target. We note that if this was successful, other actinide materials could be prepared in a similar manner, for example utilizing thin  $^{233}\text{U}$  foils on a backing material for on-line purposes.

## 5.8 Summary and outlook

In this chapter various aspects related to the creation of thorium ion beams via laser resonance ionization of filament-based dispensers,  $^{233}\text{U}$  alpha-recoil sources and in on-line fusion-evaporation reactions have been discussed. Although the goal has been the specific challenge of creating a  $^{229}\text{Th}$  ion beam and its uniquely low-lying isomer for future study with high-resolution collinear laser spectroscopy at IGISOL, many of the results presented here are highly relevant to the current focus of research in heavy elements at various gas-cell facilities.

The complicated atomic structure of actinide elements has created a rich set of phenomena as seen through the creation of a laser ion source for thorium from filament dispensers. Even though high flux thorium and plutonium ion beams have been created by in-gas-cell resonance laser ionization, the excitation schemes and broad structures seen in the wavelength spectra of both elements will be further investigated in future studies.

The  $^{233}\text{U}$  alpha-recoil source and the testing of the new gas cell will continue with



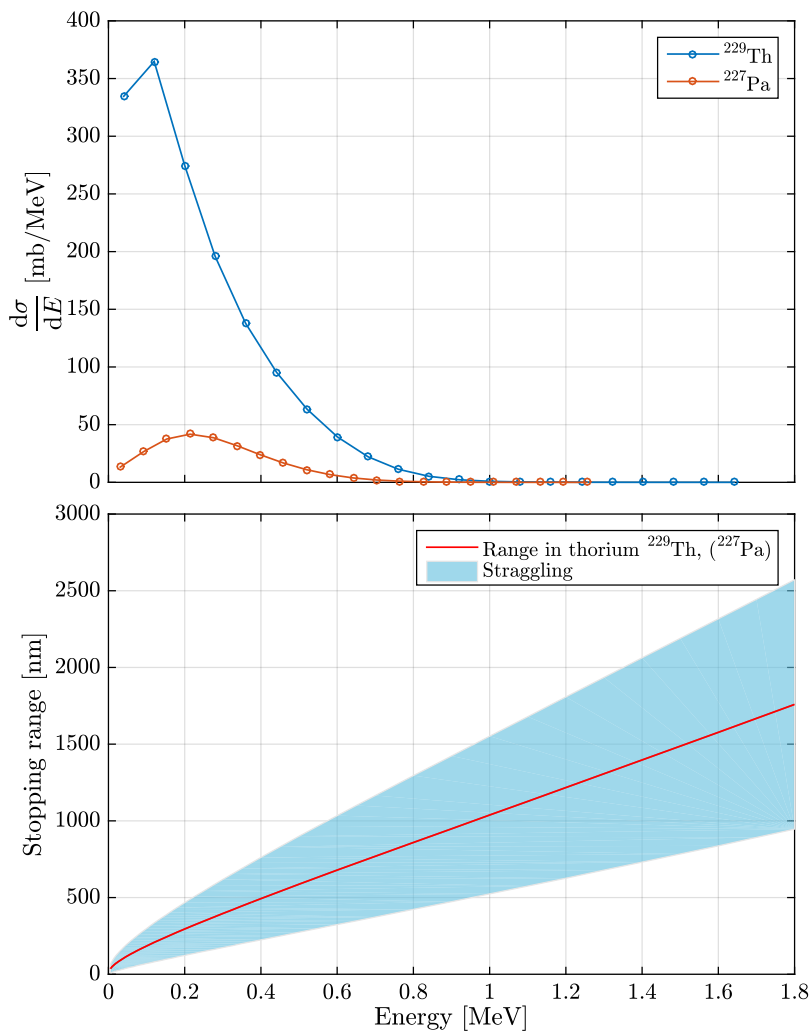


**Figure 5.39.** The differential production cross sections for  $^{229}\text{Th}$  and  $^{227}\text{Pa}$  from Talys simulations (upper plot) with the range of  $^{229}\text{Th}$  and  $^{227}\text{Pa}$  ions in metallic  $^{232}\text{Th}$  from Srim (lower plot).

the future acquisition of new sources from TU Vienna. Careful manufacturing in both how the  $^{233}\text{U}$  is applied to the substrate and the smoothness of the substrate itself is required in order to ensure the highest recoil efficiency. With the new sources and continued gas-cell development, a high yield off-line ion source for  $^{229g,m}\text{Th}$  is planned to be realized, with the possibility of manipulating the charge states for further spectroscopy. The first test source is currently being manufactured and the recoil efficiency is to be measured in the near future.

A first on-line experiment to study the creation of singly-charged  $^{229}\text{Th}^+$  ion beams through fusion-evaporation by bombarding a  $^{232}\text{Th}$  target with high-energy protons has been realized. This experiment highlighted, through the measurement of alpha-decay lines of the fusion-evaporation products, that several heavy actinide isotopes can be successfully produced and extracted as ion beams from the IGISOL gas cell, even in the presence of the plasma created by the competing fission channel. This has not only given confidence to the realization of a high on-line yield of  $^{229m}\text{Th}$ , but also promises access to elements and radioisotopes previously not studied using optical techniques, where fundamental ground state nuclear structure including spins, electromagnetic moments and changes in mean-square charge radii may be accessed for the first time. This would complement efforts underway at other facilities utilizing heavy-ion fusion-evaporation reactions and in-flight separators. The development of new, more durable, targets also from long-lived radioisotopes in the actinide region, could expand the accessible isotopes for spectroscopic studies. Furthermore, the chemical non-selectivity of the IGISOL method can be a great advantage if the reaction cross sections, especially relative changes in them, are to be experimentally determined.



## Chapter 6

# Summary and outlook

The work in this thesis commenced during the construction phase of the new IGISOL-4 radioactive ion beam facility. One of the most critical aspects which, to date, continues to influence all experiments, is the careful preparation placed on attaining a high purity of the buffer gas. The gas purification system of the IGISOL facility, constructed by the author, is presented along with several aspects of gas-phase chemistry which has resulted in fingerprints to indicate that a high purity has been reached. Charge exchange processes, chemical reactions within the gas cell and formation of contaminant ion beams are all discussed. To further reduce the contaminant beams, the construction of a cryocooler connected to a gas cell will be finalized in the near future. This will be characterized using a new off-line ion guide quadrupole mass spectrometer station with the aim of performing studies on the elemental dependence of extraction and impurity behavior as a function of temperature.

The improvements in gas purity have had an immediate impact on the availability of atomic beams, in particular those associated with highly reactive elements such as plutonium and thorium which have been studied in detail during this work. The creation of pure ion beams of several plutonium isotopes has been demonstrated by combining atom evaporation from filament dispensers and laser resonance ionization inside a gas cell. During the development of the plutonium laser ion source, a collisional quenching phenomenon was discovered to have a significant effect on the ionization process. The resonance excitation, which had been efficiently realized in earlier hot-cavity work performed under vacuum, showed little response in the gaseous environment of the gas cell. This led to a fruitful collaboration with Nagoya University, Japan, and joint investigations of the plutonium ionization scheme with a frequency-doubled grating-based Ti:sapphire laser. This resulted in a dramatically expanded set of atomic levels and a clearer understanding of the behavior of the ionization scheme, which

was lacking prior to this work.

An interesting approach to alleviate the reduced efficiency due to the collisional phenomena would be to perform laser ionization in the supersonic gas jet formed downstream from the gas cell. A reduction in both density and temperature would not only result in fewer collisional losses, but directly translates into a reduction in line broadening of the atomic transitions. In recent years, efforts have begun to exploit the gas jet for high-resolution resonance ionization spectroscopy [197], culminating in the pioneering on-line measurement of actinium isotopes around the  $N=126$  shell closure [30]. Although the broadening in the jet is substantially reduced in comparison to the gas cell conditions, the achievable linewidth is limited by the residual Doppler effect. It is noteworthy that this could be reduced even further by the cryogenic approach as mentioned above. By reducing the gas temperature inside the gas cell, a reduction of the temperature in the supersonic jet can be expected.

Thorium, of great interest due to its low-lying  $^{229}\text{Th}$  nuclear isomeric state, was also a focus of this thesis. Similar to plutonium, the filament-based dispenser for thorium was successful in the creation of a thorium ion beam, however, the required filament temperature resulted in significant molecular contaminant beams. This prompted the study of several different types of filament dispenser and an investigation into beam purification by accelerating the ions through the high density gas-jet region in order to use collisional-induced dissociation. Although the ion beam was cleaned from molecular contaminants, it has been shown that the collisions do not have sufficient energy to break molecular bonds and a so-called size-exclusion ion beam extraction method of purification has been suggested to explain the results.

In addition to creating a laser ion source from filament dispensers,  $^{233}\text{U}$  alpha-recoil sources have been characterized for the production of  $^{229}\text{Th}$  beams. By mounting such sources into the volume of a new design of gas cell, intense beams of  $^{229}\text{Th}^{3+}$  are expected to be realized given sufficient source material. By experimenting with a  $^{233}\text{U}$  source in a gas cell, charge state manipulation from  $^{229}\text{Th}^{3+}$  to  $^{229}\text{Th}^{2+}$  has been demonstrated following the addition of a trace amount of Xe which is added to the helium buffer gas. The existing in-house  $^{233}\text{U}$  sources were, however, shown through implantation measurements to have a surprisingly low recoil efficiency and a series of Rutherford Backscattering measurements at a Pelletron accelerator validated the assumption of contaminants in the sources leading to a likely explanation of the poor efficiency. In the mean time, new  $^{233}\text{U}$  alpha-recoil sources have been requested and are being developed by TU Vienna.

Finally, on-line production of  $^{229}\text{Th}$  was experimentally investigated in fusion-evaporation reactions using  $^{232}\text{Th}$  targets. The on-line method is planned to be used in the investigation of the  $^{229}\text{Th}^{1+}$  isomeric state in order to resolve

outstanding questions regarding the nature of the isomer in this singly-charged state. In these experiments the detection of several alpha-active isotopes, namely  $^{223}\text{Ac}$  and  $^{227}\text{Pa}$ , allowed for an estimation of the  $^{229}\text{Th}$  production rate of up to a few thousand per second. During the experiment significant target damage was observed as result of the requirement of thin targets to reduce the competing fission channel. This has prompted an investigation into new methods of target production, for example, a novel drop-on-demand inkjet printing technique [196] to produce thin but durable thorium targets. Expanding the target manufacturing to long-lived actinide isotopes in general could lead to the production and high-resolution optical spectroscopy of several new isotopes and measurement of their nuclear properties.



# Appendix A

## On-line alpha spectra

This appendix presents the alpha spectra taken at other isobars in addition to those shown in the on-line production for  $^{229}\text{Th}$ , section 5.7 in chapter 5. These are the results of implantation of mass-separated ion beams created in  $^{232}\text{Th}(p, x)\text{Y}$  fusion-evaporation reactions with protons at a beam energy of 50 MeV.



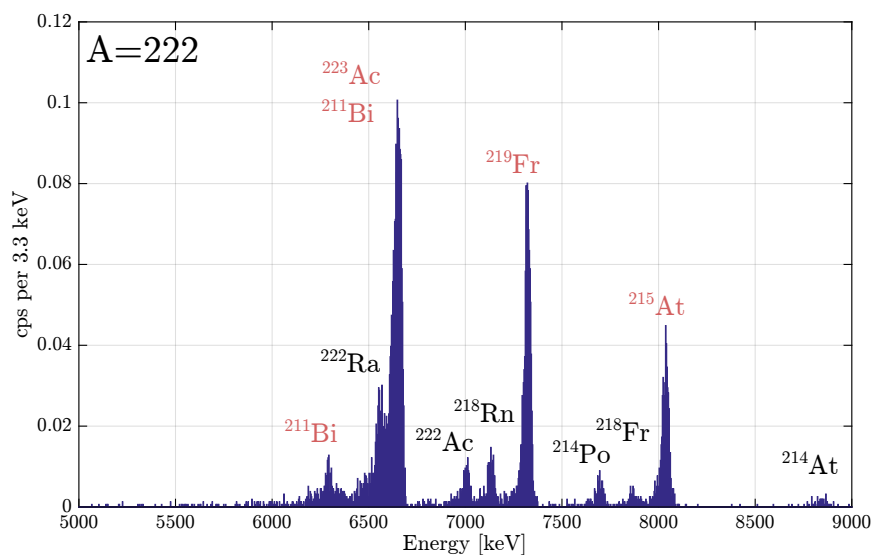


**Figure A.1.** The alpha spectrum recorded from a Si detector following implantation of  $A/q=222$  beam. Beams of  $A=222$  isotopes are detected as labeled in black in the figure, but with much smaller intensity than  $^{223}\text{Ac}$  or  $^{227}\text{Pa}$ . The  $^{223}\text{Ac}$  and its daughters are due to beam leakage from the neighboring isobar.

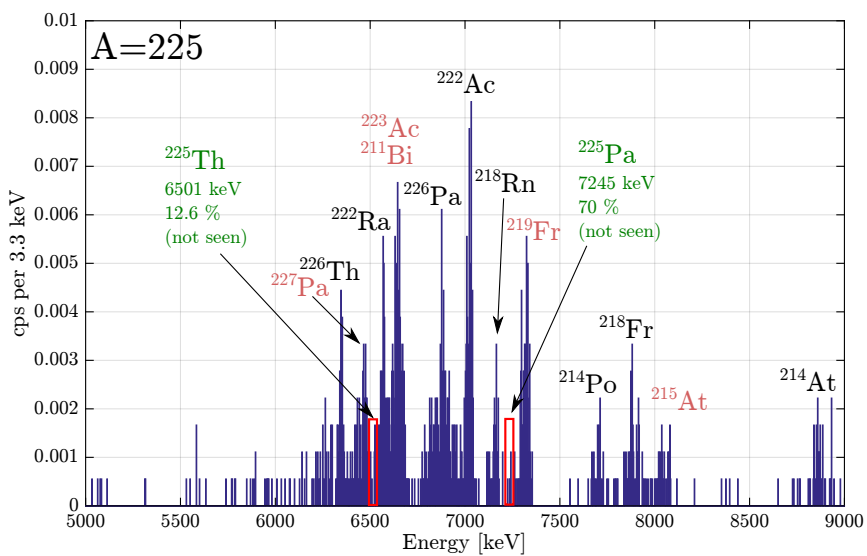


**Figure A.2.** The alpha spectrum recorded from a Si detector following implantation of  $A/q=225$  beam. No  $A=225$  isotopes are observed. Several contaminant isotopes from neighboring masses are seen with low intensity.



# References

- [1] Y. Blumenfeld, T. Nilsson, and P. Van Duppen, *Facilities and methods for radioactive ion beam production*, *Physica Scripta*, T152, (2013), 014023, doi:[10.1088/0031-8949/2013/T152/014023](https://doi.org/10.1088/0031-8949/2013/T152/014023).
- [2] J. Ärje, J. Äystö, H. Hyvönen, P. Taskinen, V. Koponen, J. Honkanen, A. Hautojärvi, and K. Vierinen, *Submillisecond On-Line Mass Separation of Nonvolatile Radioactive Elements: An Application of Charge Exchange and Thermalization Processes of Primary Recoil Ions in Helium*, *Physical Review Letters*, 54, (1985), 99, doi:[10.1103/PhysRevLett.54.99](https://doi.org/10.1103/PhysRevLett.54.99).
- [3] I. D. Moore, P. Dendooven, and J. Ärje, *The IGISOL technique—three decades of developments*, *Hyperfine Interactions*, 223(1), (2014), 17, doi:[10.1007/s10751-013-0871-0](https://doi.org/10.1007/s10751-013-0871-0).
- [4] J. Äystö, *Development and applications of the IGISOL technique*, *Nuclear Physics A*, 693(1), (2001), 477, doi:[10.1016/S0375-9474\(01\)00923-X](https://doi.org/10.1016/S0375-9474(01)00923-X).
- [5] L. Weissman, P. A. Lofy, D. A. Davies, D. J. Morrissey, P. Schury, S. Schwarz, T. Sun, and G. Bollen, *First extraction tests of the NSCL gas cell*, *Nuclear Physics A*, 746, (2004), 655, doi:[10.1016/j.nuclphysa.2004.09.045](https://doi.org/10.1016/j.nuclphysa.2004.09.045).
- [6] W. R. Plaß, T. Dickel, S. Purushothaman, P. Dendooven, H. Geissel, J. Ebert, E. Haettner, C. Jesch, M. Ranjan, M. P. Reiter, H. Weick, F. Amjad, S. Ayet, M. Diwisch, A. Estrade, F. Farinon, F. Greiner, N. Kalantar-Nayestanaki, R. Knöbel, J. Kurcewicz, *et al.*, *The FRS Ion Catcher – A facility for high-precision experiments with stopped projectile and fission fragments*, *Nuclear Instruments and Methods in Physics Research Section B*, 317, (2013), 457, doi:[10.1016/j.nimb.2013.07.063](https://doi.org/10.1016/j.nimb.2013.07.063).
- [7] S. Schwarz, G. Bollen, S. Chouhan, J. J. Das, M. Green, C. Magsig, D. J. Morrissey, J. Ottarson, C. Sumithrarachchi, A. C. C. Villari, and A. Zeller, *The NSCL cyclotron gas stopper – Entering commissioning*, *Nuclear Instruments and Methods in Physics Research Section B*, 376, (2016), 256, doi:[10.1016/j.nimb.2015.12.035](https://doi.org/10.1016/j.nimb.2015.12.035).

- [8] G. D. Alkhazov, L. Kh. Batist, A. A. Bykov, V. D. Vitman, V. S. Letokhov, V. I. Mishin, V. N. Panteleyev, S. K. Sekatsky, and V. N. Fedoseyev, *Application of a high efficiency selective laser ion source at the IRIS facility*, Nuclear Instruments and Methods in Physics Research Section A, 306(1), (1991), 400, doi:[10.1016/0168-9002\(91\)90348-T](https://doi.org/10.1016/0168-9002(91)90348-T).
- [9] V. N. Fedoseyev, G. Huber, U. Köster, J. Lettry, V. Mishin, H. Ravn, and V. Sebastian, *The ISOLDE laser ion source for exotic nuclei*, Hyperfine Interactions, 127(1), (2000), 409, doi:[10.1023/A:1012609515865](https://doi.org/10.1023/A:1012609515865).
- [10] J. Lassen, P. Bricault, M. Dombbsky, J. P. Lavoie, C. Geppert, and K. Wendt, *Resonant Ionization Laser Ion Source Project at TRIUMF*, Hyperfine Interactions, 162(1), (2005), 69, doi:[10.1007/s10751-005-9212-2](https://doi.org/10.1007/s10751-005-9212-2).
- [11] Y. Liu, *ORNL developments in laser ion sources for radioactive ion beam production*, Hyperfine Interactions, 227(1), (2014), 85, doi:[10.1007/s10751-013-0965-8](https://doi.org/10.1007/s10751-013-0965-8).
- [12] V. N. Fedosseev, Y. Kudryavtsev, and V. I. Mishin, *Resonance laser ionization of atoms for nuclear physics*, Physica Scripta, 85(5), (2012), 058104, doi:[10.1088/0031-8949/85/05/058104](https://doi.org/10.1088/0031-8949/85/05/058104).
- [13] L. Vermeeren, N. Bijmens, M. Huyse, Y. A. Kudryavtsev, P. Van Duppen, J. Wauters, Z. N. Qamhieh, P. Thoen, E. Vandeweert, and R. E. Silverans, *An On-Line Laser Ion Source Based on Resonance Photoionization in a Gas Cell*, Physical Review Letters, 73, (1994), 1935, doi:[10.1103/PhysRevLett.73.1935](https://doi.org/10.1103/PhysRevLett.73.1935).
- [14] P. Van Duppen, B. Bruyneel, M. Huyse, Y. Kudryavtsev, P. Van Den Bergh, and L. Vermeeren, *Beams of short lived nuclei by selective laser ionization in a gas cell*, Hyperfine Interactions, 127(1), (2000), 401, doi:[10.1023/A:1012657431795](https://doi.org/10.1023/A:1012657431795).
- [15] I. D. Moore, T. Kessler, T. Sonoda, Y. Kudryavstev, K. Peräjärvi, A. Popov, K. D. A. Wendt, and J. Äystö, *A study of on-line gas cell processes at IGISOL*, Nuclear Instruments and Methods in Physics Research Section B, 268(6), (2010), 657, doi:[10.1016/j.nimb.2009.12.001](https://doi.org/10.1016/j.nimb.2009.12.001).
- [16] Y. Hirayama, Y. X. Watanabe, N. Imai, H. Ishiyama, S. C. Jeong, H. S. Jung, H. Miyatake, M. Oyaizu, S. Kimura, M. Mukai, Y. H. Kim, T. Sonoda, M. Wada, M. Huyse, Y. Kudryavtsev, and P. Van Duppen, *On-line experimental results of an argon gas cell-based laser ion source (KEK Isotope Separation System)*, Nuclear Instruments and Methods in Physics Research Section B, 376, (2016), 52, doi:[10.1016/j.nimb.2016.03.031](https://doi.org/10.1016/j.nimb.2016.03.031).
- [17] T. Sonoda, H. Iimura, M. Reponen, M. Wada, I. Katayama, V. Sonnenschein, T. Takamatsu, H. Tomita, and T. M. Kojima, *The laser*

- and optical system for the RIBF-PALIS experiment*, Nuclear Instruments and Methods in Physics Research Section A, 877, (2018), 118, doi:[10.1016/j.nima.2017.09.055](https://doi.org/10.1016/j.nima.2017.09.055).
- [18] R. Ferrer, B. Bastin, D. Boilley, P. Creemers, P. Delahaye, E. Liénard, X. Fléchar, S. Franchoo, L. Ghys, M. Huyse, Y. Kudryavtsev, N. Lecesne, H. Lu, F. Lutton, E. Mogilevskiy, D. Pauwels, J. Piot, D. Radulov, L. Rens, H. Savajols, *et al.*, *In gas laser ionization and spectroscopy experiments at the Superconducting Separator Spectrometer (S3): Conceptual studies and preliminary design*, Nuclear Instruments and Methods in Physics Research Section B, 317, (2013), 570, doi:[10.1016/j.nimb.2013.07.028](https://doi.org/10.1016/j.nimb.2013.07.028).
- [19] J. Sarén, J. Uusitalo, M. Leino, P. T. Greenlees, U. Jakobsson, P. Jones, R. Julin, S. Juutinen, S. Ketelhut, M. Nyman, P. Peura, P. Rahkila, C. Scholey, and J. Sorri, *The new vacuum-mode recoil separator MARA at JYFL*, Nuclear Instruments and Methods in Physics Research Section B, 266(19), (2008), 4196, doi:[10.1016/j.nimb.2008.05.027](https://doi.org/10.1016/j.nimb.2008.05.027).
- [20] P. Papadakis, I. Moore, I. Pohjalainen, J. Sarén, and J. Uusitalo, *Development of a low-energy radioactive ion beam facility for the MARA separator*, Hyperfine Interactions, 237(1), (2016), 152, doi:[10.1007/s10751-016-1364-8](https://doi.org/10.1007/s10751-016-1364-8).
- [21] P. Campbell, I. D. Moore, and M. R. Pearson, *Laser spectroscopy for nuclear structure physics*, Progress in Particle and Nuclear Physics, 86, (2016), 127, doi:[10.1016/j.pnpnp.2015.09.003](https://doi.org/10.1016/j.pnpnp.2015.09.003).
- [22] M. Laatiaoui, W. Lauth, H. Backe, M. Block, D. Ackermann, B. Cheal, P. Chhetri, C. E. Düllmann, P. Van Duppen, J. Even, R. Ferrer, F. Giacoppo, S. Götz, F. P. Heßberger, M. Huyse, O. Kaleja, J. Khuyagbaatar, P. Kunz, F. Lautenschläger, A. K. Mistry, *et al.*, *Atom-at-a-time laser resonance ionization spectroscopy of nobelium*, Nature, 538, (2016), 495, doi:[10.1038/nature19345](https://doi.org/10.1038/nature19345).
- [23] T. E. Cocolios, H. H. A. Suradi, J. Billowes, I. Budinčević, R. P. de Groote, S. D. Schepper, V. N. Fedosseev, K. T. Flanagan, S. Franchoo, R. F. G. Ruiz, H. Heylen, F. L. Blanc, K. M. Lynch, B. A. Marsh, P. J. R. Mason, G. Neyens, J. Papuga, T. J. Procter, M. M. Rajabali, R. E. Rossel, *et al.*, *The Collinear Resonance Ionization Spectroscopy (CRIS) experimental setup at CERN-ISOLDE*, Nuclear Instruments and Methods in Physics Research Section B, 317, (2013), 565, doi:[10.1016/j.nimb.2013.05.088](https://doi.org/10.1016/j.nimb.2013.05.088).
- [24] H. Backe, W. Lauth, M. Block, and M. Laatiaoui, *Prospects for laser spectroscopy, ion chemistry and mobility measurements of superheavy elements in buffer-gas traps*, Nuclear Physics A, 944, (2015), 492, doi:[10.1016/j.nuclphysa.2015.07.002](https://doi.org/10.1016/j.nuclphysa.2015.07.002).

- [25] A. Voss, V. Sonnenschein, P. Campbell, B. Cheal, T. Kron, I. D. Moore, I. Pohjalainen, S. Raeder, N. Trautmann, and K. Wendt, *High-resolution laser spectroscopy of long-lived plutonium isotopes*, Physical Review A, 95, (2017), 032506, doi:[10.1103/PhysRevA.95.032506](https://doi.org/10.1103/PhysRevA.95.032506).
- [26] *The nuClock project* (2018), <https://www.nuclock.eu>, Accessed on 2018-04-24.
- [27] E. Peik and M. Okhapkin, *Nuclear clocks based on resonant excitation of  $\gamma$ -transitions*, Comptes Rendus Physique, 16(5), (2015), 516, doi:[10.1016/j.crhy.2015.02.007](https://doi.org/10.1016/j.crhy.2015.02.007).
- [28] E. Peik and Chr. Tamm, *Nuclear laser spectroscopy of the 3.5 eV transition in Th-229*, Europhysics Letters, 61(2), (2003), 181, doi:[10.1209/epl/i2003-00210-x](https://doi.org/10.1209/epl/i2003-00210-x).
- [29] P. Chhetri, D. Ackermann, H. Backe, M. Block, B. Cheal, C. E. Düllmann, J. Even, R. Ferrer, F. Giacoppo, S. Götz, F. P. Heßberger, O. Kaleja, J. Khuyagbaatar, P. Kunz, M. Laatiaoui, F. Lautenschläger, W. Lauth, E. M. Ramirez, A. K. Mistry, S. Raeder, *et al.*, *Impact of buffer gas quenching on the  $^1S_0 \rightarrow ^1P_1$  ground-state atomic transition in nobelium*, The European Physical Journal D, 71(7), (2017), 195, doi:[10.1140/epjd/e2017-80122-x](https://doi.org/10.1140/epjd/e2017-80122-x).
- [30] R. Ferrer, A. Barzakh, B. Bastin, R. Beerwerth, M. Block, P. Creemers, H. Grawe, R. de Groote, P. Delahaye, X. Fléchar, S. Franchoo, S. Fritzsche, L. P. Gaffney, L. Ghys, W. Gins, C. Granados, R. Heinke, L. Hijazi, M. Huyse, T. Kron, *et al.*, *Towards high-resolution laser ionization spectroscopy of the heaviest elements in supersonic gas jet expansion*, Nature Communications, 8, (2017), 14520, doi:[10.1038/ncomms14520](https://doi.org/10.1038/ncomms14520).
- [31] W. Demtröder, *An Introduction to Atomic and Molecular Physics*, (Springer 2005).
- [32] C. W. Haigh, *The Theory of Atomic Spectroscopy: jj Coupling, Intermediate Coupling, and Configuration Interaction*, Journal of Chemical Education, 72(3), (1995), 206, doi:[10.1021/ed072p206](https://doi.org/10.1021/ed072p206).
- [33] J. J. Brehm and W. J. Mullin, *Introduction to the Structure of Matter: A Course in Modern Physics*, (John Wiley & Sons 1989).
- [34] J. E. Sturm, *Grid of expressions related to the Einstein coefficients*, Journal of Chemical Education, 67(1), (1990), 32, doi:[10.1021/ed067p32](https://doi.org/10.1021/ed067p32).
- [35] I. V. Hertel and C.-P. Schulz, *Atoms, Molecules and Optical Physics 2: Molecules and Photons - Spectroscopy and Collisions (Graduate Texts in Physics)*, (Springer 2014).

- [36] D. A. Steck, editor, *Quantum and Atom Optics*, (University of Oregon 2007), available online at <http://steck.us/teaching>.
- [37] W. Demtröder, *Laser Spectroscopy*, (Springer 2002).
- [38] T. Kessler, *Development and application of laser technologies at radioactive ion beam facilities*, Ph.D. thesis, University of Jyväskylä (2008).
- [39] B. A. Marsh, *Resonance ionization laser ion sources for on-line isotope separators (invited)*, Review of Scientific Instruments, 85(2), (2014), 02B923, doi:[10.1063/1.4858015](https://doi.org/10.1063/1.4858015).
- [40] S. M. Blinder and C. E. Nordman, *Collision theory of chemical reactions*, Journal of Chemical Education, 51(12), (1974), 790, doi:[10.1021/ed051p790](https://doi.org/10.1021/ed051p790).
- [41] C. Redondo, M. N. Sanchez Rayo, J. A. Fernandez, D. Husain, and F. Castano, *Collisional dynamics of low energy states of atomic strontium following the generation of  $Sr(5s5p\ ^1P_1)$  in the presence of He and Ar*, Physical Chemistry Chemical Physics, 6, (2004), 391, doi:[10.1039/B311711A](https://doi.org/10.1039/B311711A).
- [42] R. K. Namiotka, E. Ehrlacher, J. Sagle, M. Brewer, D. J. Namiotka, A. P. Hickman, A. D. Streater, and J. Huennekens, *Diffusion of barium atoms in the  $6s5d\ ^3D_J$  metastable levels and the  $6s^2\ ^1S_0$  ground state through noble-gas perturbers*, Physical Review A, 54, (1996), 449, doi:[10.1103/PhysRevA.54.449](https://doi.org/10.1103/PhysRevA.54.449).
- [43] E. Ehrlacher and J. Huennekens, *Excitation transfer among, and quenching of, the barium  $6s5d\ ^3D_J$  metastable levels due to collisions with argon, nitrogen, and barium perturbers*, Physical Review A, 50, (1994), 4786, doi:[10.1103/PhysRevA.50.4786](https://doi.org/10.1103/PhysRevA.50.4786).
- [44] J.-P. Visticot, P. de Pujo, O. Sublemontier, A. J. Bell, J. Berlande, J. Cuvellier, T. Gustavsson, A. Lallement, J. M. Mestdagh, P. Meynadier, and A. G. Suits, *Polarization effects in the differential cross section of the  $Ba(^1P_1-^3P_2)$  inelastic transition induced by argon*, Physical Review A, 45, (1992), 6371, doi:[10.1103/PhysRevA.45.6371](https://doi.org/10.1103/PhysRevA.45.6371).
- [45] M. Knoop, M. Vedel, and F. Vedel, *Collisional quenching and  $j$ -mixing rate constants for the 3D levels of  $Ca^+$* , Physical Review A, 58, (1998), 264, doi:[10.1103/PhysRevA.58.264](https://doi.org/10.1103/PhysRevA.58.264).
- [46] M. Knoop, M. Vedel, and F. Vedel, *Lifetime, collisional-quenching, and  $j$ -mixing measurements of the metastable 3D levels of  $Ca^+$* , Physical Review A, 52, (1995), 3763, doi:[10.1103/PhysRevA.52.3763](https://doi.org/10.1103/PhysRevA.52.3763).



- [47] G. Copley, B. P. Kibble, and L. Krause, *Experimental Evidence for the Absence of Quenching of Sodium Resonance Radiation by Inert Gases*, Physical Review, 163, (1967), 34, doi:[10.1103/PhysRev.163.34](https://doi.org/10.1103/PhysRev.163.34).
- [48] M. Czajkowski, R. Bobkowski, and L. Krause, *Depopulation of the  $5^3P_1$  state of cadmium by collisions with ground-state Cd and noble-gas atoms*, Spectrochimica Acta Part B: Atomic Spectroscopy, 46(1), (1991), 1, doi:[10.1016/0584-8547\(91\)80002-K](https://doi.org/10.1016/0584-8547(91)80002-K).
- [49] M. Czajkowski, R. Bobkowski, and L. Krause, *Depopulation of the Zn  $4^3P_1$  state by collisions with ground-state Zn and noble-gas atoms*, Spectrochimica Acta Part B: Atomic Spectroscopy, 46(8), (1991), 1161, doi:[10.1016/0584-8547\(91\)80111-F](https://doi.org/10.1016/0584-8547(91)80111-F).
- [50] D. Nuñez-Reyes, J. Kłos, M. H. Alexander, P. J. Dagdigian, and K. M. Hickson, *Experimental and theoretical investigation of the temperature dependent electronic quenching of O( $^1D$ ) atoms in collisions with Kr*, The Journal of Chemical Physics, 148(12), (2018), 124311, doi:[10.1063/1.5021885](https://doi.org/10.1063/1.5021885).
- [51] M. Lara, C. Berteloite, M. Paniagua, F. Dayou, S. D. Le Picard, and J.-M. Launay, *Experimental and theoretical study of the collisional quenching of S( $^1D$ ) by Ar*, Physical Chemistry Chemical Physics, 19, (2017), 28555, doi:[10.1039/C7CP05279K](https://doi.org/10.1039/C7CP05279K).
- [52] C. Redondo, M. N. S. Rayo, J. A. Fernández, D. Husain, and F. Castaño, *Collisionally induced intramultiplet mixing of Sr( $5^3P_J$ ) metastable states by Ne, Kr and Xe atoms*, Chemical Physics Letters, 331(5), (2000), 365, doi:[10.1016/S0009-2614\(00\)01221-5](https://doi.org/10.1016/S0009-2614(00)01221-5).
- [53] H. J. Yuh and P. J. Dagdigian, *Intramultiplet mixing in collisions of calcium  $4s4p^3P_J^o$  with helium: Measurement of state-to-state cross sections*, Physical Review A, 28, (1983), 63, doi:[10.1103/PhysRevA.28.63](https://doi.org/10.1103/PhysRevA.28.63).
- [54] E. E. Nikitin, *Theory of Nonadiabatic Collision Processes Including Excited Alkali Atoms*, pp. 317–377, (Wiley-Blackwell1975), doi:[10.1002/9780470143803.ch5](https://doi.org/10.1002/9780470143803.ch5).
- [55] A. Berger, J. Billowes, J. Das, S. Dutta, G. Gwinner, C. H. Holbrow, T. Kühn, T. Lauritsen, S. L. Rolston, J. Schecker, G. D. Sprouse, and F. Xu, *A resonance cell for on-line optical spectroscopy of accelerator produced radioactive atoms*, Nuclear Instruments and Methods in Physics Research Section A, 311(1), (1992), 224, doi:[10.1016/0168-9002\(92\)90868-5](https://doi.org/10.1016/0168-9002(92)90868-5).
- [56] A. Kramida, Y. Ralchenko, and J. Reader, *NIST Atomic Spectra Database Levels* (2018), <https://www.nist.gov/pml/atomic-spectra-database>, Accessed on 2018-02-28.

- [57] J. Blaise and J.-F. Wyart, *Selected Constants Energy Levels and Atomic Spectra of Actinides* (2018), <http://web2.lac.u-psud.fr/lac/Database/Contents.html>, Accessed on 2018-03-01.
- [58] G. Sanna and G. Tomassetti, *Introduction to Molecular Beams Gas Dynamics*, (Imperial College Press , Singapore 2014).
- [59] S. P. Tang and J. B. Fenn, *Experimental Determination of the Discharge Coefficients for Critical Flow through an Axisymmetric Nozzle*, *AIAA Journal*, 16(1), (1978), 41, doi:[10.2514/3.60854](https://doi.org/10.2514/3.60854).
- [60] B. S. Bokstein, M. I. Mendeleev, and D. J. Srolovitz, *Thermodynamics and Kinetics in Materials Science : A Short Course*, (OUP Oxford 2005).
- [61] A. Achterberg, *An Introduction to Astrophysical (Magneto)hydrodynamics and Plasmas, Revised Version (Lecture notes of Natuurkundige Grondslagen van de Sterrenkunde A)* (2005).
- [62] S. Chapman and T. G. Cowling, *The Mathematical Theory of Non-uniform Gases: An Account of the Kinetic Theory of Viscosity, Thermal Conduction and Diffusion in Gases*, (Cambridge University Press 1953), 2nd edition, reprint edition.
- [63] O. Reynolds, *III. An experimental investigation of the circumstances which determine whether the motion of water shall be direct or sinuous, and of the law of resistance in parallel channels*, *Proceedings of the Royal Society of London*, 35(224-226), (1883), 84, doi:[10.1098/rspl.1883.0018](https://doi.org/10.1098/rspl.1883.0018).
- [64] B. R. Munson, D. F. Young, and T. H. Okiishi, *Fundamentals of fluid mechanics*, (John Wiley & Sons 1998).
- [65] D. R. Lide, *CRC Handbook of Chemistry and Physics, 84th Edition*, (Taylor & Francis 2003).
- [66] B. H. Mahan, *Mechanism for Ion—Neutral Association Reactions*, *The Journal of Chemical Physics*, 43(9), (1965), 3080, doi:[10.1063/1.1697280](https://doi.org/10.1063/1.1697280).
- [67] E. C. Beaty and P. L. Patterson, *Mobilities and Reaction Rates of Ions in Helium*, *Physical Review*, 137, (1965), A346, doi:[10.1103/PhysRev.137.A346](https://doi.org/10.1103/PhysRev.137.A346).
- [68] T. Martens, A. Bogaerts, W. J. M. Brok, and J. V. Dijk, *The dominant role of impurities in the composition of high pressure noble gas plasmas*, *Applied Physics Letters*, 92(4), (2008), 041504, doi:[10.1063/1.2839613](https://doi.org/10.1063/1.2839613).
- [69] D. J. Morrissey, G. Bollen, M. Facina, and S. Schwarz, *Pulsed extraction of ionization from helium buffer gas*, *Nuclear Instruments and Methods in Physics Research Section B*, 266(21), (2008), 4822, doi:[10.1016/j.nimb.2008.07.018](https://doi.org/10.1016/j.nimb.2008.07.018).

- [70] D. K. Bohme, N. G. Adams, M. Mosesman, D. B. Dunkin, and E. E. Ferguson, *Flowing Afterglow Studies of the Reactions of the Rare-Gas Molecular Ions  $\text{He}_2^+$ ,  $\text{Ne}_2^+$ , and  $\text{Ar}_2^+$  with Molecules and Rare-Gas Atoms*, The Journal of Chemical Physics, 52(10), (1970), 5094, doi:[10.1063/1.1672747](https://doi.org/10.1063/1.1672747).
- [71] V. G. Anicich, U. S. N. Aeronautics, S. Administration, and J. P. L. (U.S.), *An Index of the Literature for Bimolecular Gas Phase Cation-Molecule Reaction Kinetics*, JPL Publication, (Jet Propulsion Laboratory, National Aeronautics and Space Administration (NASA) 2003).
- [72] R. G. Mortimer, *Physical Chemistry*, (Academic Press/Elsevier 2008).
- [73] T. Kessler, I. D. Moore, Y. Kudryavtsev, K. Peräjärvi, A. Popov, P. Ronkanen, T. Sonoda, B. Tordoff, K. Wendt, and J. Äystö, *Off-line studies of the laser ionization of yttrium at the IGISOL facility*, Nuclear Instruments and Methods in Physics Research Section B, 266(4), (2008), 681, doi:[10.1016/j.nimb.2007.11.076](https://doi.org/10.1016/j.nimb.2007.11.076).
- [74] I. D. Moore, *New concepts for the ion guide technique*, Nuclear Instruments and Methods in Physics Research Section B, 266(19), (2008), 4434, doi:[10.1016/j.nimb.2008.05.054](https://doi.org/10.1016/j.nimb.2008.05.054).
- [75] J. Huikari, P. Dendooven, A. Jokinen, A. Nieminen, H. Penttilä, K. Peräjärvi, A. Popov, S. Rinta-Antila, and J. Äystö, *Production of neutron deficient rare isotope beams at IGISOL; on-line and off-line studies*, Nuclear Instruments and Methods in Physics Research Section B, 222(3), (2004), 632, doi:[10.1016/j.nimb.2004.04.164](https://doi.org/10.1016/j.nimb.2004.04.164).
- [76] G. Savard, J. Clark, C. Boudreau, F. Buchinger, J. E. Crawford, H. Geissel, J. P. Greene, S. Gulick, A. Heinz, J. K. P. Lee, A. Levand, M. Maier, G. Münzenberg, C. Scheidenberger, D. Seweryniak, K. S. Sharma, G. Sprouse, J. Vaz, J. C. Wang, B. J. Zabransky, *et al.*, *Development and operation of gas catchers to thermalize fusion-evaporation and fragmentation products*, Nuclear Instruments and Methods in Physics Research Section B, 204, (2003), 582, doi:[10.1016/S0168-583X\(02\)02134-1](https://doi.org/10.1016/S0168-583X(02)02134-1).
- [77] T. Sonoda, T. Tsubota, M. Wada, I. Katayama, T. M. Kojima, and M. Reponen, *A gas circulation and purification system for gas-cell-based low-energy RI-beam production*, Review of Scientific Instruments, 87(6), (2016), 065104, doi:[10.1063/1.4953111](https://doi.org/10.1063/1.4953111).
- [78] Y. Kudryavtsev, B. Bruyneel, M. Huyse, J. Gentens, P. Van den Bergh, P. Van Duppen, and L. Vermeeren, *A gas cell for thermalizing, storing and transporting radioactive ions and atoms. Part I: Off-line studies with*

- a laser ion source*, Nuclear Instruments and Methods in Physics Research Section B, 179(3), (2001), 412, doi:[10.1016/S0168-583X\(01\)00575-4](https://doi.org/10.1016/S0168-583X(01)00575-4).
- [79] D. A. Hutcheon, S. Bishop, L. Buchmann, M. L. Chatterjee, A. A. Chen, J. M. D'Auria, S. Engel, D. Gigliotti, U. Greife, D. Hunter, A. Hussein, C. C. Jewett, N. Khan, M. Lamey, A. Laird, W. Liu, A. Olin, D. Ottewell, J. G. Rogers, G. Roy, *et al.*, *The DRAGON facility for nuclear astrophysics at TRIUMF-ISAC: design, construction and operation*, Nuclear Instruments and Methods in Physics Research Section A, 498(1), (2003), 190, doi:[10.1016/S0168-9002\(02\)01990-3](https://doi.org/10.1016/S0168-9002(02)01990-3).
- [80] J. C. Wikne and E. A. Olsen, *An automatic, low cost recovery system for  $^3\text{He}$* , Nuclear Instruments and Methods in Physics Research, 200(2), (1982), 179, doi:[10.1016/0167-5087\(82\)90429-X](https://doi.org/10.1016/0167-5087(82)90429-X).
- [81] W. Wagner, *New vapour pressure measurements for argon and nitrogen and a new method for establishing rational vapour pressure equations*, Cryogenics, 13(8), (1973), 470, doi:[10.1016/0011-2275\(73\)90003-9](https://doi.org/10.1016/0011-2275(73)90003-9).
- [82] T. T. Nichols and V. P. Utgikar, *Wagner Equation Predicting Entire Curve for Pure Fluids from Limited VLE Data: Error Dependency Upon Data Interval & Fully-Determined Case*, International Journal of Thermodynamics, 21, (2018), 38, doi:[10.5541/ijot.372148](https://doi.org/10.5541/ijot.372148).
- [83] L. A. Forero and J. A. Velásquez, *Wagner liquid–vapour pressure equation constants from a simple methodology*, The Journal of Chemical Thermodynamics, 43(8), (2011), 1235, doi:[10.1016/j.jct.2011.03.011](https://doi.org/10.1016/j.jct.2011.03.011).
- [84] R. E. Bedford, G. Bonnier, H. Maas, and F. Pavese, *Recommended values of temperature on the International Temperature Scale of 1990 for a selected set of secondary reference points*, Metrologia, 33(2), (1996), 133, doi:[10.1088/0026-1394/33/2/3](https://doi.org/10.1088/0026-1394/33/2/3).
- [85] *NIST Standard Reference Database Number 69* (2018), the National Institute of Standards and Technology (NIST) <https://webbook.nist.gov/chemistry/>, Accessed on 2018-05-01.
- [86] R. Span and W. Wagner, *A New Equation of State for Carbon Dioxide Covering the Fluid Region from the Triple-Point Temperature to 1100 K at Pressures up to 800 MPa*, Journal of Physical and Chemical Reference Data, 25(6), (1996), 1509, doi:[10.1063/1.555991](https://doi.org/10.1063/1.555991).
- [87] A. G. M. Ferreira and L. Q. Lobo, *The sublimation of argon, krypton, and xenon*, The Journal of Chemical Thermodynamics, 40(12), (2008), 1621, doi:[10.1016/j.jct.2008.07.023](https://doi.org/10.1016/j.jct.2008.07.023).
- [88] W. Wagner, T. Riethmann, R. Feistel, and A. H. Harvey, *New Equations for the Sublimation Pressure and Melting Pressure of  $\text{H}_2\text{O}$  Ice Ih*,

- Journal of Physical and Chemical Reference Data, 40(4), (2011), 043103, doi:[10.1063/1.3657937](https://doi.org/10.1063/1.3657937).
- [89] K. Jousten, *Handbook of Vacuum Technology, 2nd edition*, (Wiley-VCH 2016).
- [90] S. Cavenati, C. A. Grande, and A. E. Rodrigues, *Adsorption Equilibrium of Methane, Carbon Dioxide, and Nitrogen on Zeolite 13X at High Pressures*, Journal of Chemical & Engineering Data, 49(4), (2004), 1095, doi:[10.1021/je0498917](https://doi.org/10.1021/je0498917).
- [91] S. A. Stern and F. S. DiPaolo, *The Adsorption of Atmospheric Gases on Molecular Sieves at Low Pressures and Temperatures. The Effect of Preadsorbed Water*, Journal of Vacuum Science and Technology, 4(6), (1967), 347, doi:[10.1116/1.1492561](https://doi.org/10.1116/1.1492561).
- [92] Y. Wang, B. Helvensteijn, N. Nizamidin, A. M. Erion, L. A. Steiner, L. M. Mulloth, B. Luna, and M. D. LeVan, *High Pressure Excess Isotherms for Adsorption of Oxygen and Nitrogen in Zeolites*, Langmuir, 27(17), (2011), 10648, doi:[10.1021/la201690x](https://doi.org/10.1021/la201690x).
- [93] A. J. Kidnay and M. J. Hiza, *Physical adsorption in cryogenic engineering*, Cryogenics, 10(4), (1970), 271, doi:[10.1016/0011-2275\(70\)90053-6](https://doi.org/10.1016/0011-2275(70)90053-6).
- [94] A. A. Valverde, G. Bollen, M. Brodeur, R. A. Bryce, K. Cooper, M. Eibach, K. Gulyuz, C. Izzo, D. J. Morrissey, M. Redshaw, R. Ringle, R. Sandler, S. Schwarz, C. S. Sumithrarachchi, and A. C. C. Villari, *First Direct Determination of the Superallowed  $\beta$ -Decay  $Q_{EC}$  Value for  $^{14}\text{O}$* , Physical Review Letters, 114, (2015), 232502, doi:[10.1103/PhysRevLett.114.232502](https://doi.org/10.1103/PhysRevLett.114.232502).
- [95] R. G. Barry and R. J. Chorley, *Atmosphere, Weather, and Climate*, (Taylor & Francis 2010).
- [96] J. B. Laudenslager, W. T. H. Jr., and M. T. Bowers, *Near thermal energy charge transfer reactions of rare gas ions with diatomic and simple polyatomic molecules: The importance of Franck-Condon factors and energy resonance on the magnitude of the rate constants*, The Journal of Chemical Physics, 61(11), (1974), 4600, doi:[10.1063/1.1681779](https://doi.org/10.1063/1.1681779).
- [97] C. Collins, Z. Chen, V. Gylys, H. Jahani, J. Pouvesle, and J. Stevefelt, *The importance of three-body processes to reaction kinetics at atmospheric pressures-I: Archetype reactions of He species with  $\text{N}_2$* , IEEE Journal of Quantum Electronics, 22(1), (1986), 38, doi:[10.1109/JQE.1986.1072863](https://doi.org/10.1109/JQE.1986.1072863).
- [98] V. G. Anicich, J. B. Laudenslager, W. T. H. Jr., and J. H. Futrell, *Product distributions for some thermal energy charge transfer reactions*

- of rare gas ions*, The Journal of Chemical Physics, 67(10), (1977), 4340, doi:[10.1063/1.434579](https://doi.org/10.1063/1.434579).
- [99] P. Karvonen, I. D. Moore, T. Sonoda, T. Kessler, H. Penttilä, K. Peräjärvi, P. Ronkanen, and J. Äystö, *A sextupole ion beam guide to improve the efficiency and beam quality at IGISOL*, Nuclear Instruments and Methods in Physics Research Section B, 266(21), (2008), 4794, doi:[10.1016/j.nimb.2008.07.022](https://doi.org/10.1016/j.nimb.2008.07.022).
- [100] A. Saastamoinen, I. D. Moore, M. Ranjan, P. Dendooven, H. Penttilä, K. Peräjärvi, A. Popov, and J. Äystö, *Characterization of a cryogenic ion guide at IGISOL*, Nuclear Instruments and Methods in Physics Research Section A, 685, (2012), 70, doi:[10.1016/j.nima.2012.05.031](https://doi.org/10.1016/j.nima.2012.05.031).
- [101] S. Purushothaman, P. Dendooven, I. Moore, H. Penttilä, J. Ronkainen, A. Saastamoinen, J. Äystö, K. Peräjärvi, N. Takahashi, and K. Gloos, *Cryogenic helium as stopping medium for high-energy ions*, Nuclear Instruments and Methods in Physics Research Section B, 266(19), (2008), 4488, doi:[10.1016/j.nimb.2008.05.096](https://doi.org/10.1016/j.nimb.2008.05.096).
- [102] S. Purushothaman, M. P. Reiter, E. Haettner, P. Dendooven, T. Dickel, H. Geissel, J. Ebert, C. Jesch, W. R. Plass, M. Ranjan, H. Weick, F. Amjad, S. Ayet, M. Diwisch, A. Estrade, F. Farinon, F. Greiner, N. Kalantar-Nayestanaki, R. Knöbel, J. Kurcewicz, *et al.*, *First experimental results of a cryogenic stopping cell with short-lived, heavy uranium fragments produced at 1000 MeV/u*, EPL (Europhysics Letters), 104(4), (2013), 42001, doi:[10.1209/0295-5075/104/42001](https://doi.org/10.1209/0295-5075/104/42001).
- [103] M. Ranjan, P. Dendooven, S. Purushothaman, T. Dickel, M. P. Reiter, S. Ayet, E. Haettner, I. D. Moore, N. Kalantar-Nayestanaki, H. Geissel, W. R. Plaß, D. Schäfer, C. Scheidenberger, F. Schreuder, H. Timersma, J. Van de Walle, and H. Weick, *Design, construction and cooling system performance of a prototype cryogenic stopping cell for the Super-FRS at FAIR*, Nuclear Instruments and Methods in Physics Research Section A, 770, (2015), 87, doi:[10.1016/j.nima.2014.09.075](https://doi.org/10.1016/j.nima.2014.09.075).
- [104] C. Droese, S. Eliseev, K. Blaum, M. Block, F. Herfurth, M. Laatiaoui, F. Lautenschläger, E. M. Ramirez, L. Schweikhard, V. V. Simon, and P. G. Thirolf, *The cryogenic gas stopping cell of SHIPTRAP*, Nuclear Instruments and Methods in Physics Research Section B, 338, (2014), 126, doi:[10.1016/j.nimb.2014.08.004](https://doi.org/10.1016/j.nimb.2014.08.004).
- [105] Penttilä, H., Elomaa, V. -V., Eronen, T., Hakala, J., Jokinen, A., Kankainen, A., Moore, I. D., Rahaman, S., Rinta-Antila, S., Rissanen, J., Rubchenya, V., Saastamoinen, A., Weber, C., and Äystö, J., *Fission yield studies at the IGISOL facility*, The European Physical Journal A, 48(4), (2012), 43, doi:[10.1140/epja/i2012-12043-4](https://doi.org/10.1140/epja/i2012-12043-4).

- [106] S. El Youbi, *An off-line ion guide quadrupole mass spectrometer system*, Master's thesis, University of Jyväskylä (2017).
- [107] S. A. Ahmad, W. Klempt, R. Neugart, E. W. Otten, P.-G. Reinhard, G. Ulm, and K. Wendt, *Mean square charge radii of radium isotopes and octupole deformation in the  $^{220-228}\text{Ra}$  region*, Nuclear Physics A, 483(2), (1988), 244, doi:[10.1016/0375-9474\(88\)90534-9](https://doi.org/10.1016/0375-9474(88)90534-9).
- [108] B. Cheal and D. H. Forest, *Collinear laser spectroscopy at the new IGISOL 4 facility*, Hyperfine Interactions, 223(1-3), (2014), 223, doi:[10.1007/978-94-007-5555-0\\_22](https://doi.org/10.1007/978-94-007-5555-0_22).
- [109] B. Cheal and D. H. Forest, *Collinear laser spectroscopy techniques at JYFL*, Hyperfine Interactions, 223(1), (2014), 63, doi:[10.1007/s10751-012-0608-5](https://doi.org/10.1007/s10751-012-0608-5).
- [110] M. L. Bissell, K. T. Flanagan, M. D. Gardner, M. Avgoulea, J. Billowes, P. Campbell, B. Cheal, T. Eronen, D. H. Forest, J. Huikari, A. Jokinen, I. D. Moore, A. Nieminen, H. Penttilä, S. Rinta-Antila, B. Tordoff, G. Tungate, and J. Äystö, *On the decrease in charge radii of multi-quasi particle isomers*, Physics Letters B, 645(4), (2007), 330, doi:[10.1016/j.physletb.2006.12.054](https://doi.org/10.1016/j.physletb.2006.12.054).
- [111] S. Raeder, A. Hakimi, N. Stöbener, N. Trautmann, and K. Wendt, *Detection of plutonium isotopes at lowest quantities using in-source resonance ionization mass spectrometry*, Analytical and Bioanalytical Chemistry, 404(8), (2012), 2163, doi:[10.1007/s00216-012-6238-6](https://doi.org/10.1007/s00216-012-6238-6).
- [112] E. F. Worden, L. R. Carlson, S. A. Johnson, J. A. Paisner, and R. W. Solarz, *Ionization potential of neutral atomic plutonium determined by laser spectroscopy*, Journal of the Optical Society of America B, 10(11), (1993), 1998, doi:[10.1364/JOSAB.10.001998](https://doi.org/10.1364/JOSAB.10.001998).
- [113] V. Sonnenschein, I. D. Moore, I. Pohjalainen, M. Reponen, S. Rothe, and K. Wendt, *Intracavity Frequency Doubling and Difference Frequency Mixing for Pulsed ns Ti:Sapphire Laser Systems at On-Line Radioactive Ion Beam Facilities*, Proceedings of the Conference on Advances in Radioactive Isotope Science (ARIS2014), 6, (2015), 030126, doi:[10.7566/JSPSCP.6.030126](https://doi.org/10.7566/JSPSCP.6.030126).
- [114] M. W. J. Chase, editor, *NIST-JANAF Thermochemical Tables 2 Volume-Set (Journal of Physical and Chemical Reference Data Monographs)*, (American Institute of Physics 1998).
- [115] H. Tomita, A. Nakamura, D. Matsui, R. Ohtaka, V. Sonnenschein, K. Saito, K. Kato, M. Ohashi, V. Degner, K. Wendt, M. Morita, T. Sakamoto, T. Kawai, T. Okumura, I. Moore, and T. Iguchi, *Development of Two color Resonance Ionization Scheme for Th using an*

- Automated Wide-Range Tunable Ti:Sapphire Laser System*, Progress in Nuclear Science and technology, 5, (in press).
- [116] P. A. Franken, A. E. Hill, C. W. Peters, and G. Weinreich, *Generation of Optical Harmonics*, Physical Review Letters, 7, (1961), 118, doi:[10.1103/PhysRevLett.7.118](https://doi.org/10.1103/PhysRevLett.7.118).
- [117] P. F. Moulton, *Spectroscopic and laser characteristics of Ti : Al<sub>2</sub>O<sub>3</sub>*, Journal of the Optical Society of America B, 3(1), (1986), 125, doi:[10.1364/JOSAB.3.000125](https://doi.org/10.1364/JOSAB.3.000125).
- [118] V. Sonnenschein, *Laser developments and high resolution resonance ionization spectroscopy of actinide elements*, Ph.D. thesis, University of Jyväskylä (2015).
- [119] D. N. Nikogosyan, *Beta barium borate (BBO)*, Applied Physics A Solids and Surfaces, 52(6), (1991), 359, doi:[10.1007/bf00323647](https://doi.org/10.1007/bf00323647).
- [120] J. Blaise, M. S. Fred, W. T. Carnall, H. M. Crosswhite, and H. Crosswhite, *Measurement and Interpretation of Plutonium Spectra*, chapter 12, pp. 173–198, (American Chemical Society 1983), doi:[10.1021/bk-1983-0216.ch012](https://doi.org/10.1021/bk-1983-0216.ch012).
- [121] E. W. T. Richards and A. Ridgeley, *Preliminary classification in the plutonium I spectrum*, Spectrochimica Acta, 21(9), (1965), 1449, doi:[10.1016/0371-1951\(65\)80057-1](https://doi.org/10.1016/0371-1951(65)80057-1).
- [122] M. Reponen, I. D. Moore, I. Pohjalainen, V. Sonnenschein, and A. Jokinen, *The FURIOS laser ion source at IGISOL-4*, Nuclear Instruments and Methods in Physics Research Section B, 317, (2013), 422, doi:[10.1016/j.nimb.2013.05.061](https://doi.org/10.1016/j.nimb.2013.05.061).
- [123] S. Raeder, B. Bastin, M. Block, P. Creemers, P. Delahaye, R. Ferrer, X. Fléchar, S. Franchoo, L. Ghys, L. P. Gaffney, C. Granados, R. Heinke, L. Hijazi, M. Huyse, T. Kron, Y. Kudryavtsev, M. Laatiaoui, N. Lecesne, F. Luton, I. D. Moore, *et al.*, *Developments towards in-gas-jet laser spectroscopy studies of actinium isotopes at LISOL*, Nuclear Instruments and Methods in Physics Research Section B, 376, (2016), 382, doi:[10.1016/j.nimb.2015.12.014](https://doi.org/10.1016/j.nimb.2015.12.014).
- [124] C. Granados, P. Creemers, R. Ferrer, L. P. Gaffney, W. Gins, R. de Groote, M. Huyse, Y. Kudryavtsev, Y. Martínez, S. Raeder, S. Sels, C. Van Beveren, P. Van den Bergh, P. Van Duppen, K. Wrzosek-Lipska, A. Zadvornaya, A. E. Barzakh, B. Bastin, P. Delahaye, L. Hijazi, *et al.*, *In-gas laser ionization and spectroscopy of actinium isotopes near the N = 126 closed shell*, Physical Review C, 96, (2017), 054331, doi:[10.1103/PhysRevC.96.054331](https://doi.org/10.1103/PhysRevC.96.054331).



- [125] W. Kälber, G. Meisel, J. Rink, and R. C. Thompson, *Two-step Optical Excitation for Doppler Linewidth Reduction and Motion Study of Ions Stored in a Paul Trap*, *Journal of Modern Optics*, 39(2), (1992), 335, doi:[10.1080/09500349214550331](https://doi.org/10.1080/09500349214550331).
- [126] O. A. Herrera-Sancho, M. V. Okhapkin, K. Zimmermann, C. Tamm, E. Peik, A. V. Taichenachev, V. I. Yudin, and P. Głowacki, *Two-photon laser excitation of trapped  $^{232}\text{Th}^+$  ions via the 402-nm resonance line*, *Physical Review A*, 85, (2012), 033402, doi:[10.1103/PhysRevA.85.033402](https://doi.org/10.1103/PhysRevA.85.033402).
- [127] M. Santos, J. Marçalo, A. Pires de Matos, J. K. Gibson, and R. G. Haire, *Gas-Phase Oxidation Reactions of Neptunium and Plutonium Ions Investigated via Fourier Transform Ion Cyclotron Resonance Mass Spectrometry*, *The Journal of Physical Chemistry A*, 106(31), (2002), 7190, doi:[10.1021/jp025733f](https://doi.org/10.1021/jp025733f).
- [128] Y. Liu, C. U. Jost, A. M. II, D. W. Stracener, C. L. Williams, C. J. Gross, R. K. Grzywacz, M. Madurga, K. Miernik, D. Miller, S. Padgett, S. V. Paulauskas, K. P. Rykaczewski, and M. Wolinska-Cichocka, *On-line commissioning of the HRIBF resonant ionization laser ion source*, *Nuclear Instruments and Methods in Physics Research Section B*, 298, (2013), 5, doi:[10.1016/j.nimb.2012.12.041](https://doi.org/10.1016/j.nimb.2012.12.041).
- [129] A. M. Sjödin, N. Lecesne, O. Bajeat, T. Kron, J. Lassen, F. Le Blanc, R. Leroy, L. Maunoury, B. Osmond, S. Raeder, S. Rothe, V. Sonnenshein, and K. Wendt, *Status of GISELE: a resonant ionization laser ion source for the production of radioactive ions at GANIL*, *Hyperfine Interactions*, 216(1), (2013), 121, doi:[10.1007/s10751-013-0846-1](https://doi.org/10.1007/s10751-013-0846-1).
- [130] S. Franchoo, *The Alto Tandem and Isol Facility at IPN Orsay*, volume 6, p. 020041, (The Physical Society of Japan 2015), doi:[10.7566/JPSCP.6.020041](https://doi.org/10.7566/JPSCP.6.020041).
- [131] S. Wilkins, *Collinear resonance ionization spectroscopy of exotic francium and radium isotopes*, Ph.D. thesis, University of Manchester (2017).
- [132] M. Reponen, *Resonance laser ionization developments for IGISOL-4*, Ph.D. thesis, University of Jyväskylä (2012).
- [133] K. Chrysalidis, *RILIS Elements: samarium* (2018), <https://riliselements.web.cern.ch/riliselements/?element=Sm>, Accessed on 2018-03-14.
- [134] L. von der Wense, B. Seiferle, M. Laatiaoui, J. B. Neumayr, H.-J. Maier, H.-F. Wirth, C. Mokry, J. Runke, K. Eberhardt, C. E. Düllmann, N. G. Trautmann, and P. G. Thirolf, *Direct detection of the  $^{229}\text{Th}$  nuclear clock transition*, *Nature*, 533, (2016), 47, doi:[10.1038/nature17669](https://doi.org/10.1038/nature17669).

- [135] L. von der Wense, *On the direct detection of  $^{229\text{m}}\text{Th}$* , Ph.D. thesis, Ludwig Maximilian University of Munich (2016).
- [136] B. R. Beck, J. A. Becker, P. Beiersdorfer, G. V. Brown, K. J. Moody, J. B. Wilhelmy, F. S. Porter, C. A. Kilbourne, and R. L. Kelley, *Energy Splitting of the Ground-State Doublet in the Nucleus  $^{229}\text{Th}$* , Physical Review Letters, 98, (2007), 142501, doi:[10.1103/PhysRevLett.98.142501](https://doi.org/10.1103/PhysRevLett.98.142501).
- [137] B. R. Beck, C. Wu, P. Beiersdorfer, G. V. Brown, J. A. Becker, K. J. Moody, J. B. Wilhelmy, F. S. Porter, C. A. Kilbourne, and R. L. Kelley, *Improved Value for the Energy Splitting of the Ground-State Doublet in the Nucleus  $^{229\text{m}}\text{Th}$* , Proceedings - 12th International Conference on Nuclear Reaction Mechanisms, LLNL-PROC, (2009), 415170.
- [138] C. J. Campbell, A. G. Radnaev, A. Kuzmich, V. A. Dzuba, V. V. Flambaum, and A. Derevianko, *Single-Ion Nuclear Clock for Metrology at the 19th Decimal Place*, Physical Review Letters, 108, (2012), 120802, doi:[10.1103/PhysRevLett.108.120802](https://doi.org/10.1103/PhysRevLett.108.120802).
- [139] E. V. Tkalya, *Proposal for a Nuclear Gamma-Ray Laser of Optical Range*, Physical Review Letters, 106, (2011), 162501, doi:[10.1103/PhysRevLett.106.162501](https://doi.org/10.1103/PhysRevLett.106.162501).
- [140] E. Litvinova, H. Feldmeier, J. Dobaczewski, and V. Flambaum, *Nuclear structure of lowest  $^{229}\text{Th}$  states and time-dependent fundamental constants*, Physical Review C, 79, (2009), 064303, doi:[10.1103/PhysRevC.79.064303](https://doi.org/10.1103/PhysRevC.79.064303).
- [141] V. V. Flambaum, *Enhanced Effect of Temporal Variation of the Fine Structure Constant and the Strong Interaction in  $^{229}\text{Th}$* , Physical Review Letters, 97, (2006), 092502, doi:[10.1103/PhysRevLett.97.092502](https://doi.org/10.1103/PhysRevLett.97.092502).
- [142] J. Thielking, M. V. Okhapkin, P. Glowacki, D. M. Meier, L. von der Wense, B. Seiferle, C. E. Düllmann, P. G. Thirolf, and E. Peik, *Laser spectroscopic characterization of the nuclear-clock isomer  $^{229\text{m}}\text{Th}$* , Nature, 556(7701), (2018), 321, doi:[10.1038/s41586-018-0011-8](https://doi.org/10.1038/s41586-018-0011-8).
- [143] V. Sonnenschein, S. Raeder, A. Hakimi, I. D. Moore, and K. Wendt, *Determination of the ground-state hyperfine structure in neutral  $^{229}\text{Th}$* , Journal of Physics B: Atomic, Molecular and Optical Physics, 45(16), (2012), 165005, doi:[10.1088/0953-4075/45/16/165005](https://doi.org/10.1088/0953-4075/45/16/165005).
- [144] W. Kälber, J. Rink, K. Bekk, W. Faubel, S. Göring, G. Meisel, H. Rebel, and R. C. Thompson, *Nuclear radii of thorium isotopes from laser spectroscopy of stored ions*, Zeitschrift für Physik A Atomic Nuclei, 334(1), (1989), 103, doi:[10.1007/BF01294392](https://doi.org/10.1007/BF01294392).

- [145] C. J. Campbell, A. G. Radnaev, and A. Kuzmich, *Wigner Crystals of  $^{229}\text{Th}$  for Optical Excitation of the Nuclear Isomer*, Physical Review Letters, 106, (2011), 223001, doi:[10.1103/PhysRevLett.106.223001](https://doi.org/10.1103/PhysRevLett.106.223001).
- [146] E. V. Tkalya, C. Schneider, J. Jeet, and E. R. Hudson, *Radiative lifetime and energy of the low-energy isomeric level in  $^{229}\text{Th}$* , Physical Review C, 92, (2015), 054324, doi:[10.1103/PhysRevC.92.054324](https://doi.org/10.1103/PhysRevC.92.054324).
- [147] E. Ruchowska, W. A. Plóciennik, J. Żylicz, H. Mach, J. Kvasil, A. Algora, N. Amzal, T. Bäck, M. G. Borge, R. Boutami, P. A. Butler, J. Cederkäll, B. Cederwall, B. Fogelberg, L. M. Fraile, H. O. U. Fynbo, E. Hagebø, P. Hoff, H. Gausemel, A. Jungclaus, *et al.*, *Nuclear structure of  $^{229}\text{Th}$* , Physical Review C, 73, (2006), 044326, doi:[10.1103/PhysRevC.73.044326](https://doi.org/10.1103/PhysRevC.73.044326).
- [148] B. Seiferle, L. von der Wense, and P. G. Thirolf, *Lifetime Measurement of the  $^{229}\text{Th}$  Nuclear Isomer*, Physical Review Letters, 118, (2017), 042501, doi:[10.1103/PhysRevLett.118.042501](https://doi.org/10.1103/PhysRevLett.118.042501).
- [149] N. Trautmann, *Accurate determination of the first ionization potential of actinides by laser spectroscopy*, Journal of Alloys and Compounds, 213-214, (1994), 28, doi:[10.1016/0925-8388\(94\)90876-1](https://doi.org/10.1016/0925-8388(94)90876-1).
- [150] F. F. Karpešhin and M. B. Trzhaskovskaya, *Impact of the electron environment on the lifetime of the  $^{229}\text{Th}^m$  low-lying isomer*, Physical Review C, 76, (2007), 054313, doi:[10.1103/PhysRevC.76.054313](https://doi.org/10.1103/PhysRevC.76.054313).
- [151] S. G. Porsev, V. V. Flambaum, E. Peik, and C. Tamm, *Excitation of the Isomeric  $^{229m}\text{Th}$  Nuclear State via an Electronic Bridge Process in  $^{229}\text{Th}^+$* , Physical Review Letters, 105, (2010), 182501, doi:[10.1103/PhysRevLett.105.182501](https://doi.org/10.1103/PhysRevLett.105.182501).
- [152] Y. Liu and D. W. Stracener, *A resonant ionization laser ion source at ORNL*, Nuclear Instruments and Methods in Physics Research Section B, 376, (2016), 68, doi:[10.1016/j.nimb.2015.12.015](https://doi.org/10.1016/j.nimb.2015.12.015).
- [153] Y. Liu, *Oak Ridge National Laboratory, Private communication by email* (April, 2018).
- [154] V. Sonnenschein, I. D. Moore, S. Raeder, A. Hakimi, A. Popov, and K. Wendt, *The search for the existence of  $^{229m}\text{Th}$  at IGISOL*, The European Physical Journal A, 48(4), (2012), 52, doi:[10.1140/epja/i2012-12052-3](https://doi.org/10.1140/epja/i2012-12052-3).
- [155] R. Ferrer, N. Bree, T. E. Cocolios, I. G. Darby, H. D. Witte, W. Dexters, J. Diriken, J. Elseviers, S. Franchoo, M. Huyse, N. Kesteloot, Y. Kudryavtsev, D. Pauwels, D. Radulov, T. Roger, H. Savajols, P. Van Duppen, and M. Venhart, *In-gas-cell laser ionization spectroscopy in the vicinity of  $^{100}\text{Sn}$ : Magnetic moments and mean-square charge radii of*

- N=50–54 Ag*, Physics Letters B, 728, (2014), 191, doi:[10.1016/j.physletb.2013.11.055](https://doi.org/10.1016/j.physletb.2013.11.055).
- [156] T. Sonoda, T. E. Cocolios, J. Gentens, M. Huyse, O. Ivanov, Y. Kudryavtsev, D. Pauwels, P. Van den Bergh, and P. Van Duppen, *The Laser Ion Source Trap (LIST) coupled to a gas cell catcher*, Nuclear Instruments and Methods in Physics Research Section B, 267(17), (2009), 2918, doi:[10.1016/j.nimb.2009.06.085](https://doi.org/10.1016/j.nimb.2009.06.085).
- [157] S. Geldhof, S. El Youbi, I. D. Moore, I. Pohjalainen, V. Sonnenschein, R. Terabayashi, and A. Voss, *Development of a saturated absorption spectroscopy setup at IGISOL for characterisation of Fabry-Pérot interferometers*, Hyperfine Interactions, 238(1), (2016), 7, doi:[10.1007/s10751-016-1385-3](https://doi.org/10.1007/s10751-016-1385-3).
- [158] J. P. Marangos, *Electromagnetically induced transparency*, Journal of Modern Optics, 45(3), (1998), 471, doi:[10.1080/09500349808231909](https://doi.org/10.1080/09500349808231909).
- [159] S. Zhou, J. Li, M. Schlangen, and H. Schwarz, *Spin-Selective Thermal Activation of Methane by Closed-Shell [TaO<sub>3</sub>]<sup>+</sup>*, Angewandte Chemie International Edition, 55(25), (2016), 7257, doi:[10.1002/anie.201601965](https://doi.org/10.1002/anie.201601965).
- [160] E. Uggerud and P. J. Derrick, *Theory of collisional activation of macromolecules. Impulsive collisions of organic ions*, The Journal of Physical Chemistry, 95(3), (1991), 1430, doi:[10.1021/j100156a073](https://doi.org/10.1021/j100156a073).
- [161] *Simion v8.1*, [www.simion.com](http://www.simion.com). Scientific Instrument Services, Ringoes, NJ, USA.
- [162] S. Zhou, M. Schwarz, and H. Schwarz, *Technical University of Berlin, Private communication by email* (October, 2017).
- [163] R. Johnsen and M. A. Biondi, *Mobilities of Uranium and Mercury Ions in Helium*, The Journal of Chemical Physics, 57s(12), (1972), 5292, doi:[10.1063/1.1678220](https://doi.org/10.1063/1.1678220).
- [164] V. Barci, G. Ardisson, G. Barci-Funel, B. Weiss, O. El Samad, and R. K. Sheline, *Nuclear structure of <sup>229</sup>Th from  $\gamma$ -ray spectroscopy study of <sup>233</sup>U  $\alpha$ -particle decay*, Physical Review C, 68, (2003), 034329, doi:[10.1103/PhysRevC.68.034329](https://doi.org/10.1103/PhysRevC.68.034329).
- [165] A. H. Jaffey, K. F. Flynn, W. C. Bentley, and J. O. Karttunen, *New determination of the <sup>233</sup>U specific activity and half-life*, Physical Review C, 9, (1974), 1991, doi:[10.1103/PhysRevC.9.1991](https://doi.org/10.1103/PhysRevC.9.1991).
- [166] Z. Varga, A. Nicholl, and K. Mayer, *Determination of the <sup>229</sup>Th half-life*, Physical Review C, 89, (2014), 064310, doi:[10.1103/PhysRevC.89.064310](https://doi.org/10.1103/PhysRevC.89.064310).

- [167] L. von der Wense, B. Seiferle, M. Laatiaoui, and P. G. Thirolf, *Determination of the extraction efficiency for  $^{233}\text{U}$  source  $\alpha$ -recoil ions from the MLL buffer-gas stopping cell*, The European Physical Journal A, 51(3), (2015), 29, doi:[10.1140/epja/i2015-15029-8](https://doi.org/10.1140/epja/i2015-15029-8).
- [168] B. Tordoff, *Development of resonance ionization techniques at the Jyväskylä IGISOL*, Ph.D. thesis, University of Manchester (2007).
- [169] J. F. Ziegler, M. D. Ziegler, and J. P. Biersack, *SRIM – The stopping and range of ions in matter (2010)*, Nuclear Instruments and Methods in Physics Research Section B, 268(11), (2010), 1818, doi:[10.1016/j.nimb.2010.02.091](https://doi.org/10.1016/j.nimb.2010.02.091).
- [170] A. K. Jain, R. Raut, and J. K. Tuli, *Nuclear Data Sheets for  $A = 225$* , Nuclear Data Sheets, 110(6), (2009), 1409, doi:[10.1016/j.nds.2009.04.003](https://doi.org/10.1016/j.nds.2009.04.003).
- [171] M. Putkonen, T. Sajavaara, L. Niinistö, and J. Keinonen, *Analysis of ALD-processed thin films by ion-beam techniques*, Analytical and Bioanalytical Chemistry, 382(8), (2005), 1791, doi:[10.1007/s00216-005-3365-3](https://doi.org/10.1007/s00216-005-3365-3).
- [172] G. Friedbacher and H. Bubert, editors, *Surface and Thin Film Analysis: A Compendium of Principles, Instrumentation, and Applications*, (Wiley-VCH 2011).
- [173] H. R. Verma, editor, *Atomic and Nuclear Analytical Methods*, (Springer 2007).
- [174] M. Mayer, *SIMNRA, a simulation program for the analysis of NRA, RBS and ERDA*, AIP Conference Proceedings, 475(1), (1999), 541, doi:[10.1063/1.59188](https://doi.org/10.1063/1.59188).
- [175] V. S. Yemel'Yanov, A. I. Yevstyukhin, and J. V. Dunworth, *The Metallurgy of Nuclear Fuel: Properties and Principles of the Technology of Uranium, Thorium and Plutonium*, (Pergamon Press 1969).
- [176] R. Spohr, P. M. Guyon, W. A. Chupka, and J. Berkowitz, *Threshold Photoelectron Detector for Use in the Vacuum Ultraviolet*, Review of Scientific Instruments, 42(12), (1971), 1872, doi:[10.1063/1.1685027](https://doi.org/10.1063/1.1685027).
- [177] J.-F. Wyart and V. Kaufman, *Extended Analysis of Doubly Ionized Thorium ( $\text{Th III}$ )*, Physica Scripta, 24(6), (1981), 941, doi:[10.1088/0031-8949/24/6/006](https://doi.org/10.1088/0031-8949/24/6/006).
- [178] O. A. Herrera-Sancho, N. Nemitz, M. V. Okhapkin, and E. Peik, *Energy levels of  $\text{Th}^+$  between 7.3 and 8.3 eV*, Physical Review A, 88, (2013), 012512, doi:[10.1103/PhysRevA.88.012512](https://doi.org/10.1103/PhysRevA.88.012512).

- [179] E. B. Saloman, *Energy Levels and Observed Spectral Lines of Krypton, Kr I through Kr XXXVI*, Journal of Physical and Chemical Reference Data, 36(1), (2007), 215, doi:[10.1063/1.2227036](https://doi.org/10.1063/1.2227036).
- [180] I. Velchev, W. Hogervorst, and W. Ubachs, *Precision VUV spectroscopy of Ar I at 105 nm*, Journal of Physics B: Atomic, Molecular and Optical Physics, 32(17), (1999), L511.
- [181] *COMSOL Multiphysics v5.0*, [www.comsol.com](http://www.comsol.com). COMSOL AB, Stockholm, Sweden.
- [182] *COMSOL 5.0 CFD Module User's Guide* (2014), comsol 5.0.
- [183] D. C. Wilcox, *Turbulence Modeling for CFD (Second Edition)*, (D C W Industries 1998).
- [184] A. Bondi, *van der Waals Volumes and Radii*, The Journal of Physical Chemistry, 68(3), (1964), 441, doi:[10.1021/j100785a001](https://doi.org/10.1021/j100785a001).
- [185] V. V. Elomaa, T. Eronen, U. Hager, J. Hakala, A. Jokinen, A. Kankainen, I. D. Moore, S. Rahaman, J. Rissanen, V. Rubchenya, C. Weber, and J. Äystö, *Light-ion-induced reactions in mass measurements of neutron-deficient nuclides close to  $A = 100$* , The European Physical Journal A, 40(1), (2009), 1, doi:[10.1140/epja/i2008-10732-1](https://doi.org/10.1140/epja/i2008-10732-1).
- [186] T. Eronen, V. S. Kolhinen, V. V. Elomaa, D. Gorelov, U. Hager, J. Hakala, A. Jokinen, A. Kankainen, P. Karvonen, S. Kopecky, I. D. Moore, H. Penttilä, S. Rahaman, S. Rinta-Antila, J. Rissanen, A. Saastamoinen, J. Szerypo, C. Weber, and J. Äystö, *JYFLTRAP: a Penning trap for precision mass spectroscopy and isobaric purification*, The European Physical Journal A, 48(4), (2012), 46, doi:[10.1140/epja/i2012-12046-1](https://doi.org/10.1140/epja/i2012-12046-1).
- [187] V. S. Kolhinen, T. Eronen, D. Gorelov, J. Hakala, A. Jokinen, K. Jokiranta, A. Kankainen, M. Koikkalainen, J. Koponen, H. Kulmala, M. Lantz, A. Mattera, I. D. Moore, H. Penttilä, T. Pikkarainen, I. Pohjalainen, M. Reponen, S. Rinta-Antila, J. Rissanen, C. R. Triguero, *et al.*, *Recommissioning of JYFLTRAP at the new IGISOL-4 facility*, Nuclear Instruments and Methods in Physics Research Section B, 317, (2013), 506, doi:[10.1016/j.nimb.2013.07.050](https://doi.org/10.1016/j.nimb.2013.07.050).
- [188] *The Chart of Nuclides* (2018), national Nuclear Data Center, <http://www.nndc.bnl.gov/chart/index.jsp>, Accessed on 2018-04-15.
- [189] A. J. Koning, S. Hilaire, and M. C. Duijvestijn, *TALYS-1.0*, International Conference on Nuclear Data for Science and Technology, p. 211, doi:[10.1051/ndata:07767](https://doi.org/10.1051/ndata:07767).

- [190] E. Browne, *Nuclear Data Sheets for A = 215, 219, 223, 227, 231*, Nuclear Data Sheets, 93(4), (2001), 763, doi:[10.1006/ndsh.2001.0016](https://doi.org/10.1006/ndsh.2001.0016).
- [191] H. C. Suk, J. E. Crawford, and R. B. Moore, *Absolute ( $p, xn$ ) cross-section measurements on  $^{232}\text{Th}$* , Nuclear Physics A, 218(2), (1974), 418, doi:[10.1016/0375-9474\(74\)90014-1](https://doi.org/10.1016/0375-9474(74)90014-1).
- [192] M. Lefort, G. N. Simonoff, and X. Tarrago, *Réactions nucléaires de spallation induites sur le thorium par des protons de 150 et 82 MeV*, Nuclear Physics, 25, (1961), 216, doi:[10.1016/0029-5582\(61\)90154-7](https://doi.org/10.1016/0029-5582(61)90154-7).
- [193] W. W. Meinke, G. C. Wick, and G. T. Seaborg, *High-energy excitation functions in the heavy region*, Journal of Inorganic and Nuclear Chemistry, 3(2), (1956), 69, doi:[10.1016/0022-1902\(56\)80071-7](https://doi.org/10.1016/0022-1902(56)80071-7).
- [194] N. Otuka, E. Dupont, V. Semkova, B. Pritychenko, A. I. Blokhin, M. Aikawa, S. Babykina, M. Bossant, G. Chen, S. Dunaeva, R. A. Forrest, T. Fukahori, N. Furutachi, S. Ganesan, Z. Ge, O. O. Gritzay, M. Herman, S. Hlavač, K. Katō, B. Lalremruata, *et al.*, *Towards a More Complete and Accurate Experimental Nuclear Reaction Data Library (EXFOR): International Collaboration Between Nuclear Reaction Data Centres (NRDC)*, Nuclear Data Sheets, 120, (2014), 272, doi:[10.1016/j.nds.2014.07.065](https://doi.org/10.1016/j.nds.2014.07.065).
- [195] K. B. Gikal, E. M. Kozulin, A. A. Bogachev, N. T. Burtebaev, A. V. Edomskiy, I. M. Itkis, M. G. Itkis, G. N. Knyazhev, K. V. Kovalchuk, T. N. Kvochkina, E. Piasecki, V. A. Rubchenya, S. K. Sahiev, W. H. Trzaska, and E. Vardaci, *Proton induced fission of  $^{232}\text{Th}$  at intermediate energies*, Physics of Atomic Nuclei, 79(9), (2016), 1367, doi:[10.1134/S1063778816090040](https://doi.org/10.1134/S1063778816090040).
- [196] R. Haas, S. Lohse, C. E. Düllmann, K. Eberhardt, C. Mokry, and J. Runke, *Development and characterization of a Drop-on-Demand inkjet printing system for nuclear target fabrication*, Nuclear Instruments and Methods in Physics Research Section A, 874, (2017), 43, doi:[10.1016/j.nima.2017.08.027](https://doi.org/10.1016/j.nima.2017.08.027).
- [197] Y. Kudryavtsev, R. Ferrer, M. Huyse, P. Van den Bergh, and P. Van Duppen, *The in-gas-jet laser ion source: Resonance ionization spectroscopy of radioactive atoms in supersonic gas jets*, Nuclear Instruments and Methods in Physics Research Section B, 297, (2013), 7, doi:[10.1016/j.nimb.2012.12.008](https://doi.org/10.1016/j.nimb.2012.12.008).